Dissertation zur Erlangung des Doktorgrades

der Fakultät für Chemie und Pharmazie

der Ludwig-Maximilians-Universität München

Structural Possibilities of 3rd and 4th Main Group Nitridophosphates

Sebastian Josef Ambach

aus

Speyer, Deutschland

2024

Erklärung

Diese Dissertation wurde im Sinne von §7 der Promotionsordnung vom 28. November 2011 von Herrn Prof. Dr. Wolfgang Schnick betreut.

Eidesstattliche Versicherung

Diese Dissertation wurde eigenständig und ohne unerlaubte Hilfsmittel erarbeitet.

München, den 06.06.2024

_____

Sebastian Josef Ambach

Dissertation eingereicht am:	17.05.2024
1. Gutachter:	Prof. Dr. Wolfgang Schnick
2. Gutachter:	Prof. Dr. Dirk Johrendt
Mündliche Prüfung am:	13.08.2024

Die reinste Form des Wahnsinns ist es,

alles beim Alten zu belassen und zu hoffen,

dass sich etwas ändert.

− Albert Einstein −

Danksagung

Mein besonderer Dank gilt meinem Doktorvater Herrn Prof. Dr. Wolfgang Schnick für die freundliche Aufnahme in seine Arbeitsgruppe und die Möglichkeit, dort meine Doktorarbeit anfertigen zu können. Vielen Dank für die stetige Unterstützung, bereits beginnend mit der Bachelorarbeit im Jahr 2017. Außerdem danke ich für die große Freiheit bei der Gestaltung meiner eigenen Forschung und die zahlreichen zur Verfügung stehenden Mittel zur Synthese und Analytik.

Ein großer Dank gilt auch Herrn Prof. Dr. Dirk Johrendt für die prompte Übernahme des Zweitgutachtens meiner Dissertation.

Des Weiteren danke ich Herrn Prof. Dr. Oliver Oeckler, Frau Prof. Dr. Silvia Markic, Herrn Prof. Dr. Thomas Klapötke und Herrn Prof. Dr. Hans-Christian Böttcher für die prompte und bereitwillige Teilnahme als Prüfer und Prüferinnen in meinem Rigorosum.

Ein herzlicher Dank gilt Dr. Sebastian Vogel, der mich während der Bachelorarbeit für die Festkörperchemie begeistern konnte, mich während der Masterarbeit sehr unterstützt hat und schließlich allerlei Hilfestellung zum Beginn meiner Promotion gegeben hat. Dies alles hat mir den Einstieg in das wissenschaftliche Arbeiten und die selbstständige Forschung erheblich erleichtert.

Meinen Praktikantinnen und Praktikanten Philip Sebrantke, Jan Becker, Sophie Falkai und Tim Reska danke ich für ihre tatkräftige Unterstützung bei meinen Forschungsprojekten und ihr Interesse an der Festkörperchemie. Aus den meisten ihrer jeweiligen Projekte sind schöne Arbeiten hervorgegangen.

Thomas Miller und Dr. Dieter Rau danke ich für die Hilfe bei Betreuung der Pulverdiffraktometer und gelegentlichen Hochtemperatur-Messungen. Wolfgang Wünschheim gilt mein Dank für die Unterstützung bei zahlreichen EDV-technischen Herausforderungen. Christian Minke danke ich für die Messung eine Vielzahl an NMR-Spektren und EDX-Proben. Dr. Peter Mayer und Reinhard Pritzl danke ich für die Messung vieler nicht immer streustarker Einkristalle.

Frau Olga Lorenz danke ich für die zuverlässige Bewältigung allerlei organisatorischer Aufgaben.

Des Weiteren möchte ich mich bei allen Kooperationspartnern und Kooperationspartnerinnen bedanken: Monika Pointner und Oliver Oeckler für die Mikrofokusmessungen am DESY, Kristian Witthaut für schnelle DFT-Berechnungen bei verschiedensten Fragestellungen, Dr. Shrikant Bhat und Dr. Robert Farla für die großzügige Bereitstellung von Messzeit und experimentelle Hilfe an der Hochdruckpresse am DESY, Reinhard Pritzl und Stefanie Schneider für die tägliche und nächtliche Unterstützung bei Experimenten an vorheriger, Maxim Bykov, Elena Bykova und Georg Krach für das zur Verfügung stellen von Messzeit für Diamantstempelzellen und die Auswertung der Daten, Thomas Bräuniger für die kompetente Auswertung und Diskussion von NMR-Spektren, sowie Aylin Koldemir und Rainer Pöttgen für die Messung von Sn-Mößbauer Spektren. Ohne diese Hilfe wäre keine der Publikationen in der jeweiligen Form möglich gewesen.

Meinen ehemaligen und gegenwärtigen Laborkolleginnen, Laborkollegen und Freunden Dr. Sebastian Vogel, Dr. Sebastian Wendl, Dr. Stefanie Schneider, Reinhard Pritzl, Marwin Dialer, Georg Krach und Amalina Buda möchte ich für eine sehr schöne, kurzweilige und interessante Zeit in D2.110 danken, bei der Spaß und wissenschaftliche Diskussionen nie zu kurz kamen. Laborübergreifend gilt außerdem mein Dank Mirjam Zipkat, Stefan Rudel, Than Chau, Florian Engelsberger, Sophia Wandelt, Jennifer Steinadler und Monika Pointner für Hilfe bei (zumeist) wissenschaftlichen Fragestellungen und Unternehmungen außerhalb der Universität.

Zudem möchte ich allen Mitgliedern der Arbeitskreise Schnick, Johrendt und Lotsch für die angenehme Arbeitsatmosphäre und Zeit im zweiten Stockwerk danken.

Ein herzlicher Dank gilt auch all meinen Freundinnen und Freunden außerhalb der Universität. Die zahlreichen Schafkopfabende, Bergtouren und sonstigen Unternehmungen waren ein großartiger Ausgleich zu der täglichen Arbeit im Labor.

Zuletzt, aber vielleicht am wichtigsten, will ich meinen Eltern Angelika und Eberhard, meinen Großeltern Hildegard und Josef sowie meinen Geschwistern Andreas und Isabella danken. Ohne deren Unterstützung während der langen Jahre des Studiums wäre ich nicht dahin gelangt, wo ich jetzt bin.

Table of Contents

1 Introduction 1

1.1 Nitrogen on Planet Earth 1
1.2 Nitride Materials 2
1.3 Nitridophosphates – Structural Chemistry and Application 3
1.4 3rd and 4th Main Group Cations in Nitrides 5
1.5 3rd and 4th Main Group Nitridophosphates 6
1.6 Nitridophosphate Syntheses – Challenges and Techniques 9
1.7 Large-Volume Press and Diamond Anvil Cell 10
1.8 Reaction Mechanisms in Inorganic Chemistry 12
1.9 Scope of this Thesis 14
1.10 References 16

2 Combining *M*N_6 Octahedra and PN_5 Trigonal Bipyramids in the Mica-like Nitridophosphates *M*P_6N_{11} (*M* = Al, In) 22

2.1 Introduction 23
2.2 Results and Discussion 24
2.3 Summary 29
2.4 Acknowledgements 29
2.5 References 30

3 Structural Influence of Lone Pairs in GeP_2N_4, a Germanium(II) Nitridophosphate 33

3.1 Introduction 34
3.2 Results and Discussion 35
3.3 Summary 39
3.4 Acknowledgements 40
3.5 References 41

4 Building Nitridic Networks with Phosphorus and Germanium – from $Ge^{II}P_2N_4$ to $Ge^{IV}PN_3$ 44

4.1 Introduction 45
4.2 Experimental Section 46
4.3 Results and Discussion 49
4.4 Conclusion 54
4.5 Acknowledgements 55
4.6 References 56

5 Mixed Tin Valence in the Tin(II/IV)-Nitridophosphate $Sn_3P_8N_{16}$ 60

5.1 Introduction 61
5.2 Results and Discussion 62
5.3 Conclusion 70
5.4 Experimental Section 70
5.5 Acknowledgements 73
5.6 References 74

6 Nitride Synthesis Under High-Pressure High-Temperature Conditions – Unprecedented *in-situ* Insight into the Reaction 78

6.1 Introduction 79
6.2 Experimental Section 81
6.3 Results and Discussion 84
6.4 Conclusion 91
6.5 Acknowledgements 92
6.6 References 93

7 Summary 95

7.1 Combining MN_6 Octahedra and PN_5 Trigonal Bipyramids in the Mica-like Nitridophosphates MP_6N_{11} (*M* = Al, In) 96
7.2 Structural Influence of Lone Pairs in GeP_2N_4, a Germanium(II) Nitridophosphate 97
7.3 Building Nitridic Networks with Phosphorus and Germanium – from $Ge^{II}P_2N_4$ to $Ge^{IV}PN_3$ 98
7.4 Mixed Tin Valence in the Tin(II/IV)-Nitridophosphate $Sn_3P_8N_{16}$ 99
7.5 Nitride Synthesis Under High-Pressure High-Temperature Conditions – Unprecedented *in-situ* Insight into the Reaction 100

8 Discussion and Outlook 101

8.1 Progress in 3rd and 4th Main Group Nitridophosphates 101
8.2 Insight into a Reaction Mechanism 103
8.3 Concluding Synopsis 105
8.4 References 106

9 Appendix 108

9.1 Supporting Information for Chapter 2 108
9.2 Supporting Information for Chapter 3 123
9.3 Supporting Information for Chapter 4 137
9.4 Supporting Information for Chapter 5 152
9.5 Supporting Information for Chapter 6 159

10 Miscellaneous 162

10.1 List of Publications in this Thesis 162

10.2 List of Publications beyond this Thesis 164

10.3 Conference Contributions and Oral Presentations 165

10.4 Deposited Crystal Structures 166

Chapter 1

Introduction

1.1 Nitrogen on Planet Earth

It is invisible, yet omnipresent in the environment and essential for life on planet Earth − nitrogen. Besides oxygen (20.95 vol-%), argon (0.93 vol-%) and trace gases such as CO_2, Ne and He (all combined 0.04 vol-%), Earth's atmosphere consists of 78.08 vol-% gaseous N_2 molecules (Figure 1.1).[1] Under ambient conditions, the N_2 molecule is considered chemically inert due to its stable triple bond (941 $kJ \cdot mol^{-1}$), negative electron affinity (−0.07 eV) and negative redox potential (E^0 = −0.736 V | $N_{2(g)}$, NH_3/OH^-).[2–4] Using the nitrogenase enzyme family, however, bacteria are able to reduce N_2 molecules to ammonia (NH_3) and subsequently various ammonium (NH_4^+) salts, known as nitrogen fixation.[5] The ammonium salts can be oxidized to nitrite (NO_2^-) and nitrate (NO_3^-) species in a process called nitrification.[6] On the one hand, nitrates serve as nutrients for plants (assimilation), which in turn are degraded again to ammonium salts by bacteria and fungi (ammonification).[7] On the other hand, nitrates can be denitrified and released as molecular N_2, completing the nitrogen cycle.[8]

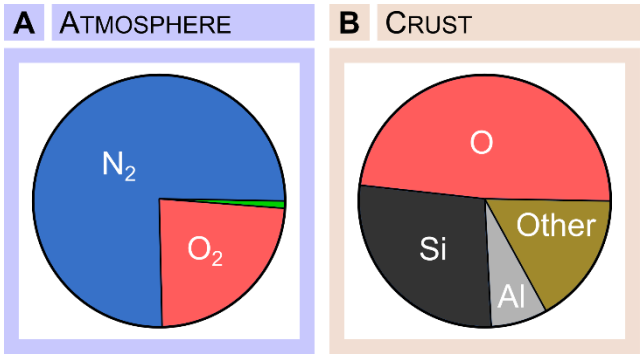

Figure 1.1: While the main constituent of Earth's atmosphere is molecular N_2 (A), Earth's crust is mostly comprised of oxidic materials (B). This is due to the different reactivities of the O_2 and N_2 molecule and the omnipresence of water. Fractions are displayed in weight-%.[9]

While nature has developed the cycle outlined above to include nitrogen in organic life, inorganic minerals are mostly of oxidic nature. Compared to N_2 and without catalytic activity, O_2 is much more reactive due to its predominant diradical form (nominal double bond energy: 498 $kJ \cdot mol^{-1}$), positive electron affinity (+1.46 eV) and high redox potential (E^0 = +1.229 V | $O_{2(g)}$, $H^+/H_2O_{(l)}$).[2,4,10] Only very rarely, naturally occurring nitrides such as sinoite (Si_2N_2O),

osbornite (TiN), nierite (Si_3N_4), siderazot (Fe_5N_2), carlsbergite (CrN), quingsongite (BN) or rodalite ($(Fe,Ni)_4N$) are encountered.[11–17] These examples are mostly found within meteorites, where extreme pressures and temperatures have activated nitrogen for chemical reactions.

Nevertheless, nitride materials are essential for modern high-performance applications, which is why research on synthetic nitrides is considered a hot topic. On the following pages, section 1.2 gives a short overview over structures and applications of the most important third and fourth main group nitrides. Section 1.3 continues with a more detailed view on a fifth main group nitride class, phosphorus nitrides and nitridophosphates. Section 1.4 addresses the cations relevant for this thesis, which are Al, In, Ge, and Sn. The structural part is completed in section 1.5 with an overview over all currently known third and fourth main group nitridophosphates, with the exclusion of the results of this thesis. The remaining sections focus on the practical side of nitride chemistry and provide an overview over nitridophosphate syntheses (1.6), with a highlight on high-pressure methods (1.7), and inorganic reaction mechanisms (1.8).

1.2 Nitride Materials

Since the term “nitride” covers a wide range of materials, compounds are often subclassed by their network forming cations.

Boron nitrides and nitridoborates are comprised of B in oxidation state +III and N in oxidation state −III. The probably best-known representative, binary boron nitride (BN), occurs in three modifications: the ambient-pressure modification hexagonal boron nitride (*h*-BN) as well as the high-pressure modifications cubic boron nitride (*c*-BN) and wurtzite-type boron nitride (*w*-BN).[18] *h*-BN has a graphite-like structure with stacked layers of hexagonal rings, consisting of three boron and three nitrogen atoms each.[19] Unlike in graphite, the hexagonal rings are stacked on top of each other without shifting, creating columns of alternating B and N atoms perpendicular to the layers. This structural setup allows *h*-BN to be investigated for its promising electronic properties, besides an established use e.g., as solid lubricant additive.[20,21] *c*-BN crystallizes in the sphalerite structure-type and exhibits exceptional hardness.[22]

Analogous to the B/N system, aluminum nitride and the corresponding class of nitridoaluminates are built up from Al^{+III} and N^{-III}. Binary AlN crystallizes in the wurtzite structure-type, is electrically insulating (band gap 6.2 eV) and shows exceptional high thermal conductivity (320 $W \cdot m^{-1} \cdot K^{-1}$) alongside a low thermal expansion ($4.3 \cdot 10^{-6}$ $ppm \cdot K^{-1}$) and high temperature stability.[23–26] A metastable modification was found in the sphalerite structure-type.[27] At around 16 GPa, AlN transforms into its high-pressure modification with the NaCl

structure-type.[28] Amongst nitridoaluminates, $Sr[LiAl_3N_4]:Eu^{2+}$ shows exceptional luminescent properties and is commercially used in light-emitting diodes.[29]

Like AlN, the heavier homologs GaN and InN crystallize in the wurtzite structure-type at ambient pressure with a metastable modification in the sphalerite structure-type, while high-pressure modifications exhibit the NaCl structure-type.[30–33] GaN, a wide band gap semiconductor (3.4 eV), enabled the fabrication of highly efficient blue light emitting diodes (LEDs).[34,35] InN can be used to tune the band gap of GaN by synthesis of solid solutions $In_xGa_{1-x}N$, viable for LED and solar energy devices.[36]

Looking at the fourth main group, Si_3N_4 stands out with its structural and application versatility. At ambient pressure, α-Si_3N_4 and the high-temperature modification β-Si_3N_4 are known.[37,38] β-Si_3N_4 shows an exceptional high thermal, mechanical and chemical stability combined with a low density, enabling its use as high-performance ceramics in e.g., engines and bearings.[39–42] At 15 GPa and temperatures above 1800 °C, the spinel-type γ-Si_3N_4 is formed, featuring high hardness and ultra-incompressibility.[43,44] Finally, density functional theory (DFT) calculations predicted a post-spinel modification at pressures above 160 GPa.[45]

1.3 Nitridophosphates – Structural Chemistry and Application

While the third and fourth main group nitrides described previously are established key elements for modern industry, fifth main group nitrides, especially phosphorus nitrides and nitridophosphates, are currently investigated for a multitude of applications. To name some examples, binary phosphorus nitride P_3N_5 is used as gate insulator in metal-insulator field-effect transistors (MISFETs).[46,47] Furthermore, it was analyzed regarding its use as flame retardant and for pyrotechnics safety.[48,49] A nitridic clathrate, $P_4N_4(NH)_4(NH)_3$, may be viable for gas storing, e.g., ammonia.[50] $Ba_3P_5N_{10}Br:Eu^{2+}$ and $AEP_8N_{14}Eu^{2+}$ (*AE* = Ca, Sr, Ba) were proposed as warm-white and ultra-narrow-band blue emitters, respectively.[51–53] Last, but not least, various lithium nitridophosphates exhibit lithium ion conductivity.[54–56]

This diversity of applications is made possible by a high structural flexibility of the nitridophosphate network. The elemental combination of nitridophosphates (P/N) is isoelectronic to that of oxosilicates (Si/O). Consequently, similar structural motifs can be expected. And indeed, while oxosilicate networks are mostly comprised of SiO_4 tetrahedra, the most common structural units found in nitridophosphates are PN_4 tetrahedra (Figure 1.2). The tetrahedra can occur isolated (e.g., Li_7PN_4), connected to small units (e.g., $Li_{12}P_3N_9$), chains (e.g., Zn_2PN_3), layers (e.g., $Li_5P_2N_5$) or a 3D-network (e.g., α-P_3N_5).[57–61] Besides PN_4 tetrahedra, PN_5 pyramids, either square-based (e.g., γ-P_3N_5) or trigonal bipyramidal (e.g., γ-HP_4N_7) and PN_6 octahedra (e.g., β-BP_3N_6 and δ-P_3N_5) have been observed.[62–65] Recently, even trigonal-planar PN_3 units were reported in Ba_3PN_3O.[66]

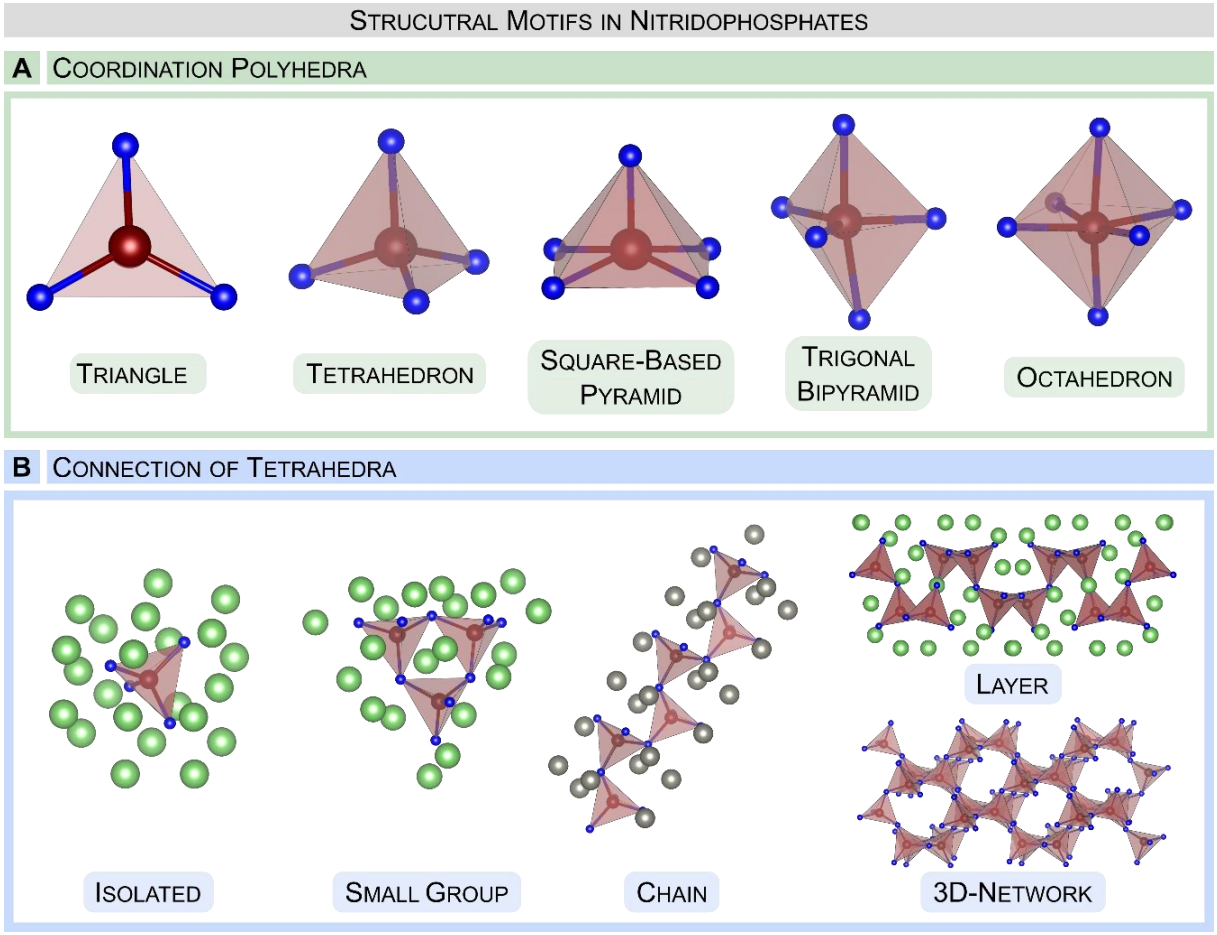

Figure 1.2: Structural motifs in nitridophosphates. (A) Coordination polyhedra reported in literature: PN_3 triangle (Ba_3PN_3O), PN_4 tetrahedron (e.g., α-P_3N_5), PN_5 square-based pyramid (e.g., γ-P_3N_5), PN_5 trigonal bipyramid (e.g., γ-HP_4N_7) and PN_6 octahedron (e.g., β-BP_3N_6). (B) Connection possibilities of PN_4 tetrahedra: isolated (e.g., Li_7PN_4), small group (e.g., $Li_{12}P_3N_9$), chain (e.g., Zn_2PN_3), layer (e.g., $Li_5P_2N_5$) and 3D-network (e.g., α-P_3N_5). Coordination polyhedra of cations are omitted for clarity.[57–64,66]

Closely related to the coordination number and nature of tetrahedral connections is the degree of condensation κ, defined as the ratio of tetrahedral center atoms (C) to ligand atoms (L):

$$\kappa = {}^{N(C)}/_{N(L)} \tag{1}$$

Commonly, the low end of κ is found at ${}^1/_4$, i.e. isolated tetrahedra. The high end, however, depends on the class of materials and terminates in the binary parent compounds. For oxosilicates, κ is limited to ${}^1/_2$, suggesting all-side vertex-sharing SiO_4 tetrahedra, which are found in SiO_2. An increase of κ beyond ${}^1/_2$ can be achieved by connecting more than two tetrahedra via a common vertex, which, however, has never been observed for O in pure

oxosilicates. In contrast, N in nitridophosphates regularly connects up to three tetrahedral vertices. Thus, the degree of condensation terminates with $\kappa = {}^{3}/_{5}$ in binary P_3N_5. Another structural limitation of oxosilicates is driven by electrostatics, preventing a possible edge or even face sharing of SiO_4 tetrahedra.[67] Only one controversially discussed example of edge-sharing SiO_4 tetrahedra is found in literature for fibrous SiO_2.[68] Due to the less polarized P–N bonds compared to the more ionic Si–O bonds, nitridophosphates in turn can feature edge sharing of tetrahedra (e.g. α-P_3N_5).[61,69] With these features in mind, nitridophosphates show, in theory, an even higher structural flexibility than oxosilicates.

1.4 3rd and 4th Main Group Cations in Nitrides

To complete the structural overview for this thesis, a brief look at the cations of Al, In, Ge, and Sn in nitrides is required, including their typical coordination polyhedra and redox chemistry (Figure 1.3).

For aluminum and indium, reported coordination polyhedra are limited to MN_4 tetrahedra and MN_6 octahedra (M = Al, In). While MN_4 tetrahedra are the common structural motif for ambient and low-pressure compounds as seen in the binary nitrides MN, MN_6 octahedra are rarely encountered in high-pressure polymorphs (e.g., NaCl-type MN) and materials (e.g., $AlP_6O_{3x}(NH)_{3-3x}N_9$).[23,28,30,33,70] Both elements are exclusively found in oxidation state +III.

The coordination possibilities for germanium and tin, in contrast, are much more versatile, which may partly be due to their occurrence as cations M^{II} and M^{IV} (M = Ge, Sn). The combination Ge^{II}/N usually forms bent $Ge^{II}N_2$ units as reported for example in Ca_2GeN_2.[71] Ge^{III}/N is found in Ge_2N_6 units, with a Ge–Ge bond (e.g., $Ca_6[Ge_2N_6]$).[72] Ge^{IV}/N most commonly result in GeN_4 tetrahedra, which are found either isolated (e.g., Ca_4GeN_4), connected by shared vertices (e.g., $Ca_5Ge_2N_6$), shared edges (e.g., $Sr_5Ge_2N_6$) or condensed to a 3D-network (e.g., $CaGeN_2$).[71,73,74] Rarely, also trigonal $Ge^{IV}N_3$ units (e.g., $Ba_9(GeN_3)_3N$) were reported.[75] While the coordination motifs mentioned above are typical ambient pressure phases, high-pressure polymorphs can exhibit $Ge^{IV}N_6$ octahedra, (e.g., spinel-type Ge_3N_4).[76]

For Sn^{II}, either trigonal $Sn^{II}N_3$ pyramids (e.g., $Sn_6[P_{12}N_{24}]$) or distorted square-based $Sn^{II}N_4$ pyramids (e.g., $Sn(CN_2)$), each with Sn as the apex, were reported.[77,78] Sn^{IV} shows $Sn^{IV}N_4$ tetrahedra and $Sn^{IV}N_6$ octahedra, e.g. in spinel-type Sn_3N_4.[79] After compression of the same compound to 25 GPa, hints of $Sn^{IV}N_5$ trigonal bipyramids were found.[80]

The structural possibilities are further expanded, as the elements M (M = Al, In, Ge, Sn) occur in nitridic compounds with no direct M–N bond or coordination: all four elements have been reported in nitridic MAX-phases (e.g., Ti_2AlN, Ti_2InN, V_2GeN, Hf_2SnN) and Ge forms anions, such as Ge^{-II} in $Sr_3Ge_2N_2$ and Ge^{-IV} in $Sr_{11}Ge_4N_6$.[81–86] This, however, is beyond the scope of this thesis.

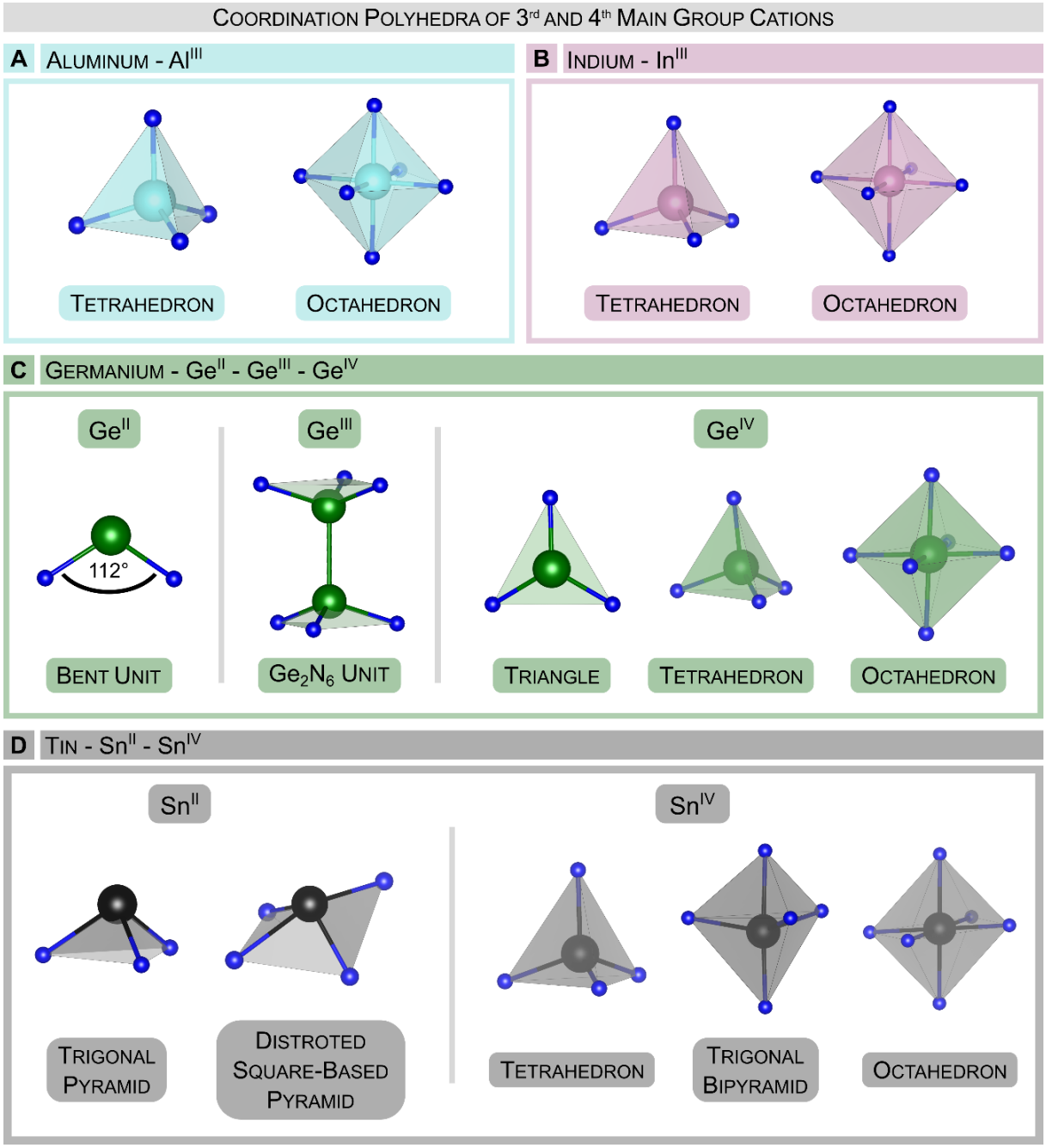

Figure 1.3: Coordination polyhedra of Al^{III}, In^{III}, Ge^{II}, Ge^{IV}, Sn^{II} and Sn^{IV} in nitrides. Al and In are found in tetrahedral or octahedral coordination.[23,28,30,33] Ge and Sn exhibit more versatile coordination polyhedra due to their different oxidation states.[71–80]

1.5 3rd and 4th Main Group Nitridophosphates

Considering the structural possibilities of a nitridophosphate network combined with the versatility of 3rd and 4th main group cations, one could expect an abundance of materials with intriguing structure types and properties. To date, however, only nine such compounds are published in literature, namely *α*- and *β*-BP_3N_6, $AlP_6O_{3x}(NH)_{3-3x}N_9$, $AEAlP_8N_{15}(NH)$ (*AE* = Ca,

Sr, Ba), $SrAl_5P_4N_{10}O_2F_3$, $Ga_{16/3}P_{12}N_{24}O_2$, $SiPN_3$, $SiP_2N_4(NH)$, $Sn_6[P_{12}N_{24}]$, displayed in Figure 1.4 as graphical overview.[64,70,77,87–92] The synthetic strategies and structural features of these compounds are outlined in the following paragraph.

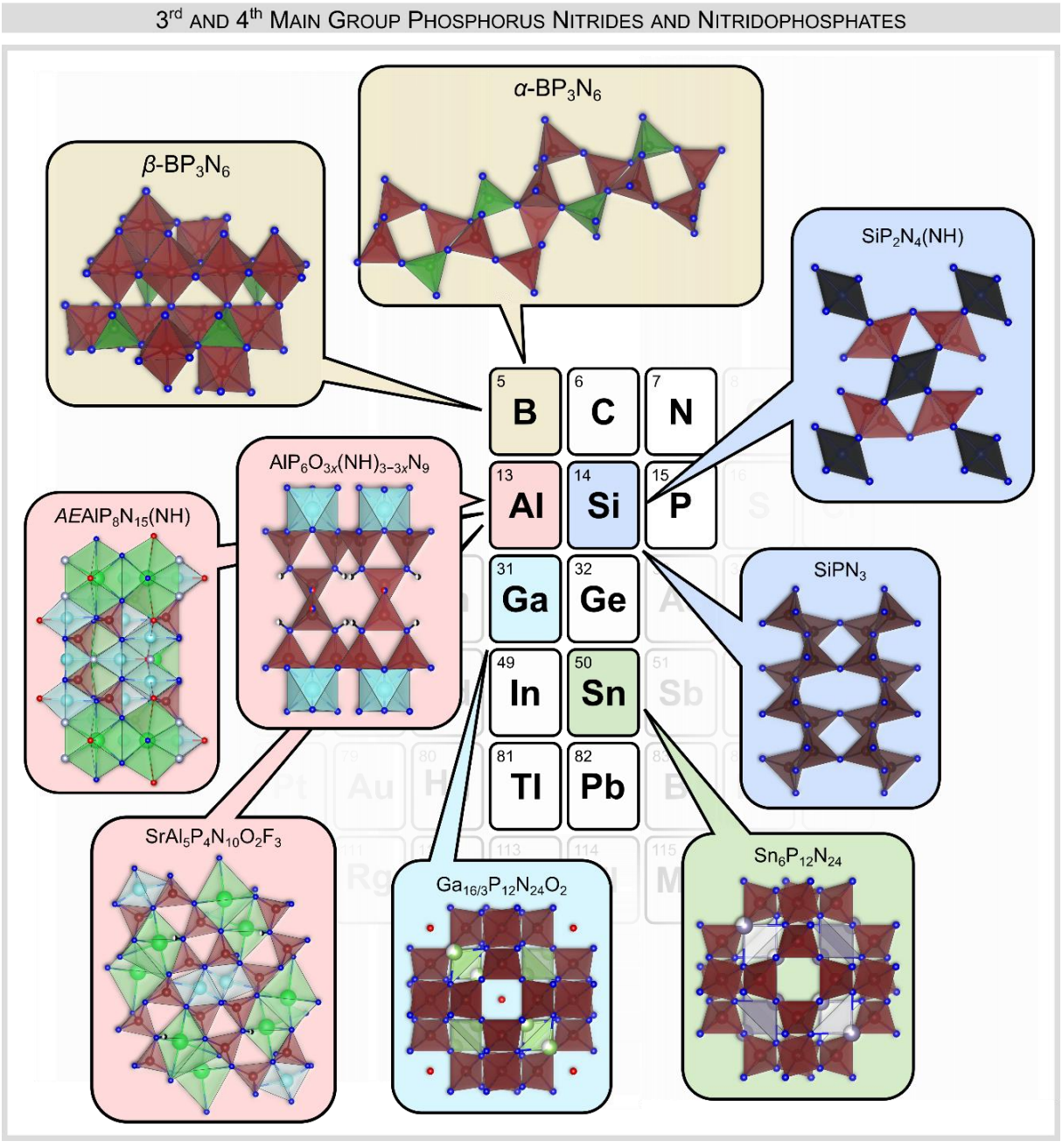

Figure 1.4: Third and fourth main group phosphorus nitrides and nitridophosphates as of before this thesis. Despite an abundance of structural possibilities, only 9 compounds are known: *α*- and *β*-BP_3N_6, $AlP_6O_{3x}(NH)_{3-3x}N_9$, *AE*$AlP_8N_{15}(NH)$ (*AE* = Ca, Sr, Ba), $SrAl_5P_4N_{10}O_2F_3$, $Ga_{16/3}P_{12}N_{24}O_2$, $SiPN_3$, $SiP_2N_4(NH)$, and $Sn_6P_{12}N_{24}$.[64,70,77,87–92]

The preparation of $SiPN_3$, one of the first ternary non-metal nitrides, required the development of a multi-step synthesis from a molecular precursor with the desired stoichiometry and pre-organized structure.[91] The much simpler approach of reacting the binary nitrides P_3N_5 and Si_3N_4 often fails due to very small inter-diffusion coefficients of the starting materials and tendency for irreversible thermal decomposition at elevated temperatures. Only recently, this problem was overcome in very few high-pressure high-temperature reactions.[93–96] The structure of $SiPN_3$ shows a defect wurtzite-type network comprised of $(Si/P)N_4$ tetrahedra with 50:50 mixed Si and P occupation. The necessity of pre-aligned precursors and complex multi-step syntheses for non-metal nitrides was overcome with the discovery of the boron phosphorus nitride α-BP_3N_6.[87] In a high-pressure high-temperature reaction of $(PNCl_2)_3$, NH_4N_3 and *h*-BN at 8 GPa and 1100 °C, *in-situ* generated HCl activates the otherwise inert *h*-BN. A more detailed discussion of this synthetic strategy is given in chapter 1.8. The structure of α-BP_3N_6 features elements of both α-P_3N_5 and *c*-BN: vertex- and edge-sharing PN_4 tetrahedra alongside BN_4 tetrahedra. By laser heating at 42 GPa in a diamond anvil cell, α-BP_3N_6 transforms into the phosphorus nitridoborate β-BP_3N_6.[64] β-BP_3N_6 is built up from BN_4 tetrahedra and PN_6 octahedra, which were observed for the first time within this compound. Further exploring the synthetic approach of α-BP_3N_6 by reacting $(PNCl_2)_3$, NH_4N_3 and Si_3N_4 at 8 GPa and 1100 °C led to the discovery of $SiP_2N_4(NH)$.[92] It forms a condensed 3D-network of PN_4 tetrahedra and SiN_6 octahedra with the imide group located at a bridging N atom between two tetrahedra. $Ga_{16/3}P_{12}N_{24}O_2$ was synthesized in a metathesis reaction from GaF_3 and $LiPN_2$ in a tantalum ampoule at 800 °C.[90] Structurally, Ga cations and isolated oxide anions are located within a sodalite-type network of PN_4 tetrahedra. A closely related structure was found for $Sn_6P_8N_{16}$.[77] Prepared from elemental Sn and HPN_2 at 820 °C in an evacuated silica glass ampoule, PN_4 tetrahedra form a sodalite-type structure as well with Sn^{II} located in the center of the β-cages. Finally, all known aluminum nitridophosphates were synthesized in high-pressure high-temperature reactions at 5 GPa and temperatures up to 1400 °C, starting from Al and HPN_2 ($AlP_6O_{3x}(NH)_{3-3x}N_9$), $AE(N_3)_2$, P_3N_5, AlN and NH_4F ($AEAlP_8N_{15}(NH)$; *AE* = Ca, Sr, Ba), and $Sr(N_3)_2$, PON, P_3N_5, AlN and NH_4F ($SrAl_5P_4N_{10}O_2F_3$), respectively.[70,88,89] $AlP_6O_{3x}(NH)_{3-3x}N_9$ shows a layered structure of AlN_6 octahedra and $P(N/O)_4$ tetrahedra with mixed N/O occupancy. $AEAlP_8N_{15}(NH)$ is built up from a 3D-network of PN_4 tetrahedra containing AlN_6 octahedra and $SrAl_5P_4N_{10}O_2F_3$ shows a 3D-network of PN_4 tetrahedra as well, with clusters of edge-sharing AlN_4F_2, AlN_3OF_2 and AlN_3O_2F octahedra.

One of the reasons for such a low number of known compounds, despite the various successful preparation methods, might be the sophisticated challenges posed by nitridophosphate syntheses. The next section will address these challenges and show the established ways of overcoming them.

1.6 Nitridophosphate Syntheses – Challenges and Techniques

While naturally occurring nitrides are already an exception, as discussed in the beginning of this introduction, the subclass phosphorus nitrides and nitridophosphates remains accessible exclusively by synthetic methods with the exception of interstellar observed PN molecule.[97] This can be attributed to several reasons, one of which is the necessity to exclude moisture and oxygen. In the presence of oxygen, the formation of P–O bonds, leading to oxophosphates, is favored over the formation of P–N bonds due to their different bond energies of 407 kJ·mol^{-1} and 290 kJ·mol^{-1}, respectively.[98] While techniques such as the preparation of starting materials inside a glove box solves the former issue, the main challenge might be the negative electron affinity of N (−0.07 eV).[3] Since N^{3-} anions are only stabilized by their surrounding coordination environment, external influences may easily initiate their oxidation. In case of nitridophosphates, the oxidation results in the irreversible elimination of N_2 with the simultaneous reduction of P^V to P^{III} or even elemental P^0. Common precursors like P_3N_5 readily decompose (Equation 2) at around 850 °C, which is well below the crystallization point of most nitridophosphates (regularly > 1000 °C), especially highly condensed ones.[61]

$$2\ P_3N_5 \longrightarrow 6\ \text{“PN”} + 2\ N_2 \longrightarrow 6\ P + 5\ N_2 \qquad (2)$$

Following Le Chatelier’s principle, the elimination of gaseous N_2 can be suppressed by applying pressure during the heating period of the reaction. Several methods have proven successful in the course of nitridophosphates research. Starting at the lowest pressure range, reactions in (silica) glass ampoules are employed for a multitude of syntheses. For example, *α*- and *β*-P_3N_5 can be prepared from $(PNCl_2)_3$ and NH_4Cl.[99] Gaseous HCl is formed as byproduct, slightly increasing the pressure within the reaction ampoule. With a few exceptions, ampoule syntheses usually yield compounds with a low degree of condensation due to the limited pressure range. This typically goes along with a high susceptibility to hydrolysis and thermal decomposition.

In order to achieve higher pressures, autoclaves and the hot isostatic press (HIP) have proven themselves for the preparation of a multitude of nitridophosphates.[100,101] These techniques, however, are limited in pressure and temperature by their materials. State of the art materials for autoclaves are the superalloys Inconel® 718 (max. 600 °C, 0.3 GPa) and Haynes® (max. 800 °C, 0.17 GPa).[102] The HIP is limited to pressures in the megapascal range and temperatures up to 2000 °C.[103]

The next steps upwards on the pressure scale are done with large-volume presses (LVPs) and diamond anvil cells (DACs). Both techniques have been used in this thesis and therefore are outlined in more detail in the next section.

1.7 Large-Volume Press and Diamond Anvil Cell

Over the last decades, various techniques have been developed for pressure generation and its transmission onto the sample using LVPs. The most common techniques are known as the Piston cylinder, the Paris-Edinburgh press, the belt apparatus and multi-anvil devices.[104–107] For the latter, the general concept is to use multiple stages of anvils to distribute the uniaxial pressure of a downward pressure bolt nearly isotropical. While there are various possibilities for the detailed technical implementation of this concept, the state of the art setup is referred to as Kawai-type and is exemplarily described here as used for this thesis.[108]

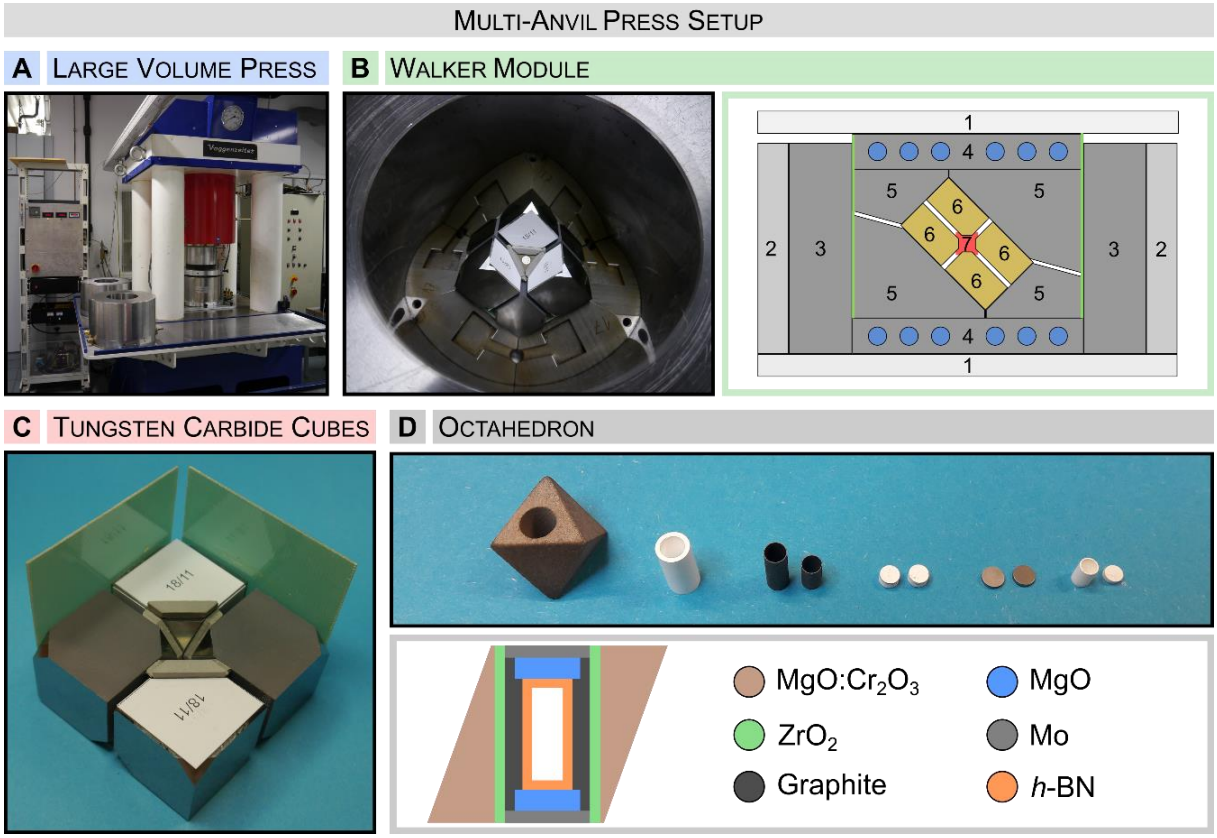

Figure 1.5: Large-volume press using the multi-anvil setup with Kawai-type geometry. (A) Large-volume press with control units for pressure and temperature. (B) Walker module with six steel anvils (5) inside steel rings (2,3) for guidance. The top and bottom parts (1) are made of aluminum with built in cooling pipes (4). The steel anvils form a cubic compression space for the tungsten carbide cubes (6) and the octahedron (7). (C) Electrically isolated tungsten carbide cubes with truncated corners, forming an octahedral compression space. (D) Octahedron with the sample chamber (white).

The first stage consists of six steel anvils to initially distribute the hydraulically generated uniaxial pressure to an inner cubic compression space, guided by outer steel rings (Walker module).[109] The cubic space is filled with eight electrically isolated tungsten carbide (WC) cubes with truncated corners. This truncation gives space for the innermost stage, a $MgO:Cr_2O_3$ octahedron, containing the actual sample chamber. The size of this assembly is characterized by the ratio of the truncated edge length (*TEL*) of the WC cubes and the size of the octahedron edge length (*OEL*): *OEL*/*TEL*, each in millimeter. An assembly size of 18/11, typically used for this thesis, will give a sample volume of approximately 35 mm^3. The octahedron itself is prepared with a ZrO_2 sleeve, graphite heaters, MgO spacers, Mo discs and an *h*-BN sample chamber, as shown in Figure 1.5. A detailed guide to the setup and assembly preparation is given in Chapters 2 – 5, including the corresponding supporting information, and the literature.[110,111] Using the multi-anvil setup, high-end pressures of >100 GPa are achievable, however, pressures for routine experiments are usually below 20 GPa with temperatures up to 1800 °C.[112]

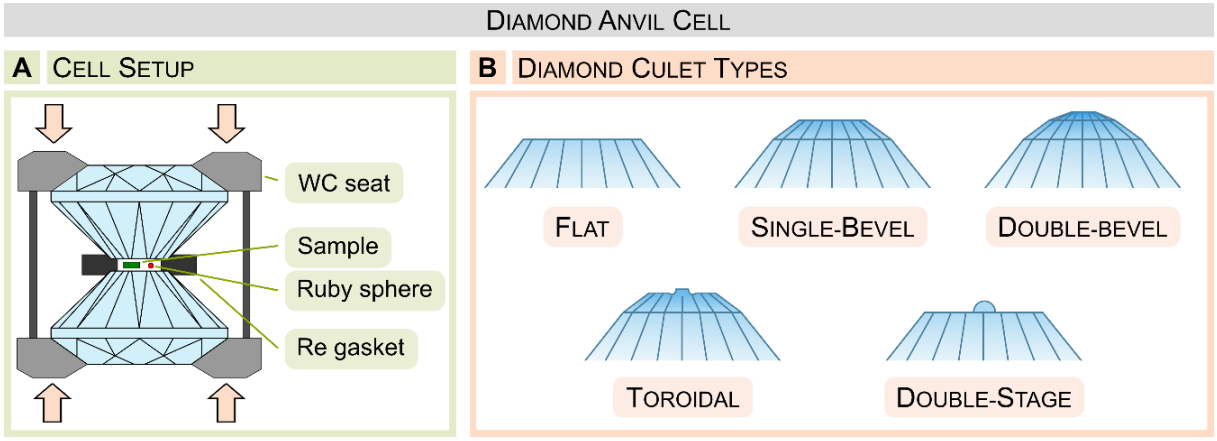

Figure 1.6: Schematic overview of diamond anvil cells. (A) Typical cell setup. (B) Diamond culet types.

As the name implies, experiments with large-volume presses yield a relatively large amount of product, considering high-pressure standards. Diamond anvil cells, in contrast, are mostly used for single particle or even single-crystal experiments, but therefore overcome the pressure-limitation of LVPs by approximately one magnitude, allowing pressures up to 1000 GPa.[113] In general, a DAC consists of two opposing seats for the diamonds, typically made out of tungsten carbide (Figure 1.6). The polished culets of the diamonds (diameter: 500 µm – tip of a sphere) form the sample chamber, surrounded by a drilled-through and indented Rhenium gasket. The shape and size of the culets are selected depending on the target pressure: flat culet diamonds allow pressures up to approximately 150 GPa, with an

increase up to ca. 400 GPa when using single- or double-beveled diamonds.[114] For achieving even higher pressures, toroidal and double-staged diamonds were developed.[113,115] The sample chamber contains the actual sample, an internal pressure standard (often a ruby sphere, alternatives are Ne, Au, Pt or NaCl), and a pressure transmitting medium (e.g. Ne or N_2).[116,117] To increase the pressure, the diamonds are moved towards each other by an external force, either screw- or membrane-driven.

Historically, one of the biggest advantages of DACs over LVPs was the transparency of the diamonds for a wide range of the electromagnetic spectrum, enabling the *in-situ* observation of the samples under high pressures (e.g. X-ray diffraction, various spectroscopic methods). An example for such a study is described in Chapter 4. Recent advances, however, enabled similar possibilities for LVPs, e.g., at beamline station P61B at PETRA III, DESY. During this PhD project, these possibilities were exploited to study the reaction mechanism of a nitridophosphate synthesis, which is presented in Chapter 6.

1.8 Reaction Mechanisms in Inorganic Chemistry

While it is common practice in organic chemistry to investigate reaction mechanisms, a majority of syntheses in inorganic chemistry are of explorative nature. A thorough understanding of a reaction, however, enables key follow-up processes: Reaction conditions like temperature, pressure or time can be optimized towards higher yields, lower energy consumption and lower cost. Specific starting materials can be selected to target structural features of reaction products or to suppress the formation of undesired byproducts. Finally, a fundamental synthetic idea can be transferred to comparable reactions, enabling targeted material synthesis with tailored material properties.

Being aware of the importance of this knowledge, efforts have been made to understand kinetics and reaction mechanisms, either from theoretical calculations or experimental data. The latter often uses differential scanning calorimetry (DSC), nuclear magnetic resonance (NMR) spectroscopy or powder X-ray diffraction (PXRD) as examination techniques.[118] A mechanistic model is then derived by mathematically describing the data obtained, which provides insight into the processes during the actual reaction. Following this workflow, several models have been established.

- Nucleation models best describe the processes of crystallization, decomposition, phase transition, desolvation, adsorption and hydration. The corresponding process starts at a nucleation site, typically a crystal imperfection or surface, which provides a minimal activation energy.[119–128]
- Contraction models, a special case of nucleation models, describe the nucleation start at the surface of a crystal, proceeding towards its center.[119]

- Diffusion models are most commonly used to describe the formation of a new compound from two or more starting materials.[129,130] A fundamental work of Tamman introduced the idea of melt free ion diffusion at grain boundaries.[131] At reactant-depended temperature, the most mobile ions of two or more species start to diffuse into each other, forming a layer of the reaction product. As this layer grows, diffusion pathways lengthen and the reaction rate drastically decreases. Taking into consideration the additional temperature dependence of the diffusion rate, the empirical Equation 3 was proposed to describe the product layer thickness:

$$z = a \cdot \ln(t) + c \tag{3}$$

(z: layer thickness, a: temperature-dependent constant, t: reaction time, c: constant)

The mathematical description used for the examination of solid-state reaction mechanisms later on is a slight modification of Equation 3, published by Jander in 1927:[132]

$$z^2 = 2 \cdot t \cdot c \tag{4}$$

(z: layer thickness, t: reaction time, c: constant depending on diffusion coefficients)

Herein, the product layer thickness is described as quadratic dependent on the reaction time.

All models outlined above were derived from ambient pressure data. While high-pressure synthetic techniques have been established and actively improved over decades, studies on formation mechanisms, especially for nitride reactions, are still rare, if present at all.

In case of high-pressure syntheses of nitridophosphates, a toolbox of synthetic approaches has been developed, partially with mechanistic suggestions based on *ex-situ* information. Several synthesis strategies can be grouped as flux assisted methods, enhancing diffusion processes:

- The high-pressure metathesis, first established for transition metal nitridophosphates, starts from $LiPN_2$ and a metal halide MX_y (M = transition metal, X = halide, y = index depending on the transition metal oxidation state).[133] During the reaction a lithium halide LiX is formed as byproduct, typically featuring a high lattice energy and thus being a driving force for the reaction. Additionally, LiX acts as flux agent due to its molten state at reaction conditions.
- The Li_3N self-flux method is used for the synthesis of lithium nitridophosphates.[134] As the name implies, Li_3N is simultaneously used as a precursor and molten flux agent during the reaction.

- NH_4Cl has been added as mineralizer for enhanced single-crystal growth.[135] While it completely dissociates into gaseous NH_3 and HCl at 350 °C at ambient pressure, under high pressures it is considered to form a liquid phase with the equilibrium described in Equation 5:[136,137]

$$(NH_4^+ + Cl^-)_{(l)} \leftrightarrow (NH_3 + HCl)_{(l)} \quad (5)$$

Further strategies involve the *in-situ* formation of HCl and HF, e.g., by using $(PNCl_2)_3$ and NH_4N_3 or NH_4F as reactants, to form reactive intermediate species with materials such as BN or TiN, which are considered inert otherwise.[87,138] Lastly, the azide route starts from P_3N_5 and a metal azide to form the corresponding metal nitridophosphate and N_2.[50] Azides are suggested to decompose under elevated pressure releasing molecular N_2, the increased partial pressure of which further inhibits the decomposition of nitrides. The to date single more detailed reaction mechanism is proposed by Wendl *et al*. in an azide route reaction.[139] It was assumed that the strontium imidonitridophosphate $SrP_6N_8(NH)_4$ is an intermediate species on the way to SrP_8N_{14} by replacing the imide groups with PN_4 tetrahedra.

Chapter 6 of this thesis will provide the first experimental *in-situ* insight into a high-pressure high-temperature nitridophosphate reaction. To keep simplicity for the first experiments, the nitride route, reacting P_3N_5 and a metal nitride, was chosen to be most suitable, as no molten state or decomposition are supposed to be involved.

1.9 Scope of this Thesis

Up to date, the number of 3rd and 4th main group phosphorus nitrides and nitridophosphates is quite manageable: only *α*- and *β*-BP_3N_6, $AlP_6O_{3x}(NH)_{3-3x}N_9$, *AE*$AlP_8N_{15}(NH)$ (*AE* = Ca, Sr, Ba), $SrAl_5P_4N_{10}O_2F_3$, $Ga_{16/3}P_{12}N_{24}O_2$, $SiPN_3$, $SiP_2N_4(NH)$, $Sn_6P_{12}N_{24}$ are known.[64,70,77,87–92]

The first part of this thesis focuses on expanding the number of known compounds of 3rd and 4th main group nitridophosphates. Five new compounds were synthesized in explorative high-pressure high-temperature experiments and thoroughly characterized with special attention on structural features. Chapter 2 deals with the discovery of the isotypic nitridophosphates MP_6N_{11} (*M* = Al, In). Their layered structure is closely related to the oxosilicate mica class, however shows an unprecedented connection of trigonal bipyramidal PN_5 units. Chapter 3 describes the synthesis of $Ge^{II}P_2N_4$ by reduction of $Ge^{IV}{}_3N_4$ in a reaction with P_3N_5. A structural influence of the Ge lone pair is discussed with the prospect on the systematic exchange of alkaline earth cations with Ge^{II}. In Chapter 4, GeP_2N_4 single crystals were used in a DAC experiment to determine its elastic properties and analyze a displacive phase transition. Laser heating resulted in the formation of the novel $GePN_3$, showing GeN_6 octahedra as high-pressure structural motif. The first part is concluded with Chapter 5, which deals with the characterization

of $Sn_3P_8N_{16}$. Structurally it is closely related to GeP_2N_4 and shows Sn in the mixed oxidation states +II and +IV.

The second part of this thesis, i.e. Chapter 6, investigates the formation mechanism of nitridophosphates under high-pressure high-temperature conditions. The large-volume press located at beamline P61B at DESY is used to *in-situ* monitor the synthesis of Zn_2PN_3 and deduct ideas for a reaction mechanism.

1.10 References

[1] H. B. Singh, *Composition, Chemistry, and Climate of the Atmosphere*, Vol. 1, Van Nostrand Reinhold Company, New York, **1995**, p. 22.

[2] E. Riedel, C. Janiak, *Anorganische Chemie*, Vol. 8, Walter de Gruyter, Berlin, **2011**, p. 128.

[3] T. Andersen, H. K. Haugen, H. Hotop, *J. Phys. Chem. Ref. Data* **1999**, *28*, 1511.

[4] S. G. Bratsch, *J. Phys. Chem. Ref. Data* **1989**, *18*, 1.

[5] B. M. Hoffman, D. Lukoyanov, Z.-Y. Yang, D. R. Dean, L. C. Seefeldt, *Chem. Rev.* **2014**, *114*, 4041.

[6] M. Alexander, *Soil Nitrogen*, Vol. 10, American Society of Agronomy, Madison, **1965**, pp. 307.

[7] J. N. Ladd, R. B. Jackson, *Nitrogen in Agricultural Soils*, Vol. 22, American Society of Agronomy, Crop Science Society of America, Soil Science Society of America, Madison, **1982**, pp. 173.

[8] M. K. Firestone, *Nitrogen in Agricultural Soils*, Vol. 22, American Society of Agronomy, Crop Science Society of America, Soil Science Society of America, Madison, **1982**, pp. 289.

[9] R. L. Parker, *Data of Geochemistry*, Vol. 6, United States Government Printing Office, Washington, **1967**, pp. 1.

[10] C. Blondel, *Phys. Scr.* **1995**, *T58*, 31.

[11] A. E. Rubin, *Am. Min.* **1997**, *82*, 1001.

[12] F. A. Bannister, *Mineral. Mag. J. Mineral. Soc.* **1941**, *26*, 36.

[13] M. R. Lee, S. S. Russell, J. W. Arden, C. T. Pillinger, *Meteoritics* **1995**, *30*, 387.

[14] S. Bette, T. Theye, H.-J. Bernhardt, W. P. Clark, R. Niewa, *Minerals* **2021**, *11*, 290.

[15] H. J. Axon, J. Kinder, C. W. Haworth, J. W. Horsfield, *Mineral. Mag.* **1981**, *44*, 107.

[16] L. F. Dobrzhinetskaya, R. Wirth, J. Yang, H. W. Green, I. D. Hutcheon, P. K. Weber, E. S. Grew, *Am. Min.* **2014**, *99*, 764.

[17] H. P. Nielsen, V. F. Buchwald, *Proc. Lunar Planet. Sci.* **1981**, *1981*, 1343.

[18] T. Sōma, A. Sawaoka, S. Saito, *Mater. Res. Bull.* **1974**, *9*, 755.

[19] R. S. Pease, *Acta Crystallogr.* **1952**, *5*, 356.

[20] K. Zhang, Y. Feng, F. Wang, Z. Yang, J. Wang, *J. Mater. Chem. C* **2017**, *5*, 11992.

[21] Y. Kimura, T. Wakabayashi, K. Okada, T. Wada, H. Nishikawa, *Wear* **1999**, *232*, 199.

[22] R. H. Wentorf, *J. Chem. Phys.* **1961**, *34*, 809.

[23] H. Ott, *Z. Phys.* **1924**, *22*, 201.

[24] W. M. Yim, E. J. Stofko, P. J. Zanzucchi, J. I. Pankove, M. Ettenberg, S. L. Gilbert, *J. Appl. Phys.* **1973**, *44*, 292.

[25] Y. Baik, R. A. L. Drew, *Key Eng. Mater.* **1996**, *1996*, 553.

[26] H. Kitagawa, Y. Shibutani, S. Ogata, *Model. Simul. Mater. Sci. Eng.* **1995**, *3*, 521.

[27] I. Petrov, E. Mojab, R. C. Powell, J. E. Greene, L. Hultman, J.-E. Sundgren, *Appl. Phys. Lett.* **1992**, *60*, 2491.

[28] H. Vollstädt, E. Ito, M. Akaishi, S. Akimoto, O. Fukunaga, *Proc. Jpn. Acad. Ser. B* **1990**, *66*, 7.

[29] P. Pust, V. Weiler, C. Hecht, A. Tücks, A. S. Wochnik, A.-K. Henß, D. Wiechert, C. Scheu, P. J. Schmidt, W. Schnick, *Nat. Mater.* **2014**, *13*, 891.

[30] R. Juza, H. Hahn, *Z. Anorg. Allg. Chem.* **1938**, *239*, 282.

[31] S. Strite, D. Chandrasekhar, D. J. Smith, J. Sariel, H. Chen, N. Teraguchi, H. Morkoç, *J. Cryst. Growth* **1993**, *127*, 204.

[32] H. Yamane, M. Shimada, F. J. DiSalvo, *Mater. Lett.* **2000**, *42*, 66.

[33] M. Ueno, M. Yoshida, A. Onodera, O. Shimomura, K. Takemura, *Phys. Rev. B* **1994**, *49*, 14.

[34] H. Morkoç, S. Strite, G. B. Gao, M. E. Lin, B. Sverdlov, M. Burns, *J. Appl. Phys.* **1994**, *76*, 1363.

[35] S. Nakamura, M. R. Krames, *Proc. IEEE* **2013**, *101*, 2211.

[36] D. V. P. McLaughlin, J. M. Pearce, *Metall. Mater. Trans. A* **2013**, *44*, 1947.

[37] I. Kohatsu, J. W. McCauley, *Mater. Res. Bull.* **1974**, *9*, 917.

[38] R. Grün, *Acta Crystallogr. B* **1979**, *35*, 800.

[39] M. J. Hoffmann, *MRS Bull.* **1995**, *20*, 28.

[40] Y. Ukyo, S. Wada, *J. Ceram. Soc. Jpn.* **1989**, *97*, 872.

[41] F. L. Riley, *J. Am. Ceram. Soc.* **2000**, *83*, 245.

[42] M. Jiang, R. Komanduri, *Wear* **1998**, *215*, 267.

[43] A. Zerr, G. Miehe, G. Serghiou, M. Schwarz, E. Kroke, R. Riedel, H. Fueß, P. Kroll, R. Boehler, *Nature* **1999**, *400*, 340.

[44] J. Z. Jiang, H. Lindelov, L. Gerward, K. Ståhl, J. M. Recio, P. Mori-Sanchez, S. Carlson, M. Mezouar, E. Dooryhee, A. FitchD. J. Frost, *Phys. Rev. B* **2002**, *65*, 161202(R).

[45] P. Kroll, J. von Appen, *Phys. Status Solidi B* **2001**, *266*, R6.

[46] Y. Hirota, T. Kobayashi, *J. Appl. Phys.* **1982**, *53*, 5037.

[47] Y.-H. Jeong, K.-H. Choi, S.-K. Jo, B. K. Bongkoo Kang, *Jpn. J. Appl. Phys.* **1995**, *34*, 1176.

[48] M. S. Choudhary, J. K. Fink, K. Lederer, H. A. Krässig, *J. Appl. Polym. Sci.* **1987**, *34*, 863.

[49] E.-C. Koch, S. Cudziło, *Angew. Chem. Int. Ed.* **2016**, *55*, 15439.

[50] F. Karau, W. Schnick, *Angew. Chem. Int. Ed.* **2006**, *45*, 4505.

[51] A. Marchuk, W. Schnick, *Angew. Chem. Int. Ed.* **2015**, *54*, 2383.

[52] A. Marchuk, S. Wendl, N. Imamovic, F. Tambornino, D. Wiechert, P. J. Schmidt, W. Schnick, *Chem. Mater.* **2015**, *27*, 6432.

[53] S. Wendl, L. Eisenburger, P. Strobel, D. Günther, J. P. Wright, P. J. Schmidt, O. Oeckler, W. Schnick, *Chem. Eur. J.* **2020**, *26*, 7292.

[54] S. Schneider, L. G. Balzat, B. V. Lotsch, W. Schnick, *Chem. Eur. J.* **2023**, *29*, e202202984.

[55] S. Schneider, S. T. Kreiner, L. G. Balzat, B. V. Lotsch, W. Schnick, *Chem. Eur. J.* **2023**, *29*, e202301986.

[56] S. Schneider, E.-M. Wendinger, V. Baran, A.-K. Hatz, B. V. Lotsch, M. Nentwig, O. Oeckler, T. Bräuniger, W. Schnick, *Chem. Eur. J.* **2023**, *29*, e202300174.

[57] W. Schnick, J. Luecke, *J. Solid State Chem.* **1990**, *87*, 101.

[58] E.-M. Bertschler, R. Niklaus, W. Schnick, *Chem. Eur. J.* **2017**, *23*, 9592.

[59] S. J. Sedlmaier, M. Eberspächer, W. Schnick, *Z. Anorg. Allg. Chem.* **2011**, *637*, 362.

[60] E.-M. Bertschler, R. Niklaus, W. Schnick, *Chem. Eur. J.* **2018**, *24*, 736.

[61] S. Horstmann, E. Irran, W. Schnick, *Angew. Chem. Int. Ed.* **1997**, *36*, 1873.

[62] K. Landskron, H. Huppertz, J. Senker, W. Schnick, *Angew. Chem. Int. Ed.* **2001**, *40*, 2643.

[63] D. Baumann, W. Schnick, *Angew. Chem. Int. Ed.* **2014**, *53*, 14490.

[64] S. Vogel, M. Bykov, E. Bykova, S. Wendl, S. D. Kloß, A. Pakhomova, S. Chariton, E. Koemets, N. Dubrovinskaia, L. Dubrovinsky, W. Schnick, *Angew. Chem. Int. Ed.* **2019**, *58*, 9060.

[65] D. Laniel, F. Trybel, A. Néri, Y. Yin, A. Aslandukov, T. Fedotenko, S. Khandarkhaeva, F. Tasnádi, S. Chariton, C. Giacobb, E. L. Bright, M. Hanfland, V. Prakapenka, W. Schnick, I. A. Abrikosov, L. Dubrovinsky, N. Dubrovinskaia, *Chem. Eur. J.* **2022**, *28*, e202201998.

[66] R. Pritzl, K. Witthaut, M. Dialer, A. T. Buda, V. Milman, L. Bayarjargal, B. Winkler, W. Schnick, *Angew. Chem. Int. Ed.* **2024**, *63*, e202405849.

[67] L. Pauling, *J. Am. Chem. Soc.* **1929**, *51*, 1010.

[68] A. Weiss, A. Weiss, *Z. Anorg. Allg. Chem.* **1954**, *276*, 95.

[69] R. Marchand, F. Tessier, A. Le Sauze, N. Diot, *Int. J. Inorg. Mater.* **2001**, *3*, 1143.

[70] L. Neudert, F. Heinke, T. Bräuniger, F. J. Pucher, G. B. Vaughan, O. Oeckler, W. Schnick, *Chem. Commun.* **2017**, *53*, 2709.

[71] S. J. Clarke, F. J. DiSalvo, *Inorg. Chem.* **2000**, *39*, 2631.

[72] L. Link, M. Pathak, F. Jach, P. Koželj, A. Ormeci, P. Höhn, R. Niewa, *Angew. Chem. Int. Ed.* **2021**, *60*, 7691.

[73] S. C. Junggeburth, O. Oeckler, W. Schnick, *Z. Anorg. Allg. Chem.* **2008**, *634*, 1309.

[74] M. Maunaye, J. Guyader, Y. Laurent, J. Lang, *Bull. de Minér.* **1971**, *94*, 347.

[75] D. G. Park, F. J. DiSalvo, *Bull. Kor. Chem. Soc.* **2008**, *29*, 2413.

[76] G. Serghiou, G. Miehe, O. Tschauner, A. Zerr, R. Boehler, *J. Chem. Phys.* **1999**, *111*, 4659.

[77] F. J. Pucher, C. Frhr. von Schirnding, F. Hummel, V. R. Celinski, J. Schmedt auf der Günne, B. Gerke, R. Pöttgen, W. Schnick, *Eur. J. Inorg. Chem.* **2015**, *2015*, 382.

[78] M. Löber, K. Dolabdjian, M. Ströbele, C. P. Romao, H.-J. Meyer, *Inorg. Chem.* **2019**, *58*, 7845.

[79] N. Scotti, W. Kockelmann, J. Senker, St. Traßel, H. Jacobs, *Z. Anorg. Allg. Chem.* **1999**, *625*, 1435.

[80] K. Niwa, T. Inagaki, T. Ohsuna, Z. Liu, T. Sasaki, N. A. Gaida, M. Hasegawa, *CrystEngComm* **2020**, *22*, 3531.

[81] D. Y. Kovalev, M. A. Luginina, A. E. Sytschev, *Russ. J. Non-Ferr. Met.* **2017**, *58*, 303.

[82] W. Jeitschko, H. Nowotny, F. Benesovsky, *Monatsh. Chem.* **1964**, *95*, 178.

[83] N. Kubitza, B. Beckmann, S. Jankovic, K. Skokov, A. A. Riaz, C. Schlueter, A. Regoutz, O. Gutfleisch, C. S. Birkel, *Chem. Mater.* **2024**, *36*, 1375.

[84] M. W. Barsoum, *Prog. Solid State Chem.* **2000**, *28*, 201.

[85] S. J. Clarke, G. R. Kowach, F. J. DiSalvo, *Inorg. Chem.* **1996**, *35*, 7009.

[86] Z. A. Gál, S. J. Clarke, *Chem. Commun.* **2005**, 728.

[87] S. Vogel, A. T. Buda, W. Schnick, *Angew. Chem. Int. Ed.* **2018**, *57*, 13202.

[88] M. M. Pointner, O. Oeckler, W. Schnick, *Chem. Eur. J.* **2023**, *29*, e202301960.

[89] M. M. Pointner, R. M. Pritzl, J. M. Albrecht, L. Blahusch, J. P. Wright, E. L. Bright, C. Giacobbe, O. Oeckler, W. Schnick, *Chem. Eur. J.* **2024**, e202400766.

[90] D. Günther, L. Eisenburger, W. Schnick, O. Oeckler, *Z. Anorg. Allg. Chem.* **2022**, *648*, e202200280.

[91] H. P. Baldus, W. Schnick, J. Luecke, U. Wannagat, G. Bogedain, *Chem. Mater.* **1993**, *5*, 845.

[92] S. Vogel, A. T. Buda, W. Schnick, *Angew. Chem. Int. Ed.* **2019**, *58*, 3398.

[93] M. Dialer, M. M. Pointner, P. Strobel, P. J. Schmidt, W. Schnick, *Inorg. Chem.* **2024**, *663*, 1480.

[94] M. Dialer, K. Witthaut, T. Bräuniger, P. J. Schmidt, W. Schnick, *Angew. Chem. Int. Ed.* **2024**, *63*, e202401419.

[95] M. Dialer, R. M. Pritzl, S. L. Wandelt, D. Khalyavin, P. J. Schmidt, W. Schnick, *Chem. Mater.* **2024**, *36*, 3933.

[96] M. Dialer, M. M. Pointner, S. L. Wandelt, P. Strobel, P. J. Schmidt, L. Bayarjargal, B. Winkler, W. Schnick, *Adv. Opt. Mater.* **2024**, *12*, 2302668.

[97] L. M. Ziurys, *Astrophys. J.* **1987**, *321*, L81.

[98] E. Riedel, C. Janiak, *Anorganische Chemie*, Vol. 8, Walter de Gruyter, Berlin, New York, **2011**, p. 124.

[99] W. Schnick, J. Lücke, F. Krumeich, *Chem. Mater.* **1996**, *8*, 281.

[100] M. Mallmann, S. Wendl, W. Schnick, *Chem. Eur. J.* **2020**, *26*, 2067.

[101] S. Wendl, S. Mardazad, P. Strobel, P. J. Schmidt, W. Schnick, *Angew. Chem. Int. Ed.* **2020**, *59*, 18240.

[102] J. Häusler, S. Schimmel, P. Wellmann, W. Schnick, *Chem. Eur. J.* **2017**, *23*, 12275.

[103] H. V. Atkinson, S. Davies, *Met. Mater. Trans. A* **2000**, *31*, 2981.

[104] C. A. Parsons, *Nature* **1920**, *104*, 709.

[105] S. Klotz, T. Hansen, E. Lelièvre-Berna, L. Amand, J. Maurice, C. Payre, *JNR* **2020**, *21*, 117.

[106] H. T. Hall, *Rev. Sci. Instrum.* **1960**, *31*, 125.

[107] N. Kawai, S. Endo, *Rev. Sci. Instrum.* **1970**, *41*, 1178.

[108] N. Kawai, M. Togaya, A. Onodera, *Proc. Jpn. Acad.* **1973**, *49*, 623.

[109] D. Walker, M. A. Carpenter, C. M. Hitch, *Am. Miner.* **1990**, *75*, 1020.

[110] D. Walker, *Am. Miner.* **1991**, *76*, 1092.

[111] H. Huppertz, *Z. Kristallogr. – Cryst. Mater.* **2004**, *219*, 330.

[112] D. Yamazaki, E. Ito, T. Yoshino, N. Tsujino, A. Yoneda, X. Guo, F. Xu, Y. Higo, K. Funakoshi, *Phys. Earth Planet. Inter.* **2014**, *228*, 262.

[113] N. Dubrovinskaia, L. Dubrovinsky, N. A. Solopova, A. Abakumov, S. Turner, M. Hanfland, E. Bykova, M. Bykov, C. Prescher, V. B. Prakapenka, S. Petitgirard, I. Chuvashova, B. Gasharova, Y.-L. Mathis, P. Ershov, I. Snigireva, A. Snigirev, *Sci. Adv.* **2016**, *2*, e1600341.

[114] W. C. Moss, K. A. Goettel, *Appl. Phys. Lett.* **1987**, *50*, 25.

[115] A. Dewaele, P. Loubeyre, F. Occelli, O. Marie, M. Mezouar, *Nat. Commun.* **2018**, *9*, 2913.

[116] R. A. Forman, G. J. Piermarini, J. D. Barnett, S. Block, *Science* **1972**, *176*, 284.

[117] Y. Fei, A. Ricolleau, M. Frank, K. Mibe, G. Shen, V. Prakapenka, *Proc. Nat. Acad. Sci. U. S. A.* **2007**, *104*, 9182.

[118] A. Khawam, D. R. Flanagan, *J. Phys. Chem. B* **2006**, *110*, 17315.

[119] V. Erukhimovitch, J. Baram, *Phys. Rev. B* **1994**, *50*, 5854.

[120] J. Graetz, J. J. Reilly, *J. Phys. Chem. B* **2005**, *109*, 22181.

[121] V. J. Anderson, H. N. W. Lekkerkerker, *Nature* **2002**, *416*, 811.

[122] A. K. Burnham, R. K. Weese, B. L. Weeks, *J. Phys. Chem. B* **2004**, *108*, 19432.

[123] S. Wang, Q. Gao, J. Wang, *J. Phys. Chem. B* **2005**, *109*, 17281.

[124] B. Cantor, *Philos. Trans. R. Soc. Lond. A* **2003**, *361*, 409.

[125] C. Wu, P. Wang, X. Yao, C. Liu, D. Chen, G. Q. Lu, H. Cheng, *J. Phys. Chem. B* **2005**, *109*, 22217.

[126] V. K. Peterson, D. A. Neumann, R. A. Livingston, *J. Phys. Chem. B* **2005**, *109*, 14449.

[127] L.-C. Sögütoglu, M. Steiger, J. Houben, D. Biemans, H. R. Fischer, P. Donkers, H. Huinink, O. C. G. Adan, *Cryst. Growth Des.* **2019**, *19*, 2279.

[128] R. A. Sullivan, R. J. Davey, G. Sadiq, G. Dent, K. R. Back, J. H. Ter Horst, D. Toroz, R. B. Hammond, *Cryst. Growth Des.* **2014**, *14*, 2689.

[129] K. Hardel, *Angew. Chem. Int. Ed. Engl.* **1972**, *11*, 173.

[130] H. Schäfer, *Angew. Chem. Int. Ed. Engl.* **1971**, *10*, 43.

[131] G. Tammann, F. Westerhold, B. Garre, E. Kordes, H. Kalsing, *Z. Anorg. Allg. Chem.* **1925**, *149*, 21.

[132] W. Jander, *Z. Anorg. Allg. Chem.* **1927**, *163*, 1.

[133] S. D. Kloss, W. Schnick, *Angew. Chem. Int. Ed.* **2015**, *54*, 11250.

[134] E.-M. Bertschler, T. Bräuniger, C. Dietrich, J. Janek, W. Schnick, *Angew. Chem. Int. Ed.* **2017**, *56*, 4806.

[135] A. Marchuk, F. J. Pucher, F. W. Karau, W. Schnick, *Angew. Chem. Int. Ed.* **2014**, *53*, 2469.

[136] A. F. Holleman, N. Wiberg, *Lehrbuch der Anorganischen Chemie*, Vol. 102, Walter de Gruyter, Berlin, **2007**, p. 670.

[137] C. W. F. T. Pistorius, *J. Chem. Phys.* **1969**, *50*, 1436.

[138] L. Eisenburger, V. Weippert, C. Paulmann, D. Johrendt, O. Oeckler, W. Schnick, *Angew. Chem. Int. Ed.* **2022**, *61*, e202202014.

[139] S. Wendl, W. Schnick, *Chem. Eur. J.* **2018**, *24*, 15889.

Chapter 2

Combining MN$_6$ Octahedra and PN$_5$ Trigonal Bipyramids in the Mica-like Nitridophosphates MP$_6$N$_{11}$ (M = Al, In)

Published in: *Angew. Chem. Int. Ed.* **2023**, *62*, e202303580

Authors: Sebastian J. Ambach, Monika Pointner, Sophie Falkai, Carsten Paulmann, Oliver Oeckler, Wolfgang Schnick

DOI: https://doi.org/10.1002/anie.202303580

Abstract: Layered silicates are a very versatile class of materials with high importance to humanity. The new nitridophosphates MP$_6$N$_{11}$ (M = Al, In), synthesized from MCl$_3$, P$_3$N$_5$ and NH$_4$N$_3$ in a high-pressure high-temperature reaction at 1100 °C and 8 GPa, show a mica-like layer setup and feature rare nitrogen coordination motifs. The crystal structure of AlP$_6$N$_{11}$ was elucidated from synchrotron single-crystal diffraction data (space group *Cm* (no. 8), a = 4.9354(10), b = 8.1608(16), c = 9.0401(18) Å, β = 98.63(3)°), enabling Rietveld refinement of isotypic InP$_6$N$_{11}$. It is built up from layers of PN$_4$ tetrahedra, PN$_5$ trigonal bipyramids and MN$_6$ octahedra. PN$_5$ trigonal bipyramids have been reported only once and MN$_6$ octahedra are sparsely found in the literature. AlP$_6$N$_{11}$ was further characterized by energy-dispersive X-ray (EDX), IR and NMR spectroscopy. Despite the vast amount of known layered silicates, there is no isostructural compound to MP$_6$N$_{11}$ as yet.

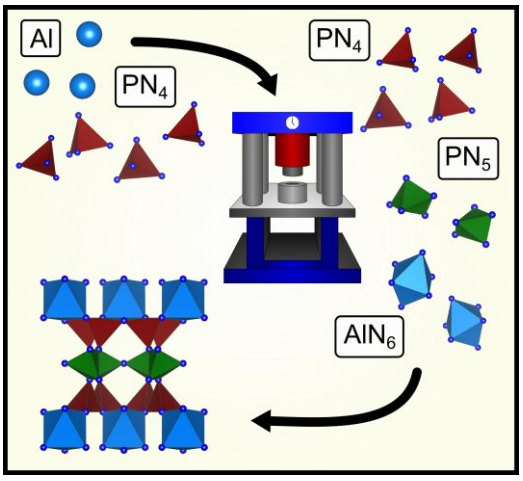

2.1 Introduction

Naturally abundant (oxo)silicates dominate the solid earth crust with a volume fraction of more than 90%.[1] Despite the limited number of primary building units of the Si/O-networks, predominantly SiO_4 tetrahedra, this class features an immense structural diversity. This includes isolated tetrahedra or small groups thereof, ribbons, layers and 3D-frameworks. Layered silicate structures often consist of stacked SiO_4 tetrahedral (T) and MO_6 (M = Al, Mg, Fe, …) octahedral (O) layers and various cations between oxide layers. Layer stacking between cations usually occurs in two ways: T-O or T-O-T, the latter being typical for micas, a subgroup of layered silicates. Combining these possibilities leads to a large structural variety and a similarly broad field of application, such as ceramics, building materials, (photo)catalysis, adsorbents, feed additives or biomedical applications.[2–10] Furthermore, clay minerals have even been discussed to play an important role in the origin of life.[11, 12] The structural limitation of oxygen, usually connecting only up to two tetrahedral centers, is overcome when O is formally replaced by N and Si by P, leading to the class of nitridophosphates. Due to the isoelectronic combination Si/O and P/N, both form similar structural elements, however, with one key difference: In nitridophosphates, N has the possibility to regularly connect up to three tetrahedral P centers, enabling an even larger structural diversity.[13] Occasionally, even edge-sharing PN_4 tetrahedra have been reported (e.g. in α-P_3N_5, α-HP_4N_7 or P_4ON_6). In contrast, edge-sharing SiO_4 tetrahedra have only claimed once, namely for fibrous silica.[14–17] This suggests a plethora of layered silicate minerals isostructural with or closely related to nitridophosphates. However, so far only one such example is known, namely $AESi_3P_4N_{10}(NH)_2$ (AE = Mg, Ca, Sr).[18]

Nitridophosphates are versatile materials, ranging from semiconductors or luminescent materials (when doped with Eu^{2+}) to flame-retardants, safety materials in pyrotechnics, ion conductors or gas storage materials.[19–26] Extending their crystal chemistry in analogy to the manifold structural possibilities of layered silicates, their field of application would widely increase.

In contrast to naturally abundant (oxo)silicates, nitridophosphates are a purely synthetic class of materials. One reason for this is their susceptibility to irreversible thermal decomposition, releasing molecular nitrogen. For their formation, however, often temperatures way above the point of decomposition are necessary. Following Le Chatelier's principle, applying pressure prevents the formation of N_2 and allows high-temperature syntheses to be carried out. Typically, high pressure also affects coordination numbers, increasing the usual fourfold coordination in PN_4 tetrahedra. Thereby, PN_5-pyramids, either square-based in γ-P_3N_5, or trigonal-bipyramidal in γ-HP_4N_7 were observed and even PN_6-octahedra in β-BP_3N_6 could be enforced recently by applying a pressure of 46 GPa.[27–30]

2.2 Results and Discussion

In this contribution, we report on the highly condensed nitridophosphates MP_6N_{11} (M = Al, In), which adopt a mica-like structure with rare coordination motifs. The title compounds were synthesized in a high-pressure high-temperature reaction at 8 GPa and 1100 °C starting from MCl_3, P_3N_5 and NH_4N_3 (Equation 1). Starting materials were ground in a glove box under an argon atmosphere, tightly packed into a h-BN crucible and reacted in a multianvil press.[31] Further details on the synthesis are given in the Supporting Information.

$$4\ MCl_3 + 8\ P_3N_5 + 3\ NH_4N_3 \rightarrow 4\ MP_6N_{11} + 12\ HCl + 4\ N_2 \quad (1)$$

The reactions yielded a gray, microcrystalline powder, which is stable at ambient conditions. In both cases, best yields were obtained using only 10% of the required stoichiometric amount of NH_4N_3. Without this significant deviation from the ideal stoichiometry, diverse unknown side phases are formed, presumably containing H due to the high partial pressure of HCl. The *in situ* generated HCl seems to act as a mineralizer enhancing single-crystal growth, as it is known for the ability to reversibly cleave P−N bonds.[32] Thereby plate-shaped single crystals of AlP_6N_{11} up to 70 × 70 µm² in length and width (Figure 2.1) were obtained. In contrast, InP_6N_{11} forms small acicular single crystals that are only up to two µm long.

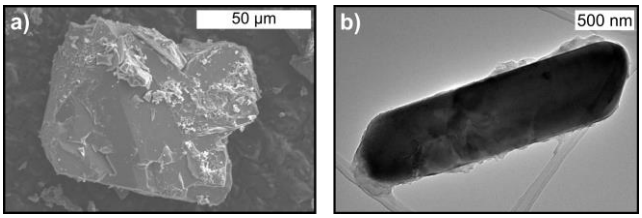

Figure 2.1: Exemplary a) scanning electron microscope (SEM) image of a plate-shaped single crystal of AlP_6N_{11} and b) transmission electron microscope (TEM) image of a small needle-shaped crystallite of InP_6N_{11}.

MP_6N_{11} (M = Al, In) can be interpreted as the formal reaction product of MN and P_3N_5 in a molar ratio of 1:2. A direct high-pressure high-temperature reaction of these compounds, however, does not yield MP_6N_{11}. Instead, MN results as the main crystalline constituent alongside minor unknown phases and an amorphous portion, which the higher reactivity of MCl_3 compared to MN may explain. Coherent with this, the synthesis of analogous GaP_6N_{11} was not possible as yet. With the required usage of $GaCl_3$, the powder mixture starts to react with the boron nitride crucible and forms BP_3N_6 as the only crystalline product.[30]

The crystal structure of AlP_6N_{11} was elucidated from synchrotron single-crystal X-ray diffraction data (space group *Cm* (no. 8), a = 4.9354(10), b = 8.1608(16), c = 9.0401(18) Å, β = 98.63(3)°).[33] The data were collected at beamline P24 at DESY (Hamburg, Germany;

more information in the Supporting Information). The elemental compositions of both title compounds were analyzed by energy-dispersive X-ray (EDX) spectroscopy (Tables S1.2 and S1.3). In the respective samples, MP_6N_{11} was confirmed as the main crystalline constituent by Rietveld refinement (Figures S1.2 and S1.3).

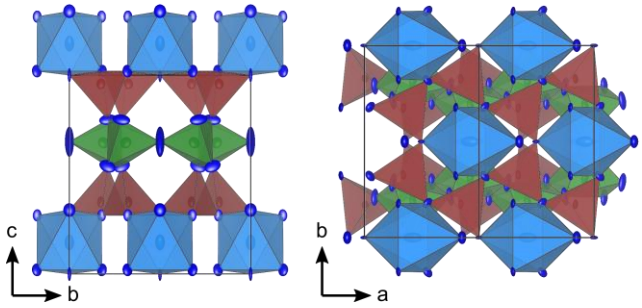

Figure 2.2: The layered crystal structure of AlP_6N_{11} consists of AlN_6 octahedra (blue), PN_5 trigonal bipyramids (green) and PN_4 tetrahedra (red). Displacement ellipsoids are displayed at 90% probability level.

The layered structure of AlP_6N_{11} is built up from AlN_6 octahedra, PN_4 tetrahedra and PN_5 trigonal bipyramids (Figures 2.2 and 2.3). The AlN_6 octahedra are not interconnected, while both PN_4 tetrahedra and PN_5 trigonal bipyramids form *sechser* rings, as defined by Liebau.[1] A more detailed view on the layered structure is provided in the Supporting Information (Figure S1.1). This setup is comparable to layered silicates, however, to the best of our knowledge, there is no clay mineral or mica, which is isotypic to MP_6N_{11}, probably because trigonal bipyramids SiO_5 have only been reported for exceptional oxosilicates.[34, 35] A related layer sequence is found in the mica clintonite ($Ca(Mg,Al)_3(Al_3Si)O_{10}(OH)_2$), with the exception of $(Al,Si)O_6$ octahedra instead of PN_5 trigonal bipyramids (Figure S1.1).[36]

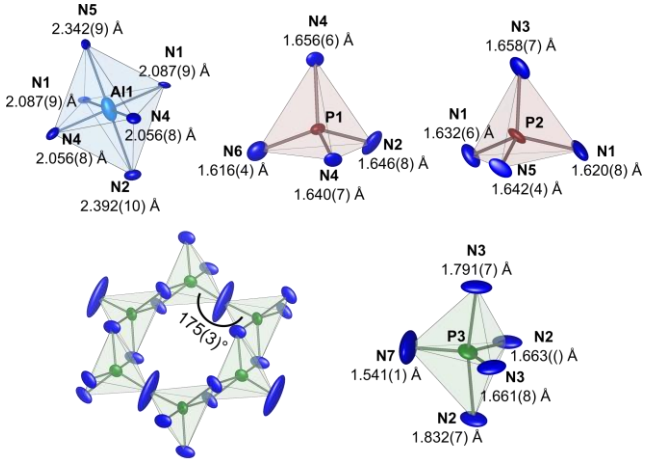

Figure 2.3: Coordination polyhedra of Al1, P1, P2 and P3 in AlP_6N_{11}.

The AlN_6 octahedra, rarely found in the literature (e.g. $AlP_6O_{3x}(NH)_{3-x}N_9$ or rock salt-type high-pressure AlN), are significantly elongated along one axis, leading to Al-N bond lengths of 2.056(8) and 2.087(9) Å in the equatorial plane and 2.342(9) and 2.392(10) Å in the axial direction, respectively.[37, 38] Typical Al−N distances in octahedral coordination, as found in the aforementioned compounds, vary around 2.0 Å. N−Al−N angles are between 87.5(4) and 92.6(4)° and thus in a typical range for octahedra of ideally 90°. P−N distances (1.6283(8) − 1.6492(11) Å) and N−P−N angles (102.7(4) − 122.2(4)°) in the PN_4 tetrahedra can be compared to other nitridophosphates, e.g. P_3N_5 or $AlP_6O_{3x}(NH)_{3-x}N_9$.[12, 37] So far, trigonal bipyramidal PN_5 units were only observed in the high-pressure polymorph γ-HP_4N_7, where two longer and three shorter bonds appear.[26] Comparable bond lengths and angles can be observed in AlP_6N_{11}, with 1.832(7) and 1.791(7) Å for the longer and 1.5408(13) – 1.663(8) Å for the shorter bonds. As in γ-HP_4N_7, PN_5 units share edges, forming infinite strands along [100], however, with a major difference. While in γ-HP_4N_7 these strands do not interact with each other, they are directly interconnected via the N7 atom in AlP_6N_{11}. This leads to an energetically unfavorable, almost linear coordination (175(3)°) of N7, resulting in a large thermal displacement ellipsoid with its largest displacement perpendicular to the P3···P3 vector (Figure 2.3). This feature has not yet been described for nitridophosphates. However, it appears in oxosilicates, e.g. $K_3NdSi_7O_{17}$.[39] Such angles of approximately 180° can be seen as a time and position average rather than an actual bond angle. Its real value, at any instant in time, is likely to be much smaller than 180°. This is also consistent with a small P3−N7 distance of 1.5408(13) Å in case of the almost linear coordination, which would be larger with smaller bond angles. Other comparable bond lengths in trigonal bipyramids show values of 1.661(8) (P3−N3) and 1.663(8) Å (P3−N2). Even at low temperatures (173(2) K) this observation does not change.

The electrostatic plausibility of the crystal structure and polyhedral distortions were analyzed by charge distribution (CHARDI), bond-valence-sum (BVS) and minimal bonding ellipsoid (MBE) calculations, all of which confirm the consistency of the structure model.[41–43] Corresponding results and more detailed information are provided in the supporting information (Tables S1.11 and S1.12, Figure S1.9).

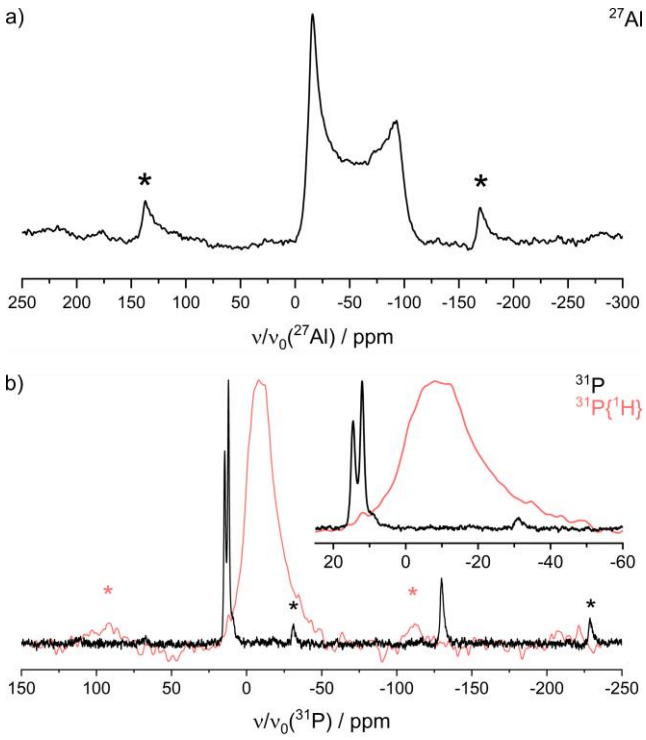

Figure 2.4: Solid-state MAS NMR spectra of AlP_6N_{11}. a) One signal in the ^{27}Al spectrum. b) Three signals in the ^{31}P (black) and one signal in the ^{31}P{^{1}H} (red) spectra. The number of signals is consistent with the structure model in *Cm*, showing no evidence of H in AlP_6N_{11}. Sidebands are marked with asterisks.

Data obtained from X-ray diffraction initially suggest the higher symmetric space group *C*2/*m* (no.12) instead of the chosen *Cm* (no. 8). This, however, would cause two major issues. First, the nitrogen atom connecting the PN_5-strands (N7, Figure 2.3) is forced into the energetically unfavorable linear coordination with a P3−N7−P3 angle of exactly 180°. Avoiding this by introducing a 50:50 split position of N7 still results in large displacement ellipsoids. Second, a twofold axis would lead to the crystallographic equivalency of all P sites of the PN_4 tetrahedra. This is not consistent with the results of ^{31}P NMR spectroscopy (Figure 2.4b).

The ^{31}P spectrum shows one signal at δ = −130.0 ppm, corresponding to penta-coordinated P in the PN_5 trigonal bipyramids. A comparable chemical shift was reported for P in γ-HP_4N_7 (δ = −103.0 ppm), which also contains trigonal bipyramidal PN_5 units.[26] Additionally, two signals at δ = 14.5 and 12.0 ppm are observed, which is a typical range for fourfold N-coordinated P, as observed e.g. in $AlP_6O_{3x}(NH)_{3-x}N_9$.[36] These signals suggest two independent crystallographic P sites for PN_4 tetrahedra, which is met in space group *Cm* but not in *C*2/*m* (only one P site). Whereas X-ray diffraction averages over long distances and may render space group *C*2/*m* acceptable, NMR spectroscopy is sensitive to short-range interactions and rules out *C*2/*m* in the local environment. Thus, we prefer space group *Cm* for

the structure model. The measure of similarity, calculated by the COMPSTRU tool of the Bilbao Crystallographic Server, has a value of $\Delta = 0.114$, indicating only small deviations between both structure models.[44–49] For this reason, possible ferroelectric properties caused by the non-centrosymmetric structure would be minimal, if measureable at all. Additionally, a high-temperature phase transition from space group *Cm* to *C*2/*m* could be possible, however would require temperature-dependent solid-state NMR-measurements.

Structure elucidation of AlP_6N_{11} enabled Rietveld refinement (Figure S1.3) for InP_6N_{11} (a = 4.9723(2), b = 8.2930(3), c = 9.2627(4) Å, β = 99.217(1))°). In contrast to AlP_6N_{11}, the ^{31}P NMR spectrum of InP_6N_{11} (Figure S1.5) shows only one signal for tetrahedrally coordinated P (δ = 6.8 ppm). This may be a superposition of two separate signals, leading to space group *Cm*, as in case of AlP_6N_{11}. On the other hand, based on NMR results space group *C*2/*m* is feasible for the structure model of InP_6N_{11}. As we see no apparent reason for a change in space group, we prefer *Cm* for InP_6N_{11} as well. In−N distances of the elongated InN_6 octahedra range from 2.21(7) to 2.29(7) Å in the equatorial plane, comparable to rock salt-type high-pressure InN, and from 2.33(6) to 2.60(5) Å along the axial direction.[40] All bond lengths and angles of the P−N polyhedra are comparable to AlP_6N_{11}. The c lattice parameter is expanded by 2.4% from 9.0401(18) Å in AlP_6N_{11} to 9.2627(4) Å in InP_6N_{11}.

To rule out imide functionality in MP_6N_{11} (M = Al, In), which might be introduced by the starting material NH_4N_3 or short contact with air before the synthesis, IR- and solid-state NMR spectra (Figure 4) were recorded. As in the case of $EASi_3P_4N_{12}H_2$ (*EA* = Mg, Ca, Sr), N−H valence modes are typically observed at around 3400 cm^{-1} in IR-spectra, whereas the spectrum of AlP_6N_{11} shows no such absorption band (Figure S1.6).[16]

As a much more sensitive probe towards hydrogen, solid-state NMR measurements show the same result. The ^{27}Al (spin $I = {}^5/_2$) spectrum shows one broad signal between δ = 0 and −100 ppm, which is in line with one crystallographic Al site. The shift is comparable to octahedrally coordinated Al as reported in the literature.[36, 50] The signal of the ^{31}P{^{1}H} cross polarized spectrum does not match any positions of the signals in the direct ^{31}P spectrum, indicating the absence of hydrogen in AlP_6N_{11}. The broad signal in the ^{31}P{^{1}H} cross polarized spectrum may be explained by a minor amorphous side phase, containing both P and H. The ^{1}H NMR and all other NMR spectra of AlP_6N_{11} can be found in the Supporting Information (Figure S1.4).

Despite the thermal sensitivity of many nitridophosphates, AlP_6N_{11} is stable up to at least 950 °C under argon atmosphere (Figure S1.7) and shows a thermal volume expansion of 16.0 ppm/K, which is small compared to silicate clay minerals and micas.[51, 52] In the former, the lattice parameter perpendicular to the layers usually shows a much higher thermal expansion than the ones parallel to the layers. In AlP_6N_{11}, however, the increase in volume is caused by the expansion of the lattice parameter perpendicular to the layers and only one lattice

parameter parallel to the layers. The second parallel lattice parameter only shows a very small increase in length. (Figure S1.8) This behavior may be a feature of the nearly linear coordinated N7 atom (Figure 2.3). Upon expansion along [010], the P3−N7−P3 angle would be further stretched towards the energetically unfavorable value of 180°.

2.3 Summary

Summing up, we synthesized the mica-analogous nitridophosphates MP_6N_{11} (M = Al, In), which contain the rare structure motifs of MN_6 octahedra and PN_5 trigonal bipyramids. As the second nitridic compound structurally mimicking layered silicate minerals, this gives proof that nitridophosphates should systematically be able to adopt structures of the former and $AESi_3P_4N_{10}(NH)_2$ (AE = Mg, Ca, Sr) is not just a stand-out curiosity. Exploring nitridic analogs of layered silicate minerals, with the aim to expand the already wide variety of structures and applications of nitridophosphates, seems an intriguing approach for further studies. Targeting compositions and structures known from nature promises to yield a vast amount of new nitridophosphates with applications as essential as the ones of silicate clay minerals and micas.

2.4 Acknowledgements

We gratefully acknowledge the financial support by Deutsche Forschungsgemeinschaft (projects SCHN 377/18-1 and OE530/6-1). The Deutsches Elektronensynchrotron (DESY, Hamburg) is acknowledged for granting beamtime (project I-20210953). Laetitia Bradaczek, Alexander Feige, Niklas Langer and Lennart Staab are acknowledged for help during the beam time. Furthermore, the authors thank Christian Minke and Amalina Buda for the SEM and EDX measurements as well as solid-state NMR experiments.

2.5 References

[1] F. Liebau in *Structural Chemistry of Silicates. Structure, Bonding, and Classification*, Springer Berlin Heidelberg, Berlin, Heidelberg, **1985**, pp. 212−229. The term "*sechser ring*" has been defined by Liebau and is derived from the German word "sechs" (engl. six), describing a ring formed by six polyhedra.

[2] F. Bergaya, G. Lagaly in *Handbook of Clay Science*, Vol. 2, Elsevier, Amsterdam, Boston, Heidelberg, London, New York, Oxford, Paris, San Diego, San Francisco, Singapore, Sydney, Tokyo, **2006**, pp. 1−19.

[3] H. H. Murray, *Appl. Clay Sci.* **1991**, *5*, 379.

[4] M. Valásková, *Ceram. Silik.* **2015**, *59*, 331.

[5] M. Ghadiri, W. Chrzanowski, R. Rohanizadeh, *RSC Adv.* **2015**, *5*, 29467.

[6] Y. Zou, Y. Hu, Z. Shen, L. Yao, D. Tang, S. Zhang, S. Wang, B. Hu, G. Zhao, X. Wang, *J. Environ. Sci.* **2022**, *115*, 190.

[7] W. D. Johns, *Annu. Rev. Earth Planet. Sci.* **1979**, *7*, 183.

[8] C. H. Zhou, J. Keeling, *Appl. Clay Sci.* **2013**, *74*, 3.

[9] M. Nadziakiewicza, S. Kehoe, P. Micek, *Animals* **2019**, *9*, 714.

[10] V. Reyes-Zamudio, C. Angeles-Chávez, J. Cervantes, *J. Therm. Anal. Calorim.* **2011**, *104*, 405.

[11] A. Weiss, *Angew. Chem. Int. Ed. Engl.* **1981**, *20*, 850.

[12] J. T. Kloprogge, H. Hartmann, *Life* **2022**, *12*, 259.

[13] S. D. Kloß, W. Schnick, *Angew. Chem. Int. Ed.* **2019**, *58*, 7933.

[14] S. Horstmann, E. Irran, W. Schnick, *Angew. Chem. Int. Ed.* **1997**, *36*, 1873.

[15] S. Horstmann, E. Irran, W. Schnick, *Angew. Chem. Int. Ed.* **1997**, *36*, 1992.

[16] J. Ronis, B. Bondars, A. Vitola, T. Millers, J. Schneider, F. Frey, *J. Solid State Chem.* **1995**, *115*, 265.

[17] A. Weiss, A. Weiss, *Z. Anorg. Allg. Chem.* **1954**, *276*, 95.

[18] L. Eisenburger, P. Strobel, P. J. Schmidt, T. Bräuniger, J. Wright, E. L. Bright, C. Giacobbe, O. Oeckler, W. Schnick, *Angew. Chem. Int. Ed.* **2022**, *61*, e202114902.

[19] Y. Hirota, T. Kobayashi, *J. Appl. Phys.* **1982**, *53*, 5037.

[20] Y.-H. Jeong, K.-H. Choi, S.-K. Jo, B. K. Bongkoo Kang, *Jpn. J. Appl. Phys.* **1995**, *34*, 1176.

[21] F. J. Pucher, A. Marchuk, P. J. Schmidt, D. Wiechert, W. Schnick, *Chem. Eur. J.* **2015**, *21*, 6443.

[22] S. Wendl, L. Eisenburger, P. Strobel, D. Günther, J. P. Wright, P. J. Schmidt, O. Oeckler, W. Schnick, *Chem. Eur. J.* **2020**, *26*, 7292.

[23] M. S. Choudhary, J. K. Fink, K. Lederer, H. A. Krässig, *J. Appl. Polym. Sci.* **1987**, *34*, 863.

[24] E.-C. Koch, S. Cudziło, *Angew. Chem. Int. Ed.* **2016**, *55*, 15439.

[25] W. Schnick, J. Luecke, *Solid State Ion.* **1990**, *38*, 271.

[26] F. Karau, W. Schnick, *Angew. Chem. Int. Ed* **2006**, *45*, 4505.

[27] K. Landskron, H. Huppertz, J. Senker, W. Schnick, *Angew. Chem. Int. Ed.* **2001**, *40*, 2643.

[28] D. Baumann, W. Schnick, *Angew. Chem. Int. Ed.* **2014**, *53*, 14490.

[29] S. Vogel, M. Bykov, E. Bykova, S. Wendl, S. D. Kloß, A. Pakhomova, S. Chariton, E. Koemets, N. Dubrovinskaia, L. Dubrovinsky W. Schnick, *Angew. Chem. Int. Ed.* **2019**, *58*, 9060.

[30] K. Landskron, H. Huppertz, J. Senker, W. Schnick, *Z. Anorg. Allg. Chem.* **2002**, *628*, 1465.

[31] H. Huppertz, *Z. Kristallogr. – Cryst. Mater.* **2004**, *219*, 330.

[32] S. Vogel, A. T. Buda, W. Schnick, *Angew. Chem. Int. Ed.* **2018**, *57*, 13202.

[33] Deposition number 2241809 contains the supplementary crystallographic data for this paper. These data are provided free of charge by the joint Cambridge Crystallographic Data Centre and Fachinformationszentrum Karlsruhe.

[34] A. Pakhomova, E. Bykova, M. Bykov, K. Glazyrin, B. Gasharova, H.-P. Liermann, M. Mezouar, L. Gorelova, S. Krivovichev, L. Dubrovinsky, *IUCrJ* **2017**, *4*, 671.

[35] F. Liebau, *Inorganica Chim. Acta* **1984**, *89*, 1.

[36] J. A. MacKinney, C. I. Mora, S. W. Bailey, *Am. Min.* **1988**, *73*, 365.

[37] L. Neudert, F. Heinke, T. Bräuniger, F. J. Pucher, G. B. Vaughan, O. Oeckler, W. Schnick, *Chem. Commun.* **2017**, *53*, 2709.

[38] H. Vollstädt, E. Ito, M. Akaishi, S. Akimoto, O. Fukunaga, *Proc. Jpn. Acad. Ser. B* **1990**, *66*, 7.

[39] S. M. Haile, B. J. Wuensch, *Acta Crystallogr. B* **2000**, *56*, 773.

[40] M. Ueno, M. Yoshida, A. Onodera, O. Shimomura, K. Takemura, *Phys. Rev. B Condens. Matter* **1994**, *49*, 14.

[41] K. Momma, F. Izumi, *J. Appl. Crystallogr.* **2011**, 44, 1272.

[42] A. S. Wills, VaList - A bond valence calculation and analysis program, London, **2010**.

[43] J. Cumby, J. P. Attfield, *Nat. Commun.* **2017**, *8*, 14235.

[44] G. Bergerhoff, M. Berndt, K. Brandenburg, T. Degen, *Acta Crystallogr. B* **1999**, *55*, 147.

[45] M. I. Aroyo, J. M. Perez-Mato, D. Orobengoa, E. Tasci, G. de la Flor, A. Kirov, *Bulg. Chem. Commun.* **2011**, *43*, 183.

[46] M. I. Aroyo, J. M. Perez-Mato, C. Capillas, E. Kroumova, S. Ivantchev, G. Madariaga, A. Kirov & H. Wondratschek, *Z. Kristallogr.* **2006**, *221*, 15.

[47] M. I. Aroyo, A. Kirov, C. Capillas, J. M. Perez-Mato & H. Wondratschek, *Acta Crystallogr. A* **2006**, *62*, 115.

[48] G. de la Flor, D. Orobengoa, E. Tasci, J. M. Perez-Mato and M. I. Aroyo, *J. Appl. Crystallogr.* **2016**, *49*, 653.

[49] E.S. Tasci, G. de la Flor, D. Orobengoa, C. Capillas, J.M. Perez-Mato, M.I. Aroyo, *EPJ Web Conf.* **2012**, *22*, 00009.

[50] T. Bräuniger, M. Jansen, *Z. Anorg. Allg. Chem.* **2013**, *639*, 857.

[51] H. A. McKinstry, *Am. Min.* **1965**, *50*, 212.

[52] M. Gemmi, M. Merlini, A. Pavese, N. Curetti, *Phys. Chem. Miner.* **2008**, *35*, 367.

Chapter 3

Structural Influence of Lone Pairs in GeP_2N_4, a Germanium(II) Nitridophosphate

Published in: *Angew. Chem. Int. Ed.* **2023**, *62*, e202215393

Authors: Sebastian J. Ambach, Cody Somers, Tristan de Boer, Lucien Eisenburger, Alexander Moewes, Wolfgang Schnick

DOI: https://doi.org/10.1002/anie.202215393

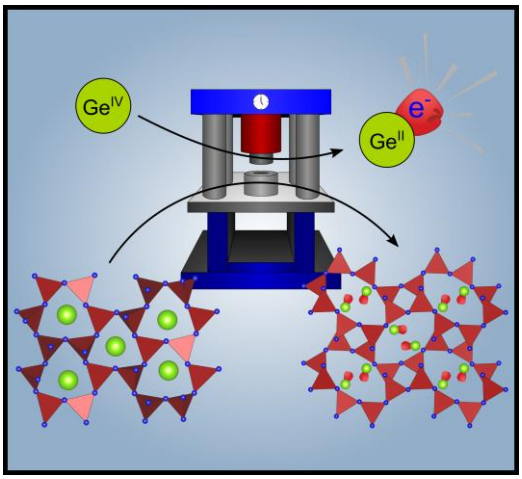

Abstract: Owing to their widespread properties, nitridophosphates are of high interest in current research. Explorative high-pressure high-temperature investigations yielded various compounds with stoichiometry MP_2N_4 (M = Be, Ca, Sr, Ba, Mn, Cd), which are discussed as ultra-hard or luminescent materials, when doped with Eu^{2+}. Herein, we report the first germanium nitridophosphate, GeP_2N_4, synthesized from Ge_3N_4 and P_3N_5 at 6 GPa and 800 °C. The structure was determined by single-crystal X-ray diffraction and further characterized by energy-dispersive X-ray spectroscopy, density functional theory calculations, IR and NMR spectroscopy. The highly condensed network of PN_4-tetrahedra shows a strong structural divergence to other MP_2N_4 compounds, which is attributed to the stereochemical influence of the lone pair of Ge^{2+}. Thus, the formal exchange of alkaline earth cations with Ge^{2+} may open access to various compounds with literature-known stoichiometry, however, new structures and properties.

3.1 Introduction

Nitridophosphates are an extremely diverse class of materials attracting high interest in current research. Their wide range of applications and intriguing materials properties emerge from the structural versatility, which competes with the earth's predominant class of materials, the (oxo)silicates.[1] Due to the isoelectronic combination of elements Si/O and P/N, both form similar structural motifs, most commonly SiO_4- and PN_4-tetrahedra. In the majority of cases, these building blocks are arranged in three-dimensional anionic networks or two-dimensional layers. The isoelectronic relation is mirrored in analogous crystal structures of oxosilicates and nitridophosphates, e.g. the silicate mineral paracelsian $BaAl_2Si_2O_8$ and $LiNdP_4N_8$ or the recently discovered mica analogues $AESi_3P_4N_{10}(NH)_2$ (*AE* = Mg, Ca, Sr) as well as various SiO_2 analogue modifications of PON.[2–8] Due to the fact that N can connect up to three tetrahedra in nitridophosphates and features both corner and edge sharing connections, while O in oxosilicates usually is limited to two connections and corner sharing, the structural versatility of the former may even surpass the one of the latter. Consequently, the degree of condensation κ, given as the atomic ratio between tetrahedral centres (*T*) and ligands (*X*) by $\kappa = {}^{N(T)}/_{N(X)}$, is limited to a maximum of ½ in oxosilicates (SiO_2), but can reach a maximum of ${}^3/_5$ in nitridophosphates (P_3N_5).[9]

Even though most highly condensed ($\kappa \geq ½$) nitridophosphates are stable under ambient conditions, their initial synthesis remains a sophisticated issue. In presence of oxygen, the formation of oxides is favored over the formation of nitrides, as P–O-bonds are more stable than P–N-bonds. Furthermore, owing to the positive electron affinity of N, nitride ions are prone to oxidation and the formation of N_2 at elevated temperatures, while P^V may easily be reduced to P^{III} or P^0 or even P^{-III}. P_3N_5, a key precursor in many nitridophosphate syntheses, for instance, decomposes at 850 °C, while usually temperatures above 1000 °C are necessary for product crystallization.[10] Following Le Chatelier's principle, decomposition can be suppressed by applying pressure, which enables high temperature syntheses.

Employing the high-pressure approach, explorative research yielded numerous highly condensed nitridophosphates. Compounds with a degree of condensation of $\kappa = ½$, for example, were found for a broad variety of cations and show intriguing materials properties. In the group of APN_2 (*A* = H, Li, Na), $LiPN_2$ was discussed for its Li-conductivity, while HPN_2 is a sought-after precursor for nitridophosphate synthesis.[11–15] AEP_2N_4 (*AE* = Be, Ca, Sr, Ba) shows exceptional high hardness for Be in case of a high-pressure modification as well as promising luminescent properties in case of Ca, Sr and Ba, when doped with Eu^{2+}.[16–19] Furthermore, it was even possible to synthesize two of the first transition metal nitridophosphates, namely MP_2N_4 (*M* = Mn, Cd).[20] Most synthetic approaches for these compounds start from metal azides in combination with HPN_2 or P_3N_5. Due to their explosiveness, the azides may be replaced by the respective metal nitrides or even metal

powders. Most named compounds incorporating a cation with charge +2 (Ca^{2+}, Sr^{2+}, Mn^{2+}, Cd^{2+}) crystallize isotypically in a structure closely related to the megacalsilite ($KAlSiO_4$) type.[21] BeP_2N_4 and BaP_2N_4 exhibit their own structure types, however, with related structural units.

3.2 Results and Discussion

In this contribution, we present GeP_2N_4, the first representative of germanium(II) nitridophosphates and the first compound in this class with a degree of condensation of ½ incorporating a p-block cation. The title compound was synthesized under high-pressure high-temperature conditions at 6 GPa and 800 °C in a 1000 t hydraulic press with a modified Walker-type module. According to equation 1 GeP_2N_4 is formed from Ge_3N_4 and P_3N_5 by reduction of Ge^{IV} to Ge^{II} and partial oxidation of N^{-III} to N^0 in N_2. A second synthetic approach starts from elemental Ge, P_3N_5 and NH_4N_3 (Equation 2).

$$Ge_3N_4 + 2\ P_3N_5 \longrightarrow 3\ GeP_2N_4 + N_2 \quad (1)$$

$$3\ Ge + 2\ P_3N_5 + NH_4N_3 \longrightarrow 3\ GeP_2N_4 + 2\ H_2 + N_2 \quad (2)$$

The starting materials were finely ground under argon atmosphere, tightly packed into an h-BN crucible and reacted in the multianvil apparatus, yielding a dark gray powder.[22] Further details on the synthesis are given in the supporting information. A reaction temperature of exactly 800 °C is necessary, as temperatures below 800 °C lead to an incomplete reaction, whilst temperatures above 800 °C already degrade GeP_2N_4 to elemental Ge and an amorphous side phase, most likely containing the remaining P and N. This temperature dependence was already observed for nitridogermanates, e.g. $Ca_{1-x}Li_xAl_{1-x}Ge_{1+x}N_3$ ($x \approx 0.2$).[23] Even at 800 °C, GeP_2N_4 starts to decompose in small amounts during synthesis. Decomposition products, especially elemental Ge, however, can be removed by washing the sample with a 1:1 vol-% mixture of 30% H_2O_2 and concentrated NaOH. The washed samples contain single crystals up to 20 µm length, as shown by scanning electron microscopy (SEM) images (Figures 3.1 and S2.1). The elemental composition of GeP_2N_4 was analyzed and confirmed by energy dispersive X-ray spectroscopy (EDX) measurements (Table S2.1).

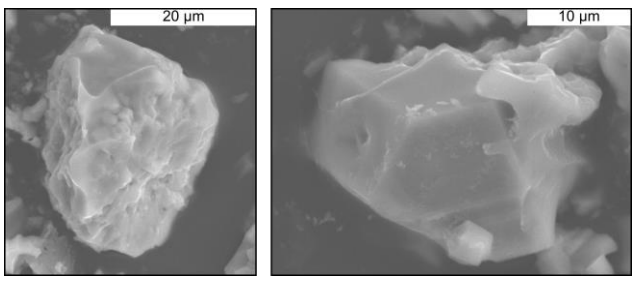

Figure 3.1: Exemplary SEM images of single crystals of GeP_2N_4. Crystals are up to 20 µm in length and width.

The structure of GeP_2N_4 was elucidated from inversion twinned single-crystal X-ray diffraction data (*Pna*2_1 (no. 33), a = 9.547(1), b = 7.542(1), c = 4.6941(6) Å, Z = 4, R_1 = 0.0240; more details can be found in the supporting information).[24] The polar space group *Pna*2_1 allows potentially intriguing materials properties, such as pyro-, piezo- or ferroelectricity, an electrooptic effect or second harmonic generation. Using the structure model combined with powder X-ray diffraction data, GeP_2N_4 was identified as the main constituent of samples by Rietveld refinement (Figure S2.3).

In contrast to most MP_2N_4 phases, which crystallize isostructurally (*M* = Ca, Sr, Mn, Cd) or consist of similar structural units (*M* = Be), the structure of GeP_2N_4 shows only few similarities to the aforementioned. It is built up from all-side vertex-sharing PN_4-tetrahedra, forming a three-dimensional anionic P/N-network. The network can be described by undulated chains of PN_4-tetrahedra (blue, orange) along [100], which consist of pairs of two tetrahedra, pointing alternatingly up and down along [010] (Figure 3.2). The connection of these chains form stacked *vierer* and *achter* rings along [001] as defined by Liebau.[1]

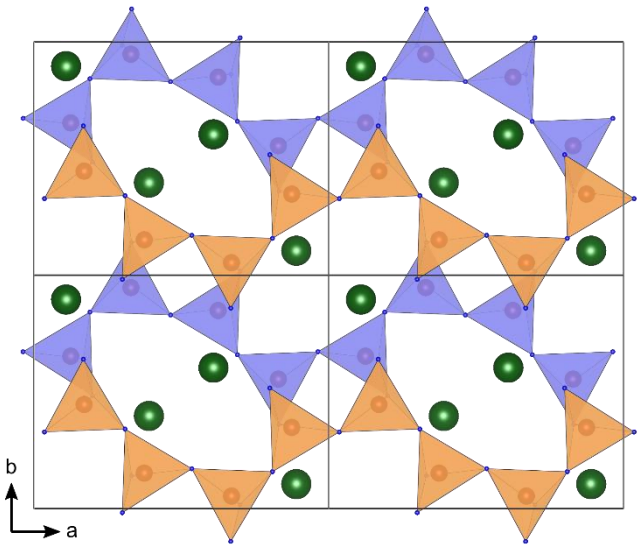

Figure 3.2: The crystal structure of GeP_2N_4 consists of all-side vertex-sharing PN_4-tetrahedra, forming undulated chains along [100] (orange, blue). The chains are interconnected and form *vierer* and *achter* rings.

Two Ge2+-ions are located within each achter ring, while the vierer rings stay empty. The point symbol, describing the network topology, was determined by the TOPOS software to be $\{4^2.6^3.8\}$, which matches with the paracelsian and LiNdP4N8 framework.[2,3,25] Whilst the anionic P/N framework is similar to the one of paracelsian and $LiNdP_4N_8$, the cation positions are not. Viewing along [001], Ba in paracelsian and Nd in $LiNdP_4N_8$ are located along the longitudinal axis of the achter rings, whereas Ge is located on the shorter transverse axis (Figure S2.2). We attribute this structural divergence to a strong stereochemical effect of the

lone pair at Ge^{2+}, forcing the cations onto positions with the least electrostatic repulsion. We assume that for the same reason the crystal structure of GeP_2N_4 shows no relation to other MP_2N_4 (M = Be, Ca, Sr, Ba, Mn, Cd) phases, with the exception of PN_4-tetrahedra as basic building blocks. This feature is unprecedented in nitridophosphates, however, was theoretically investigated by Dronskowski *et al.* for alkaline-earth transition-metal chalcogenides.[26]

Distances (1.596(3) – 1.654(4) Å) and angles (102.42(19) – 117.4(2)°) in PN_4-tetrahedra of GeP_2N_4 are comparable to $LiNdP_4N_8$ and other MP_2N_4 (M = Be, Ca, Sr, Ba, Mn, Cd) compounds. Ge^{2+} is threefold coordinated by N, forming a trigonal pyramid (Figure 3.3). Thus far, this coordination geometry is unprecedented in solid-state materials, which tend to form angled

GeN_2^{4-}-units, e.g. in $Ba_3Ge_2N_2$, and was only observed in molecules, e.g. various aza-macrocyclic complexes.[27,28] DFT calculations support the observed bonding situation of Ge. Visualizing the electron density, it shows electron density between Ge1 and all coordinating nitrogen atoms N1/N2/N4 (Figure 3.4). All three interatomic Ge–N distances (2.012(5) – 2.150(4) Å) and N–Ge–N angles (85.87(15) – 92.78(15)°) are in a close range and thus support the bonding situation, too. The Ge–N distances in GeP_2N_4 are slightly longer compared to those of the angled GeN_2^{4-}-units in $Ba_3Ge_2N_2$ (1.873(8) – 1.883(11) Å), showing the typical trend of increased bond lengths with increased coordination numbers. A Ge–Ge distance of 3.5127(7) Å rules out a single bond between cations, as observed in various organometallic compounds.[29,30]

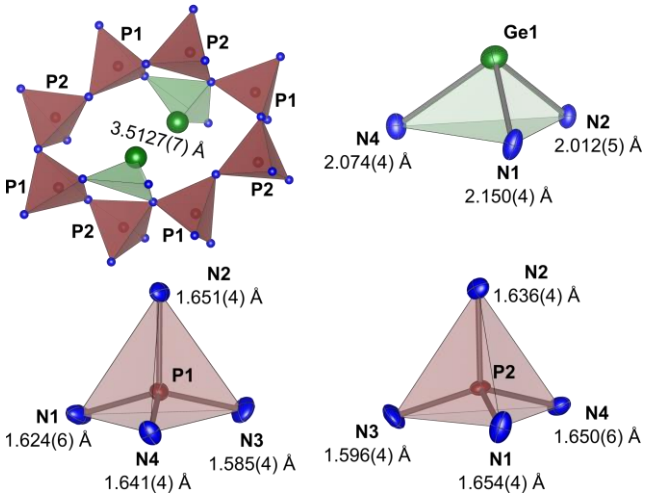

Figure 3.3: Coordination polyhedra of P1, P2 and Ge1. The thermal ellipsoids are shown at 90% probability level.

Polyhedral distortions in GeP_2N_4 were analyzed calculating the minimal bonding ellipsoids (MBE) using the software PIEFACE, showing regular PN_4-tetrahedra (Figure S2.8).[31] Furthermore, the electrostatic plausibility of the structure model was confirmed by calculating

effective charges using the CHARDI and BVS method.[32,33] The results and more detailed information is provided in the supporting information.

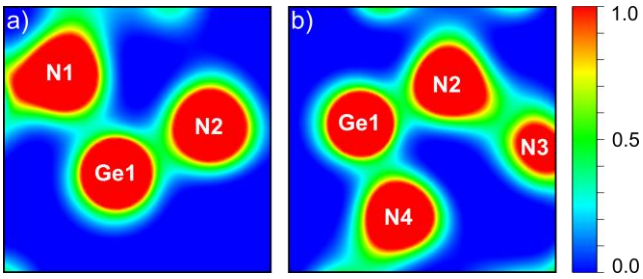

Figure 3.4: Electron localization plot for visualization of the Ge–N bonding situation. Ge1 forms three bonds to the coordinating atoms N1, N2 and N4. a) Shared electron density between Ge1 and N1/N2. b) Shared electron density between Ge1 and N2/N4. No shared electron density is observed in between Ge1 and N3.

Beyond the detailed view on the bonding situation between Ge and N, the electronic structure of GeP_2N_4 was examined by calculating the density of states (DOS) as shown in figure 5. The calculations reveal three distinct regions from −20 eV to −15 eV, from −14 eV to −6 eV and from −6 eV to the fermi edge at 0 eV.

The lowest energy region is almost exclusively dominated by contributions of P and N, equating to strong P–N-bonds, forming the covalent nitridophosphate network. The middle region shows contributions of all elements and is mainly dominated by Ge–N and further contributions of P–N bonds. States close to the fermi edge show a high contribution of Ge, originating from the lone electron pair. Further detailed plots on the density of states can be found in the supporting information (Figures S2.9 and S2.10).

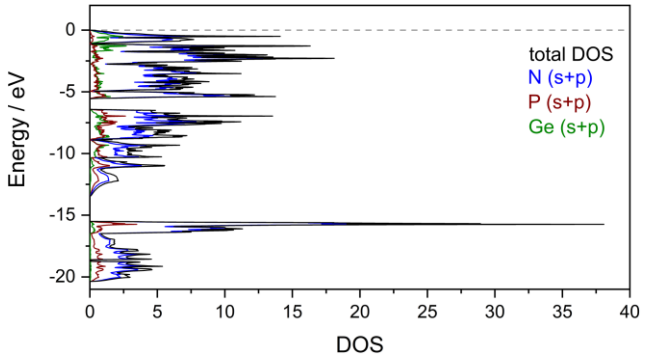

Figure 3.5: Calculated density of states (DOS) for GeP_2N_4. The total DOS and contributions of individual elements are color-coded.

To rule out incomplete condensation and the presence of imide groups, which either may form as contact to air and moisture cannot be completely avoided during synthesis or using

NH_4N_3 as a reactant according to Equation 2, samples were analyzed by FTIR-spectroscopy (Figure S2.7) and solid-state NMR-spectroscopy (Figures 6 and S6).

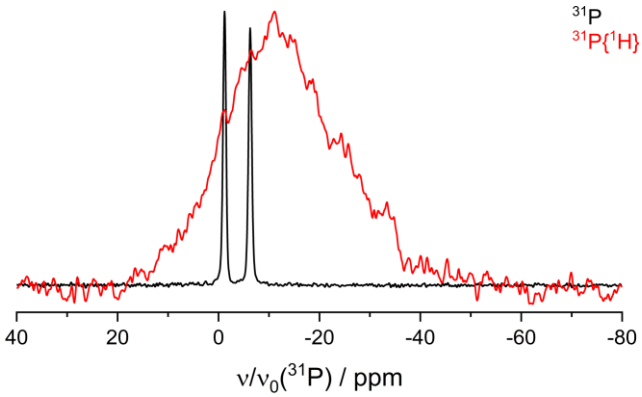

Figure 3.6: ^{31}P NMR spectrum of GeP_2N_4 (black) showing two signals with intensity ratio 1:1. These signals do not match with the ^{31}P{^{1}H} NMR spectrum (red), which indicates the absence of hydrogen in GeP_2N_4.

The ^{31}P-spectrum shows two signals with an integrated intensity ratio of 1:1, which corresponds to two crystallographic P sites with the same multiplicity (4*a*). The chemical shifts (δ = −1.20 ppm, δ = −6.27 ppm) are in the typical range of PN_4-tetrahedra next to metal cations, as observed in other MP_2N_4 (*M* = Sr, Ba, Mn, Cd) compounds.[18–20] The ^{31}P{^{1}H} cross polarized spectrum contains no signal matching the ^{31}P signals of GeP_2N_4, indicating the absence of hydrogen in the crystal structure of GeP_2N_4. Furthermore, the FTIR-spectrum shows no N–H absorption band, which supports all previous results.

As the synthesis of GeP_2N_4 is extremely sensitive to small changes in temperature, the thermal expansion and stability of GeP_2N_4 was examined by temperature-dependent powder X-ray diffraction experiments (Figure S2.4). It was found, that GeP_2N_4 shows an extremely small thermal expansion of the unit cell (average: 10.5 ppm/K) in the range from 25 to 800 °C (Figure S2.5), the critical temperature threshold observed during synthesis. Upon further heating, GeP_2N_4 decomposes irreversibly into amorphous materials and on cooling no recrystallisation or formation of another compound is observed. Such low thermal expansion, sometimes even negative, is usually observed for zeolites and extremely porous materials and attributed to an internal expansion into the pores of the crystal structure.[34] As GeP_2N_4 features the same degree of condensation as zeolites as well as large rings containing Ge^{2+}, a similar behavior seems reasonable.

3.3 Summary

Summarizing, we have synthesized GeP_2N_4, the first MP_2N_4 compound with a p-block cation and the first example of a germanium(II) nitridophosphate. The synthesis was carried out under

high pressure and high temperature starting from P_3N_5 and Ge_3N_4. The structure was determined by single-crystal X-ray diffraction and analyzed for its plausibility by Rietveld-refinement, MBE, CHARDI and BVS calculations. The density of states and bonding situation between Ge and N was theoretically analyzed using DFT calculations and an electron localization function. Further characterization of GeP_2N_4 was done by means of FTIR- and NMR-spectroscopy and temperature dependent powder X-ray diffraction. As shown here, the formal exchange of alkaline-earth cations with Ge^{2+} is possible, however, leads to a comprehensive structural change due to the stereochemical influence of the lone pair at Ge^{2+}. Using this possibility with other literature-known alkaline-earth nitridophosphates, we expect access to a variety of new structures with intriguing materials properties or even the possibility of targeted structural tuning by mixing germanium with alkaline-earth metals.

3.4 Acknowledgements

Financial support by the Deutsche Forschungsgemeinschaft (project SCHN 377/18) is gratefully acknowledged as well as support by the Natural Sciences and Engineering Research Council of Canada and the Canada Research Chair program. Compute Canada and the Plato computing cluster at the University of Saskatchewan are acknowledged for computational resources. The authors thank Tim Reska for his experimental support during his internship. Furthermore, we thank Christian Minke for the NMR experiments as well as SEM and EDX measurements.

3.5 References

[1] F. Liebau, *Structural Chemistry of Silicates. Structure, Bonding, and Classification*, Springer, Berlin, **1985**, pp. 1–6. The terms "*vierer ring*" and "*achter ring*" have been defined by Liebau and are derived from the German words "vier" (engl. four) and "acht" (engl. eight), describing rings consisting of the respective amount of tetrahedra.

[2] J. V. Smith, *Acta. Crystallogr.* **1953**, *6*, 613.

[3] S. D. Kloss, W. Schnick, *Angew. Chem. Int. Ed.* **2015**, *54*, 11250.

[4] L. Eisenburger, P. Strobel, P. J. Schmidt, T. Bräuniger, J. Wright, E. L. Bright, C. Giacobbe, O. Oeckler, W. Schnick, *Angew. Chem. Int. Ed.* **2022**, *61*, e202114902.

[5] J.-M. Léger, J. Haines, L. S. de Oliveira, C. Chateau, A. Le Sauze, R. Marchand, S. Hull, *J. Phys Chem. Solids* **1999**, *60*, 145.

[6] D. Baumann, S. J. Sedlmaier, W. Schnick, *Angew. Chem. Int. Ed.* **2012**, *51*, 4707.

[7] D. Baumann, R. Niklaus, W. Schnick, *Angew. Chem. Int. Ed.* **2015**, *54*, 4688.

[8] S. Vogel, D. Baumann, R. Niklaus, E. Bykova, M. Bykov, N. Dubrovinskaia, L. Dubrovinsky, W. Schnick, *Angew. Chem. Int. Ed.* **2018**, *57*, 6691.

[9] F. Liebau, *Angew. Chem. Int. Ed.* **1999**, *38*, 1733.

[10] A. Stock, H. Grüneberg, *Ber. Dtsch. Chem. Ges.* **1907**, *40*, 2573.

[11] W. Schnick, J. Lücke, *Z. Anorg. Allg. Chem.* **1992**, *610*, 121.

[12] A. Marchuk, F. J. Pucher, F. W. Karau, W. Schnick, *Angew. Chem. Int. Ed.* **2014**, *53*, 2469.

[13] W. Schnick, J. Lücke, *Z. Anorg. Allg. Chem.* **1990**, *588*, 19.

[14] W. Schnick, J. Lücke, *Solid State Ion.* **1990**, *38*, 2713.

[15] K. Landskron, S. Schmid, W. Schnick, *Z. Anorg. Allg. Chem.* **2001**, *627*, 2469.

[16] S. Vogel, M. Bykov, E. Bykova, S. Wendl, S. D. Kloß, A. Pakhomova, N. Dubrovinskaia, L. Dubrovinsky, W. Schnick, *Angew. Chem. Int. Ed.* **2020**, *59*, 2730.

[17] F. J. Pucher, A. Marchuk, P. J. Schmidt, D. Wiechert, W. Schnick, *Chem. Eur. J.* **2015**, *21*, 6443.

[18] F. W. Karau, W. Schnick, *J. Solid State Chem.* **2005**, *178*, 135.

[19] F. W. Karau, L. Seyfarth, O. Oeckler, J. Senker, K. Landskron, W. Schnick, *Chem. Eur. J.* **2007**, *13*, 6841.

[20] F. J. Pucher, F. W. Karau, J. Schmedt auf der Günne, W. Schnick, *Eur. J. Inorg. Chem.* **2016**, *2016*, 1497.

[21] A. P. Khomyakov, G. N. Nechelyustov, E. Sokolova, E. Bonaccorsi, S. Merlino, M. Pasero, *Canad. Mineral.* **2002**, *40*, 961.

[22] H. Huppertz, *Z. Kristallogr. Cryst. Mater.* **2004**, *219*, 330.

[23] J. Häusler, L. Eisenburger, O. Oeckler, W. Schnick, *Eur. J. Inorg. Chem.* **2018**, *2018*, 759.

[24] Deposition Number 2210954 contains the supplementary crystallographic data for this paper. These data are provided free of charge by the joint Cambridge Crystallographic Data Centre and Fachinformationszentrum Karlsruhe Access Structures service.

[25] V. A. Blatov, A. P. Shevchenko, D. M. Proserpio, *Cryst. Growth Des.* **2014**, *14*, 3576.

[26] K. Eickmeiner, R. Poschkamp, R. Dronskowski, S. Steinberg, *Eur. J. Inorg. Chem.* **2022**, e202200360.

[27] H. Yamane, F. J. DiSalvo, *J. Alloys Compd.* **1996**, *241*, 69.

[28] M. Everett, A. Jolleys, W. Levason, M. E. Light, D. Pugh, G. Reid, *Dalton Trans.* **2015**, *44*, 20898.

[29] J. Li, C. Schenk, C. Goedecke, G. Frenking, C. Jones, *J. Am. Chem. Soc.* **2011**, *133*, 18622.

[30] S. Nagendran, S. S. Sen, H. W. Roesky, D. Koley, H. Grubmüller, A. Pal, R. Herbst-Irmer, *Organometallics* **2008**, *27*, 5459.

[31] J. Cumby, J. P. Attfield, *Nat. Commun.* **2017**, *8*, 14235.

[32] R. Hoppe, S. Voigt, H. Glaum, J. Kissel, H. P. Müller, K. Bernet, *J. less-common Met.* **1989**, *156*, 105.

[33] A. S. Wills, VaList - A bond valence calculation and analysis program, London, **2010**.

[34] P. Tschaufeser, S. C. Parker, *J. Phys. Chem.* **1995**, *99*, 10609.

Chapter 4

Building Nitridic Networks with Phosphorus and Germanium – from $Ge^{II}P_2N_4$ to $Ge^{IV}PN_3$

Published in: *Inorg. Chem.* **2024**, *63*, 8502

Authors: Sebastian J. Ambach, Georg Krach, Elena Bykova, Kristian Witthaut, Nico Giordano, Maxim Bykov, Wolfgang Schnick

DOI: https://doi.org/10.1002/acs.inorgchem.4c01202

Abstract: Nitridophosphates and nitridogermanates attract high interest in current research due to their structural versatility. Herein, the elastic properties of GeP_2N_4 were investigated by single-crystal X-ray diffraction (XRD) upon compression to 44.4(1) GPa in a diamond anvil cell. Its isothermal bulk modulus was determined to be 82(6) GPa. At 44.4(1) GPa, laser heating resulted in the formation of multiple crystalline phases, one of which was identified as the unprecedented germanium nitridophosphate $GePN_3$. Its structure was elucidated from single-crystal XRD data (*C*2/*c* (no. 15), *a* = 8.666(5), *b* = 8.076(4), *c* = 4.691(2) Å, *β* = 101.00(7)°) and is built up from layers of GeN_6 octahedra and PN_4 tetrahedra. The GeN_6 octahedra form double zigzag chains, while the PN_4 tetrahedra are found in single zigzag chains. $GePN_3$ can be recovered to ambient conditions with a unit cell volume increase of about 12%. It combines P^V and Ge^{IV} in a condensed nitridic network for the first time.

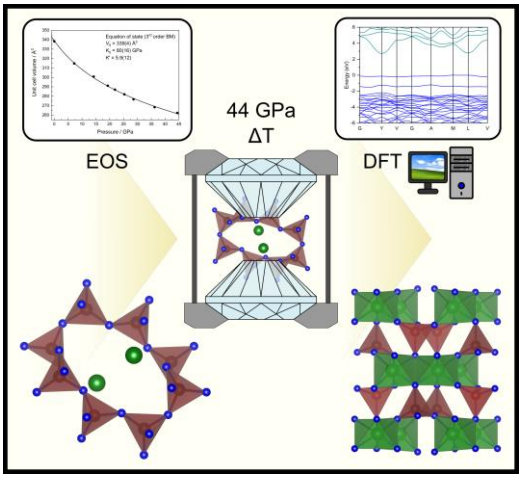

4.1 Introduction

Nitrides are considered to be one of the most diverse and versatile classes in structural chemistry, besides the naturally occurring oxides.[1] As the term 'nitride' covers a very broad range of compounds, these are often subclassed according to the network-forming elements, e.g. nitridoborates, nitridosilicates, nitridogermanates or nitridophosphates. Investigations on the different subclasses attract high interest in current research, as they exhibit desirable properties for modern applications, such as high mechanical hardness, high thermal stability or extraordinary luminescent properties when doped with Eu^{2+}.[2–9]

Nitridophosphates, built up from anionic P^V/N units in combination with various cations, stand out with a high structural versatility. Analogous to the isoelectronic combination of elements Si/O, forming SiO_4 tetrahedra, compounds mostly consist of PN_4 tetrahedra as basic structural building units. The tetrahedra can be found isolated, connected to small rings, chains, layers or 3D-networks.[10–14] Interconnections of tetrahedra are mostly realized as vertex-sharing, however, edge-sharing has also been reported.[14–16] Besides PN_4 tetrahedra, PN_5 pyramids, either square based (e.g. in *γ*-P_3N_5) or trigonal bipyramidal (e.g. in *γ*-HP_4N_7 or MP_6N_{11} (*M* = Al, In)) are occasionally encountered.[17–19] Even PN_6 octahedra have been reported, e. g. in *β*-BP_3N_6 at 42 GPa and *δ*-P_3N_5 at 72 GPa.[20,21] This abundance of structural motifs leads to nitridophosphates finding usage in a broad range of applications. For example, the binary phosphorus(V) nitride P_3N_5 is used as a gate insulator in metal-insulator-semiconductor field-effect transistors (MISFETs) and was also investigated as a flame retardant or for safety in pyrotechnics.[22–25] The nitridic clathrate $P_4N_4(NH)_4(NH)_3$ was investigated as a gas storage material.[26] $Ba_3P_5N_{10}Br:Eu^{2+}$ and $AEP_8N_{14}:Eu^{2+}$ (*AE* = Ca, Sr, Ba) were reported as warm-white and ultra-narrow-band blue emitting phosphors, respectively.[9,27] Moreover, various lithium nitridophosphates were analyzed regarding their usage as Li ion conductors.[28–30]

Nitridogermanates are characterized by Ge^{II}/N, Ge^{III}/N or Ge^{IV}/N anionic building units. Combinations of Ge^{II}/N usually form bent $[Ge^{II}N_2]^{4-}$ units, e.g. in Ca_2GeN_2.[31] Ge^{III} in nitrides is found in $[Ge_2N_6]^{12-}$ units with a Ge−Ge bond, e.g. in $Ca_6[Ge_2N_6]$, while combinations of Ge^{IV}/N most commonly form $[Ge^{IV}N_4]^{8-}$ tetrahedra, analogous to nitridophosphates.[32] The tetrahedra can be found isolated (e.g. in Sr_4GeN_4), connected by shared vertices (e.g. in $Ca_5Ge_2N_6$) or edges (e.g. in $Sr_5Ge_2N_6$) or condensed to a 3D-network (e.g. in $CaGeN_2$).[31,33–35] Rarely, also trigonal planar $[Ge^{IV}N_3]^{5-}$ units (e.g. in $Ba_9(GeN_3)_3N$) were observed.[36] A spinel-type high-pressure modification of the germanium nitride Ge_3N_4 even shows $[Ge^{IV}N_6]^{14-}$ octahedra.[37] Materials properties of nitridogermanates have hardly been investigated. $ZnGeN_2$ was reported as a semiconductor material and recent calculations predicted promising optical and electronic properties for $Li_4Sr_3Ge_2N_6$.[38–40] Apart from the most common oxidation states +IV

and +II, the diverse redox chemistry of Ge in nitrides led to infinite Zintl-ion Ge^{2-} chains (e.g. in $Sr_3Ge_2N_2$) and Ge^{4-} anions (e.g. in $Sr_{11}Ge_4N_6$).[41,42]

Considering the various structural possibilities, the combination of phosphorus and germanium simultaneously in a nitridic network, leading to germanium phosphorus nitrides and germanium nitridophosphates, seems promising to yield a large number of new structure types with intriguing materials properties. To date, there is only a single ternary compound in the Ge/P/N-system, namely the germanium(II) nitridophosphate $Ge^{II}P_2N_4$.[41] Structurally, Ge^{2+} cations are embedded in an anionic network of PN_4 tetrahedra. This classifies GeP_2N_4 as a nitridophosphate, showing a structural influence of the Ge^{2+} lone pair. In this contribution, we report on the elastic properties of GeP_2N_4 up to 44 GPa in a diamond anvil cell (DAC) as well as its transformation to $Ge^{IV}PN_3$, the first representative of a germanium nitridophosphate comprised of Ge^{IV} and P^{V}.

4.2 Experimental Section

High-Pressure High-Temperature Synthesis of GeP_2N_4

The sample of GeP_2N_4 used for this contribution was synthesized in a previous work.[43[P_3N_5 and Ge_3N_4 were finely ground together in an argon-filled glovebox (MBraun, < 1 ppm H_2O, < 1 ppm O_2). The powder was tightly packed into an h-BN crucible (Henze, Kempten), which was closed with an h-BN lid and surrounded by two graphite heaters (Schunk Kohlenstofftechnik GmbH, Zolling). The heaters were placed in a ZrO_2 sleeve (Cesima Ceramics, Wust-Fischbeck) and centered in a drilled-through octahedron (MgO doped with 5% Cr_2O_3, 18 mm edge length, Ceramic Substrates & Components Ltd, Isle of Wight) using MgO spacers (Cesima Ceramics, Wust-Fischbeck). The assembly was contacted by a Mo disc from each side and placed in the center of eight electrically insulated WC cubes (32 mm edge length, 11 mm truncated edge length, 7% Co doped, Hawedia, Marklkofen). A more detailed description of the sample preparation can be found in the literature.[44,45]

The assembly was compressed to 6 GPa within 170 min by a 1000 t hydraulic press using the multi-anvil technique and a modified Walker-module. Subsequently, the sample was heated to 800 °C within 60 min, the temperature was held for 240 min, cooled down within 60 min and finally decompressed to ambient pressure within 500 min. The recovered sample was separated from all assembly parts and washed with a 1:1 vol-% mixture of conc. NaOH and H_2O_2 to remove excess elemental Ge. The product formed as colorless block-shaped crystals and was analyzed by energy-dispersive X-ray (EDX) spectroscopy and powder X-ray diffraction (PXRD).

Scanning Electron Microscopy and Energy-Dispersive X-Ray Spectroscopy

The sample was carbon-coated by an electron beam evaporator (BAL-TEC MED 020, Bal Tec AG) to ensure electrical conductivity and transferred into a Helios Nanolab G3 UC (FEI, Hilsboro) scanning electron microscope (SEM), equipped with a X-Max 80 SDD detector (Oxford instrument, Abingdon). Image acquisition and energy-dispersive X-ray (EDX) analyses were performed using the Aztec software.[46]

Powder X-Ray Diffraction (PXRD) and Rietveld Refinement: For measurements, the sample was finely ground and sealed in a glass capillary (0.3 mm outside diameter, Hilgenberg, Malsfeld). The capillary was centered on a rotating goniometer head and subsequent data acquisition was done on a STOE Stadi P diffractometer (STOE & Cie GmbH, Darmstadt) in modified Debye-Scherrer geometry with Cu-$K_{\alpha1}$ radiation (λ = 1.5406 Å), a MYTHEN 1K strip detector and a Ge(111) monochromator.

PXRD data were fitted using the Rietveld method with the single-crystal model published in literature as starting model.[43,47] Peak profiles were described by the fundamental parameter approach, a preferred orientation of the crystallites was accounted for with a 4th order spherical harmonic function and the background was modeled by a shifted Chebyshev polynomial.[48,49] The refinement was performed using the TOPAS Academic suite of software.[50]

Synchrotron Measurements and Data Analysis

In-situ X-ray diffraction (XRD) data were collected at the Extreme Conditions Beamline P02.2 (PETRA III) at Deutsches Elektronen-Synchrotron (DESY, Hamburg), using laser-heated diamond anvil cells (DAC).[51] For measurements, the X-ray beam (λ = 0.2905 Å) was focused to 1.8×1.4 µm^2 (FWHM horizontal×vertical) by a Kirkpatrick-Baez mirror system. X-ray diffraction data were collected on a PerkinElmer XRD 1621 flat-panel detector. Powder X-ray diffraction (PXRD) patterns were obtained by radial integration of single frames using Dioptas.[52] For the DAC, Ne was used as pressure transmitting medium and simultaneously served as an internal pressure standard (see next section for more details). After masking diamond and sample reflections in PXRD patterns, reflections of Ne were identified, its lattice parameters were refined using the Pawley method (in TOPAS Academic) and the pressure was calculated using the equation of state of Ne established by Fei *et al*.[50,53,54]

Single-crystal data of GeP_2N_4 were collected by ω scans (ω_{max} = ±31°; $\Delta\omega$ = 0.5°; exposure time = 1 s) in the pressure range from ambient pressure to 44.4(1) GPa using 125/100/50 µm Pt absorbers for X-ray attenuation (Table S2). Single-crystal data of $GePN_3$ (ω scans; ω_{max} = ±31°; $\Delta\omega$ = 0.5°; exposure time = 1 s) were collected at 44.4(1) GPa and ambient pressure without X-ray attenuation. Data analysis was performed with the CrysAlisPro software.[55] To calibrate the instrument model for CrysAlisPro, a single crystal of ortho-enstatite

($(Mg_{1.93},Fe_{0.06})(Si_{1.93}, Al_{0.06})O_6$, a = 8.8117(2), b = 5.18320(10), c = 18.2391(3) Å) was used. After laser-heating the sample at 44.4(1) GPa, the single crystals fragmented into multiple phases and domains. Using the CrysAlisPro reciprocal space viewer (Ewald Explorer) and Domain Auto Finder (DaFi), reflections of different domains were grouped for separate indexing and subsequent data reduction.[56]

For each pressure point, XRD data of GeP_2N_4 were solved by SHELXT using direct methods. Structure refinement against F^2 was done by SHELXL with the least-squares method.[57] The structure of $GePN_3$ was solved and refined from XRD data at 44.4(1) GPa in an analogous way to GeP_2N_4. The structure model of $GePN_3$ at ambient pressure was refined against F^2 with the least-squares method using the high-pressure model as a starting point.

Laser-Heated Diamond Anvil Cell

The high-pressure experiments were carried out in a BX90 diamond anvil cell, equipped with two Boehler-Almax-type diamonds with 250 µm culets.[58] The diamonds were separated by a Re gasket, which was pre-indented to 30 µm thickness and a 100 µm diameter hole was laser-drilled to form the sample chamber. The cell was loaded with two single-crystals of GeP_2N_4 and gas-loaded in Ne (Sanchez-Technologies gas loader), which served simultaneously as a pressure transmitting medium and internal pressure standard. After step-wise compression to 44.4(1) GPa at ambient temperature (Table S3.2), the sample was heated from both sides using a near-infrared (NIR) fiber laser (λ = 1070 mm, focused to 20×20 µm^2) in continuous wave mode. After a short flash, the sample was cooled down to ambient temperature and XRD data were collected. Due to the short heating period, the temperature could not be determined.

Equation of State

Using the pressure-dependent data of the lattice parameters from ambient pressure to 44.4(1) GPa, the volume of the unit cell of GeP_2N_4 was described by a third order Birch-Murnaghan equation of state (Equation 1).[59,60] The data fitting was performed using EoSFit7.[61]

$$p(V)=\frac{3}{2} K_0 \left[\left(\frac{V_0}{V}\right)^{\frac{7}{3}} - \left(\frac{V_0}{V}\right)^{\frac{5}{3}}\right] \cdot \left[1+\frac{3}{4}(K'-4)\left\{\left(\frac{V_0}{V}\right)^{\frac{2}{3}}-1\right\}\right] \quad (1)$$

(K_0: isothermal bulk modulus, V: unit cell volume, V_0: unit cell volume at a theoretical pressure of 0, K' partial pressure derivative of the isothermal bulk modulus)

Minimal Bonding Ellipsoid Calculations

All coordination polyhedra can be described as an ellipsoid with all ligand atoms of the polyhedron on its surface. The resulting minimal bonding ellipsoid is characterized by its radii $R1$, $R2$ and $R3$, the mean radius R and its standard deviation $\sigma(R)$ and the displacement of

the central atom from the ellipsoid center. The calculated shape parameter S gives an indication for oblate (S < 0), regular (S ≈ 0) or prolate (S > 0) shaped polyhedra. Minimal bonding ellipsoid calculations of the $GePN_3$ structure model at ambient pressure were performed using PIEFACE.[62]

Charge Density in Solids Calculations

CHARDI calculations of the $GePN_3$ structure model at 44.4(1) GPa and ambient pressure were performed using the VESTA software.[63]

Density Functional Theory Calculations

With the Vienna ab initio simulation package (VASP) first principle electronic structure calculations were performed based on periodic density functional theory calculations.[64–67] Within VASP core and valence electrons are separated exploiting projector-augmented waves (PAW).[68,69] The exchange and correlation energy is calculated using the generalized gradient approximation (GGA), as described by Perdew, Burke and Ernzerhof (PBE).[70] For a broader analysis of the band gap additional calculations were performed using the meta-GGA functional modified Becke-Johnson (MBJ).[71,72] For this, non-spherical contributions to the gradient of the density in the PAW spheres were included. To ensure a well converged structure, the Brillouin zone was sampled on a 5x5x7 Γ-centered *k*-point grid and the interpolation of the *k* space was done via Gaussian smearing with a SIGMA value of 0.02. The energy convergence criterion was set to 10^{-7} eV and the residual atomic forces were relaxed until the convergence criterion of 10^{-5} eV/Å was reached. The plane wave energy cutoff was set to 520 eV. The band structure was calculated for the Bloch vector k along the lines Γ (0,0,0) to Y (−0.5,0.5,0) to V (0,0.5,0) to Γ (0,0,0) to A (0,0,0.5) to M (-0.5,0.5,0.5) to L (0,0.5,0.5) and back to V (0,0.5,0). The energy zero is taken at the Fermi level.

4.3 Results and Discussion

For *in-situ* experiments, a DAC was loaded with two single crystals of GeP_2N_4 and Ne as pressure-transmitting medium. The DAC was compressed at ambient temperature in steps of approximately 5 GPa up to 44.4(1) GPa. At each step, single-crystal data were collected to follow the evolution of the lattice parameters and possible structural changes (Figures 4.1 and 4.2).

The lattice parameters *a* and *c* of the GeP_2N_4 unit cell possess similar compressibilities, while the lattice is noticeably more compressible along *b* (Figure 4.1d, Table S3.2). Its isothermal bulk modulus of 82(6) GPa was determined by fitting the pressure-volume data using a third-order Birch-Murnaghan equation of state (Figure 4.1a).[59,60] The Ge-Ge distances decrease from 3.5080(4) Å at ambient pressure to 2.784(5) Å at 44.4(1) GPa. This can be explained by

the structural effect of the Ge^{2+} lone pair. Other compounds of the same stoichiometry MP_2N_4 (M = Ca, Sr, Ba, Mn, Cd) all crystallize isotypically in a structure that is closely related to the megacalsilite ($KAlSiO_4$) type.[73] GeP_2N_4, on the other hand, has a completely different structure type, which can be explained by the increased space requirement of the Ge^{2+} cation compared to Ca, Sr, Ba, Mn and Cd. A detailed discussion of this effect, the description of the GeP_2N_4 structure and comparison with similar network types is provided in the literature.[43,74,75]

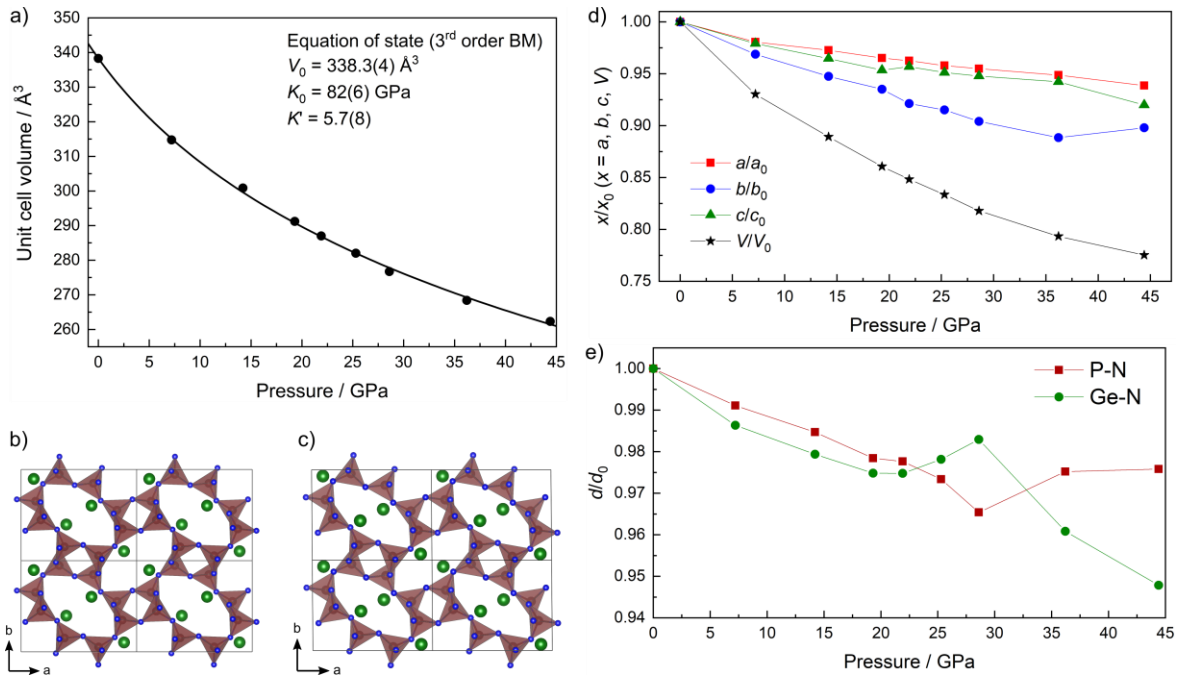

Figure 4.1: a) Equation of state of GeP_2N_4. Pressure-volume data were fitted using a third-order Birch-Murnaghan equation of state. b) GeP_2N_4 structure at ambient pressure (space group $Pna2_1$). c) GeP_2N_4 structure at 44.4(1) GPa (space group $P112_1$). Ge atoms are shown in green, N atoms in blue and PN_4 tetrahedra in red. For comparison, the lattice parameters of the monoclinic phase ($P112_1$) are not standardized, to correspond to the lattice parameters of the orthorhombic phase ($Pna2_1$). d) Evolution of the lattice parameters and unit cell volume of GeP_2N_4 during compression. e) Evolution of the P–N and Ge–N bong lengths of GeP_2N_4 during compression.

While widening the *achter*-rings at ambient pressure, the lone pairs simultaneously are the softest part regarding compression.[76] With increasing pressure, the rings become significantly more narrow, decreasing the N–N distance across the transverse axis from 4.94(1) to 4.15(6) Å (Figure 4.2). This matches with the non-isotropical contraction of the *b* lattice parameter, as the rings are stacked along *c* in the *ab* lattice plane. Structurally, the *achter*-rings are distorted by a combination of slight tetrahedra displacement and rotation. This also

causes a displacive phase transition from the initial $Pna2_1$ symmetry to the translationsgleiche subgroup $P112_1$ in the pressure range between 19.3(1) and 21.9(1) GPa (Table S3.2). Hereby, each Wyckoff site of the $Pna2_1$ symmetry is split into two sites of the $P112_1$ symmetry (Figure S3.3). The order of the phase transition could not be determined, as the pressure difference between individual data points is too large. Generally, Ge−N bonds are slightly more compressible compared to P−N bonds (Figure 4.1e, Table S3.3). However, the reduction in symmetry reverts this up to a pressure of 28.6(1) GPa.

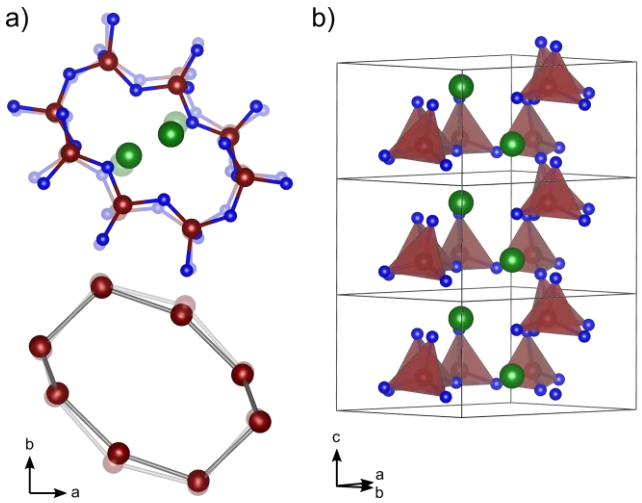

Figure 4.2: a) Overlay of the *achter*-rings of GeP_2N_4 containing the Ge^{2+} cations at ambient pressure (faded) and 44.4(1) GPa (opaque). During compression at ambient temperature, the rings show a significant distortion, resulting in a symmetry reduction from orthorhombic ($Pna2_1$) to monoclinic ($P112_1$) symmetry between 19.3(1) and 21.9(1) GPa. a) *achter*-ring with N (blue) and Ge (green) cations. b) Stacking of the Ge^{2+} cations within an *achter*-ring along [001] direction. Parts of the unit cell contents are omitted for clarity.

Except for the symmetry reduction, no evidence for a second phase transition was observed during compression at ambient temperature. To induce a further transition, one of the single crystals was offline laser-heated at 44.4(1) GPa (λ = 1070 nm, see Supporting Information for further details). After a short flash, a significant change in the XRD pattern was observed, suggesting the formation of grains with multiple crystalline phases. From the integration of one of the collected data sets, the previously unknown germanium nitridophosphate $GePN_3$ was discovered. Its structure was solved and refined in space group $C2/c$ (no. 15, a = 8.666(5), b = 8.076(4), c = 4.691(2) Å, β = 101.00(7)° at 44.4(1) GPa; more details are provided in Table 4.1 and Tables S3.4−S3.11).

Table 4.1: Crystallographic data of $GePN_3$ at 44.4(1) GPa and ambient pressure from single-crystal refinement. Standard deviations are given in parentheses.

Formula	**$GePN_3$**	
Pressure / GPa	44.4(1)	0.00010(1)
Crystal system	monoclinic	
Space group	*C2/c* (no. 15)	
a / Å	8.666(5)	9.065(5)
b / Å	8.076(4)	8.454(5)
c / Å	4.691(2)	4.8743(11)
β / °	101.00(7)	101.61(3)
Cell volume / $Å^3$	322.3(3)	365.9(3)
Formula units / unit cell	8	
Calculated X-ray density / $g \cdot cm^{-3}$	6.001	5.286
θ range / °	$1.95 < \theta < 16.03$	$1.95 < \theta < 16.28$
R_{int}; R_σ	0.0621; 0.0897	0.0266; 0.0206
Goodness of fit	1.108	1.095
R-values [$I \geq 2\sigma(I)$]	R_1 = 0.0644; *wR*2 = 0.1416	R_1 = 0.0409; *wR*2 = 0.1075
R-values (all data)	R_1 = 0.1048; *wR*2 = 0.1749	R_1 = 0.0513; *wR*2 = 0.1159
$\Delta\rho_{min}$, $\Delta\rho_{max}$ / $e \cdot Å^3$	–1.306; 1.482	–0.873; 0.743

A theoretical reaction pathway may be formulated as in Equation 2:

$$Ge^{II}P_2N_4 \rightarrow Ge^{IV}PN_3 + P^{III}N \rightarrow GePN_3 + P^0 + ½\ N_2 \quad (2)$$

Ge^{II} is oxidized to Ge^{IV}, while P^V may be reduced to P^{III} in PN and finally to elemental P, oxidizing the nitride anion to elemental N due to the extreme conditions during laser heating.[77,78]

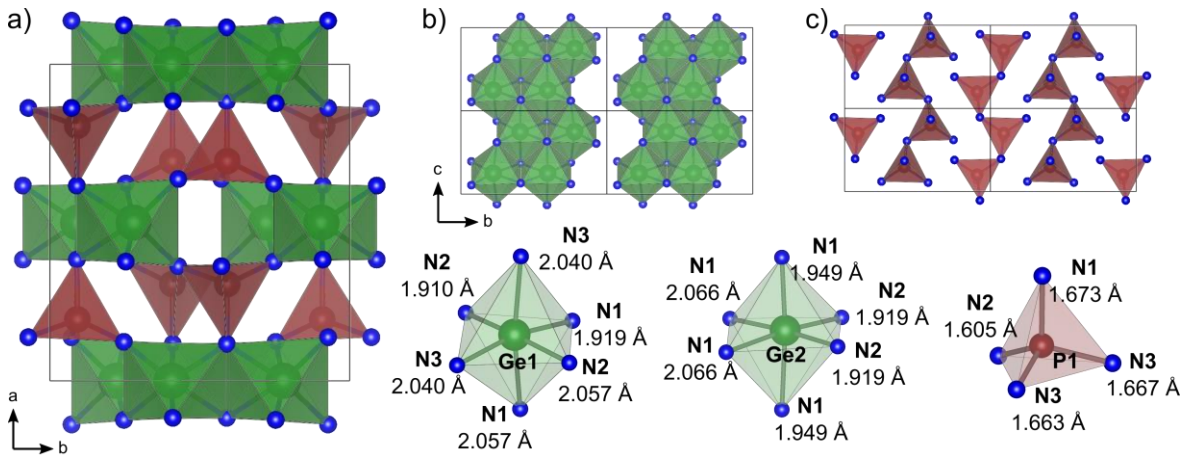

Figure 4.3: Structure and polyhedra of $GePN_3$ at ambient pressure. Standard uncertainties of interatomic distances are omitted for clarity. a) Unit cell of $GePN_3$ along [001]. b) GeN_6 octahedra forming double zigzag chains. c) PN_4 tetrahedra forming single zigzag chains.

The structure of $GePN_3$ is built up from alternating layers of GeN_6 octahedra, previously only observed in spinel-type hp-Ge_3N_4, and PN_4 tetrahedra along [100] (Figure 4.3). Each layer of GeN_6 octahedra consists of double zigzag chains of edge-sharing GeN_6 octahedra with no interconnection between the chains. The PN_4 layer consists of single zigzag chains of vertex-sharing PN_4 tetrahedra with no connection in between chains as well. The point symbol, describing the network topology, was determined to be $\{3^{11}.4^{19}.5^{6}\}2\{3^{14}.4^{29}.5^{12}\}\{3^{18}.4^{28}.5^{9}\}$. Hereby, each bracket describes the local topology of a vertex (e.g. Ge, P). The size of a shortest cycle consisting of neighboring vertices is given as a number, and its respective amount originating at the vertex is indicated as a superscript number.[79] This matches the network topology of the isotypic germanate $CoGeO_3$, sharing the same structural setup with CoO_6 octahedra and GeO_4 tetrahedra.[80] Considering the occurrence of GeN_6 octahedra, $GePN_3$ presented herein can be interpreted as a high-pressure polymorph of an as yet undiscovered ambient-pressure phase, which is possibly isotypic to $SiPN_3$.[81]

At 44.4(1) GPa, Ge–N distances range between 1.96(2) and 1.84(2) Å, slightly shorter compared to spinel-type hp-Ge_3N_4.[35] P–N distances are between 1.57(2) and 1.65(3) Å. After pressure-quenching to ambient pressure, the cell still contained single crystals of $GePN_3$, suggesting the compound to be metastable at ambient conditions. The unit cell volume increases by 12% from 322.3(3) to 365.9(3) $Å^3$, caused by an isotropic expansion of the lattice parameters by about 5% each (Table S3.4). The Ge–N distances of the GeN_6 octahedra increase to 1.910(6)−2.066(11) Å, comparable to GeN_6 octahedra in spinel-type hp-Ge_3N_4 and trigonal pyramidal coordinated GeN_3 units in GeP_2N_4.[37,43] The P–N distances are also increased to values between 1.673(7) and 1.605(12) Å, typical for e.g. α-P_3N_5.[14]

The GeN_6 octahedra are slightly distorted with the Ge^{4+} cation out of its geometrical center position in the [010] direction. This increases the distance to a neighboring Ge^{4+} atom in the same zigzag chain, reducing the electrostatic repulsion. This effect is quantified alongside other polyhedral properties in minimal bonding ellipsoid (MBE) calculations (Figures S3.5 and S3.6, Tables S3.14 and S3.15). For an additional electrostatic plausibility analysis, CHARDI calculations were performed (Tables S3.12 and S3.13). All theoretical cation and anion charges are within a small error margin of 4% from the calculated values. Density functional theory (DFT) calculations for ambient conditions were performed to gain insight in the electronic structure of $GePN_3$ (Figures 4, S3.7 and S3.8). The electronic band structures reveal an indirect band gap between 2.7 eV (Perdew-Burke-Ernzerhof, PBE) and 3.1 (modified Becke-Johnson, MBJ). The density of states (DOS) is dominated by contributions of N, which is due to the other elements Ge and P being present in their highest oxidation states.

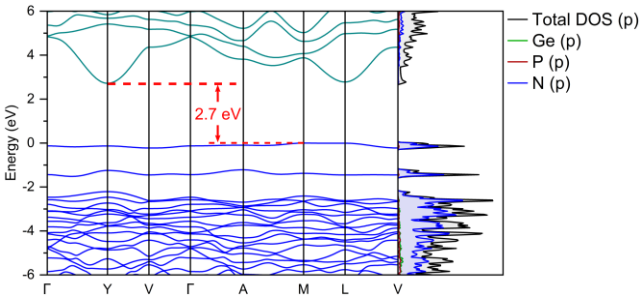

Figure 4.4: Band structure of $GePN_3$ with an indirect band gap (red) of 2.7 eV. The total projected density of states (DOS) is dominated by N (atom-projected density of states in blue).

4.4 Conclusion

In summary, we investigated the elastic properties of GeP_2N_4 up to 44.4(1) GPa to analyze a possible structural effect of the lone pair of Ge^{2+} under pressure. The lattice parameters *a* and *c* possess similar compressibilities, while the lattice parameter *b* is noticeably more compressible due to the *achter*-rings containing Ge^{2+} located in the *ab* lattice plane. The ring distortion causes a symmetry reduction from $Pna2_1$ to $P112_1$ in the pressure range between 19.3(1) and 21.9(1) GPa. The isothermal bulk modulus of GeP_2N_4 was determined from pressure-volume data to be 82(6) GPa. Laser heating at 44.4(1) GPa facilitates a conversion from GeP_2N_4 to the novel germanium nitridophosphate $GePN_3$. The structure of $GePN_3$ was elucidated from single-crystal XRD data at 44.4(1) GPa. It consists of alternating layers made up of GeN_6 octahedra and PN_4 tetrahedra, which form double zigzag chains and single zigzag chains along [001], respectively. This layered setup is isotypic to the germanate $CoGeO_3$ and shows a calculated indirect band gap between 2.7 and 3.1 eV. $GePN_3$ combines P^V and Ge^{IV} in a nitridic network for the first time. In view of the wide structural possibilities, germanium

nitridophosphates seem promising to yield unprecedented structure types with potential intriguing materials properties. The currently high pressure needed to obtain $GePN_3$ may be significantly reduced for other germanium nitridophosphates in future experiments, as nitridophosphates and nitridogermanates can be obtained separately in simple ampoule syntheses.

4.5 Acknowledgements

The authors gratefully acknowledge financial support by the Deutsche Forschungsgemeinschaft (project SCHN 377/18). G.K. acknowledges financial support by the Friedrich-Naumann-Foundation for PhD fellowship with funds from the Federal Ministry of Education and Research (Bundesministerium für Bildung und Forschung, BMBF). M.B. acknowledges the support of Deutsche Forschungsgemeinschaft (DFG Emmy-Noether Program project BY112/2−1). Co-funded by the European Union (ERC, HIPMAT, 101077963). The views and opinions expressed are, however, those of the author(s) only and do not necessarily reflect those of the European Union or the European Research Council. Neither the European Union nor the granting authority can be held responsible for them. We acknowledge DESY (Hamburg, Germany), a member of the Helmholtz Association HGF, for the provision of experimental facilities. Parts of the presented research were carried out at beamline P02.2 (proposal no. I-20220809).

4.6 References

[1] F. Liebau, *Angew. Chem. Int. Ed.* **1999,** *38*, 1733.

[2] B. Blaschkowski, H. Jing, H.-J. Meyer, *Angew. Chem. Int. Ed.* **2002**, *41*, 3322.

[3] J. Haines, J. M. Léger, G. Bocquillon, *Annu. Rev. Mater. Res.* **2001**, *31*, 1.

[4] R. H. Wentorf, *J. Chem. Phys.* **1957**, *26*, 956.

[5] A. Zerr, G. Miehe, G. Serghiou, M. Schwarz, E. Kroke, R. Riedel, H. Fueß, P. Kroll, R. Boehler, *Nature* **1999**, *400*, 340.

[6] J. Z. Jiang, F. Kragh, D. J. Frost, K. StÃ¥hl, H. Lindelov, *J. Phys. Condens. Matter* **2001**, *13*, L515.

[7] J. Tian, W. Zhuang, *Inorg. Chem. Front.* **2021**, *8*, 4933.

[8] R. Mueller-Mach, G. Mueller, M. R. Krames, H. A. Höppe, F. Stadler, W. Schnick, T. Juestel, P. Schmidt, *Phys. Status Solidi A* **2005**, *202*, 1727.

[9] A. Marchuk, W. Schnick, *Angew. Chem. Int. Ed.* **2015**, *54*, 2383.

[10] W. Schnick, J. Luecke, *J. Solid State Chem.* **1990**, *87*, 101.

[11] E.-M. Bertschler, R. Niklaus, W. Schnick, *Chem. Eur. J.* **2017**, *23*, 9592.

[12] S. J. Sedlmaier, M. Eberspächer, W. Schnick, *Z. Anorg. Allg. Chem.* **2011**, *637*, 362.

[13] E.-M. Bertschler, R. Niklaus, W. Schnick, *Chem. Eur. J.* **2018**, *24*, 736.

[14] S. Horstmann, E. Irran, W. Schnick, *Angew. Chem. Int. Ed.* **1997**, *36*, 1873.

[15] S. Horstmann, E. Irran, W. Schnick, *Angew. Chem. Int. Ed.* **1997**, *36*, 1992.

[16] J. Ronis, B. Bondars, A. Vitola, T. Millers, J. Schneider, F. Frey, *J. Solid State Chem.* **1995**, *115*, 265.

[17] K. Landskron, H. Huppertz, J. Senker, W. Schnick, *Angew. Chem. Int. Ed.* **2001**, *40*, 2643.

[18] D. Baumann, W. Schnick, *Angew. Chem. Int. Ed.* **2014**, *53*, 14490.

[19] S. J. Ambach, M. Pointner, S. Falkai, C. Paulmann, O. Oeckler, W. Schnick, *Angew. Chem. Int. Ed.* **2023**, *62*, e202303580.

[20] S. Vogel, M. Bykov, E. Bykova, S. Wendl, S. D. Kloß, A. Pakhomova, S. Chariton, E. Koemets, N. Dubrovinskaia, L. Dubrovinsky, W. Schnick, *Angew. Chem. Int. Ed.* **2019**, *58*, 9060.

[21] D. Laniel, F. Trybel, A. Néri, Y. Yin, A. Aslandukov, T. Fedotenko, S. Khandarkhaeva, F. Tasnádi, S. Chariton, C. Giacobbe, E. L. Bright, M. Hanfland, V. Prakapenka, W. Schnick, I. A. Abrikosov, L. Dubrovinsky, N. Dubrovinskaia, *Chem. Eur. J.* **2022**, *28*, e202201998.

[22] Y. Hirota, T. Kobayashi, *J. Appl. Phys.* **1982**, *53*, 5037.

[23] Y.-H. Jeong, K.-H. Choi, S.-K. Jo, B. K. B. Kang, *Jpn. J. Appl. Phys.* **1995**, *34*, 1176.

[24] M. S. Choudhary, J. K. Fink, K. Lederer, H. A. Krässig, *J. Appl. Polymer Sci.* **1987**, *34*, 863.

[25] E.-C. Koch, S. Cudzilo, *Angew. Chem. Int. Ed.* **2016**, *55*, 15439.

[26] F. Karau, W. Schnick, *Angew. Chem. Int. Ed* **2006**, *45*, 4505.

[27] S. Wendl, L. Eisenburger, P. Strobel, D. Günther, J. P. Wright, P. J. Schmidt, O. Oeckler, W. Schnick, *Chem. Eur. J.* **2020**, *26*, 7292.

[28] S. Schneider, S. T. Kreiner, L. G. Balzat, B. V. Lotsch, W. Schnick, *Chem. Eur. J.* **2023**, *29*, e202309186.

[29] S. Schneider, E.-M. Wendinger, V. Baran, A.-K. Hatz, B. V. Lotsch, M. Nentwig, O. Oeckler, T. Bräuniger, W. Schnick, W. *Chem. Eur. J.* **2023**, *29*, e202300174.

[30] S. Schneider, L. G. Balzat, B. V. Lotsch, W. Schnick, *Chem. Eur. J.* **2023**, *29*, e202202984.

[31] S. J. Clarke, F. J. DiSalvo, *Inorg. Chem.* **2000**, *39*, 2631−2634.

[32] L. Link, M. Pathak, F. Jach, P. Koželj, A. Ormeci, P. Höhn, R. Niewa, *Angew. Chem. Int. Ed.* **2021**, *60*, 7691.

[33] L. Link, R. Niewa, *Z. Anorg. Allg. Chem.* **2020**, *646*, 1105.

[34] S. C. Junggeburth, O. Oeckler, W. Schnick, *Z. Anorg. Allg. Chem.* **2008**, *634*, 1309.

[35] M. Maunaye, J. Guyader, Y. Laurent, J. Lang, *Bull. Minéral.* **1971**, *1971*, 347.

[36] D. G. Park, F. J. DiSalvo, *Bull. Korean Chem. Soc.* **2008**, *29*, 2413.

[37] G. Serghiou, G. Miehe, O. Tschauner, A. Zerr, R. Boehler, *J. Chem. Phys.* **1999**, *111*, 4659.

[38] W. L. Larson, H. P. Maruska, D. A. Stevenson, *J. Electrochem. Soc.* **1974**, *121*, 1673.

[39] S. Limpijumnong, S. N. Rashkeev, W. R. L. Lambrecht, *MRS Internet J. Nitride Semicond. Res.* **1999**, *4*, 600.

[40] O. Boudrifa, A. Bouhemadou, N. Guechi, S. Bin-Omran, Y. Al-Douri, R. Khenata, *J. Alloys Compd.* **2015**, *618*, 84.

[41] S. J. Clarke, G. R. Kowach, F. J. DiSalvo, *Inorg. Chem.* **1996**, *35*, 7009.

[42] Z. A. Gál, S. J. Clarke, *Chem. Comm.* **2005**, 728.

[43] S. J. Ambach, C. Somers, T. de Boer, L. Eisenburger, A. Moewes, W. Schnick, *Angew. Chem. Int. Ed.* **2023**, *62*, e202215393.

[44] D. Walker, M. A. Carpenter, C. M. Hitch, *Am. Min.* **1990**, *75*, 1020.

[45] H. Huppertz, *Z. Kristallogr. Cryst. Mater.* **2004**, *219*, 330.

[46] Oxford Instruments, AZtecEnergy, Abington, 2016.

[47] H. M. A. Rietveld, *J. Appl. Crystallogr.* **1969**, *2*, 65.

[48] R. W. Cheary, A. A. Coelho, *J. Appl. Crystallogr.* **1992**, *25*, 109.

[49] R. W. Cheary, A. A. Coelho, J. P. Cline, *J. Res. Natl. Inst. Stand. Technol.* **2004**, *109*, 1.

[50] A. A. Coelho, *J. Appl. Crystallogr.* **2018**, *51*, 210.

[51] Z. Konôpková, W. Morgenroth, R. Husband, N. Giordano, A. Pakhomova, O. Gutowski, M. Wendt, K. Glazyrin, A. Ehnes, J. T. Delitz, A. F. Goncharov, V. P. Prakapenka, H.-P. Liermann, *J. Synchrotron Rad.* **2021**, *28*, 1747.

[52] C. Prescher, V. B. Prakapenka, *High Press. Res.* **2015**, *35*, 223.

[53] G. S. Pawley, *J. Appl. Crystallogr.* **1981**, *14*, 357.

[54] Y. Fei, A. Ricolleau, M. Frank, K. Mibe, G. Shen, V. Prakapenka, *Proc. Natl. Acad. Sci. U. S. A*. **2007**, *104*, 9182.

[55] Rigaku Oxford Diffraction, CrysAlisPro Software system, version 171.39.46, Rigaku Corporation, Oxford, UK, 2014.

[56] A. Aslandukov, M. Aslandukov, N. Dubrovinskaia, L. Dubrovinsky, *J. Appl. Crystallogr.* **2022**, *55*, 1383.

[57] G. M. Sheldrick, *Acta Crystallogr. Sect. A Found. Crystallogr.* **2015**, *71*, 3.

[58] I. Kantor, V. Prakapenka, A. Kantor, P. Dera, A. Kurnosov, S. Sinogeikin, N. Dubrovinskaia, L. Dubrovinsky, *Rev. Sci. Instrum.* **2012**, *83*, 125102.

[59] F. Birch, *Phys. Rev.* **1947**, *71*, 809.

[60] F. D. Murnaghan, *Proc. Natl. Acad. Sci. USA.* **1944**, *30*, 244.

[61] J. Gonzalez-Platas, M. Alvaro, F. Nestola, R. Angel, *Appl. Crystallogr.* **2016**, *49*, 1377.

[62] J. Cumby, J. P. Attfield, *Nat. Commun.* **2017**, *8*, 14235.

[63] K. Momma, F. Izumi, *J. Appl. Crystallogr.* **2011**, *44*, 1272.

[64] G. Kresse, J. Hafner, *Phys. Rev. B Condens. Matter* **1993**, *47*, 558.

[65] G. Kresse, J. Hafner, *Phys. Rev. B Condens. Matter* **1994**, *49*, 14251−14271.

[66] G. Kresse, J. Furthmüller, *Phys. Rev. B Condens. Matter* **1996**, *54*, 11169.

[67] G. Kresse, J. Furthmüller, *Comput. Mater. Sci.* **1996**, *6*, 15.

[68] G. Kresse, D. Joubert, *Phys. Rev. B Condens. Matter* **1999**, *59*, 1758.

[69] P. E. Blöchl, *Phys. Rev. B Condens. Matter* **1994**, *50*, 17953.

[70] J. P. Perdew, K. Burke, M. Ernzerhof, *Phys. Rev. Lett.* **1996**, *77*, 3865.

[71] A. D. Becke, E. R. Johnson, *J. Chem. Phys.* **2006**, *124*, 221101.

[72] F. Tran, P. Blaha, *Phys. Rev. Lett.* **2009**, *102*, 226401.

[73] A. P. Khomyakov, G. N. Nechelyustov, E. Sokolova, E. Bonaccorsi, S. Merlino, M. Pasero, *Can. Mineral.* **2002**, *40*, 961.

[74] J. V. Smith, *Acta Crystallogr.* **1953**, *6*, 613.

[75] S. D. Kloß, W. Schnick, *Angew. Chem. Int. Ed.* **2015**, *54*, 11250.

[76] F. Liebau, *Structural Chemistry of Silicates. Structure, Bonding, and Classification*, Springer, Berlin, **1985**, pp. 1–6. The term "*achter-ring*" has been defined by Liebau and is derived from the German word "acht" (engl. eight), describing rings consisting of the respective amount of tetrahedra.

[77] R. M. Atkins, P. L. Timms, *Spectrochim. Acta A: Mol. Biomol. Spectrosc.* **1977**, *33*, 853.

[78] R. Ahlrichs, M. Bär, H. S. Plitt, H. Schnöckel, *Chem. Phys. Lett.* **1989**, *161*, 179.

[79] V. A. Blatov, M. O'Keeffe, D. M. Proserpio, *CrystEngComm.* **2010**, *12*, 44.

[80] D. R. Peacor, *Z. Kristallogr. Cryst. Mater.* 2015, 126, 299.

[81] H.-P. Baldus, W. Schnick, J. Lücke, U. Wannagat, G. Bogedain, *Chem. Mater.* **1993**, *5*, 845.

Chapter 5

Mixed Tin Valence in the Tin(II/IV)-Nitridphosphate $Sn_3P_8N_{16}$

Published in: *Chem. Eur. J.* **2024**, *accepted*

Authors: Sebastian J. Ambach, Aylin Koldemir, Kristian Witthaut, Sandra Kreiner, Thomas Bräuniger, Rainer Pöttgen, Wolfgang Schnick

DOI: https://doi.org/10.1002/chem.202401428

Abstract: $Sn_3P_8N_{16}$ combines the structural versatility of nitridophosphates and Sn within one compound. It was synthesized as dark gray powder in a high-pressure high-temperature reaction at 800 °C and 6 GPa from Sn_3N_4 and P_3N_5. The crystal structure was elucidated from single-crystal diffraction data (space group *C*2/*m* (no. 12), *a* = 12.9664(4), *b* = 10.7886(4), *c* = 4.8238(2) Å, *β* = 109.624(1)°) and shows a 3D-network of PN_4 tetrahedra, incorporating Sn in oxidation states +II and +IV. The Sn cations are located within eight-membered rings of vertex-sharing PN_4 tetrahedra, stacked along the [001] direction. A combination of solid-state nuclear magnetic resonance spectroscopy, ^{119}Sn Mössbauer spectroscopy and density functional theory calculations was used to confirm the mixed oxidation of Sn. Temperature-dependent powder X-ray diffraction measurements reveal a low thermal expansion of 3.6 ppm/K up to 750 °C, beyond which $Sn_3P_8N_{16}$ starts to decompose.

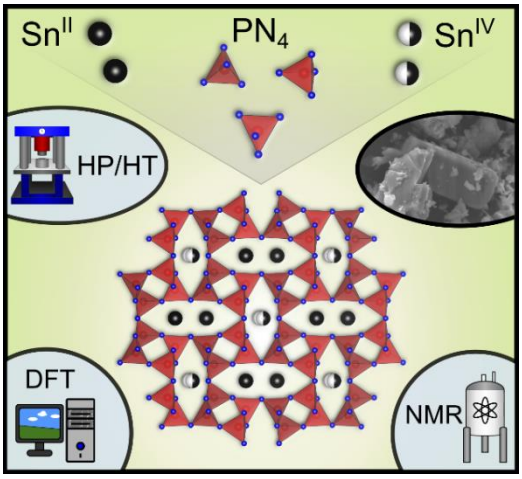

5.1 Introduction

In solid-state chemistry, the combination of elements providing a versatile network structure, such as P/N in nitridophosphates, and cations that have different oxidation states and coordination polyhedra, is promising to lead to new materials with potentially intriguing properties.

As an earth abundant element, tin and its naturally occurring compounds have been widely used for several thousand years.[1] Even in modern society, tin compounds have a wide range of applications. Catalysts containing Sn play an important role in the (electro)catalysis of mostly organic and rarely inorganic reactions.[2–4] Besides catalysis, tin oxide-based materials are found in solar energy conversion, antistatic coatings as well as electrochromic devices and were analyzed regarding their use as anodes in Li-ion batteries.[5–11] Furthermore, Sn is suitable for nanowire fabrication and can be found in sensor materials.[12–15] This wide range of applications originate from the versatile redox and coordination chemistry of Sn. Besides occurring in Zintl phases and intermetallic compounds, Sn is mostly found as a cation in oxidation states +II or +IV.[16–18] Depending on oxidation states and coordinating atoms, various coordination motifs are encountered in solid-state compounds. Oxygen coordinated Sn^{IV} most commonly forms SnO_6 octahedra, e.g. in rutile-type SnO_2, whereas Sn^{II} is found in square-based SnO_4 pyramids, e.g. in SnO.[19,20] Sn^{IV} in tetrahedral coordination can be found in SnS_4 tetrahedra (e.g. in Cu_2MnSnS_4).[21] Nitrogen coordinated Sn^{IV} also shows SnN_4 tetrahedra (e.g. in γ-Sn_3N_4), presumably SnN_5 trigonal bipyramids (in Sn_3N_4 at around 25 GPa) and SnN_6 octahedra (e.g. in γ-Sn_3N_4 or SnN_2). Sn^{II} is coordinated threefold in trigonal SnN_3 pyramids (e.g. in $Sn_6[P_{12}N_{24}]$) or fourfold in distorted square-based SnN_4 pyramids (e.g. in $Sn(CN_2)$).[22–26]

Nitridophosphates, a relatively young subclass of nitrides, attract high interest in current research due to their versatile structural variabilities. Because of the isoelectronic combination Si/O and P/N, nitridophosphates mirror structural elements of oxosilicates. Most commonly, PN_4 tetrahedra are found, either isolated (e.g. in Li_7PN_4) or connected to small groups (e.g. in $Li_{12}P_3N_9$), chains (e.g. in Zn_2PN_3), layers (e.g. in $Li_5P_2N_5$) or 3D networks (e.g. in α-P_3N_5).[27–31] Rarely, also square-based or trigonal bipyramidal PN_5 units were reported in γ-P_3N_5, γ-HP_4N_7 or MP_6N_{11} (*M* = Al, In), respectively.[32–34] Recently, even PN_6 octahedra were observed in high-pressure diamond anvil cell experiments at 42 and 72 GPa.[35,36] Since N in nitridophosphates can regularly connect up to three tetrahedral vertices, in and edge-sharing of tetrahedra is possible, whereas O in oxosilicates is usually limited to two vertices and vertex-sharing, the structural versatility of nitridophosphates should theoretically exceed that of oxosilicates. Subsequent to the manifold structural possibilities, various applications of nitridophosphates have emerged. The binary P_3N_5 is used as a gate insulator in metal-insulator field-effect transistors (MISFETs) and was analyzed regarding application as flame retardant and for

safety in pyrotechnics.[37–40] $Ba_3P_5N_{10}Br:Eu^{2+}$ and $AEP_8N_{14}:Eu^{2+}$ (*AE* = Ca, Sr, Ba) were proposed as warm-white and ultra-narrow-band blue emitters, respectively.[41,42] Furthermore, various lithium nitridophosphates show Li ion conductivity.[43–45]

Combining the structural potential of nitridophosphates with the versatility of tin, unprecedented structure types with a widely increased field of applications can be expected. Currently, there is only a single compound in the Sn/P/N system, namely, the tin nitridophosphate $Sn^{II}_6[P_{12}N_{24}]$.[23] It crystallizes in a sodalite-type framework structure, foreshadowing the potential of tin nitridophosphates, considering the importance of zeolites in today's industry. An additional combination of Sn^{II} and Sn^{IV} within the same compound, currently studied especially in binary systems like Sn/S, is predicted to show intriguing electronic properties.[46–48]

The novel $Sn_3P_8N_{16}$ presented herein combines nitridophosphates with Sn^{II} and Sn^{IV} cations for the first time. A combination of solid-state NMR spectroscopy, Mössbauer spectroscopy and theoretical calculations is used to confirm the presence of both Sn oxidation states. Simultaneously, the comparatively sparse data on ^{119}Sn NMR spectroscopy in the literature is expanded.

5.2 Results and Discussion

Synthesis

$Sn_3P_8N_{16}$ was synthesized from Sn_3N_4 and P_3N_5 in a 3:8 molar ratio under high-pressure high-temperature conditions in a 1000 t multi-anvil hydraulic press according to Equation 1. During the reaction, Sn^{IV} in Sn_3N_4 is partially reduced to Sn^{II} in $Sn_3P_8N_{16}$, while N^{-III} is oxidized to N^0. The sum formula of $Sn_3P_8N_{16}$ can be interpreted as $Sn^{II}_2Sn^{IV}P_8N_{16}$.

$$3\ Sn_3N_4 + 8\ P_3N_5 \rightarrow 3\ Sn_3P_8N_{16} + 2\ N_2 \quad (1)$$

Sn_3N_4 and P_3N_5 were finely ground under argon atmosphere and transferred into the multi-anvil apparatus as described in the experimental section. After compression to 6 GPa within 170 min, the assembly was heated to 800 °C within 60 min, the temperature was held for 240 min and subsequently cooled to ambient temperature within 60 min. While a wide pressure range (3 – 9 GPa) was found to be suitable for the reaction, the temperature must be 800 °C. Lower temperatures lead to an incomplete reaction, whilst higher temperatures facilitate the degradation to elemental Sn and an amorphous phase, most likely consisting of P/N species.

The product was obtained as dark gray powder and is stable towards air and moisture. Small amounts of elemental Sn in the reaction product were removed by washing the powdered sample with concentrated HCl. Figure 5.1 shows the Rietveld refinement of a typical sample after washing, using the single-crystal structure model as a starting point.

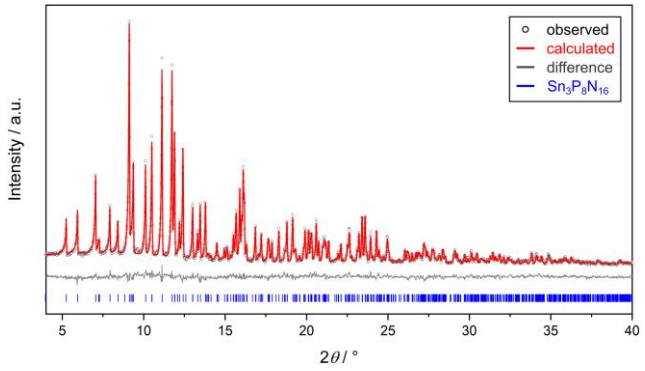

Figure 5.1: Graphical representation of the Rietveld-refinement for $Sn_3P_8N_{16}$ with observed intensities (black circles), calculated intensities (red line), difference plot (gray line) and positions of Bragg reflections (blue bars).

Temperature-Dependent Powder X-Ray Diffraction

Temperature dependent powder X-ray diffraction (PXRD) patterns of a $Sn_3P_8N_{16}$ sample were recorded between ambient temperature and 950 °C with steps of 50 °C and 100 °C during heating and cooling, respectively (Figure 5.2). Apparently, $Sn_3P_8N_{16}$ is stable up to 900 °C. Above 900 °C, it decomposes into most likely amorphous P/N species and molten Sn, which crystallizes as β-Sn at 50 °C during cooling. A detailed view on the data (Figure S4.1) suggests, that $Sn_3P_8N_{16}$ has a very small thermal expansion of 3.6 ppm/K up to 750 °C, beyond which the decomposition already initiates. The strong reflection at $2\theta = 8.7°$, appearing at 950 °C, can be assigned to cristobalite (SiO_2), which is formed due to crystallization of the silica glass capillary.

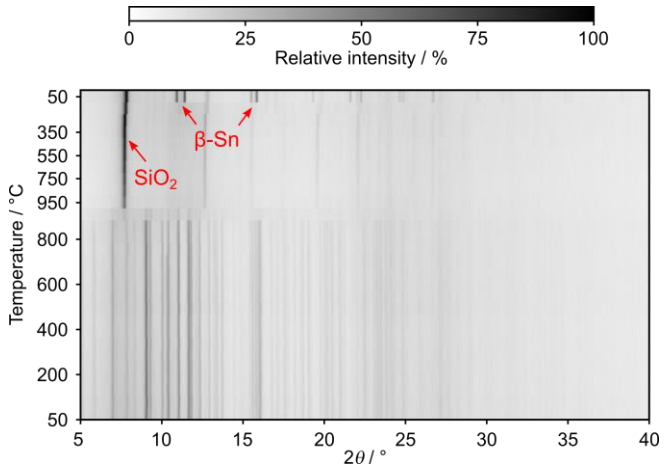

Figure 5.2: Temperature dependent PXRD patterns of $Sn_3P_8N_{16}$. $Sn_3P_8N_{16}$ decomposes at 900 °C. At 950 °C, the silica glass capillary starts to crystallize. At 50 °C, molten Sn from the decomposition of $Sn_3P_8N_{16}$ crystallizes as β-Sn.

Scanning Electron Microscopy and Energy-Dispersive X-Ray Spectroscopy

SEM images show typical block-shaped single crystals up to 10 µm length and width (Figure 5.3).

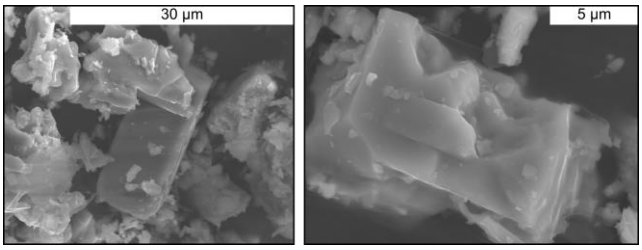

Figure 5.3: SEM images of a sample of $Sn_3P_8N_{16}$ after washing with concentrated HCl.

The elemental analysis of such crystals by EDX spectroscopy suggests an averaged composition of $Sn_{3.0(4)}P_{8.3(8)}N_{15.6(9)}O_{1.2(4)}$, which is close to $Sn_3P_8N_{16}$ (more detailed data is given in Table S1). The oxygen content may be attributed to surface hydrolysis due to harsh washing conditions with concentrated HCl.

Crystal Structure

The structure of $Sn_3P_8N_{16}$ was elucidated from single-crystal X-ray diffraction (XRD) data (space group *C*2/*m* (no. 12), a = 12.9664(4), b = 10.7886(4), c = 4.8238(2) Å, β = 109.624(1)°, Z = 2, R_1 = 2.92%; for additional crystallographic data, see Table 5.1 and Tables S4.2−4.5).[49]

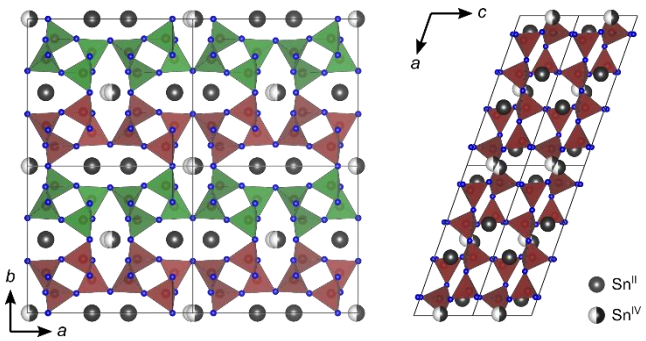

Figure 5.4: Crystal structure of $Sn_3P_8N_{16}$ along [001] and [010]. In [001] direction, *achter*-rings containing the Sn cations are visible. In [010] direction, *sechser*-rings and *vierer*-rings are formed.

Table 5.1: Crystallographic data on $Sn_3P_8N_{16}$. Standard deviations are given in parentheses.

Formula	**$Sn_3P_8N_{16}$**
Crystal system	monoclinic
Space group	*C*2/*m* (no. 12)
a / Å	12.9664(4)
b / Å	10.7886(4)
c / Å	4.8238(2)
β / Å	109.624(1)
Cell volume / Å^3	635.60(4)
Formula units / unit cell	2
Calculated X-ray density / g·cm^{-3}	4.33
Molecular weight / g·mol^{-1}	827.99
Linear absorption coefficient / cm^{-1}	6.9
T_{min}/T_{max}	0.890
Temperature / K	299(2)
Absorption correction	multi-scan
Radiation	Mo-Kα (λ = 0.71973 Å)
F(000)	764
θ range / °	$3.336 \leq \theta \leq 36.395$
Total no. of reflections	7342
Independent reflections [$I \geq 2\sigma(I)$ / all]	852 / 978
R_{int}	0.0382
Refined parameters	70
Goodness of fit	1.094
R-values [$I \geq 2\sigma(I)$]	R_1 = 0.0292; *wR*2 = 0.0600
R-values [all data]	R_1 = 0.0376; *wR*2 = 0.0636
$\Delta\rho_{max}$, $\Delta\rho_{max}$ / e·Å^3	1.23; –1.02

The structure of $Sn_3P_8N_{16}$ is built from *vierer*-rings of PN_4 tetrahedra, which are connected to infinite chains along [100].[50] This interconnection forms *achter*-rings, stacked in [001] direction, with a longitudinal axis alternating along [100] and [010] (Figure 5.4). Along the [010] direction, *sechser*-rings and *vierer*-rings are visible.

The Sn^{IV} cations (Sn2 site), located in the cavity of *achter*-rings with the longitudinal axis along [010], are coordinated fivefold by N, forming a square-based pyramid (Figure 5.5). The Sn2 site is split and shows an occupation of 0.5. A structure solution and refinement under the

assumption of a lower symmetry than *C*2/*m* did not resolve the split position. The Sn^{II} cations (Sn1 site) are coordinated fourfold by N, forming a square-based pyramid with Sn at the top. Each *achter*-ring with a longitudinal axis along [100] contains two pyramids, with alternating orientation upwards and downwards along [001].

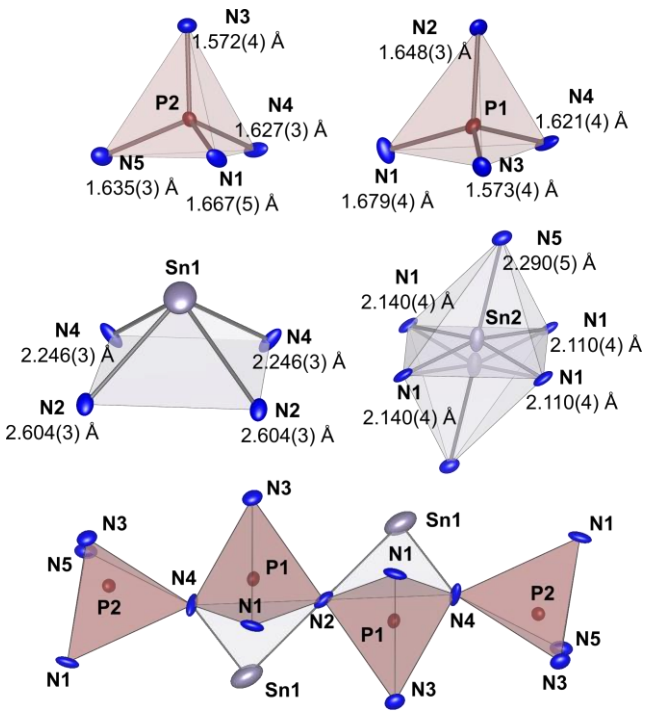

Figure 5.5: Coordination polyhedra of cations in $Sn_3P_8N_{16}$. The thermal ellipsoids are shown at 90% probability level. View along [010] of an *achter*-ring for visualization of the alternating $Sn^{II}N_4$ pyramid orientation.

The point symbol, describing the topology of the PN_4 tetrahedra network was determined by ToposPro to be $\{4^2.6^3.8\}\{4^2.6\}$.[51] This topology is closely related to the silicate mineral paracelsian and the nitridophosphates $LiNdP_4N_8$ and GeP_2N_4 (point symbol $\{4^2.6^3.8\}$).[52–54] The difference between both network types is found in the connection between *vierer*-rings (Figure S4.2). P–N bonds of the PN_4 tetrahedra are between 1.572(4) and 1.679(4) Å, which is a typical range for nitridophosphates and comparable to e.g. $Sn_6P_{12}N_{24}$.[23] The $Sn^{IV}N_5$ pyramid shows Sn–N distances between 2.110(4) and 2.140(4) Å, comparable to the Sn–N distances of $[SnN_4O_2]^{12-}$ octahedra in Sn_2N_2O.[55] The $Sn^{II}N_4$ pyramid shows Sn–N distances between 2.246(3) and 2.604(3) Å, comparable to $Sn(CN_2)$.[26]

Charge Distribution and Minimal Bonding Ellipsoid Calculations

Thus far, the oxidation states of Sn are only assumed based on charge neutrality and coordination polyhedra. To further analyze the electrostatic plausibility of the structure model,

CHARDI and MBE calculations were performed. All calculated values match the theoretical charges of the respective atom sites with a maximum deviation of 7% (Table S4.6). The minimal bonding ellipsoid calculations show regular coordination polyhedra, supporting the structure model (Table S4.7, Figure S4.3).

Solid State Magic-Angle Spinning Nuclear Magnetic Resonance Spectroscopy

To obtain information on the local atomic environments, ^{31}P and ^{119}Sn NMR spectra under magic-angle spinning (MAS) were recorded.

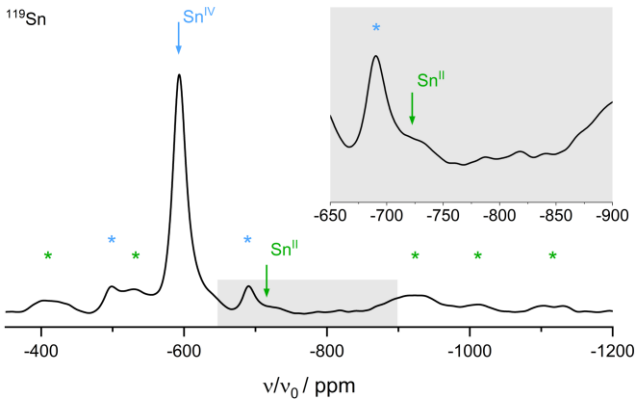

Figure 5.6: ^{119}Sn MAS NMR spectrum at 18 kHz spinning frequency, composed of two rotational side band patterns. Sn^{IV} signals are marked in blue, with the isotropic shift value being δ = −593.0 ppm. The low intensity pattern of Sn^{II} is marked in green, with the isotropic signal ($\delta \approx$ −730 ppm) identified by comparison of spectra acquired at different MAS frequencies (Figure S4).

The ^{31}P spectrum (Figure S4.4) shows two signals at δ = −3.66 and −7.86 ppm with almost identical intensities, matching the presence of two crystallographically independent P sites in the structure. To understand the appearance of the ^{119}Sn spectrum shown in Figure 5.6, it is important to realize that the NMR spectroscopic properties of Sn^{II} and Sn^{IV} differ strongly in the solid state. This is due to the presence of the lone pair at Sn^{II}, causing a chemical shift anisotropy that is much larger than that observed for Sn^{IV}. Consequently, under MAS conditions, Sn^{IV} species show only few (if any) rotational side bands, whereas Sn^{II} species tend to give very wide side band patterns.[56,57] In $Sn_3P_8N_{16}$, both Sn species are present simultaneously, and the NMR spectrum is composed of a strong signal at −593.0 ppm, with only two discernible low-intensity side bands (marked by asterisks in Figure 5.6), which can be assigned to the Sn^{IV} site. Its chemical shift is close to that of Sn^{IV} in SnO_2 (−603.0 ppm).[58] The Sn^{II} signal of $Sn_3P_8N_{16}$, on the other hand, consists of a wide side band pattern with very low intensity. By comparing spectra at different spinning speeds (Figure S4.4), the isotropic

resonance of the Sn^{II} species can be determined to be at $\delta \approx -730$ ppm. We also note that the strong resonance line in Figure 5.6 exhibits symmetrical low shoulders, which are typical for Sn spectra affected by indirect couplings.[57–59] In $Sn_3P_8N_{16}$, the predominant coupling partners are ^{14}N (99.6% natural abundance) via one bond and ^{31}P (100% n. a.) via two bonds, and these comparatively small couplings are not resolved in the spectra.[60]

^{119}Sn Mössbauer Spectroscopy

The valence states and electronic situations of the tin atoms in $Sn_3P_8N_{16}$ were estimated by ^{119}Sn Mössbauer spectroscopy. The ^{119}Sn Mössbauer spectrum of $Sn_3P_8N_{16}$ collected at 78 K is presented in Figure 5.7 along with a transmission integral fit. The corresponding fitting parameters are listed in Table S4.8. The spectrum was well reproduced with a superposition of two quadrupole split sub-signals at isomer shifts of 0.49(1) and 3.39(1) mm s^{-1} with the refined contribution of 35(1)% : 65(1)%. The observed line widths (0.82(1) and 0.97(1) mm·s^{-1}) are in the usual range and the signals could be clearly assigned to Sn^{IV} and Sn^{II}.[61] The occupancy ratio of 1:2 is in good agreement with the refined sub-signal ratio.

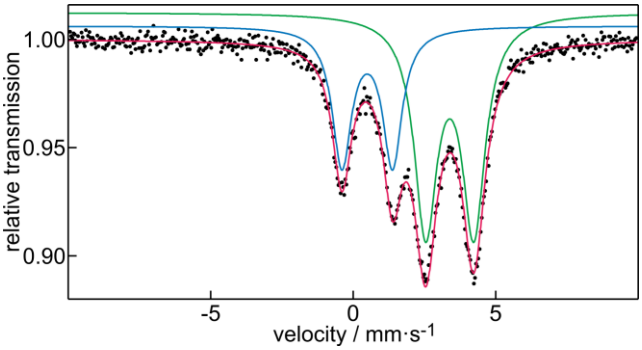

Figure 5.7: Experimental (data points) and simulated (colored lines) ^{119}Sn Mössbauer spectrum of $Sn_3P_8N_{16}$ measured at 78 K (blue: Sn^{IV}, green: Sn^{II}).

The isomer shift of the Sn^{II} atoms is at the lower border of the range of isomer shifts for divalent Sn compounds indicating lower *s* electron density at the tin nuclei.[61] This is due to the high electronegativity of the coordinating nitrogen atoms. The four closest nitrogen atoms inside the coordination sphere of Sn^{II} (2.246(3) and 2.604(3) Å) coordinate in a distorted square pyramidal arrangement with Sn at the apex, thus offering sufficient space for the lone pair of the Sn^{II} atoms. The lone pair activity is reflected in substantial quadrupole splitting of 1.69(1) mm·s^{-1}. The isomer shift and the quadrupole splitting of the Sn^{II} signal are in good agreement with literature data for $Sn_6[P_{12}N_{24}]$ (δ = 3.05(1) mm·s^{-1} and ΔE_Q = 1.58(1) mm·s^{-1}), where the tin atoms are exclusively in oxidation state +II.[23] Further examples for Sn^{II}–N coordination compounds exhibiting similar isomer shifts are given in literature.[62]

The Sn^{IV} atoms also show a significant quadrupole splitting of 1.77(1) $mm \cdot s^{-1}$. Reason for this are the four nitrogen atoms (2.110(4) and 2.140(4) Å) coordinating the Sn^{IV} atoms as base of the SnN_5 pyramid. The next nitrogen atom inside the coordination sphere, being the pyramid apex, shows a substantially higher distance (2.290(5) Å), leading to the asymmetric coordination sphere.

Density Functional Theory Calculations

Density functional theory calculations further support the mixed Sn valence and provide insight into the electronic structure of $Sn_3P_8N_{16}$. The calculated electron localization function clearly shows the electron lone pair at the Sn1 atoms (Sn^{II}), while the Sn2 atoms (Sn^{IV}) display a spherical electron density (Figure 5.8). In addition, the alternating apex orientation of the $Sn^{II}N_4$ pyramids is visible.

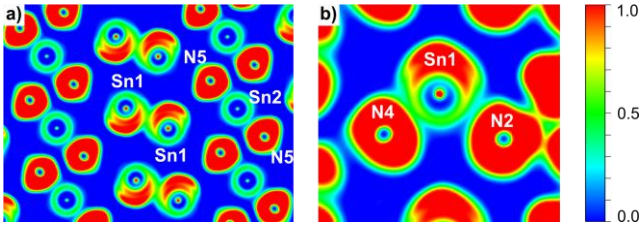

Figure 5.8: Two-dimensional ELF map to visualize the Sn^{II} lone pair. a) Cross section of the *ac* plane. The alternating orientation of the $Sn^{II}N_4$ pyramids (Sn1 atoms) are visible alongside slices of the $Sn^{IV}N_5$ square-based pyramids (Sn2 atoms). b) The cross section of a $Sn^{II}N_4$ pyramid shows the bonding situation. The lone electron pair is oriented towards the top of the pyramid. The distance from Sn1 to N4 is slightly shorter (2.246(3) Å) than to N2 (2.604(3) Å).

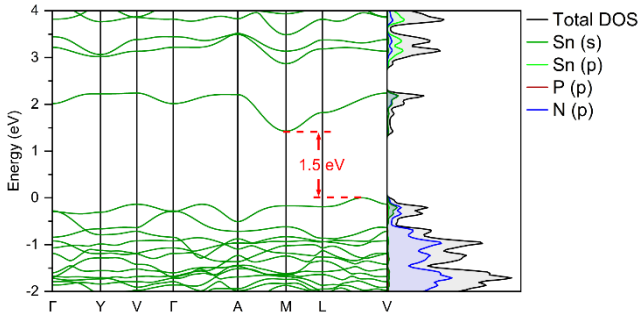

Figure 5.9: Calculated band structure of $Sn_3P_8N_{16}$. The calculations predict an indirect bandgap of 1.5 eV (PBE functional).

Band structure calculations reveal an indirect band gap between 1.5 eV (Perdew-Burke-Ernzerhof, PBE) and 2.1 eV (modified Becke-Johnson, MBJ).[63,64] The density of states (DOS)

shows three distinct regions, the first up to 0 eV, the second from 1.4 to 2.2 eV, and the third starting at 2.9 eV (Figure 5.9). The first region is dominated by N(p) and close to the Fermi level at 0 eV by Sn(s) states. The middle region only shows major contributions from Sn(s) and N(p), while the upper region is dominated by Sn(p) contributions. A more detailed view on the DOS is provided in Figures S4.5 and S4.6.

5.3 Conclusion

In summary, we synthesized the novel tin nitridophosphate $Sn_3P_8N_{16}$ in a high-pressure high-temperature reaction as dark gray powder, starting from Sn_3N_4 and P_3N_5. It crystallizes in space group *C*2/*m* (no. 12) with a = 12.9664(4), b = 10.7886(4), c = 4.8238(2) Å, and β = 109.624(1)°. The structure is built from *vierer*-rings of PN_4 tetrahedra, connected to infinite chains along [100]. The connection results in the formation of *achter*-rings, which contain Sn cations in both oxidations states +II and +IV. The mixed oxidation states of Sn were confirmed by solid-state MAS NMR spectroscopy, ^{119}Sn Mössbauer spectroscopy, CHARDI and DFT calculations. The DFT calculations allowed to visualize the lone electron pair of Sn^{II} and to determine an indirect band gap between 1.5 (PBE) and 2.1 eV (MBJ).

$Sn_3P_8N_{16}$ is the second tin nitridophosphate, besides the literature-known sodalite-type $Sn_6[P_{12}N_{24}]$ and proves that a multitude of structural motifs are possible within this class of compounds.[23] Considering the structural variety offered by a nitridophosphate network in combination with the application possibilities of Sn, continued research on tin nitridophosphates is a promising field for further investigations towards new compounds with intriguing materials properties.

5.4 Experimental Section

Synthesis of Starting Materials

The detailed synthesis procedure of Sn_3N_4 will be published in a subsequent paper.

P_3N_5 was prepared according to Stock *et al*. by ammonolysis of P_4S_{10}.[65] A quartz tube, containing a quartz boat, was placed in a tube furnace and dried at 1000°C for 2 h at a reduced pressure of 10^{-3} mbar to exclude moisture. Afterwards, the quartz boat was loaded with 8 g of P_4S_{10} (Sigma-Aldrich, 99.99%), centered in the outer tube and the whole apparatus was saturated with NH_3 (Air Liquide, 5.0) for 1 h. The tube furnace was subsequently heated to 850 °C with 7 K/min, the temperature was held for 4 h and cooled down to ambient temperature with 7 K/min. The purity of the orange powder was analyzed by powder X-ray diffraction and CHNS-analyses (calcd. (%) C 0, H 0, N 42.98, S 0; found (%) C 0, H 0, N 43.16, S 0).

Synthesis of $Sn_3P_8N_{16}$

$Sn_3P_8N_{16}$ was prepared from Sn_3N_4 and P_3N_5 in a 3:8 molar ratio in a high-pressure, high-temperature reaction at 6 GPa and 800 °C. The starting materials were ground together in a glove box (MBraun, < 1 ppm O2, < 1 ppm H2O) under argon atmosphere and tightly packed into an h-BN crucible. The crucible was closed with an h-BN lid and centered in a smaller and a larger graphite heater, using MgO spacers. The heaters were surrounded by a ZrO_2 sleeve, which was closed by Mo disks on each end and centered in a drilled-through MgO:Cr_2O_3 octahedron. The assembly was placed in the center of a cube of eight electrically isolated WC cubes (32 mm edge length, 11 mm corner truncation, 7% Co doped) and transferred into the multi-anvil apparatus. A more detailed description of the setup can be found in literature.[66,67] The reaction was carried out in a 1000 t hydraulic press with a modified Walker module. The starting materials were compressed to 6 GPa within 160 min, heated to 800 °C within 60 min, the temperature was held for 240 min and subsequently cooled down to ambient temperature within 60 min. After decompression within 500 min, the dark gray sample was recovered from the octahedron parts and washed with concentrated HCl to remove excess elemental Sn.

Single-Crystal X-Ray Diffraction

Single-crystal X-ray diffraction data was collected as combined φ- and ω-scans on a Bruker D8 Venture TXS diffractometer with rotating anode (Mo-Kα radiation, λ = 0.71073 Å) and multilayer monochromator. Indexing, integration, absorption correction by the multi-scan-method and space group determination was done with the APEX3 software package.[68–70] The structure was solved via Direct Methods and refinement by the least-squares method using SHELXS and SHELXL.[71,72] The results were visualized using VESTA.[73]

Charge Distribution and Minimal Bonding Ellipsoid Calculations

CHARDI calculations on the single-crystal structure model of $Sn_3P_8N_{16}$ were performed with VESTA.[73]

MBE analyses of the coordination polyhedra were done by the software PIEFACE.[74] All polyhedra are described as ellipsoids with minimized surface area, which contains all ligand atoms. Each ellipsoid is characterized by its three radii $R1$, $R2$ and $R3$, its mean radius $\langle R \rangle$ with the standard deviation $\sigma(R)$ and the displacement of the central atom from the ellipsoid center.

Powder X-Ray Diffraction

For powder X-ray diffraction measurements (Ag-$K\alpha_1$ radiation, λ = 0.55954 Å), the samples were finely ground and sealed in a glass capillary (0.3 mm outer diameter, Hilgenberg, Malsfeld). Afterwards, the capillary was centered on the rotating goniometer head of a STOE

Stadi P diffractometer (STOE & Cie GmbH, Darmstadt) with modified Debye-Scherrer geometry, a MYTHEN 1K strip detector and Ge(111) monochromator.

Rietveld Refinement

Using collected PXRD data and the single-crystal structure model as starting point, the Rietveld refinement was performed with the TOPAS Academic software.[75,76] Peak profiles were described by the fundamental parameter approach, the background was modeled by a shifted Chebyshev polynomial and a 4th order spherical harmonic function was used to account for a potential preferred crystallite orientation.[77,78]

Temperature-Dependent Powder X-Ray Diffraction

For temperature-dependent PXRD measurements, the sample was finely ground and sealed in a silica glass capillary with 0.3 mm outer diameter (Hilgenberg, Malsfeld). The capillary was heated in steps of 50 °C from 50 °C to 950 °C and subsequently cooled in steps of 100 °C back to 50 °C with a heating and cooling rate of 10 K/min each. At each step, PXRD data was collected within 2 h at constant temperature on a STOE Stadi P diffractometer (STOE & Cie GmbH, Darmstadt) with Ag-Kα_1 radiation (λ = 0.55954 Å), Ge(111)-monochromator, IP-PSD detector and a STOE resistance graphite heater for temperature control.

Scanning Electron Microscopy and Energy Dispersive X-Ray Spectroscopy

For preparation, a sample was placed on a self-adhesive carbon foil and coated with carbon by an electron beam evaporator (BAL-TEC MED 020, BalTec AG, Pfäffikon) to ensure electric conductivity. The sample was transferred into a Dualbeam Helios Nanolab G3 UC (FEI, Hilsboro) electron microscope, equipped with an X-Max 80 SSD detector (Oxford Instruments, Abingdon). SEM images and EDX data were recorded with an acceleration voltage of 20 kV and processed with the Aztec software.[79]

Solid State Magic-Angle Spinning Nuclear Magnetic Resonance Spectroscopy

For solid-state MAS NMR spectroscopic measurements, a sample was finely ground and tightly packed into a ZrO_2 rotor with an outer diameter of 2.5 mm. Spectra of ^{31}P (20 kHz spinning frequency) and ^{119}Sn (18 kHz, 22 kHz, 24 kHz spinning frequency) were recorded on an Avance III 500 spectrometer (Bruker, Karlsruhe) with a 11.7 T magnet (500.25 MHz ^{1}H frequency) and a double resonance MAS probe.

^{119}Sn Mössbauer Spectroscopy

A $Ca^{119m}SnO_3$ source was used for the ^{119}Sn Mössbauer spectroscopic experiments. Source, sample and detector were arranged in the usual transmission geometry. To reduce the tin *K* X-rays emitted by this source a palladium foil (0.05 mm) was inserted in front of the detector.

The sample was mixed with *α*-quartz and was placed inside a thin-walled PMMA container at a thickness corresponding to about 7 mg Sn per cm^2. The sample was cooled to 78 K using a commercial liquid nitrogen-bath cryostat, while the source was kept at room temperature. Fitting and plotting of the spectra was performed with the WinNormos for Igor6 program package and graphical editing with the program CorelDRAW2017.[80,81]

Density Functional Theory Calculation

We investigated $Sn_3P_8N_{16}$ with first principle electronic structure calculations performed with the Vienna *ab initio* simulation package (VASP).[82–84] Within VASP, core and valence electrons are separated exploiting projector-augmented waves (PAW).[85,86] The exchange and correlation energy is calculated using the generalized gradient approximation (GGA), as described by Perdew, Burke and Ernzerhof (PBE).[63] Additionally for the analysis of the band gap, calculations were performed using the meta-GGA functional modified Becke-Johnson (MBJ).[64,87] For this, non-spherical contributions to the gradient of the density in the PAW spheres where included. For the structure optimization (RMM-DIIS) and the band gap calculation, the Brillouin zone was sampled on a 4x4x7 Γ-centered *k*-point grid and the interpolation of the *k* space was done via tetrahedron method with Blöchl corrections.[88,89] The energy convergence criterion was set to 10^{-7} eV and the residual atomic forces were relaxed until the convergence criterion of 10^{-5} eV/Å was reached. The plane wave energy cutoff was set to 520 eV. The band structure was calculated for the Bloch vector k along the lines Γ (0,0,0) to Y (−0.5,0.5,0) to V (0,0.5,0) to Γ (0,0,0) to A (0,0,0.5) to M (-0.5,0.5,0.5) to L (0,0.5,0.5) and back to V (0,0.5,0). The energy zero is taken at the Fermi level. A bonding analysis was performed by calculating the electron localization function (ELF) with an electronic convergence criterion of 10^{-8} eV.[90]

5.5 Acknowledgements

We gratefully acknowledge financial support by the Deutsche Forschungsgemeinschaft (project SCHN 377/18). Furthermore, we thank Reinhard Pritzl for the collection of the single-crystal dataset, Mirjam Zipkat for experimental support with the Sn_3N_4 synthesis, Amalina Buda for EDX measurements and Christian Minke for NMR experiments (all at Department of Chemistry at LMU Munich).

5.6 References

[1] A. Lucas, *J. Egypt. Archaeol.* **1928**, *14*, 97.

[2] S. Zhang, P. Kang, T. J. Meyer, *J. Am. Chem. Soc.* **2014**, *136*, 1734.

[3] A. B. Ferreira, A. Lemos Cardoso, M. J. Da Silva, *Int. Sch. Res. Notices* **2012**, *2012*, 142857.

[4] S. J. Freakley, Q. He, J. H. Harrhy, L. Lu, D. A. Crole, D. J. Morgan, E. N. Ntainjua, J. K. Edwards, A. F. Carley, A. Y. Borisevich C. J. Kiely, G. J. Hutchings, *Science* **2016**, *351*, 965.

[5] C. Bian, J. Wang, H. Liu, Y. Yan, P. Zhang, W. Yang, S. Jia, X. Guo, G. Cai, *Nano Res.* **2023**, *17*, 3035.

[6] K. Gotlib-Vainstein, I. Gouzman, O. Girshevitz, A. Bolker, N. Atar, E. Grossman, C. N. Sukenik, *ACS Appl. Mater. Interfaces* **2015**, *7*, 3539.

[7] J.-C. Manifacier, L. Szepessy, J. F. Bresse, M. Perotin, R. Stuck, *Mater. Res. Bull.* **1979**, *14*, 163.

[8] B. Pejjai, V. R. Minnam Reddy, S. Gedi, C. Park, *J. Ind. Eng. Chem.* **2018**, *60*, 19.

[9] M. Forster, *Energy* **2004**, *29*, 789.

[10] F. Belliard, *Solid State Ion.* **2000**, *135*, 163.

[11] J. Cao, F. Yan, *Energy Environ. Sci.* **2021**, *14*, 1286.

[12] T. Djenizian, I. Hanzu, M. Eyraud, L. Santinacci, *C. R. Chim.* **2008**, *11*, 995.

[13] B. Luo, D. Yang, M. Liang, L. Zhi, *Nanoscale* **2010**, *2*, 1661.

[14] A. Giberti, A. Gaiardo, B. Fabbri, S. Gherardi, V. Guidi, C. Malagù, P. Bellutti, G. Zonta, D. Casotti, G. Cruciani, *Sens. Actuators B* **2016**, *223*, 827.

[15] J. Watson, K. Ihokura, G. S. V. Coles, *Meas. Sci. Technol.* **1993**, *4*, 711.

[16] T. F. Fässler, S. Hoffmann, *Inorg. Chem.* **2003**, *42*, 5474.

[17] R. Pöttgen, *Z. Naturforsch* **2006**, *61b*, 677.

[18] R. H. Kane, B. C. Giessen, N. J. Grant, *Acta Metall*. **1966** *14*, 605.

[19] W. H. Baur, *Acta Crystallogr.* **1956**, *9*, 515.

[20] J. Pannetier, G. Denes, *Acta Crystallogr. Sect. B* **1980**, *36*, 2763.

[21] T. Bernert, A. Pfitzner, *Z. Kristallogr. – Cryst. Mater.* **2005**, *220*, 968.

[22] N. Scotti, W. Kockelmann, J. Senker, S. Traßel, H. Jacobs, *Z. Anorg. Allg. Chem.* **1999**, *625*, 1435.

[23] F. J. Pucher, C. Frhr. von Schirnding, F. Hummel, V. R. Celinski, J. Schmedt auf der Günne, B. Gerke, R. Pöttgen, W. Schnick, *Eur. J. Inorg. Chem.* **2015**, *2015*, 382.

[24] K. Niwa, H. Ogasawara, M. Hasegawa, *Dalton Trans.* **2017**, *46*, 9750.

[25] K. Niwa, T. Inagaki, T. Ohsuna, Z. Liu, T. Sasaki, N. A. Gaida, M. Hasegawa, *Cryst. Eng. Comm.* **2020**, *22*, 3531.

[26] M. Löber, K. Dolabdjian, M. Ströbele, C. P. Romao, H.-J. Meyer, *Inorg. Chem.* **2019**, *58*, 7845.

[27] W. Schnick, J. Luecke, *J. Solid State Chem.* **1990**, *87*, 101.

[28] E.-M. Bertschler, R. Niklaus, W. Schnick, *Chem. Eur. J.* **2017**, *23*, 9592.

[29] S. J. Sedlmaier, M. Eberspächer, W. Schnick, *Z. Anorg. Allg. Chem.* **2011**, *637*, 362.

[30] E.-M. Bertschler, R. Niklaus, W. Schnick, *Chem. Eur. J.* **2018**, *24*, 736.

[31] S. Horstmann, E. Irran, W. Schnick, *Angew. Chem. Int. Ed.* **1997**, *36*, 1873.

[32] K. Landskron, H. Huppertz, J. Senker, W. Schnick, *Angew. Chem. Int. Ed.* **2001**, *40*, 2643.

[33] D. Baumann, W. Schnick, *Angew. Chem. Int. Ed.* **2014**, *53*, 14490.

[34] S. J. Ambach, M. Pointner, S. Falkai, C. Paulmann, O. Oeckler, W. Schnick, *Angew. Chem. Int. Ed.* **2023**, *62*, e202303580.

[35] S. Vogel, M. Bykov, E. Bykova, S. Wendl, S. D. Kloß, A. Pakhomova, S. Chariton, E. Koemets, N. Dubrovinskaia, L. Dubrovinsky, W. Schnick, *Angew. Chem. Int. Ed.* **2019**, *58*, 9060.

[36] D. Laniel, F. Trybel, A. Néri, Y. Yin, A. Aslandukov, T. Fedotenko, S. Khandarkhaeva, F. Tasnádi, S. Chariton, C. Giacobbe, E. L. Bright, M. Hanfland, V. Prakapenka, W. Schnick, I. A. Abrikosov, L. Dubrovinsky, N. Dubrovinskaia, *Chem. Eur. J.* **2022**, *28*, e202201998.

[37] Y. Hirota, T. Kobayashi, *J. Appl. Phys.* **1982**, *53*, 5037.

[38] Y.-H. Jeong, K.-H. Choi, S.-K. Jo, B. K. Bongkoo Kang, *Jpn. J. Appl. Phys.* **1995**, *34*, 1176.

[39] M. S. Choudhary, J. K. Fink, K. Lederer, H. A. Krässig, *J. Appl. Polym. Sci.* **1987**, *34*, 863.

[40] E.-C. Koch, S. Cudziło, *Angew. Chem. Int. Ed.* **2016**, *55*, 15439.

[41] S. Wendl, L. Eisenburger, P. Strobel, D. Günther, J. P. Wright, P. J. Schmidt, O. Oeckler, W. Schnick, *Chem. Eur. J.* **2020**, *26*, 7292.

[42] A. Marchuk, W. Schnick, *Angew. Chem. Int. Ed.* **2015**, *54*, 2383.

[43] S. Schneider, S. T. Kreiner, L. G. Balzat, B. V. Lotsch, W. Schnick, *Chem. Eur. J.* **2023**, *29*, e202309186.

[44] S. Schneider, E.-M. Wendinger, V. Baran, A.-K. Hatz, B. V. Lotsch, M. Nentwig, O. Oeckler, T. Bräuniger, W. Schnick, *Chem. Eur. J.* **2023**, *29*, e202300174.

[45] S. Schneider, L. G. Balzat, B. V. Lotsch, W. Schnick, *Chem. Eur. J.* **2023**, *29*, e202202984.

[46] X. Wang, Z. Liu, X.-G. Zhao, J. Lv, K. Biswas, L. Zhang, *ACS Appl. Mater. Interfaces* **2019**, *11*, 24867.

[47] M. M. Bletskan, D. I. Bletskan, *J. Optoelectron. Adv. Mater.* **2014**, *2014*, 659.

[48] C. M. Caskey, A. Holder, S. Shulda, S. T. Christensen, D. Diercks, C. P. Schwartz, D. Biagioni, D. Nordlund, A. Kukliansky, A. Natan, D. Prendergast, B. Orvananos, W. Sun, X. Zhang, G. Ceder, D. S. Ginley, W. Tumas, J. D. Perkins, V. Stevanovic, S. Pylypenko, S. Lany, R. M. Richards, A. Zakutayev, *J. Chem. Phys.* **2016**, *144*, 144201.

[49] Deposition Number 2341441 contains the supplementary crystallographic data for this paper. These data are provided free of charge by the joint Cambridge Crystallographic Data Centre and Fachinformationszentrum Karlsruhe Access Structures service.

[50] F. Liebau, *Structural Chemistry of Silicates. Structure, Bonding, and Classification*, Springer, Berlin, 1985, pp. 1−6. The terms "*vierer-ring"*, "*sechser-ring*", and "*achter-ring*" have been defined by Liebau and are derived from the German words "*vier*" (engl. four), "*sechs*" (engl. six), and "*acht*" (engl. eight), describing rings consisting of the respective amount of tetrahedra.

[51] V. A. Blatov, A. P. Shevchenko, D. M. Proserpio, *Cryst. Growth Des.* **2014**, *14*, 3576.

[52] J. V. Smith, *Acta Crystallogr.* **1953**, *6*, 613.

[53] S. D. Kloss, W. Schnick, *Angew. Chem. Int. Ed.* **2015**, *54*, 11250.

[54] S. J. Ambach, C. Somers, T. de Boer, L. Eisenburger, A. Moewes, W. Schnick, *Angew. Chem. Int. Ed.* **2023**, *62*, e202215393.

[55] S. Bhat, L. Wiehl, S. Haseen, P. Kroll, K. Glazyrin, P. Gollé-Leidreiter, U. Kolb, R. Farla, J.-C. Tseng, E. Ionescu, T. Katsura, R. Riedel, *Chem. Eur. J.* **2020**, *26*, 2187.

[56] B. Glockzin, M. S. Oakley, A. Karmakar, A. Pominov, A. A. Mitchell, X. Ma, M. Klobukowski, V. K. Michaelis, *J. Phys. Chem. C* **2023**, *127*, 7284.

[57] P. Amornsakchai, D. C. Apperley, R. K. Harris, P. Hodgkinson, P. C. Waterfield, *Solid State Nucl. Magn. Reson.* **2004**, *26*, 160.

[58] C. Cossement, J. Darville, J.-M. Gilles, J. B. Nagy, C. Fernandez, J.-P. Amoureux, *Magn. Reson. Chem.* **1992**, *30*, 263.

[59] T. Bräuniger, S. Ghedia, M. Jansen, *Z. Anorg. Allg. Chem.* **2010**, *636*, 2399.

[60] H. Schumann, H.-J. Kroth, *Z. Naturforsch. B* **1977**, *32*, 876.

[61] P. E. Lippens, *Phys. Rev. B* **1999**, *60*, 4576.

[62] W. A. Merrill, J. Steiner, A. Betzer, I. Nowik, R. Herber, P. P. Power, *Dalton Trans.* **2008**, *43*, 5905.

[63] J. P. Perdew, K. Burke, M. Ernzerhof, *Phys. Rev. Lett.* **1996**, *77*, 3865.

[64] A. D. Becke, E. R. Johnson, *J. Chem. Phys.* **2006**, *124*, 221101.

[65] A. Stock, H. Grüneberg, *Ber. Dtsch. Chem. Ges.* **1907**, *40*, 2573.

[66] H. Huppertz, *Z. Kristallogr. – Cryst. Mater.* **2004**, *219*, 330.

[67] D. Walker, *Am. Mineral.* **1991**, *76*, 1092.

[68] SAINT, Data Integration Software, Vers. 4.0, Madison, Wisconsin (USA), **1997**.

[69] Bruker-AXS, APEX 3, Karlsruhe (Germany), **2016**.

[70] Bruker-AXS, XPREP Reciprocal Space Exploration, Karlsruhe (Germany), **2001**.

[71] G. M. Sheldrick, *Acta Crystallogr. Sect. C*, **2015**, *71*, 3.

[72] G. M. Sheldrick, *Acta Crystallogr. Sect. A*, **2015**, *71*, 3.

[73] K. Momma, F. Izumi, *J. Appl. Crystallogr.* **2011**, *44*, 1272.

[74] J. Cumby, J. P. Attfield, *Nat. Commun.* **2017**, *8*, 14235.

[75] A. A. Coelho, TOPAS-Academic, Brisbane (Australia), **2007**.

[76] H. M. Rietveld, *J. Appl. Crystallogr.* **1969**, *2*, 65.

[77] R. W. Cheary, A. Coelho, *J. Appl. Crystallogr.* **1992**, *25*, 109.

[78] R. W. Cheary, A. A. Coelho, J. P. Cline, *J. Res. Natl. Inst. Stan. Technol.* **2004**, *109*, 1.

[79] Oxford Instruments, AZtecEnergy, Abington (USA), **2016**.

[80] Brand R. A., WinNormos for Igor6, Universität Duisburg, Duisburg (Germany), **2017**.

[81] Corel Corporation: Ottowa, CorelDRAW Graphics Suite 2017, Ontario (Canada), **2017**.

[82] G. Kresse, J. Hafner, *Phys. Rev. B* **1993**, *47*, 558.

[83] G. Kresse, J. Furthmüller, *Comput. Mater. Sci.* **1996**, *6*, 15.

[84] G. Kresse, J. Furthmüller, *Phys. Rev. B* **1996**, *54*, 11169.

[85] G. Kresse, D. Joubert, *Phys. Rev. B* **1999**, *59*, 1758.

[86] P. E. Blöchl, *Phys. Rev. B* **1994**, *50*, 17953.

[87] F. Tran, P. Blaha, *Phys. Rev. Lett.* **2009**, *102*, 226401.

[88] P. Pulay, *Chem. Phys. Lett.* **1980**, *73*, 393.

[89] H. J. Monkhorst, J. D. Pack, *Phys. Rev. B* **1976**, *13*, 5188.

[90] B. Silvi, A. Savin, *Nature* **1994**, *371*, 683.

Chapter 6

Nitride Synthesis Under High-Pressure High-Temperature Conditions – Unprecedented *in-situ* Insight into the Reaction

Published in: *Inorg. Chem.* **2024**, *63*, 3535

Authors: Sebastian J. Ambach, Reinhard M. Pritzl, Shrikant Bhat, Robert Farla, Wolfgang Schnick

DOI: https://doi.org/10.1021/acs.inorgchem.3c04433

Abstract: High-pressure high-temperature (HP/HT) syntheses are essential for modern high-performance materials. Phosphorus nitride, nitridophosphate and more generally nitride syntheses benefit greatly from HP/HT conditions. In this contribution, we present the first systematic *in-situ* investigation of a nitridophosphate HP/HT synthesis, using the reaction of zinc nitride Zn_3N_2 and phosphorus(V) nitride P_3N_5 to the nitride semiconductor Zn_2PN_3 as a case study. At a pressure of 8 GPa and temperatures up to 1300 °C the reaction was monitored by energy-dispersive powder X-ray diffraction (ED-PXRD) in a large-volume press at beamline P61B at DESY. The experiments investigate the general behavior of the starting materials under extreme conditions and give insight into the reaction. During cold-compression and subsequent heating the starting materials remain crystalline above their ambient-pressure decomposition point, until a sufficient minimum temperature is reached and the reaction starts. The reaction proceeds via ion diffusion at grain boundaries with an exponential decay of the reaction rate. Raising the temperature above the minimum required value quickly completes the reaction and initiates single crystal growth. After cooling and decompression, which did not influence the resulting product, the recovered sample was analyzed by EDX-spectroscopy.

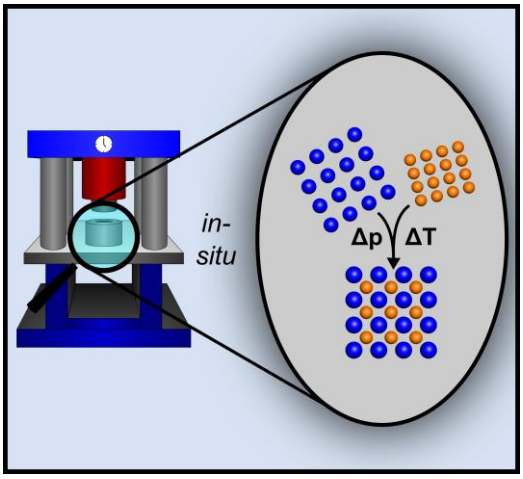

6.1 Introduction

Several high-performance ceramics such as nano-polycrystalline diamond, cubic boron nitride, BC_2N, and refractory spinel-type γ-Si_3N_4 require synthesis at high pressures.[1–6] The scale-up for production under gigapascal pressure is much more time consuming and expensive than for ceramics manufactured at ambient pressures, which are issues that can be alleviated through understanding of formation mechanisms. Unlike ambient pressure synthesis of ceramics, however, the formation of solid-state compounds under high-pressure was never monitored *in-situ* and therefore reaction mechanisms are proposed based on *ex-situ* information. The installation of large-volume-presses (LVP) at synchrotron facilities, such as beamline station P61B at PETRA III, DESY, enable *in-situ* monitoring of high-pressure high-temperature reactions.[7]

Over the past decades several models for solid-state kinetics and reaction mechanisms at ambient pressure have been developed, either from theoretical calculations or experimental data.[8] This encompasses simple order-based models, derived from kinetics in liquid homogeneous systems. Nucleation models are most commonly used to explain crystallization, phase transitions, decompositions, adsorptions, hydrations and desolvations.[9–18] In these models, all processes start at one or more nucleation sites, which provide minima for reaction activation energies due to crystal imperfections or surfaces. Special cases are grouped under the term contraction models, which assume a nucleation start at the surface of a crystal with the reaction proceeding to its center.[8] The most common model for the formation of new compounds during syntheses is the diffusion model.[19,20] A fundamental work of Tamman suggests the melt free diffusion of ions at grain boundaries of different reactants into each other, forming a layer of the product.[21] As this layer grows, the reaction rate drastically decreases due to lengthened diffusion pathways. Additionally, a reactant-depended minimum temperature is needed to initially start the diffusion and the subsequent diffusion rate exhibits a strong temperature dependence. To describe the thickness of the product layer and thus the reaction speed, the empirical equation

$$z = a \cdot \ln(t) + c \tag{1}$$

(z: layer thickness; a: temperature-dependent constant; t: reaction time; c: constant) was published. Based on further experimental data in subsequent work, Jander proposed a slightly modified equation, describing the layer thickness as quadratic dependent on the reaction time:

$$z^2 = 2 \cdot t \cdot c \tag{2}$$

(z: layer thickness; t: reaction time; c: constant depending on diffusion coefficients).[22] This model was used for various solid-state reaction mechanisms investigations later on.[23–25]

Like most of the ambient-pressure experiments above, the major part of high-pressure research is focused on oxidic materials.[26] However, another large class of compounds benefits from or sometimes even requires high pressures during syntheses: nitrides, and in particular the subclass of phosphorus nitrides and nitridophosphates.[27,28] The high temperatures needed for their synthesis are in direct contrast to their susceptibility for thermal decomposition, beyond which releasing molecular N_2 becomes thermodynamically favored because of its stable triple bond (942 kJ/mol).[29] Additionally, in phosphorus nitrides and nitridophosphates, P^{+V} is prone to reduction to P^{+III}, elemental P or even P^{-III} in phosphides, due to the reductive environment provided by the nitride anions (electron affinity of N^{3-} +0.07 eV).[30] According to Le Chatelier's principle, the decomposition and formation of gaseous N_2 during syntheses can be countered by applying pressure. Thus, syntheses typically are carried out under high temperatures and high pressures up to the gigapascal (GPa) range.

Due to the isoelectronic elemental combination P/N and Si/O, the structural diversity of nitridophosphates is predicted to be at least as large as the one of oxosilicates, consequently suggesting a field of application, which is in no way inferior. As of today, this includes the application as gate insulator in metal-insulator semiconductor field-effect transistors (MISFETs), as an oxygen eliminating material during the production of incandescent and tungsten halogen lamps and discussions regarding a use in pyrotechnics safety, as flame retardant, as gas storing material for ammonia, as candidate for a warm-white phosphor in solid state lighting and lithium ion conductivity.[31–39]

Over the past thirty years, several synthetic methods for phosphorus nitrides and nitridophosphates under high-pressure high-temperature conditions have emerged, including some mechanistic suggestions: the solid-state metathesis, the Li_3N self-flux method, the nitride route, the azide route as well as NH_4Cl, HCl and NH_4F assisted syntheses.[40–45] Starting from $LiPN_2$ and a metal halide, the solid-state metathesis uses the formation of the corresponding lithium halide as reaction driving force.[42] Additionally, the lithium halide, which is molten at reaction conditions, acts as flux agent supporting single crystal growth. Similarly, small amounts of NH_4Cl have been proven to be suitable as mineralizer by facilitating the reversible formation and cleavage of P/N bonds.[45] A comparable assumption is made for the Li_3N self-flux method, which employs Li_3N both as starting material and flux agent.[39] Additionally it was suggested, that the Li_3N flux can preserve P/N building blocks from the starting materials.[38] Transferring the well-known ion exchange to high-pressure high-temperature syntheses, it was shown that a preservation of a P/N framework is possible.[46] Recently, *in-situ* generated HCl and HF was used to activate inert starting materials such as BN or even TiN.[43,44] It is assumed that reactive intermediate species are formed during the reaction process. The azide route uses P_3N_5 and a metal azide as reactant, which is suggested to decompose under elevated pressure, releasing molecular N_2, the partial pressure of which further inhibits the

decomposition of nitrides.[35] Using this method, Wendl *et al.* proposed the to date single detailed reaction mechanism on the formation of nitridophosphates, derived from pressure-quenched samples.[47] $SrP_6N_8(NH)_4$ is assumed to be an intermediate species that condenses to SrP_8N_{14} by replacing imide groups with PN_4 tetrahedra in the crystal structure. To date, however, there is no experimental proof of any thesis.

In this contribution, we present the first systematic *in-situ* study of a high-pressure high-temperature nitridophosphate synthesis. The nitride route, reacting P_3N_5 and a metal nitride, seemed most suitable for *in-situ* XRD observation, as no molten state or decomposition are supposed to be involved. In two experiments, the synthesis of Zn_2PN_3, a nitride semiconductor, is monitored as model system *in-situ* to investigate the general behavior of the starting materials, the formation of products and the impact of cooling and decompression under extreme conditions and gain insight into the condensation mechanism.[40,48] The recovered samples are subsequently analyzed by EDX spectroscopy and SEM images.

6.2 Experimental Section

Preparation of Phosphorus(V) Nitride P_3N_5

The binary phosphorus(V) nitride P_3N_5 was prepared as partially crystalline powder according to Stock *et al*. by ammonolysis of phosphorus pentasulfide (P_4S_{10}, Acros Organics, >98%) in a constant flow of ammonia gas (NH_3, Air Liquide, 99.999%).[49] To exclude oxygen and moisture, a boat of silica glass, placed in a silica tube, was dried at 1000 °C for 8 h under a reduced pressure of 10^{-3} mbar. Afterwards, the silica boat was filled with 8 g of P_4S_{10} and centered inside the outer tube within a resistance furnace. The apparatus was saturated with NH_3 by a constant flow for 1 h at ambient temperature and consequently heated with 7 °C/min to 850 °C. After a reaction time of 4 h, the furnace was cooled down with 7 °C/min. The orange powdery product was analyzed for contaminations from elements other than P and N by powder X-ray diffraction (PXRD) and elemental CHNS-analysis (measured: C: 0%, H: 0%, N: 43.16%, S: 0%; calculated: C: 0%, H: 0%, N: 42.98%, S: 0%).

High-Pressure High-Temperature Experiments

The assembly with the starting materials for the synthesis of Zn_2PN_3 (Equation 3) was prepared as published by Sedlmaier *et al.*[40]

$$2\ Zn_3N_2 + P_3N_5 \rightarrow 3\ Zn_2PN_3 \qquad (3)$$

Stoichiometric amounts of Zn_3N_2 (Alfa Aesar, 99%) and partially crystalline α-P_3N_5 were ground together under argon atmosphere in a glovebox (O_2/H_2O < 1 ppm). An h-BN crucible was half filled with the powder mixture and half filled with MgO, both separated by a small h-BN disc and finally closed with a lid of the same material. Small pieces of tantalum foil were

attached to the top and bottom of the h-BN crucible to locate the sample by *in-situ* X-ray radiography. High-Z materials (such as Ta) exhibit greater X-ray absorption and thus appear dark in the image. The h-BN components were held in the center of a graphite heater by two MgO disks. For electrical contact, Mo rods within MgO disks were attached on the top and bottom of the graphite furnace. The described assembly was centered in a drilled-through octahedron (MgO, 5% Cr_2O_3 doped, 14 mm edge length), placed in the middle of eight electrically insulated Co-doped WC cubes with truncated corners (8% Co, 32 mm edge length, truncated edge length 8 mm). A detailed schematic sketch of the assembly can be found in the supporting information (Figure S5.1). The sample was compressed to the target pressure of 8 GPa by the Hall-type six-ram large-volume-press (LVP) Aster-15 (Voggenreiter, Mainleus, Germany), located at beamline P61B at DESY, using the 6-8 Kawai-type compression geometry.[7] The actual sample pressure was determined from the measured unit cell volume of an MgO pressure marker and its known equation of state.[50] The sample temperature was controlled by manually adjusting the heating power, using a calibration curve of heating power vs. temperature. In-situ observations were performed by energy-dispersive powder X-ray diffraction (ED-XRD) using two high-purity germanium solid-state detectors (Ge-SSD, Mirion, Canberra). The assembly was visualized with a white-beam X-ray microscope (Optique Peter, Lentilly, France).

Two experiments were carried out: the first for screening the reaction timeframe, temperature region and involved phases, and the second, to *in-situ* monitor the formation of Zn_2PN_3 with a sampling frequency of 8-10 diffraction patterns per minute (i.e. 6 – 8 s acquisitions).

Experiment for General Overview

A detector angle 2θ of ~5.13°, an incident beam slit aperture of 50 x 300 μm^2, and an exposure time of 100 s were selected for all measurements in the first experiment. During compression, powder diffraction patterns were acquired at hydraulic oil pressures of 50, 100, and 200 bar in the master ram. After reaching the target MgO pressure, the sample was heated manually to the reaction temperature of 1200 °C in steps of 100 °C. After a 30-minute hold time, the temperature was increased to 1300 °C and the sample finally cooled down to ambient temperature in 200 °C decrements (Figure 6.1). During both heating and cooling, a diffraction pattern was collected after each temperature step, with an additional 10 consecutive patterns measured immediately after the reaction temperature (1200 °C) was reached. After cooling, the sample was decompressed and a final diffraction pattern was measured at ambient pressure.

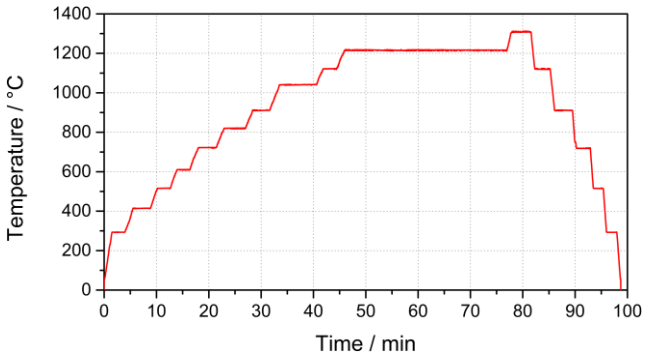

Figure 6.1: Overview of the temperature curve for the first experiment. Heating was performed manually by adjusting the heating power and converted to a specific temperature using a calibration curve previously established (Figure S2).

Time-Resolved Experiment

All measurements of the second experiment were performed with a detector angle 2θ of ~3.00° and an incident beam slit aperture of 200 x 700 µm^2. Diffraction spectra were collected continuously throughout the heating period with a 2 s exposure time. Due to system limitations, this resulted in a pattern acquired every 7-10 s (including acquisition time), equating to a sampling frequency of 6-8 patterns/minute. After compression to the target pressure (8 GPa), the sample was manually heated as shown in Figure 6.2. After cooling and decompression, the sample analyzed by energy-dispersive X-ray spectroscopy (EDX).

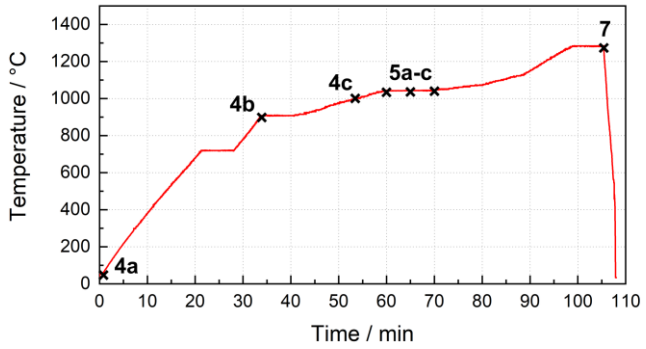

Figure 6.2: Temperature profile of the second experiment. Heating was performed manually by adjusting the heating power. Temperatures were evaluated using a calibration curve. Spectra of the highlighted points are discussed in the results section with the respective Figures.

Scanning Electron Microscopy and Energy-Dispersive X-Ray Spectroscopy

For EDX measurements, the sample was recovered from all assembly parts under argon atmosphere in a glovebox. The powdered sample was prepared on an electrically conductive,

self-adhesive carbon foil on an aluminum sample holder and coated with a thin layer of carbon (electron beam evaporator, BAL-TEC MED 020, BalTex AG, Pfäffikon, Swiss). EDX-spectra and SEM-images were recorded with a Dualbeam Helios Nanolab G3 UC electron microscope (FEI, USA) equipped with an X-Max 80 SDD detector (Oxford Instruments, UK). The data and image capturing were done using the Aztec software (Oxford instruments, UK).[51]

6.3 Results and Discussion

Experiment for General Overview

Both starting materials are known for their thermal decomposition at ambient pressure (Zn_3N_2: 400 °C under O_2 atmosphere, 600 °C under N_2 atmosphere; P_3N_5: 800 °C).[28,52] As published by Sedlmaier *et al.*, a reaction temperature of 1200 °C, thus well above the decomposition points, is required to form Zn_2PN_3. Since any experimental insights into possible decompositions and other processes under high-pressure high-temperature conditions are lacking, our first experiment monitored the entire synthesis including compression and heating phase (Figures 6.3a-d). The most intense reflections of Zn_3N_2 are each marked with the corresponding lattice plane indices. No reflections of P_3N_5 can be observed, which may be due to pressure-induced phase amorphization combined with poor X-ray scattering factors of the light atoms P and N and the partially crystalline nature of the starting material. In addition, fluorescence peaks of lead caused by the experimental setup and small unassignable reflections (marked with an asterisk) are visible in each diffraction pattern.

Figure 6.3a shows the diffraction patterns of three different compression points with their respective pressures. Comparing them, two well-known pressure-related effects can be observed. First, a compression of the unit cell, which causes a shift of the reflections to higher energies, corresponding to smaller d spacings. Second, the introduction of microscopic crystal strain, grain crushing and a dislocation increase, which leads to broadened reflections with reduced intensity. In this case, intensities decrease by about 30% from 1.3 GPa to 8.1 GPa. Zn_3N_2 shows no signs of a phase transition, (pre)reaction, or decomposition up to 8.1 GPa. Although no reflections of P_3N_5 can be observed, we assume that this is also the case here, since both show comparable materials properties.

Heating the assembly (Figure 6.3b) at a pressure of 8 GPa proves the stabilizing effect of pressure on Zn_3N_2. Until approaching the reaction temperature of 1200 °C, Zn_3N_2 shows no signs of interaction with other materials, phase transitions or intermediate formation in the diffraction patterns. The intensity ratios of Zn_3N_2 reflections begin to differ from those measured under ambient conditions, which may be explained by material texture. In addition, temperature-related effects on Zn_3N_2 reflections are observed, which partially reverse the pressure-related effects. Elevated temperatures usually lead to an expansion of the unit cells

caused by increased thermal motion, and thus to a shift of reflections to lower energies. It also anneals dislocations, as evidenced by a decreased FWHM of the reflections and their increased intensity. Up to 1100 °C, the thermal effects have little impact on the position and shape of the reflections. A pressure-induced shift of +1.3 keV and intensity decrease of about 30% compared to a temperature-induced shift of –0.7 keV and an intensity increase of about 10% is visible in the 332 main reflection.

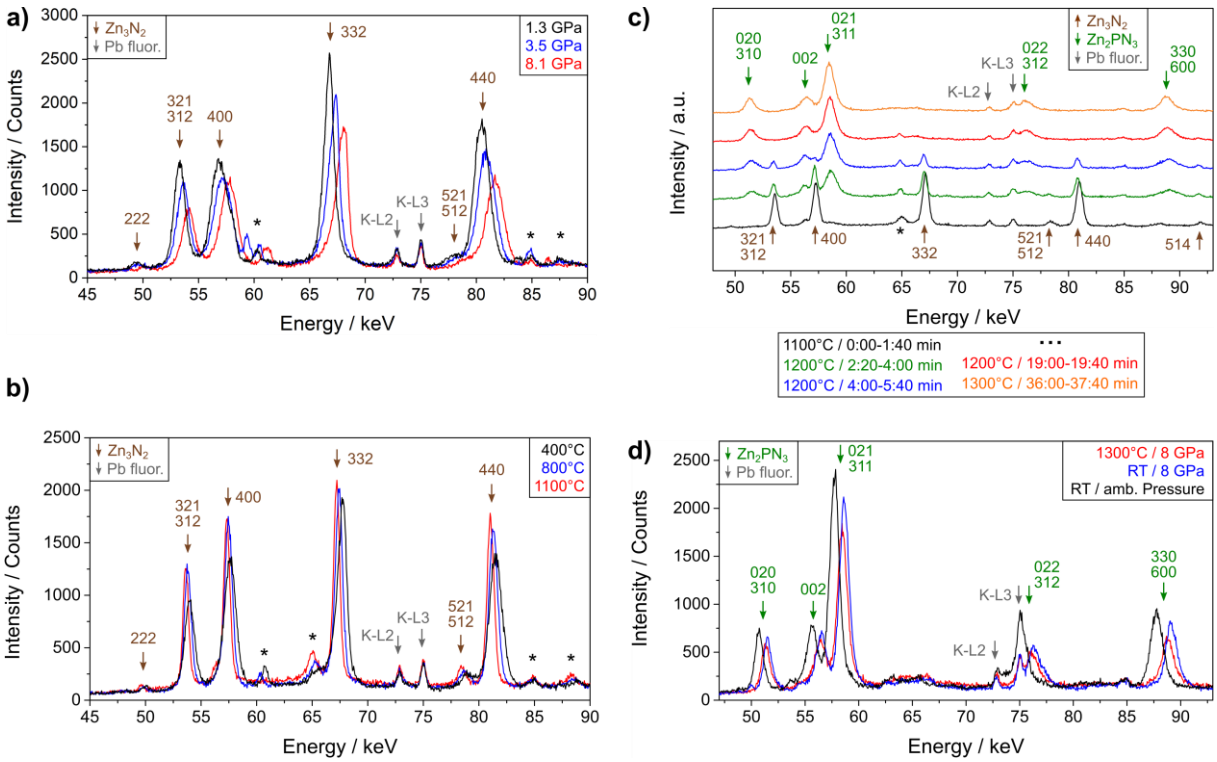

Figure 6.3: Energy-dispersive diffraction patterns (2θ ~5.13°) of the first experiment. Reflection indices of Zn_3N_2 (brown), Zn_2PN_3 (green), and Pb-fluorescence peaks (grey) are indicated with arrows. Reflections that cannot be assigned are marked with an asterisk. a) Assembly compression at 1.3 GPa (black), 3.5 GPa (blue) and 8.1 GPa (red). Pressures were determined using MgO as a pressure marker. b) Heating from ambient temperature to 1100 °C (400 °C black, 800 °C blue, 1100 °C red) at a pressure of 8 GPa. Temperatures were adjusted using a calibration curve of heating power vs. temperature c) Reaction of Zn_3N_2 and P_3N_5 to Zn_2PN_3 with time and temperature codes. d) Temperature- and pressure-quenching the assembly from 1300 °C/8 GPa (red) to ambient temperature/8 GPa (blue) to ambient pressure (black).

The reaction occurs within a short period of approximately 5 minutes (published reaction time: 10 minutes) when the assembly temperature reaches 1200 °C (Figure 6.3c).[40] During this period, the intensity of the Zn_3N_2 reflections continuously decreases until they completely

disappear, while the Zn_2PN_3 reflections appear and gain intensity. According to the ED-XRD patterns, neither a time interval with completely amorphous materials nor any crystalline intermediate species are involved in this transition. Comparatively broad, low intensity reflections of newly formed Zn_2PN_3 increase in intensity and show a reduced FWHM as time progresses. This corresponds to small Zn_2PN_3 domains at the start, which grow with time. Increasing the temperature to 1300 °C or beyond does not have any visible effect on Zn_2PN_3 or initiate its decomposition. However, a detailed look at the processes involved in the transition from Zn_3N_2 and P_3N_5 to Zn_2PN_3, is not possible on a time scale of 100 s per measurement and will be further investigated in the second experiment.

Temperature-quenching and decompressing the assembly to ambient conditions has very little effect on the sample (Figure 6.3d). The single crystals do not seem to grow further, as neither an overall intensity increase nor a decreased FWHM of the Zn_2PN_3 reflections is observed. The changed intensities of single reflections, especially 021/311 and 330/600, may be attributed to texture effects. After decompression, the 022/312 reflection overlaps with the K-L3 fluorescence line of Pb, which explains the striking intensity change. In addition, the temperature-induced shift to higher energies as well as the pressure-induced shift to lower energies are observed upon cooling and decompressing, respectively.

This overview experiment on the formation of Zn_2PN_3 has shown that until the reaction temperature is reached, Zn_3N_2 and possibly also P_3N_5 are only affected by pressure and temperature related effects and otherwise remain stable. The reaction occurs on a short time scale, while longer heating periods promote domain growth.

Time-Resolved Experiment

Since the processes involved in the formation of Zn_2PN_3 from Zn_3N_2 and P_3N_5 occur in the time frame of a few minutes, a second experiment was performed with a reduced exposure time of 2 s (resulting in a diffraction pattern every 7-10 s) and a modified heating program (Figure 6.2). To achieve sufficient intensity at such short exposure times, the incident beam slit aperture was increased from 50 x 300 μm^2 to 200 x 700 μm^2.

After compression to 8.4 GPa, the main reflections of Zn_3N_2 and partially crystalline P_3N_5 were identified (Figure 6.4a). In contrast to the overview experiment, this experiment was carried out with an enhanced detector system, allowing the observation of P_3N_5 reflections.[7] In addition, Pb fluorescence peaks from the experimental setup and MgO peaks originating from parts of the assembly are visible. Since MgO is not in contact with the starting materials at any time and is only visible due to the larger slit aperture, it does not affect the reaction, as evidenced by a constant MgO peak throughout the experimental period. The same applies to the BN and an unknown peak (marked with an asterisk), which remain constant over the entire experimental period.

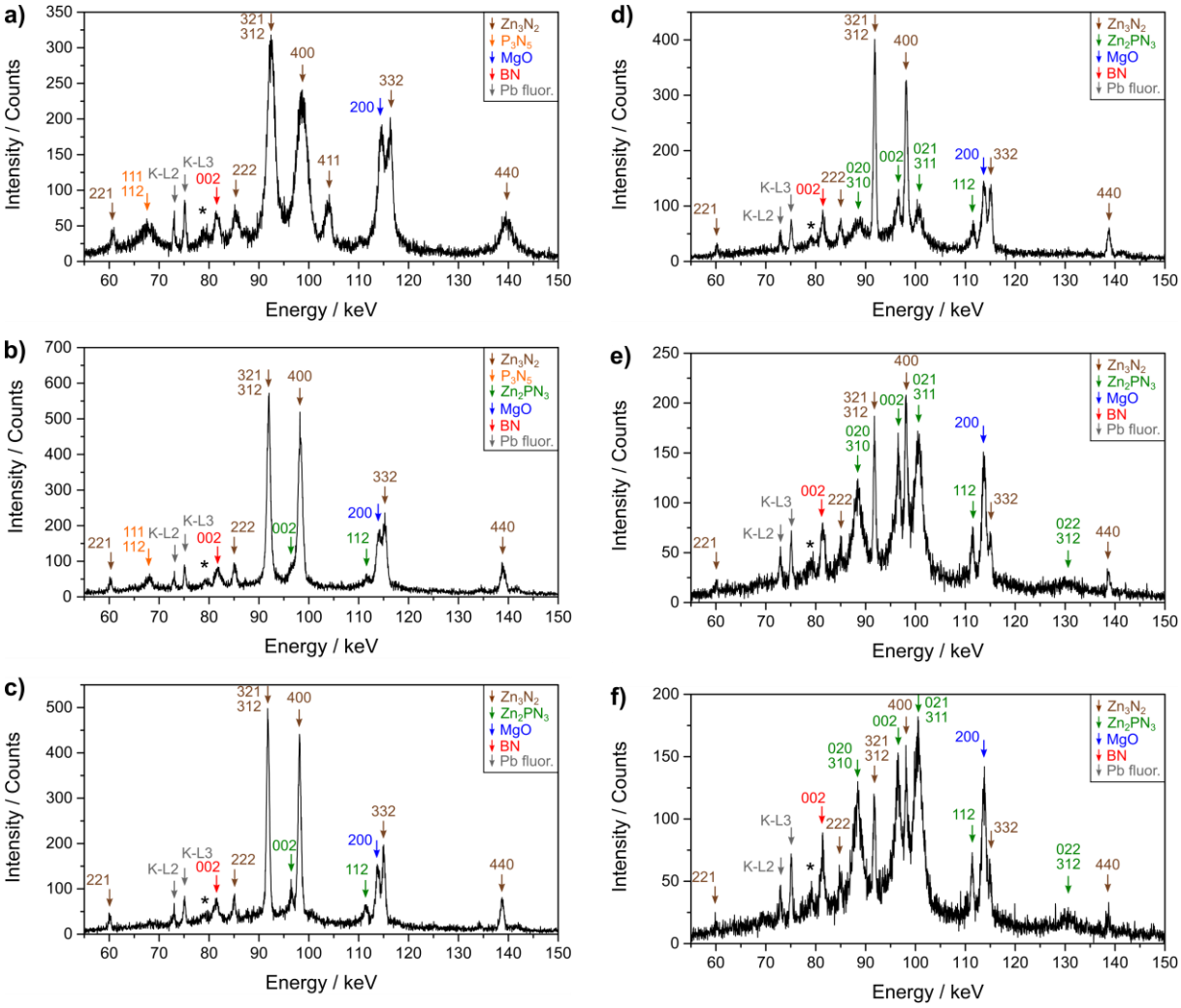

Figure 6.4: Energy-dispersive diffraction patterns (2θ ~3.00°) of the sample during the experiment. The reflections of different materials are colour coded: Zn_3N_2 (brown), P_3N_5 (orange), MgO (blue), Pb fluorescence peaks (grey), unassigned reflections (asterisks). a) At ambient temperature, the starting materials Zn_3N_2 and P_3N_5 are identified. b) At 900 °C, the first reflections of the product Zn_2PN_3 appear. c) At 1000 °C reflections of P_3N_5 disappear, while the reflections of Zn_2PN_3 become more distinct. d) Reaction start at 1050 °C. e) Diffraction pattern after 5 min at 1050 °C. f) Diffraction pattern after 10 min at 1050 °C.

Near the reaction temperature (900 °C), heating was temporarily interrupted to ensure that a uniform temperature was established throughout the sample (Figure 6.4b). As in the first experiment, recrystallization of the starting materials and a strong influence of texture can be observed. This can be seen especially in the fact that reflections 321, 312 and 400 double their intensity compared to ambient temperature and the 411 peak even disappears completely. In addition, the 002 and 112 peaks of the product Zn_2PN_3 are already visible, however with low intensity. Even after an extended time at a constant temperature of 900 °C, these reflections

do not grow noticeably. As discussed later, this may be explained by the formation of a small product layer at grain boundaries by ion diffusion. Since 900 °C might be too low to sustain a significant diffusion rate through the thickening Zn_2PN_3 layer, the reaction rate drastically decreases to almost standstill.

The same is true for further heating of the assembly to 1000 °C (Figure 6.4c). The reflections of Zn_2PN_3 increase in intensity, as higher temperatures allow further diffusion until the Zn_2PN_3 layer reaches a certain thickness again, which leads to the almost standstill. Aside from the already advanced reaction, the range of 900-1000 °C marks a turning point in the behavior of the starting materials. While up to 900 °C reflections gain intensity due to recrystallisation, above 1000 °C a reverse effect is observed. The maximum intensity (321/312 reflection) drops by about 14% in this temperature range. The same applies for P_3N_5, whose main reflections disappear completely. This supports the observation of a started reaction at grain boundaries, consuming small fractions of the starting materials.

At a temperature of 1050 °C, the reaction initiates throughout the entire sample (Figure 6.4d). The measurements reveal a further decrease in the intensity of Zn_3N_2 reflections, while the existing Zn_2PN_3 reflections gain intensity and new ones emerge due to a higher proportion of Zn_2PN_3 in the sample. After a reaction time of 5 minutes, a significant change in the diffraction pattern becomes evident, following the trend of intensity changes observed in previous measurements (Figure 6.4e). Another 5 minutes later, the reaction rate has substantially decreased, and the intensity changes of reflections are hardly noticeable anymore (Figure 6.4f).

The observations can be interpreted and explained as a transition from Zn_3N_2 and P_3N_5 towards Zn_2PN_3 by ion diffusion, a reaction mechanism regularly observed for solid-state syntheses at ambient pressure, e.g. for $NiAl_2O_4$.[24] Once the required temperature is reached, ion diffusion initiates at grain boundaries between Zn_3N_2 and P_3N_5, leading to the formation of a Zn_2PN_3 layer. As this layer grows, the diffusion pathways become longer, resulting in a slowdown of the reaction. Although the mobile ion species involved in the present reaction could not be determined, we assume that Zn^{2+} and N^{3-} ions of the Zn_3N_2 are primarily responsible, as the electrostatic diffusion barrier for P^{5+} ions might be too high and covalent bonds in PN_4 tetrahedra may not easily be broken. In the case of $NiAl_2O_4$ formation, the layer thickness shows a quadratic correlation with the reaction time. To perform a comparable analysis, the intensities of the 321/312 Zn_3N_2 and 020/310 Zn_2PN_3 peaks were monitored during the reaction to derive the amount of Zn_3N_2 remaining and the amount of Zn_2PN_3 already formed.

In case of the present reaction, a quadratic fit is not sufficient to describe the observed intensity changes; instead, an exponential growth/decay function of the general form

$$y = y_0 + A \cdot \exp(t/B) \quad (4)$$

was used (Figure 6.5) (y: degree of reaction α; y_0: degree of reaction α at t = 0; A,B: constants; t: time in minutes). The difference in reaction behavior may be attributed to the difference in bond nature of the elements involved. While the oxidic bonds of $NiAl_2O_4$ are of predominantly ionic nature, P−N bonds have a significant covalent character due to similar energies of the 3p(P) and 2p(N) orbitals.[53] The partially covalent Zn_2PN_3 layer exhibits a higher energy barrier than the ionic $NiAl_2O_4$ layer, thus the diffusion rate slows down much more with increasing product layer thickness. Equation 4 closely recalls the Avrami model, which is typically used to describe isothermal phase transitions.[54]

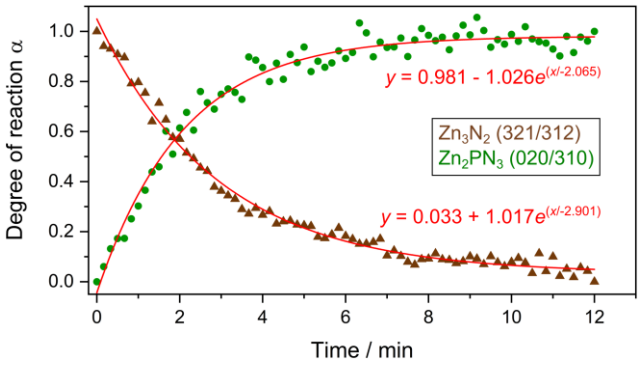

Figure 6.5: Exponential decrease in reaction rate. The areas of 321/312 Zn_3N_2 and 020/310 Zn_2PN_3 reflections were observed from the beginning of the reaction (reaching 1050 °C) to the end (increasing temperature above 1050 °C). The degree of reaction α was calculated by normalizing the areas. The data were fitted exponentially with $y = y_0 + A \cdot \exp(t/B)$.

The monitored time frame was set between reaction start, i.e. reaching 1050 °C (Figure 6.4d), and the start of a further temperature increase (Figure 6.4f), resulting in a total reaction time of 12 minutes. The 321/312 Zn_3N_2 reflection and 020/310 Zn_2PN_3 reflection were chosen for observation as both are main reflections of the respective materials and can be clearly separated from neighboring reflections. In the given time interval, the integrated area of the two peaks was calculated for each diffraction pattern. The results were normalized with respect to the initial and final points, respectively, defining the degree of reaction α between 0 and 1.

In accordance with the first experiment, the reaction proceeds rapidly within 5 minutes. Thereafter, the rate decreases drastically, leaving unreacted precursors inside the grains, which is visible in the diffraction patterns. The proposed reaction mechanism implies that no intermediate species are involved in the transition to Zn_2PN_3, which is supported by the

absence of additional reflections in the ED-XRD patterns. In addition to the absence of intermediates, the background of all patterns also remains constant at about 50 counts during the reaction, indicating that no significant amorphous parts are involved in the ion diffusion process.

Newly formed Zn_2PN_3 shows rather broad reflections with low intensity, indicating low crystallinity. Without an increase in temperature, the reaction could almost come to a standstill and the current state could be preserved for an extended period of time. This also implies an either endothermic or only slightly exothermic reaction, as a highly exothermic behavior would have the same effect as an increase in temperature. When the latter is done manually, the reaction proceeds rapidly towards Zn_2PN_3 and all reflections of Zn_3N_2 disappear, as higher temperatures allow for a higher diffusion rate and distance, enabling precursor grains to react completely. In addition, the reflections begin to show a much smaller FWHM, corresponding to single crystal growth of Zn_2PN_3 (Figure 6.6).

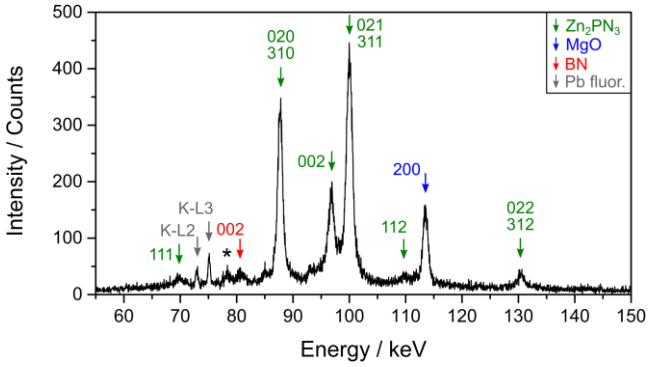

Figure 6.6: Diffraction pattern of the sample at 1300 °C. Reflections of Zn_2PN_3 (green), MgO (blue) and Pb-fluorescence peaks (gray) are marked with arrows. Two asterisks indicate not assignable reflections.

Scanning Electron Microscopy and Energy-Dispersive X-Ray Spectroscopy

To further investigate the single crystal formation of Zn_2PN_3, the sample was temperature quenched and decompressed, recovered from the assembly parts and examined by scanning electron microscopy. Figure 6.7 shows agglomerated Zn_2PN_3 single crystals up to 30 µm in length. This is consistent with the observed single crystal growth at temperatures above 1200 °C.

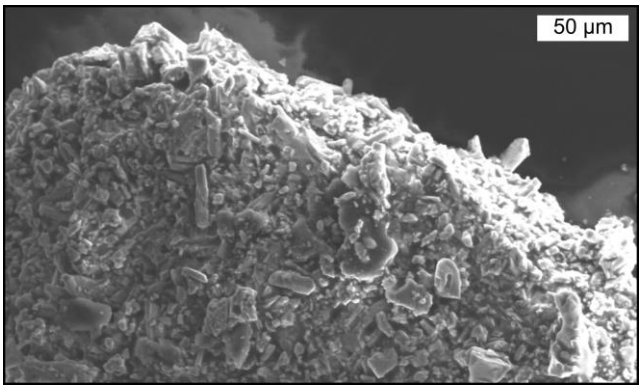

Figure 6.7: SEM image of the pressure- and temperature-quenched sample. Agglomerated single crystals of Zn_2PN_3 up to 30 µm length were formed during the reaction.

To prove that the crystallites shown in Figure 8 are Zn_2PN_3, EDX spectra were collected on different single crystals of the agglomerated particle, giving the sum formula $Zn_{2.0(2)}P_{0.8(2)}N_{1.1(3)}O_{0.2(6)}$. The anionic deviation from Zn_2PN_3 may be explained by two effects. In our experience, the light elements N and O are underestimated by the experimental setup compared to the heavier Zn. Secondly, Zn_2PN_3 is sensitive to air and an unavoidable short contact causes slow surface hydrolysis.

6.4 Conclusion

Using the large-volume press at the DESY beamline P61B in combination with synchrotron radiation, the first in-situ insights into the high-pressure high-temperature nitridophosphate synthesis are provided.

The starting materials remain crystalline above their ambient pressure decomposition point until they start to react. At sufficient temperature, most of the starting materials react within a short period of time. However, the reaction rate slows down exponentially at an intermediate constant temperature (1050 °C), which can be described by an exponential equation of the general form $y = y_0 + A \cdot \exp(t/B)$. Mechanistically, the reaction proceeds via ion diffusion at grain boundaries, which was often observed for solid-state syntheses at ambient pressure. Neither crystalline intermediate species nor a significant amorphous state is involved in the transition. Raising the temperature above the minimum required reaction temperature (1050 °C), the reaction is quickly completed. Raising the temperature even further does not have much influence on the resulting product, and the same applies to cooling and decompression. Further experiments to analyze the influence of mineralizers such as NH_4Cl or the reaction within a salt melt (high-pressure metathesis, Li_3N self-flux) may give an even deeper understanding of reaction processes and more possibilities to optimize reaction conditions.

6.5 Acknowledgements

We gratefully acknowledge the financial support by Deutsche Forschungsgemeinschaft (project SCHN 377/18-1). We acknowledge DESY (Hamburg, Germany), a member of the Helmholtz Association HGF, for the provision of experimental facilities. Parts of this research were carried out at beamline P61B (Proposal No. I-20210953) with the support from the Federal Ministry of Education and Research, Germany (BMBF, grants no.: 05K16WC2 & 05K13WC2). Furthermore, we thank Christian Minke for the SEM and EDX measurements.

6.6 References

[1] V. L. Solozhenko, S. N. Dub, N. V. Novikov, *Diam. Relat. Mater.* **2001**, *10*, 2228.

[2] G. Liu, Z. Kou, X. Yan, L. Lei, F. Peng, Q. Wang, K. Wang, P. Wang, L. Li, Y. Li, W. Li, Y. Wang, Y. Bi, Y. Leng, D. He, *Appl. Phys. Lett.* **2015**, *106*, 121901.

[3] N. Dubrovinskaia, V. L. Solozhenko, N. Miyajima, V. Dmitriev, O. O. Kurakevych, L. Dubrovinsky, *Appl. Phys. Lett.* **2007**, *90*, 101912.

[4] A. Zerr, G. Miehe, G.Serghiou, M. Schwarz, E. Kroke, R. Riedel, H. Fueß, P. Kroll, R. Boehler, *Nature* **1999**, *400*, 340.

[5] A. Zerr, M. Kempf, M. Schwarz, E. Kroke, M. Göken, R. Riedel, *J. Am. Ceram. Soc.* **2002**, *85*, 86.

[6] H. Sumiya. *SEI Tech. Rev.* **2012**, *74*, 15.

[7] R. Farla, S. Bhat, S. Sonntag, A. Chanyshev, S. Ma, T. Ishii, Z. Liu, A. Néri, N. Nishiyama, G. A. Faria, T. Wroblewski, H. Schulte-Schrepping, W. Drube, O. Seeck, T. Katsura, *J. Synchrotron Radiat.* **2022**, *29*, 409.

[8] A. Khawam, D. R. Flanagan, *J. Phys. Chem. B* **2006**, *110*, 17315.

[9] V. Erukhimovitch, J. Baram, *Phys. Rev. B* **1994**, *50*, 5854.

[10] V. J. Anderson, H. N. W. Lekkerkerker, *Nature* **2002**, *416*, 811.

[11] A. K. Burnham, R. K. Weese, B. L. A. Weeks, *J. Phys. Chem. B* **2004**, *108*, 19432.

[12] J. Graetz, J. J. Reilly, *J. Phys. Chem. B* **2005**, *109*, 22181.

[13] S. Wang, Q. Gao, J. Wang, *J. Phys. Chem. B* **2005**, *109*, 17281.

[14] B. Cantor, *Philos. Trans. R. Soc. Lond. A* **2003**, *361*, 409.

[15] C. Wu, P. Wang, X. Yao, C. Liu, D. Chen, G. Q. Lu, H. Cheng, *J. Phys. Chem. B* **2005**, *109*, 22217.

[16] V. K. Peterson, D. A. Neumann, R. A. Livingston, *J. Phys. Chem. B* **2005**, *109*, 14449.

[17] L.-C. Sögütoglu, M. Steiger, J. Houben, D. Biemans, H. R. Fischer, P. Donkers, H. Huinink, O. C. G. Adan, *Cryst. Growth Des.* **2019**, *19*, 2279.

[18] R. A. Sullivan, R. J. Davey, G. Sadiq, G. Dent, K. R. Back, J. H. Ter Horst, D. Toroz, R. B. Hammond, *Cryst. Growth Des.* **2014**, *14*, 2689.

[19] K. Hardel, *Angew. Chem. Int. Ed. Engl.* **1972,** *11*, 173.

[20] H. Schäfer, *Angew. Chem. Int. Ed. Engl.* **1971,** *10*, 43.

[21] G. Tammann, F. Westerhold, B. Garre, E. Kordes, H. Kalsing, *Z. Anorg. Allg. Chem.* **1925**, *149*, 21.

[22] W. Jander, *Z. Anorg. Allg. Chem.* **1927**, *163*, 1.

[23] B. Garre, *Z. Anorg. Allg. Chem.* **1927**, *163*, 43.

[24] F. S. Petit, E. H. Randklev, E. J. Felten, *J. Am. Ceram. Soc.* **1966**, *49*, 199.

[25] E. Koch, C. Wagner, *Z. Phys. Chem.* **1936**, *34*, 317.

[26] R. J. Hemley, *Ultrahigh Pressure Mineralogy: Physics and Chemistry of the Earth's Deep Interior*, Vol. 37, The Mineralogical Socienty of America Washington, DC, **1998**.

[27] E. Horvath-Bordon, R. Riedel, A. Zerr, P. F. McMillan, G. Auffermann, Y. Prots, W. Bronger, R. Kniep, P. Kroll, *Chem. Soc. Rev.* **2006**, *35*, 987.

[28] S. D. Kloß, W. Schnick, W. *Angew. Chem. Int. Ed.* **2019**, *58*, 7933.

[29] N. K. Kildahl, N. K. *J. Chem. Educ.* **1995**, *72*, 423.

[30] S. G. Bratsch, *J. Phys. Chem. Ref. Data* **1989**, *18*, 1.

[31] T. Kobayashi, Y. Hirota, *Electron. Lett.* **1982**, *18*, 180.

[32] M. S. Choudhary, J. K. Fink, K. Lederer, H. A. Krässig, *J. Appl. Polym. Sci.* **1987**, *34*, 863.

[33] E.-C. Koch, S. Cudziło, *Angew. Chem. Int. Ed.* **2016**, *55*, 15439.

[34] E. M. Passmore, G. L. Duggan, *J. Illum. Eng. Soc.* **1978**, *7*, 202.

[35] F. Karau, W. Schnick, W. *Angew. Chem. Int. Ed.* **2006**, *45*, 4505.

[36] A. Marchuk, W. Schnick, *Angew. Chem. Int. Ed.* **2015**, *54*, 2383.

[37] W. Schnick, J. Luecke, *Solid State Ion.* **1990**, *38*, 271.

[38] E.-M. Bertschler, C. Dietrich, J. Janek, W. Schnick, *Chem. Eur. J.* **2017**, *23*, 2185.

[39] E.-M. Bertschler, T. Bräuniger, C. Dietrich, J. Janek, W. Schnick, *Angew. Chem. Int. Ed.* **2017**, *56*, 4806.

[40] S. J. Sedlmaier, M. Eberspächer, W. Schnick, *Z. Anorg. Allg. Chem.* **2011**, *637*, 362.

[41] K. Landskron, E. Irran, W. Schnick, *Chem. Eur. J.* **1999**, *5*, 2548.

[42] S. D. Kloss, W. Schnick, *Angew. Chem. Int. Ed.* **2015**, *54*, 11250.

[43] S. Vogel, A. T. Buda, W. Schnick, *Angew. Chem. Int. Ed.* **2018**, *57*, 13202.

[44] L. Eisenburger, V. Weippert, C. Paulmann, D. Johrendt, O. Oeckler, W. Schnick, *Angew. Chem. Int. Ed.* **2022**, *61*, e202202014.

[45] A. Marchuk, F. J. Pucher, F. W. Karau, W. Schnick, *Angew. Chem. Int. Ed.* **2014**, *53*, 2469.

[46] S. Wendl, L. Seidl, P. Schüler, W. Schnick, *Angew. Chem. Int. Ed.* **2020**, *59*, 23579.

[47] S. Wendl, W. Schnick, *Chem. Eur. J.* **2018**, *24*, 15889.

[48] Y. Hinuma, T. Hatakeyama, Y. Kumagai, L. A. Burton, H. Sato,Y. Muraba, S. Iimura, H. Hiramatsu, I. Tanaka, H. Hosono, F. Oba, *Nat. Commun.* **2016**, *7*, 11962.

[49] A. Stock, H. Grüneberg, *Ber. Dtsch. Chem. Ges.* **1907**, *40*, 2573.

[50] A. Aizawa, A. Yoneda, *Phys. Earth Planet. Inter.* **2006**, *155*, 87.

[51] Oxford Instruments. *AZtecEnergy*, Abington, **2016**.

[52] R. Juza, A. Neuber, H. Hahn, *Z. Anorg. Allg. Chem.* **1938**, *239*, 273.

[53] J. B. Mann, T. L. Meek, L. C. Allen, *J. Am. Chem. Soc.* **2000**, *122*, 2780.

[54] M. Fanfoni, M. Tomellini, *Il Nuovo Cimento D* **1998**, *20*, 1171.

Chapter 7

Summary

The research objective of this cumulative dissertation thesis focused on two main topics. On the one hand, fundamental explorative research was conducted to expand the number of known 3rd and 4th main group nitridophosphates, including the thorough characterization of novel compounds. On the other hand, the formation mechanism of nitridophosphates under high-pressure high-temperature conditions was examined.

Within the first part that is covered by Chapters 2 – 5, five novel 3rd and 4th main group nitridophosphates were prepared and analyzed: MP_6N_{11} (*M* = Al, In), GeP_2N_4, $GePN_3$, and $Sn_3P_8N_{16}$. To prevent the tendency for thermal decomposition of nitridophosphates, releasing molecular N_2, all syntheses were carried out under high-pressure high-temperature conditions, following Le Chatelier's principle. The corresponding reaction conditions were achieved using a 1000 t large-volume press, with the exception of $GePN_3$, which was synthesized in a diamond anvil cell. Unprecedented structural features and structure types, elucidated from single-crystal XRD data combined with various spectroscopic methods and theoretical calculations provided intriguing insights into the structural chemistry of nitridophosphates. More detailed information on the respective publications is provided on the next pages in individual brief summary sections.

The second part of this thesis that is covered by Chapter 6, provided the first *in-situ* insight into a high-pressure high-temperature nitridophosphate reaction. The synthesis of Zn_2PN_3 via the nitride route was monitored using the large-volume press at beam line P61B at DESY. Implications of the results on the currently proposed reaction mechanisms were discussed, with a brief summary of the publication given later in this chapter.

7.1 Combining MN_6 Octahedra and PN_5 Trigonal Bipyramids in the Mica-like Nitridophosphates MP_6N_{11} (M = Al, In)

Sebastian J. Ambach, Monika Pointner, Sophie Falkai, Carsten Paulmann, Oliver Oeckler, Wolfgang Schnick, *Angew. Chem. Int. Ed.* **2023**, *62*, e202303580.

https://doi.org/10.1002/anie.202303580

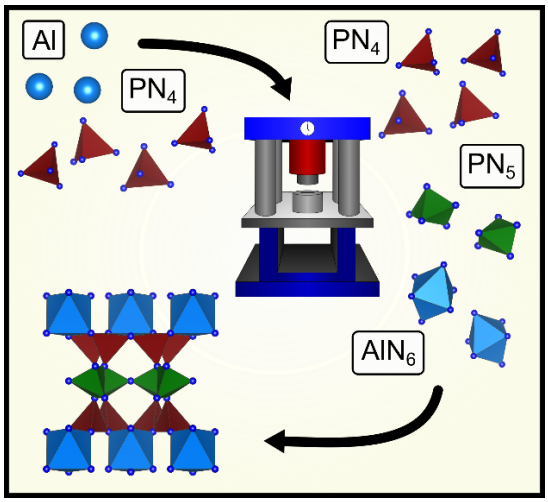

Layered silicates are a very versatile class of materials with high importance to humanity. The new nitridophosphates MP_6N_{11} (M = Al, In), synthesized from MCl_3, P_3N_5 and NH_4N_3 in a high-pressure high-temperature reaction at 1100 °C and 8 GPa, show a mica-like layer setup and feature rare nitrogen coordination motifs. The crystal structure of AlP_6N_{11} was elucidated from synchrotron single-crystal diffraction data (space group *Cm* (no. 8), a = 4.9354(10), b = 8.1608(16), c = 9.0401(18) Å, β = 98.63(3)°), enabling Rietveld refinement of isotypic InP_6N_{11}. It is built up from layers of PN_4 tetrahedra, PN_5 trigonal bipyramids and MN_6 octahedra. PN_5 trigonal bipyramids have been reported only once and MN_6 octahedra are sparsely found in the literature. AlP_6N_{11} was further characterized by energy-dispersive X-ray (EDX), IR and NMR spectroscopy. Despite the vast amount of known layered silicates, there is no isostructural compound to MP_6N_{11} as yet.

7.2 Structural Influence of Lone Pairs in GeP_2N_4, a Germanium(II) Nitridophosphate

Sebastian J. Ambach, Cody Somers, Tristan do Boer, Lucien Eigenburg, Alexander Moewes, Wolfgang Schnick, *Angew. Chem. Int. Ed.* **2023**, *62*, e202215393.

https://doi.org/10.1002/anie.202215393

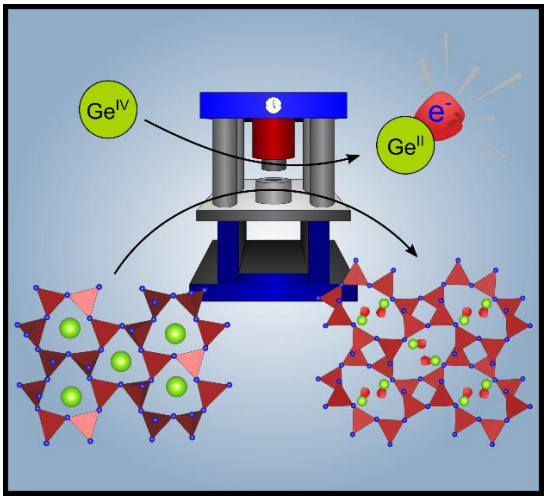

Owing to their widespread properties, nitridophosphates are of high interest in current research. Explorative high-pressure high-temperature investigations yielded various compounds with stoichiometry MP_2N_4 (M = Be, Ca, Sr, Ba, Mn, Cd), which are discussed as ultra-hard or luminescent materials, when doped with Eu^{2+}. Herein, we report the first germanium nitridophosphate, GeP_2N_4, synthesized from Ge_3N_4 and P_3N_5 at 6 GPa and 800 °C. The structure was determined by single-crystal X-ray diffraction and further characterized by energy-dispersive X-ray spectroscopy, density functional theory calculations, IR and NMR spectroscopy. The highly condensed network of PN_4-tetrahedra shows a strong structural divergence to other MP_2N_4 compounds, which is attributed to the stereochemical influence of the lone pair of Ge^{2+}. Thus, the formal exchange of alkaline earth cations with Ge^{2+} may open access to various compounds with literature-known stoichiometry, however, new structures and properties.

7.3 Building Nitridic Networks with Phosphorus and Germanium – from $Ge^{II}P_2N_4$ to $Ge^{IV}PN_3$

Sebastian J. Ambach, Georg Krach, Elena Bykova, Kristian Witthaut, Nico Giordano, Maxim Bykov, Wolfgang Schnick, *Inorg. Chem.* **2024**, 63, 8502.

https://doi.org/10.1002/acs.inorgchem.4c01202

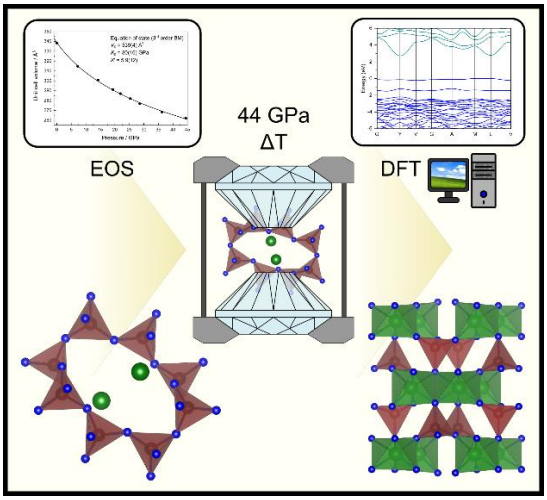

Nitridophosphates and nitridogermanates attract high interest in current research due to their structural versatility. Herein, the elastic properties of GeP_2N_4 were investigated by single-crystal X-ray diffraction (XRD) upon compression to 44.4(1) GPa in a diamond anvil cell. Its isothermal bulk modulus was determined to be 82(6) GPa. At 44.4(1) GPa, laser heating resulted in the formation of multiple crystalline phases, one of which was identified as the unprecedented germanium nitridophosphate $GePN_3$. Its structure was elucidated from single-crystal XRD data (*C*2/*c* (no. 15), *a* = 8.666(5), *b* = 8.076(4), *c* = 4.691(2) Å, *β* = 101.00(7)°) and is built up from layers of GeN_6 octahedra and PN_4 tetrahedra. The GeN_6 octahedra form double zigzag chains, while the PN_4 tetrahedra are found in single zigzag chains. $GePN_3$ can be recovered to ambient conditions with a unit cell volume increase of about 12%. It combines P^V and Ge^{IV} in a condensed nitridic network for the first time.

7.4 Mixed Tin Valence in the Tin(II/IV)-Nitridphosphate $Sn_3P_8N_{16}$

Sebastian J. Ambach, Aylin Koldemir, Kristian Witthaut, Sandra Kreiner, Thomas Bräuniger, Rainer Pöttgen, Wolfgang Schnick, *Chem. Eur. J.* **2024**, *accepted*.

https://doi.org/10.1002/chem.202401428

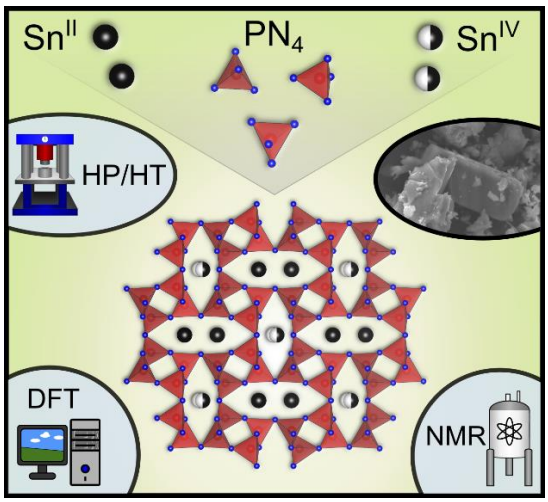

$Sn_3P_8N_{16}$ combines the structural versatility of nitridophosphates and Sn within one compound. It was synthesized as dark gray powder in a high-pressure high-temperature reaction at 800 °C and 6 GPa from Sn_3N_4 and P_3N_5. The crystal structure was elucidated from single-crystal diffraction data (space group *C*2/*m* (no. 12), a = 12.9664(4), b = 10.7886(4), c = 4.8238(2) Å, β = 109.624(1)°) and shows a 3D-network of PN_4 tetrahedra, incorporating Sn in oxidation states +II and +IV. The Sn cations are located within eight-membered rings of vertex-sharing PN_4 tetrahedra, stacked along the [001] direction. A combination of solid-state nuclear magnetic resonance spectroscopy, ^{119}Sn Mössbauer spectroscopy and density functional theory calculations was used to confirm the mixed oxidation of Sn. Temperature-dependent powder X-ray diffraction measurements reveal a low thermal expansion of 3.6 ppm/K up to 750 °C, beyond which $Sn_3P_8N_{16}$ starts to decompose.

7.5 Nitride Synthesis Under High-Pressure High-Temperature Conditions – Unprecedented *in-situ* Insight into the Reaction

Sebastian J. Ambach, Reinhard M. Pritzl, Shrikant Bhat, Robert Farla, Wolfgang Schnick, *Inorg. Chem.* **2024**, 63, 3535.

https://doi.org/10.1021/acs.inorgchem.3c04433

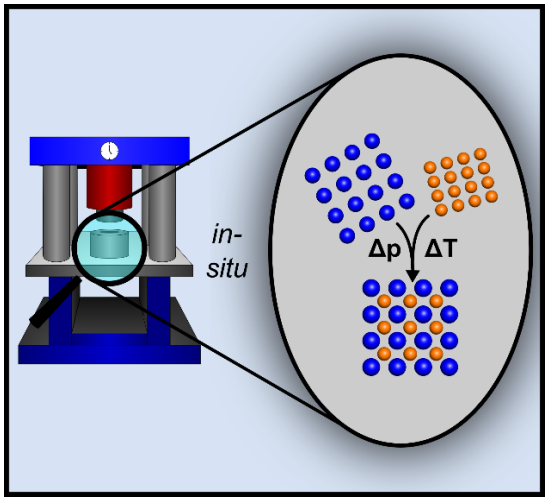

High-pressure high-temperature (HP/HT) syntheses are essential for modern high-performance materials. Phosphorus nitride, nitridophosphate and more generally nitride syntheses benefit greatly from HP/HT conditions. In this contribution, we present the first systematic *in-situ* investigation of a nitridophosphate HP/HT synthesis, using the reaction of zinc nitride Zn_3N_2 and phosphorus(V)nitride P_3N_5 to the nitride semiconductor Zn_2PN_3 as a case study. At a pressure of 8 GPa and temperatures up to 1300 °C the reaction was monitored by energy-dispersive powder X-ray diffraction (ED-PXRD) in a large-volume press at beamline P61B at DESY. The experiments investigate the general behavior of the starting materials under extreme conditions and give insight into the reaction. During cold-compression and subsequent heating the starting materials remain crystalline above their ambient-pressure decomposition point, until a sufficient minimum temperature is reached and the reaction starts. The reaction proceeds via ion diffusion at grain boundaries with an exponential decay of the reaction rate. Raising the temperature above the minimum required value quickly completes the reaction and initiates single crystal growth. After cooling and decompression, which did not influence the resulting product, the recovered sample was analyzed by EDX-spectroscopy.

Chapter 8

Discussion and Outlook

The first part of this thesis (Chapters 2 – 5) focused on the explorative high-pressure high-temperature syntheses of new 3rd and 4th main group nitridophosphates. Five novel compounds were introduced: AlP_6N_{11}, InP_6N_{11}, GeP_2N_4, $GePN_3$ and $Sn_3P_8N_{16}$, significantly expanding the previously 9 known compounds of this space to a total of 14. Section 8.1 summarizes the key characteristics of each compound in the context of previous research and highlights the most important advancements made in this thesis.

The second part (Chapter 6) presented the first *in-situ* study of a high-pressure high-temperature nitridophosphate synthesis. Section 8.2 discusses previously proposed high-pressure high-temperature mechanistic ideas in the light of the unprecedented insights and points out new opportunities made possible by this thesis.

8.1 Progress in 3rd and 4th Main Group Nitridophosphates

3rd and 4th main group nitridophosphates should in theory show manifold structure types with intriguing materials properties due to the combined versatility of the anionic nitridophosphate network with the respective cations. Contrary to this expected abundance of materials, prior to this thesis only 9 compounds were known: *α*- and *β*-BP_3N_6, $AlP_6O_{3x}(NH)_{3-3x}N_9$, *AE*$AlP_8N_{15}(NH)$ (*AE* = Ca, Sr, Ba), $SrAl_5P_4N_{10}O_2F_3$, $Ga_{16/3}P_{12}N_{24}O_2$, $SiPN_3$, $SiP_2N_4(NH)$, and $Sn_6[P_{12}N_{24}]$.[1–9]

After the successful synthesis of a novel compound over the course of this thesis, the initial interest was its structure elucidation by single-crystal X-ray diffraction to identify unprecedented structural features. Afterwards, the characterization was completed by a multitude of analytic methods and theoretical calculations, such as NMR, IR, and Mössbauer spectroscopy as well as CHARDI, BVS, MBE, DFT, and ELF calculations.

The first presented compounds in this thesis, namely MP_6N_{11} (*M* = Al, In), show a layered structural setup closely related to the silicate mica class. Due to the isoelectronic combination of elements Si/O and P/N, one would expect structures and layer setups comparable to those of oxosilicates. Although layered nitridophosphates in general are already known, such as $MH_4P_6N_{12}$ (*M* = Mg, Ca) or MP_8N_{14} (*M* = Ca, Sr, Ba), only one nitridic mica analog has been reported thus far, namely *AE*$Si_3P_4N_{10}(NH)_2$ (*AE* = Mg, Ca, Sr).[10–12] In most other cases, the layered nitridophosphate structures do not resemble layered silicate structures and rather represent a structure type on their own.

This divergence may be charge related: The conceptual transformation of an oxosilicate to the isostructural nitridophosphate involves in a first step the replacement of the SiO_4 tetrahedra layer with the corresponding layer of PN_4 tetrahedra. This poses an electrostatic challenge to the layer of counter-cations, as the $[PN_4]^{7-}$ tetrahedra are higher charged than $[SiO_4]^{4-}$ tetrahedra. In order to retain the oxosilicate stacking sequence, higher charged cations are necessary between the layers of tetrahedra. In case of the known $AESi_3P_4N_{10}(NH)_2$ (*AE* = Mg, Ca, Sr), this results in layers of AE^{2+} and Si^{4+} cations, in the case of MP_6N_{11} (*M* = Al, In), layers of M^{3+} and P^{5+} cations are found.[12] While the M^{3+} cations show a typical octahedral coordination as MN_6 octahedra, P^{5+} forms an unprecedented motif of interconnected PN_5 trigonal bipyramids. Having understood the necessity of highly charged cations in between layers of tetrahedra, further investigations will most likely bring to light a multitude of new layered silicate analog materials. Considering the current importance of silicate clay minerals in areas such as soils, absorbants, pharmaceuticals, pottery and feeds, some newly discovered materials will most likely find use in everyday applications.[13–17]

While the general field of germanium in nitrides is sparsely investigated and understood, but populated with a few compounds, Chapters 3 and 4 introduced a new class of materials: germanium nitridophosphates.

Germanium stands out with its ability to exist in oxidation state +II or +IV and also to undergo redox reactions during syntheses. As known from literature and Chapters 3 and 4, the behavior of germanium in nitrides appears to be pressure-dependent. At ambient pressure and in the low pressure range, e.g., in ampoule syntheses, nitridogermanates with GeN_4 tetrahedra as the structural unit are preferentially formed. In a pressure range starting at a few gigapascals, in experiments of this work at least 3 GPa, germanium is present in the oxidation state +II. Various experiments have shown that both the oxidation of elemental Ge^0 and the reduction of Ge^{IV} to Ge^{II} can take place. In addition, the necessity of a reaction temperature of 800 °C, which is already known from various nitridogermanates, has emerged.[18] Lower temperatures lead to incomplete reactions and higher temperatures already decompose the formed product. This temperature dependence seems to be canceled at extreme pressures >40 GPa, as observed in Chapter 4. In addition, the previously preferred oxidation state +II no longer appears to be stable and an oxidation to Ge^{IV} takes place.

The knowledge of the existence of Ge^{II} at moderate pressures opens up an extremely large scope for structural modifications. As shown in the case of GeP_2N_4 (Chapter 3), divalent cations can be formally replaced by Ge^{II}. The presence of the Ge^{II} lone pair and its space requirements can be used to influence the respective crystal structure. In the example presented in this thesis, instead of a structure related to the megacalsilite type, typical for MP_2N_4 compounds (*M* = Ca, Sr, Mn, Cd), the paracelsian structure type is obtained for GeP_2N_4.[19,20] In theory, this approach can be transferred to all nitridophosphates with divalent

cations. Initial unpublished experiments carried out over the course of this work already suggest that the formal exchange is regularly successful. To systematize and better understand the structural influence of the Ge^{II} lone pair, future studies comparing structures before and after the formal substitution of Ge^{II} seem promising.

While in the case of GeP_2N_4, a previously unknown coordination of Ge^{II}, GeN_3 trigonal pyramids with Ge^{II} at the apex, were observed, $GePN_3$ shows an already known coordination for Ge^{IV}: GeN_6 octahedra. However, the octahedral coordination of germanium by nitrogen has only been described once in the high-pressure modification of the germanium nitride Ge_3N_4, which is why this structural motif could be an indication of a high-pressure phase.[21] It can therefore be assumed that a normal pressure modification of $GePN_3$ also exists, possibly isostructural to $SiPN_3$. Furthermore, $GePN_3$ shows that Ge^{IV} and P^{V} can coexist as polyhedral centers within the same compound. This is promising for future experiments, targeting germanium phosphorus nitrides, which have mixed networks of GeN_4 and PN_4 tetrahedra. Due to the formal combination of nitridogermanates and nitridophosphates, this class of compounds could show unprecedented structural motifs and therefore possibly intriguing materials properties.

An analogous behavior to germanium nitridophosphates can be seen in tin nitridophosphates. Here, too, it is possible to observe tin in the oxidation states +II and +IV. In $Sn_3P_8N_{16,}$ presented in this work, it was even possible to have both oxidation states present in parallel. Systems with mixed-valence cations, e.g., the Sn/S system, are the subject of current investigations with regard to extraordinary electronic properties.[22] In general, tin-based compounds also exhibit desirable electronic properties, especially in the field of catalysis and photovoltaics. As already discussed for germanium, it is certainly possible to specifically substitute divalent cations with Sn^{2+} in order to bring changes in structure and properties. The literature-known zeolite-like $Sn_6[P_{12}N_{24}]$ already indicates a possible application: Sn^{II}, which protrudes into the pores of the zeolite structure, could act as an active catalytic center.[9]

8.2 Insight into a Reaction Mechanism

The insight into the reaction of P_3N_5 and Zn_3N_2 to Zn_2PN_3 in Chapter 6 has shown that nitride reactions under high-pressure high-temperature conditions proceed via ion diffusion at grain boundaries. This mechanism works analogously to reactions at normal pressure, where it has been extensively studied, e.g., for the formation of $NiAl_2O_4$.[23] Mechanistically, the reaction starts at a reactant-specific temperature at which ions of one reactant diffuse into the other reactant, or both reactants simultaneously into each other. As the result, a layer of product is formed that grows over time, which in turn lengthens the diffusion paths. Depending on the product layer thickness and provided the temperature remains constant, the reaction rate

decreases until a virtual standstill. Increasing the temperature enables longer ion diffusion paths, which allows the reaction to progress further. It can be assumed that the lower the charge of the ions and the more ionic the respective reactant, the easier the diffusion takes place. In the case of the investigated reaction of P_3N_5 and Zn_3N_2, it is likely that Zn^{2+} and N^{3-} ions of the zinc nitride preferentially diffuse into P_3N_5, which has P-N bonds with a significant covalent character and P^{5+} cations with a high charge.

Based on these findings, the previous high-pressure high-temperature synthetic routes and mechanistic concepts of nitridophosphates can now be discussed more diversely:

In general, a large number of individual grains with a high surface area and a small diameter in the reactant mixture favors a fast and uniform reaction. The following criteria should be taken into account when selecting a reactant:

- Structural units with covalent bonds or highly charged ions are preferably retained in the product.
- Ion diffusion and the overall reaction is facilitated by ionic starting materials with ions of a low charge
- Amorphous or partially amorphous starting materials facilitate ion diffusion and therefore the reaction
- Reactants should have a low temperature threshold at which ion diffusion begins
- High reaction temperatures may enable the cleavage of more covalent bonds and the diffusion of higher charged ions.

The nitride route, which was subject of the investigation in this thesis, will presumably proceed exclusively according to the ion diffusion mechanism. The synthesis of AlP_6N_{11} from $AlCl_3$, P_3N_5, and NH_4N_3 shall be briefly discussed here as an example. As described in Chapter 2, the synthesis using AlN does not succeed, whereas the synthesis with $AlCl_3$ does. This can be explained by the fact that Al−Cl bonds have a significantly more ionic character than Al−N bonds and, in addition, Cl^- has a lower charge than N^{3-}, which facilitates diffusion. Furthermore, AlP_6N_{11} contains PN_4 tetrahedra as a structural unit, which can be seen as retained from the more covalent P_3N_5. Al^{3+} from the more ionic $AlCl_3$, on the other hand, is found in a new, octahedral coordination.

Flux-based synthesis strategies such as high-pressure metathesis, the Li_3N self-flux method or the addition of NH_4Cl as a mineralizer facilitate ion diffusion, especially across more distant grain boundaries with the generated ionic flux. This should result in larger single crystals being formed in the product on the one hand, and lower temperatures being required for the synthesis on the other.

Synthetic approaches that use *in-situ* generated HCl or HF also benefit from a better understanding. As already suggested in literature, starting materials such as BN or TiN, which

under normal conditions have bonds with a significant covalent character and simultaneously a high ionic charge, both unfavorable for ion diffusion, initially react with HCl and HF to intermediate species.[1,24] The resulting halides usually show a significantly higher ionicity in their bonds, which in turn facilitates ion diffusion and enables the reaction.

The only more detailed reaction mechanism proposed by Wendl *et al.*, however, seems unlikely in the proposed form, considering the new mechanistic insights.[25] The proposal implies that in a reaction of $Sr(N_3)_2$, P_3N_5 and HPN_2, the imidonitridophosphate $SrH_4P_6N_{12}$ is formed as an intermediate, which then reacts to SrP_8N_{14} by replacing the NH groups with PN_4 tetrahedra. In this case, P^V would have to occur as a mobile species during ion diffusion, which seems unlikely. Since $SrH_4P_6N_{12}$ and SrP_8N_{14} have a very similar elemental composition, it appears more likely that the ion diffusion process occurs with Sr^{2+}, H^+ and possibly N^{3-}, formed *in-situ* from $Sr(N_3)_2$, as mobile species. Depending on the stoichiometric ratio in which the respective ions are present locally, one or the other compound is preferentially formed. Over the entire reaction mixture, it is therefore likely that both compounds are observed side by side.

With a new understanding of the individual synthesis routes for nitridophosphates, reactions can now be carried out in a much more targeted manner than in purely explorative experiments. A well-considered selection of reactants and their structural features, the reaction route and reaction conditions offer increased control over the actual reaction and thus the resulting products.

8.3 Concluding synopsis

The aim of this work was the fundamental exploration of possibilities for syntheses of novel materials with increased control over their structural features. Although some unprecedented synthetic approaches have been established for the compounds presented in the first chapters, there is still plenty of room for further exploratory research. Combining the concepts for 3rd and 4th main group nitridophosphates developed in this thesis with the insights into high-pressure high-temperature reactions provides a comprehensive basis for future research projects.

8.4 References

[1] S. Vogel, A. T. Buda, W. Schnick, *Angew. Chem. Int. Ed.* **2018**, *57*, 13202.

[2] S. Vogel, M. Bykov, E. Bykova, S. Wendl, S. D. Kloß, A. Pakhomova, S. Chariton, E. Koemets, N. Dubrovinskaia, L. Dubrovinsky, W. Schnick, *Angew. Chem. Int. Ed.* **2019**, *58*, 9060.

[3] L. Neudert, F. Heinke, T. Bräuniger, F. J. Pucher, G. B. Vaughan, O. Oeckler, W. Schnick, *Chem. Commun.* **2017**, *53*, 2709.

[4] M. M. Pointner, O. Oeckler, W. Schnick, *Chem. Eur. J.* **2023**, *29*, e202301960.

[5] M. M. Pointner, R. M. Pritzl, J. M. Albrecht, L. Blahusch, J. P. Wright, E. L. Bright, C. Giacobbe, O. Oeckler, W. Schnick, *Chem. Eur. J.* **2024**, e202400766.

[6] D. Günther, L. Eisenburger, W. Schnick, O. Oeckler, *Z. Anorg. Allg. Chem.* **2022**, *648*.

[7] H. P. Baldus, W. Schnick, J. Luecke, U. Wannagat, G. Bogedain, *Chem. Mater.* **1993**, *5*, 845.

[8] S. Vogel, A. T. Buda, W. Schnick, *Angew. Chem. Int. Ed.* **2019**, *58*, 3398.

[9] F. J. Pucher, C. Frhr. von Schirnding, F. Hummel, V. R. Celinski, J. Schmedt auf der Günne, B. Gerke, R. Pöttgen, W. Schnick, *Eur. J. Inorg. Chem.* **2015**, *2015*, 382.

[10] A. Marchuk, V. R. Celinski, J. Schmedt auf der Günne, W. Schnick, *Chem. Eur. J.* **2015**, *21*, 5836.

[11] S. Wendl, L. Eisenburger, P. Strobel, D. Günther, J. P. Wright, P. J. Schmidt, O. Oeckler, W. Schnick, *Chem. Eur. J.* **2020**, *26*, 7292.

[12] L. Eisenburger, P. Strobel, P. J. Schmidt, T. Bräuniger, J. Wright, E. L. Bright, C. Giacobbe, O. Oeckler, W. Schnick, *Angew. Chem. Int. Ed.* **2022**, *61*, e202114902.

[13] G. K. Kome, R. K. Enang, F. O. Tabi, B. Palmer, K. Yerima, *Open J. Soil Sci.* **2019**, *9*, 155.

[14] H. Tao, X. Qian, Y. Zhou, H. Cheng, *Renew. Sustain. Energy Rev.* **2022**, *164*, 112536.

[15] I. S. Khurana, S. Kaur, H. Kaur, R. K. Khurana, *Future Sci. OA* **2015**, *1*, 2056.

[16] V. A. Drebushchak, L. N. Mylnikova, T. N. Drebushchak, V. V. Boldyrev, *J. Therm. Anal. Calorim.* **2005**, *82*, 617.

[17] M. Nadziakiewicza, S. Kehoe, P. Micek, *Animals* **2019**, *9*, 714.

[18] J. Häusler, L. Eisenburger, O. Oeckler, W. Schnick, *Eur. J. Inorg. Chem.* **2018**, *2018*, 759.

[19] F. J. Pucher, A. Marchuk, P. J. Schmidt, D. Wiechert, W. Schnick, *Chem. Eur. J.* **2015**, *21*, 6443.

[20] F. J. Pucher, F. W. Karau, J. Schmedt auf der Günne, W. Schnick, *Eur. J. Inorg. Chem.* **2016**, *2016*, 1497.

[21] G. Serghiou, G. Miehe, O. Tschauner, A. Zerr, R. Boehler, *J. Chem. Phys.* **1999**, *111*, 4659.

[22] X. Wang, Z. Liu, X.-G. Zhao, J. Lv, K. Biswas, L. Zhang, *ACS Appl. Mater. Interfaces* **2019**, *11*, 24867.

[23] F. S. Pettit, E. H. Randklev, E. J. Felten, *J. Am. Ceram. Soc.* **1966**, *49*, 199.

[24] L. Eisenburger, V. Weippert, C. Paulmann, D. Johrendt, O. Oeckler, W. Schnick, *Angew. Chem. Int. Ed.* **2022**, *61*, e202202014.

[25] S. Wendl, W. Schnick, *Chem. Eur. J.* **2018**, *24*, 15889.

Chapter 9

Appendix

9.1 Supporting Information for Chapter 2

Experimental Procedures

Preparation of Starting Materials

Phosphorus(V) nitride P_3N_5 was prepared as partially crystalline powder according to Stock *et al.* from P_4S_{10} (Acros Organics, >98%) and NH_3 (Air Liquide, 99.999%).[1] The purity of the orange product was confirmed by powder X-ray diffraction and CHNS-analysis (C: 0%, H: 0%, N: 43.16, S: 0%; expected C: 0%, H: 0%, N: 42.98%, S: 0%).

NH_4N_3 was prepared from NaN_3 (Acros Organics, 99%) and NH_4NO_3 (Grüssing, 99%) following a procedure by Frierson.[2] The purity of the colorless, crystalline product was confirmed by FTIR spectroscopy and PXRD.

$AlCl_3$ (Sigma-Aldrich, 99.999%) and $InCl_3$ (Sigma-Adrich, 99.999%) were used as purchased.

High-Pressure High-Temperature Syntheses

High-pressure high-temperature syntheses were carried out in a hydraulic 1000 t press using the multianvil technique with a modified Walker-type module.[3–5] Nonstoichiometric amounts of P_3N_5, NH_4N_3 and $AlCl_3$ (Table S1) were thoroughly ground in an agate mortar. The powder was tightly packed into an h-BN crucible, which was closed with a small lid of the same material. The crucible was surrounded by two graphite heaters of different lengths, centered by MgO spacers, and subsequently placed into a ZrO_2 sleeve. The sleeve was closed with two Mo disks, each at the top and bottom and centered in a pierced octahedron (MgO, doped with 5% Cr_2O_3). The assembly was compressed by eight electrically isolated WC cubes (doped with 7% Co, 11 mm edge length, Haewdia, Marklkofen) with truncated edges (truncated edge length 11 mm). More information on the setup of the assembly can be found in literature.[5]

For both reactions, the sample was compressed to 8 GPa in 240 min and heated to 1100 °C within 60 min. The temperature was hold for 4 h and subsequently cooled down to ambient temperature within 60 min. After decompression within 600 min, the sample was recovered from all assembly parts and washed with de-ionized water to remove any residual chlorides. All samples of MP_6N_{11} (*M* = Al, In) were obtained as light gray powders and are stable against air and moisture.

Table S1.1: Weigh-in of starting materials for the syntheses of MP_6N_{11} (M = Al, In).

Compound	MCl_3 (M = Al, In)	P_3N_5	NH_4N_3
AlP_6N_{11}	17.2 mg, 0.13 mmol, 1 eq.	42.0 mg, 0.26 mmol, 2 eq.	0.8 mg, 0.01 mmol, 0.1 eq.
InP_6N_{11}	31.7 mg, 0.15 mmol, 1 eq.	46.7 mg, 0.29 mmol, 2 eq.	0.9 mg, 0.01 mmol, 0.1 eq.

Single-Crystal X-Ray Diffraction

Single-crystal diffraction data with synchrotron radiation at ambient conditions were collected at beamline P24 (DESY, Hamburg). Combined φ- and ω-scans were measured with a wavelength of λ = 0.5000 Å using a Pilatus 1M CdTe detector. Indexing and integration were performed with the CrysAlis^{PRO} software package.[6] Semi-empirical absorption correction was done with SADABS.[7] The structure was solved by direct methods using SHELX-2018 (refined against $|F|^2$ by a full-matrix least-squares method).[8,9] Results were visualized using Diamond and VESTA.[10,11]

Powder X-ray Diffraction and Rietveld Refinement

Powder X-ray diffraction patterns were measured on a STOE Stadi P diffractometer (STOE & Cie GmbH, Darmstadt) with Cu-Kα_1 (λ = 1.5406 Å) radiation, a MYTHEN 1K strip detector and a Ge(111)-monochromator in Debye-Scherrer geometry. The sample was packed into a glass capillary with an outer diameter of 0.3 mm and rotated during measurement.

Diffraction patterns were refined using the Rietveld method with TOPAS academic.[12,13] Peak profiles were fitted using the fundamental parameter approach.[14,15] The background was modeled by a shifted Chebyshev polynomial and preferred crystal orientation was described by spherical harmonics of fourth order. For Rietveld refinement of InP_6N_{11} initially the structure model of AlP_6N_{11} was used.

Temperature-Dependent Powder X-Ray Diffraction

Temperature dependent powder X-ray diffraction patterns were measured on a STOE Stadi P diffractometer (STOE & Cie GmbH, Darmstadt, Mo-Kα_1 radiation (λ = 0.71073 Å), Ge(111)-monochromator, IP-PSD detector) equipped with a resistance graphite furnace (STOE & Cie GmbH). The ground samples were sealed in a silica glass capillary (Hilgenberg, Malsfeld) with an outer diameter of 0.3 mm, heated from 50 °C to 900 °C in steps of 50 °C and subsequently cooled down to ambient temperature in steps of 100 °C, each with a rate of 10 °C/min. At every step, a diffraction pattern was measured within 1 h at constant temperature.

Scanning Electron Microscopy and Energy-Dispersive X-Ray Spectroscopy

For chemical analysis, samples were prepared on a self-adhesive carbon foil and coated with a small layer of carbon (electron beam evaporator, BAL-TEC MED 020, BalTec AG, Pfäffikon). Measurements were done at an acceleration voltage of 10 kV with a Helios Nanolab G3 UC DualBeam (FEI, Hilsboro), equipped with an X-Max 80 SSD detector (Oxford Instruments, Abingdon). Data were collected and processed using the AZtec software.[16]

Transmission Electron Microscopy

Transmission electron microscope analysis was carried out with a Titan Themis 300 (FEI, Hilsboro) equipped with a Cs DCOR Probe-Corrector, a X-FEG, a post-column filter (Enfinium ER-799), a US1000XP/FT camera system, and a windowless, 4-quadrant Super-X EDX detector. Brightfield images were recorded using a 4k × 4k FEI Ceta CMOS camera. The microscope was operated at 300 kV accelerating voltage.

Solid State Magic-Angle Spinning Nuclear Magnetic Resonance Spectroscopy

Solid-state MAS NMR spectra were recorded on an Advance III 500 (Bruker, Karlsruhe) equipped with an 11.7 T magnet operating at 500.25 MHz ^{1}H frequency and a commercial double resonance MAS probe. For measurement, the sample was ground and packed into a ZrO_2 rotor with an outer diameter of 2.5 mm. ^{1}H, ^{27}Al, ^{31}P and ^{31}P{^{1}H} spectra were collected at 20 kHz spinning frequency.

Fourier Ttransform Infrared Spectroscopy

The FTIR spectrum of AlP_6N_{11} was measured on a Spectrum BX II spectrometer (Perkin Elmer, Waltham, MA, USA) with a DuraSampler device in attenuated total reflection (ATR) mode.

Charge Distribution and Bond-Valence-Sum Calculations

CHARDI values were performed using VESTA.[11] Bond-valence-sum calculations were bone with the VaList software.[17,18]

Minimal Bonding Ellipsoid Calculations

Minimal bonding ellipsoids were calculated using the software PIEFACE.[19]

Results and Discussion

Energy-Dispersive X-Ray Spectroscopy

Several crystallites in samples of MP_6N_{11} (M = Al, In) were used for EDX data collection. No other elements than M, P, N and O were detected. The presence of O may be explained by surface hydrolysis of the microcrystalline powders. Within the precision of EDX measurements, experimental and calculated values are in good agreement.

Table S1.2: Results of EDX measurements of AlP_6N_{11}. Results are given in atomic percent with standard deviations in parentheses.

	1	2	3	4	5	Ø	Norm. (Al)
Al	5	5	6	5	5	5(1)	1
P	32	29	45	29	27	32(7)	6.2(14)
N	53	54	43	58	64	54(8)	10.5(15)
O	10	12	6	8	4	8(3)	1.5(6)

Table S1.3: Results of EDX measurements of InP_6N_{11}. Results are given in atomic percent with standard deviations in parentheses.

	1	2	3	4	5	Ø	Norm. (In)
In	5	4	5	3	4	4(1)	1
P	35	30	29	22	32	29(5)	7.0(11)
N	40	41	59	66	45	50(11)	12.0(27)
O	20	25	7	9	19	16(7)	3.8(18)

Crystallographic Data

Table S1.4: Crystallographic data of AlP_6N_{11} from single-crystal refinement. Standard deviations are given in parentheses.

Formula	**AlP_6N_{11}**
Crystal system	monoclinic
Space group	*Cm* (no. 8)
a	4.9354(10)
b	8.1608(16)
c	9.0401(18)
β	98.63(3)
Cell volume / Å^3	359.98(13)
Formula units per unit cell	2
Calculated X-ray density / g·cm^{-3}	3.385
Molar mass / g·mol^{-1}	366.91
μ / mm^{-1}	0.594
Temperature / K	293(2)
Absorption correction	Semiempirical[7]
Radiation	Synchrotron, DESY P24 (λ = 0.50000 Å)
F(000)	360
θ range / °	$3.2 \leq \theta \leq 40.6$
Total no. of reflections	3060
Independent reflections	2392
R_{int} / R_σ	0.0556 / 0.0458
Refined parameters / Restraints	88 / 2
Goodness of fit	1.057
R-values [I≥2σ(I)]	R_1 = 0.0340; wR_2 = 0.0887
R-values (all data)	R_1 = 0.0498; wR_2 = 0.0956
$\Delta\rho_{max}$, $\Delta\rho_{max}$ / e·Å^3	1.037, −0.936

Table S1.5: Wyckoff position, coordinates, equivalent thermal displacement parameters and occupancy of AlP_6N_{11} from single-crystal refinement. Standard deviations are given in parentheses.

Atom	Wyck.	*x*	*y*	*z*	U_{eq}	*occ.*
Al1	2*a*	0.4212(12)	0	0.1588(7)	0.01665(17)	1
P1	4*b*	0.00449(11)	0.17273(16)	0.36195(8)	0.0064(3)	1
P2	4*b*	0.34018(9)	0.32607(17)	0.95666(7)	0.0064(3)	1
P3	4*b*	0.4232(5)	0.18865(5)	0.6602(4)	0.00863(9)	1
N1	4*b*	0.0506(13)	0.3205(6)	0.0205(9)	0.0094(10)	1
N2	4*b*	0.0898(12)	0.2102(9)	0.5418(8)	0.0130(10)	1
N3	4*b*	0.2483(12)	0.287(1)	0.7761(7)	0.0131(9)	1
N4	4*b*	0.2950(11)	0.1776(6)	0.2946(8)	0.0066(9)	1
N5	2*a*	0	0	0	0.0076(11)	1
N6	2*a*	0.8508(15)	0	0.3215(11)	0.0106(12)	1
N7	2*a*	0.415(5)	0	0.665(3)	0.052(2)	1

Table S1.6: Anisotropic displacement parameters (U_{ij} / Å^2) of AlP_6N_{11} from single-crystal refinement. Standard deviations are given in parentheses.

Atom	U_{11}	U_{22}	U_{33}	U_{23}	U_{13}	U_{12}
Al1	0.0243(4)	0.0076(3)	0.0207(4)	0	0.0120(3)	0
P1	0.0036(6)	0.0044(5)	0.0103(8)	0.0005(4)	−0.0019(5)	0.0003(5)
P2	0.0023(5)	0.0069(5)	0.0096(8)	−0.0003(4)	−0.0008(5)	−0.000(5)
P3	0.0043(2)	0.0104(2)	0.0106(2)	−0.0021(6)	−0.0010(1)	−0.0011(7)
N1	0.007(2)	0.008(2)	0.013(2)	−0.003(1)	−0.003(2)	−0.0006(1)
N2	0.004(2)	0.021(2)	0.013(2)	0.001(2)	−0.003(2)	−0.004(2)
N3	0.004(1)	0.025(2)	0.009(2)	0.003(2)	−0.002(1)	−0.002(2)
N4	0.0017(15)	0.0062(18)	0.012(2)	0.001(1)	0.002(1)	−0.000(1)
N5	0.005(2)	0.0010(18)	0.016(3)	0	0.000(2)	0
N6	0.005(2)	0.012(3)	0.015(3)	0	0.000(2)	0
N7	0.061(3)	0.0065(9)	0.074(4)	0	−0.036(3)	0

Table S1.7: Interatomic distances (Å) of AlP_6N_{11} from single-crystal refinement. Standard deviations are given in parentheses.

Atoms	Distance / Å	Atoms	Distance / Å	Atoms	Distance / Å
Al1–N1	2.0872(82)	P1–N4	1.6561(53)	P3–N2	1.6635(78)
Al1–N4	2.0555(78)	P1–N6	1.6164(38)	P3–N2	1.8318(64)
Al1–N5	2.3424(90)	P2–N1	1.6203(72)	P3–N3	1.6609(76)
Al1–N6	2.3923(95)	P2–N1	1.6317(57)	P3–N3	1.7909(62)
P1–N2	1.6458(71)	P2–N3	1.6582(63)	P3–N7	1.5408(13)
P1–N4	1.6401(63)	P2–N5	1.6425(36)		

Table S1.8: Interatomic angles (°) of AlP_6N_{11} from single-crystal refinement. Standard deviations are given in parentheses.

Atoms	Distance / Å	Atoms	Distance / Å	Atoms	Distance / Å
N1–Al1–N1	89.1(5)	N2–P1–N4	106.2(4)	N2–P3–N3	79.4(4)
N1–Al1–N4	90.6(3)	N2–P1–N6	115.3(5)	N2–P3–N3	168.1(4)
N1–Al1–N4	179.7(4)	N2–P1–N4	104.7(4)	N2–P3–N7	95.0(10)
N1–Al1–N5	87.5(4)	N4–P1–N4	122.2(4)	N2–P3–N2	93.7(4)
N1–Al1–N6	92.6(4)	N4–P1–N6	108.3(3)	N3–P3–N3	94.7(4)
N4–Al1–N5	92.6(3)	N1–P2–N1	113.7(4)	N3–P3–N7	96.9(10)
N4–Al1–N6	87.3(3)	N1–P2–N3	102.7(4)	N3–P2–N5	116.8(5)
N5–Al1–N6	179.9(5)	N1–P2–N5	110.9(4)		
N2–P1–N4	104.7(4)	N2–P3–N2	93.7(4)	P3–N7–P3	175(3)

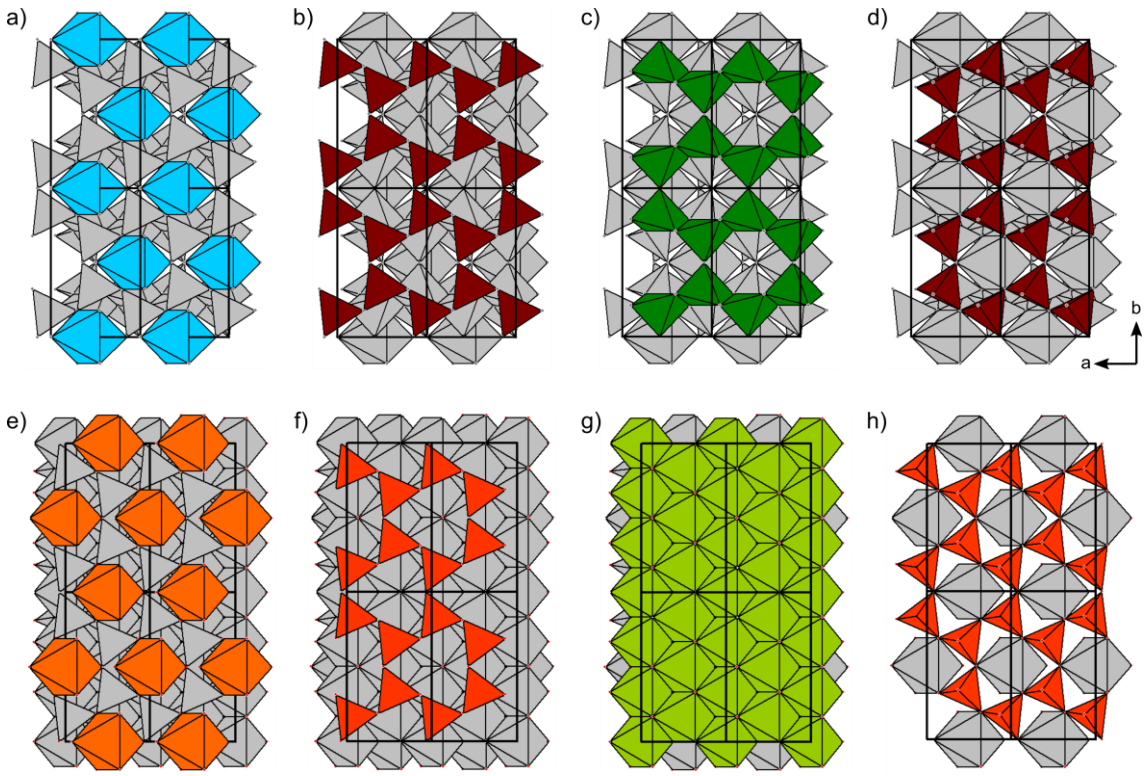

Figure S1.1: Detailed views of the different layers in the structure of AlP_6N_{11}. a) AlN_6-octahedra. b) PN_4-tetrahedra (center atom P1), forming *sechser rings*. c) PN_5 trigonal bipyramids (center atom P3), forming *sechser rings*. d) PN_4-tetrahedra (center atom P2), forming *sechser rings*.[20] The mica-group mineral clintonite $Ca(Mg,Al)_3(Al_3Si)O_{10}(OH)_2$, has a comparable layer setup, with the exception of $(Al,Si)O_6$-octahedra instead of the PN_5 trigonal bipyramids. e) CaN_6-octahedra. f) $(Si,Al)O_4$-tetrahedra. g) $(Mg,Al)O_6$-octahedra. h) $(Si,Al)O_4$-tetrahedra.

Rietveld Refinement

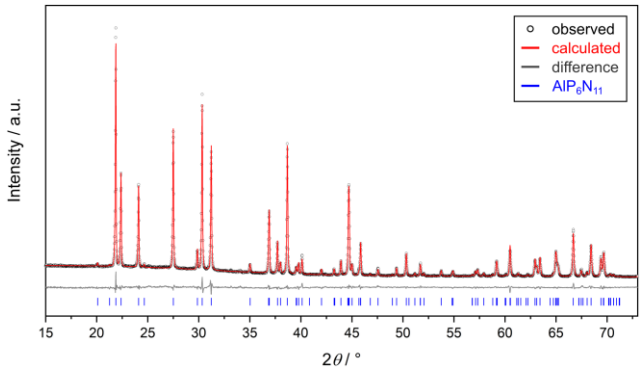

Figure S1.2: Rietveld refinement for AlP_6N_{11}. Observed (black circles) and calculated (red line) powder X-ray diffraction patterns, difference plot (gray), positions of Bragg reflections of AlP_6N_{11} (vertical blue bars).

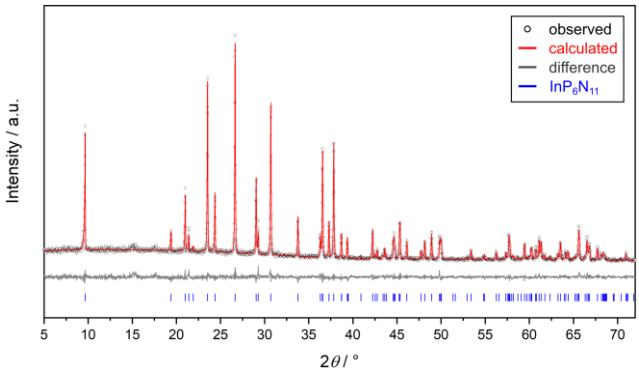

Figure S1.3: Rietveld refinement for InP_6N_{11} in space group *Cm*. Observed (black circles) and calculated (red line) powder X-ray diffraction patterns, difference plot (gray), positions of Bragg reflections of InP_6N_{11} (vertical blue bars). For refinement initially the structure model of AlP_6N_{11} was used.

Table S1.9: Wyckoff position, coordinates, isotropic thermal displacement parameters and occupancy of InP_6N_{11} from Rietveld refinement. Standard deviations are given in parentheses.

Atom	Wyck.	*x*	*y*	*z*	U_{eq}	*occ.*
In1	2*a*	0.450(9)	0	0.160(4)	0.4(2)	1
P1	4*b*	0.024(9)	0.172(1)	0.380(4)	0.4(2)	1
P2	4*b*	0.369(9)	0.326(1)	0.960(4)	0.4(2)	1
P3	4*b*	0.451(9)	0.1850(4)	0.668(4)	0.4(2)	1
N1	4*b*	0.09(1)	0.306(3)	0.016(5)	0.4(2)	1
N2	4*b*	0.11(1)	0.218(3)	0.537(4)	0.4(2)	1
N3	4*b*	0.28(1)	0.287(3)	0.765(4)	0.4(2)	1
N4	4*b*	0.31(1)	0.182(3)	0.324(4)	0.4(2)	1
N5	2*a*	0	0	0	0.4(2)	1
N6	2*a*	0.879(4)	0	0.339(2)	0.4(2)	1
N7	2*a*	0.42(1)	0	0.675(5)	0.4(2)	1

Table S1.10: Comparison of the crystallographic data from Rietveld refinements of MP_6N_{11} (M = Al, In). Standard deviations are given in parentheses.

Formula	**AlP_6N_{11}**	**InP_6N_{11}**
Crystal system	monoclinic	
Space group	*Cm* (no. 8)	
a / Å	4.917909(5)	*4*.97234(6)
b / Å	8.1186(1)	*8*.29379(9)
c / Å	8.9240(1)	9.2634(1)
β / °	98.2875(5)	99.2170(8)
Cell volume / Å^3	352.581(7)	377.124(8)
Radiation *λ* / Å	1.54056 (Cu-Kα_1)	
2*θ*-range / °	5 < 2*θ* < 120	
Data points	7714	7714
Number of parameters (thereof background)	63 (12)	63 (12)
R values	R_{Bragg} = 0.0175 R_p = 0.0377 R_{wp} = 0.0498	R_{Bragg} = 0.0302 R_p = 0.0823 R_{wp} = 0.1091
Goodness of fit	1.3555	0.9257

Solid State Magic-Angle Spinning Nuclear Magnetic Resonance Spectroscopy

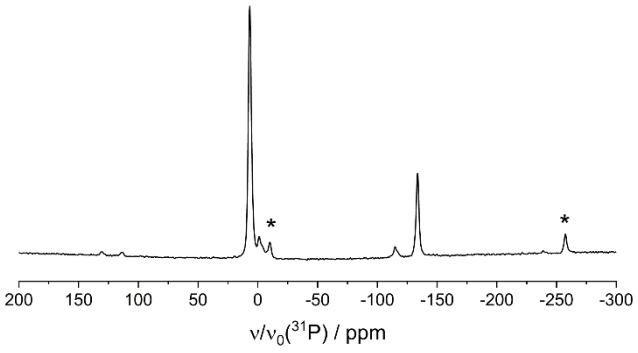

Figure S1.4: ^{31}P solid-state MAS NMR spectrum of InP_6N_{11}. In contrast to AlP_6N_{11}, only one signal for tetrahedral P sites at δ = 6.8 ppm is observed. This may either be a superposition of two signals, leading to space group *Cm* (as for AlP_6N_{11}) or space group *C*2/*m*, as suggested by X-ray diffraction data of AlP_6N_{11}, may be feasible for InP_6N_{11}. Minor signals are caused by side phase(s) in the sample, as we were not able to obtain phase pure samples on InP_6N_{11}. Sidebands are marked with asterisks.

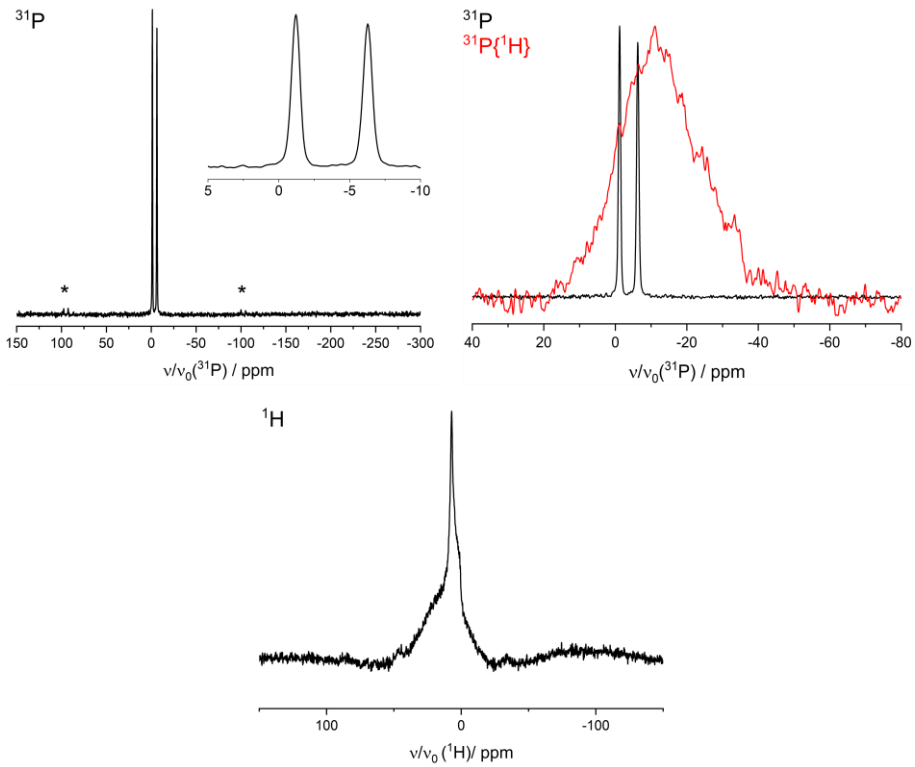

Figure S1.5: ^{27}Al, ^{1}H, and ^{31}P{^{1}H} cross-polarized solid-state MAS NMR spectra of AlP_6N_{11}. All signals observed are consistent with the structure model in *Cm*. Signals in the ^{1}H and ^{31}P{^{1}H} cross-polarized spectrum probably originate from a small amount of an amorphous side phase not visible in the powder diffraction pattern, containing both hydrogen and phosphorus. Sidebands are marked with asterisks.

Fourier Transform Infrared Spectroscopy

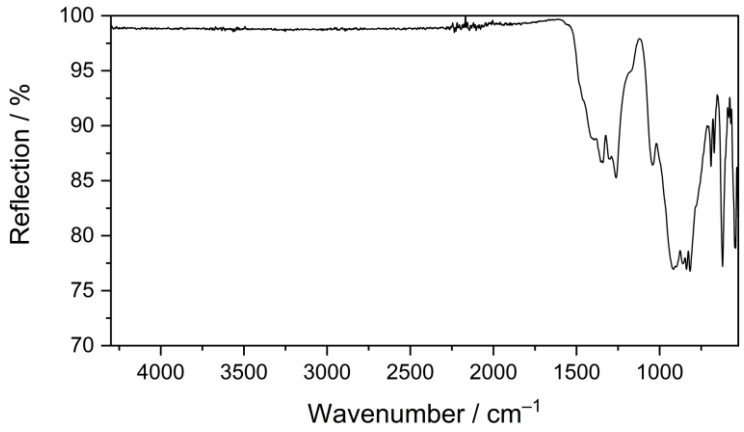

Figure S1.6: FTIR spectrum of AlP_6N_{11} in ATR mode. Absorption bands in the fingerprint region (< 1500 cm–1) originate from the P/N- and Al/N-framework. No other absorption bands, especially no N–H bands, are visible.

Temperature-Dependet Powder X-Ray Diffraction

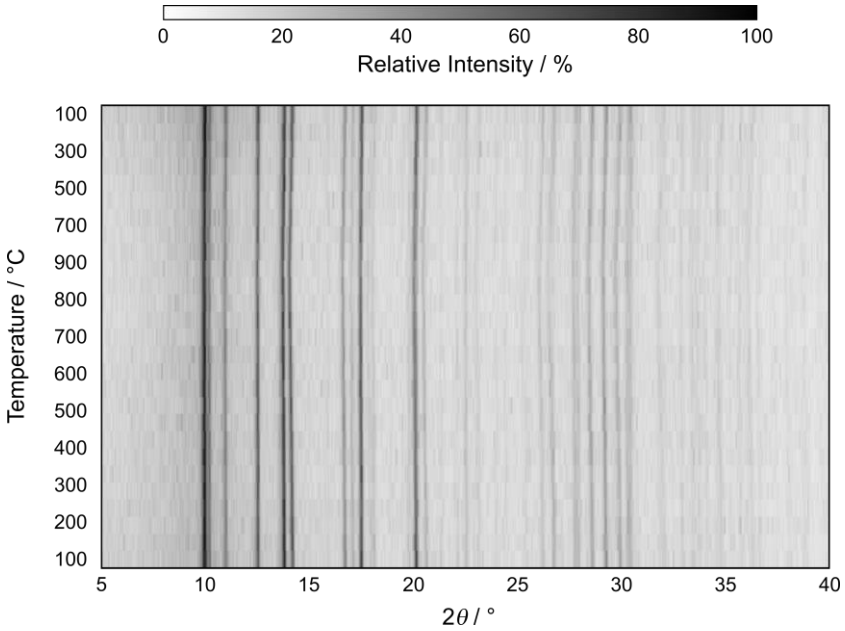

Figure S1.7: Temperature-dependent powder X-ray diffraction patterns (Mo-$K\alpha_1$ radiation, λ = 0.71073 Å) of AlP_6N_{11} under argon atmosphere. Heating to 900 °C causes a shift of reflections to lower angles, corresponding to the thermal expansion of the unit cell. Cooling reverses this effect. Neither a phase transition nor thermal decomposition is observed.

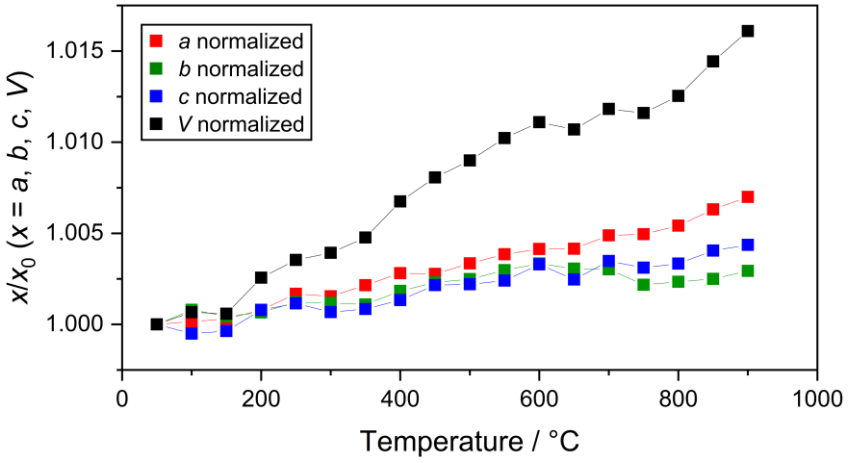

Figure S1.8: Temperature-dependent evolution of the lattice parameters and unit cell volume of AlP_6N_{11}.

Charge Distribution Calculations

Table S1.11: CHARDI values for AlP_6N_{11}. All effective coordination numbers and mean total charges of the regular polyhedra are in good agreement with the expected values. The deviation of the effective coordination number of P3 and Al1 correlate with unusually long bond lengths P/Al–N. AlP_6N_{11} might be a quenched high-pressure phase, metastable at ambient conditions, which could explain the deviation of the values.

Polyhedron	**P1 N2–N4–N4–N6**	**P2 N1–N1–N3–N5**	**P3 N2–N2–N3–N3–N7**	**Al1 N1–N1–N4–N4–N5–N6**
Average bond length / Å	1.6396	1.6381	1.6976	2.1700
Polyhedral volume / Å^3	2.2493	2.2315	4.0535	13.5140
Distortion index (bond length)	0.00707	0.00743	0.05361	0.06061
Quadratic elongation	1.0039	1.0074	-	1.0097
Bond angle variance / °^{2}	15.2959	27.9934	-	5.0994
Effective coordination number (theory)	3.9885 (4)	3.9897 (4)	4.0388 (5)	5.1302 (6)
Total charge (theory):				
P/Al	5.057 (5.0)	4.995 (5.0)	4.995 (5.0)	2.906 (3.0)
N1	-	−3.228 (−3.0)	-	−3.228 (−3.0)
N2	−2.810 (−3.0)	-	−2.810 (−3.0)	-
N3	-	−2.892 (−3.0)	−2.892 (−3.0)	-
N4	−3.092 (−3.0)	-	-	−3.092 (−3.0)
N5	-	−2.700 (−3.0)	-	−2.700 (−3.0)
N6	−2.899 (−3.0)	-	-	−2.899 (−3.0)
N7	-	-	−3.355 (−3.0)	-

Bond-Valence-Sum Calculations

Table S1.12: Results of the BVS analysis of AlP_6N_{11}. Most charges are in good agreement with the theoretical values. The deviations of Al1 and P3 correlate with unusual bond lengths in the respective polyhedra. AlP_6N_{11} might be a quenched high-pressure phase, metastable at ambient conditions, which could explain the deviation of the values.

	Al1	P1	P2	P3	N1	N2	N3	N4	N5	N6	N7
Calc.	2.41	4.91	4.93	5.37	−3.00	−3.07	−3.12	−2.90	−2.66	−2.81	−3.19
Theo.	3	5	5	5	−3	−3	−3	−3	−3	−3	−3

Minimal Bonding Ellipsoid Calculations

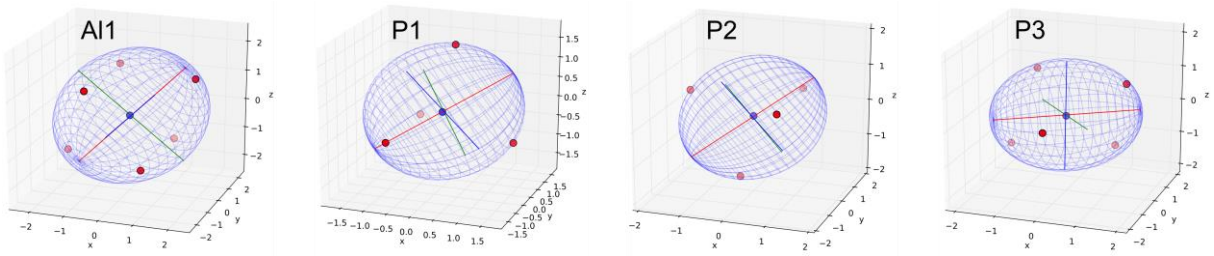

Figure S1.9: Graphical representation of the minimal bonding ellipsoids of AlN_6 octahedra, PN_4 tetrahedra and PN_5 trigonal bipyramids in AlP_6N_{11} fitted by PIEFACE (Al/P in blue, N in red).[19]

Table S1.13: Ellipsoid parameters of AlN_6 octahedra, PN_4 tetrahedra and PN_5 trigonal bipyramids in AlP_6N_{11}.

	*R*1	*R*2	*R*3	<*R*>	Sigma(*R*)	*S*	Center Displacement	Coord.
Al1	2.3833	2.0640	2.0609	2.1694	0.1513	0.1325	0.0324	6
P1	1.6998	1.6656	1.5481	1.6378	0.0650	−0.0505	0.0431	4
P2	1.7413	1.6513	1.5122	1.6349	0.0942	−0.0326	0.0425	4
P3	1.8718	1.6082	1.5621	1.6805	0.1361	0.1118	0.0626	5

References

[1] A. Stock, H. Grüneberg, *Ber. Dtsch. Chem. Ges.* **1907**, *40*, 2573.

[2] W. J. Frierson, W. F. Filbert *Inorganic Syntheses*, John Wiley & Sons, Hoboken, **1946**, pp. 136−138.

[3] D. Walker, M. A. Carpenter, C. M. Hitch, *Am. Min.* **1990**, 1020.

[4] N. Kawai, S. Endo, *Rev. of Sci. Instrum.* **1970**, *41*, 1178.

[5] H. Huppertz, *Z. Kristallogr. Cryst. Mater.* **2004**, *219*, 330.

[6] O. D. Rigaku, *CrysAlis^{PRO}*, Rigaku Oxford Diffraction Ltd, Yarnton, Oxfordshire, **2017**.

[7] G. M. Sheldrick, SADABS v.2: Multi-Scan Absorption Correction, Bruker-AXS, Kennewick, Washington, **2012**.

[8] G. M. Sheldrick, *Acta Crystallogr. Sect. C* **2015**, *71*, 3.

[9] G. M. Sheldrick, *Acta Crystallogr. Sect. A* **2015**, *71*, 3.

[10] Crystal Impact GbR, Diamond v.3.2k, Bonn, **1997−2014**.

[11] K. Momma, F. Izumi, *J. Appl. Crystallogr.* **2011**, *44*, 1272.

[12] H. M. Rietveld, *J. Appl. Crystallogr.* **1969**, *2*, 65.

[13] A. A. Coelho, TOPAS-Academic v4.1, Brisbane, **2007**.

[14] R. W. Cheary, A. Coelho, *J. Appl. Crystallogr.* **1992**, *25*, 109.

[15] R. W. Cheary, A. A. Coelho, J. P. Cline, *J. Res. Natl. Inst. Stand. Technol.* **2004**, *109*, 1.

[16] Oxford Instruments, AZtecEnergy, Abington, **2016**.

[17] N. E. Brese, M. O'Keeffe, *Acta Crystallogr. Sect. B* **1991**, *47*, 192.

[18] A. S. Wills, VaList - A bond valence calculation and analysis program, London, **2010**.

[19] J. Cumby, J. P. Attfield, *Nat. Commun.* **2017**, *8*, 14235.

[20] F. Liebau, *Structural Chemistry of Silicates. Structure, Bonding, and Classification*, Springer Berlin Heidelberg, Berlin, Heidelberg, **1985**. The term "*sechser ring*" has been defined by Liebau and is derived from the German word "sechs" (engl. six), describing a ring formed by six polyhedra.

9.2 Supporting Information for Chapter 3

Experimental Section

Preparation of Starting Materials

Phosphorus(V) nitride P_3N_5 was prepared according to Stock *et al.*[1] P_4S_{10} (Sigma-Aldrich, 99.99%) was reacted in a constant flow of ammonia (Air Liquide, 5.0) at 850 °C in a boat of quartz glass, placed in a quartz tube. Prior to synthesis, the apparatus was dried at 1000 °C for 2 h under a reduced pressure of 10^{-3} mbar. Afterwards, the quartz boat was loaded with 8 g P_4S_{10} and centered in the outer tube. The Apparatus was saturated with NH_3 for 1 h, heated with 7 °C/min to 850 °C, hold for 4 h and subsequently cooled to ambient temperature with 7 °C/min. The purity of the orange product was confirmed by powder X-ray diffraction, FTIR spectroscopy and CHNS-analyses (calcd. (%) C 0, H 0, N 42.98, S 0; found (%): C 0, H 0, N 43.16, S 0)

Ge_3N_4 (Sigma-Aldrich, ≥99.99%) was used as purchased.

High-Pressure High-Temperature Synthesis

GeP_2N_4 was synthesized in a high-pressure, high-temperature reaction from P_3N_5 and Ge_3N_4. Stoichiometric amounts of the staring materials were ground together in an argon-filled glovebox (MBraun, < 1 ppm H_2O, < 1 ppm O_2). The powder was tightly packed into an h-BN crucible, which was closed by an h-BN lid and centered in a graphite heater, using MgO spacers. The heater was surrounded by a ZrO_2 sleeve, closed with Mo disks at both the top and bottom and placed into a pierced MgO octahedron. The octahedron was surrounded by eight electrically isolated WC-cubes (doped with 7% Co, 32 mm edge length, 11 mm corner truncation) and transferred into the multianvil apparatus. More details on the assembly preparation can be found in the literature.[2,3] Reaction conditions were achieved by a 1000 t hydraulic press with a modified walker-module. The assembly was compressed to 6 GPa within 170 min and heated to 800 °C in 60 min. The temperature was hold for 240 min and subsequently cooled down to 20 °C within 60 min and decompressed to ambient pressure in 500 min. The dark gray sample was separated from all assembly parts and washed with a 1:1 vol-% solution of 30% H_2O_2 and concentrated NaOH to remove elemental germanium.

Single Crystal X-Ray Diffraction

For structure determination by SC-XRD, combined φ- and ω-scans of a GeP_2N_4 single crystal were collected on a Bruker D8 Venture TXS diffractometer with Mo-Kα radiation (λ = 0.71073 Å), rotating anode and multilayer monochromator. The data were indexed, integrated, absorption corrected (multi-scan-method) and the space group was determined using the APEX3 software package.[4–6] The structure was solved by SHELXS using direct methods and

refined against F^2 by SHELXL with the least-squares method.[7–9] The results were visualized using the VESTA software.[10]

Powder X-Ray Diffraction and Rietveld Refinement

PXRD data were collected on a STOE Stadi P diffractometer (STOE & Cie GmbH, Darmstadt) in modified Debye-Scherrer geometry with Cu-Kα_1 radiation (λ = 1.54060 Å), a MYTHEN 1K strip detector and a Ge(111) monochromator. For measurement, the ground samples were sealed in a glass capillary (0.3 mm outer diameter, Hilgenberg, Malsfeld) and centered in the beam on a rotating goniometer head.

To proof GeP_2N_4 as the main constituent of synthesized samples, the collected data were used for Rietveld refinement with the TOPAS Academic software.[11,12] During refinement, the peak profiles were described by the fundamental parameter approach, a potential preferred orientation of the crystallites was accounted for with a 4th order spherical harmonic function and the background was modeled by a shifted Chebyshev polynomial.[13,14] The results were plotted using ORIGIN.[15]

Temperature-Dependent Powder X-Ray Diffraction

The thermal behavior of GeP_2N_4 was examined by temperature-dependent powder X-ray diffraction. For measurement, the ground sample was sealed in a quartz glass capillary (0.3 mm outer diameter, Hilgenberg, Malsfeld) and heated from 25 to 1000 °C in steps of 25 °C with a heating rate of 10 °C/min. Afterwards, the sample was cooled in steps of 100 °C from 1000 °C to 25 °C with 10 °C/min. After each temperature step during heating and cooling, powder X-ray diffraction data were collected within 3 h at a constant temperature. The data collection was done on a STOE Stadi P diffractometer (STOE & Cie GmbH, Darmstadt, Mo-Kα_1 radiation (λ = 0.71073 Å, Ge(111)-monochromator, IP-PSD detector) equipped with a STOE resistance graphite furnace for temperature control.

Scanning Electron Microscopy and Energy-Dispersive X-Ray Spectroscopy

For SEM imaging and EDX measurements, the sample was prepared on a self-adhesive carbon foil and coated with carbon by an electron beam evaporator (BAL-TEC MED 020, BalTec AG, Pfäffikon) for electric conductivity. The analysis was done by a Dualbeam Helios Nanolab G3 UC (FEI, Hilsboro) with an X-Max 80 SDD detector (Oxford Instruments, Abingdon). Data and images were recorded with an acceleration voltage of 25 kV and processed with the Aztec software.[16]

Solid State Magic-Angle Spinning Nuclear Magnetic Resonance Spectroscopy

For solid-state NMR MAS measurements, the ground sample was tightly packed into a ZrO_2 rotor with an outer diameter of 2.5 mm. NMR spectra were collected at 20 kHz spinning frequency on an Avance III 500 spectrometer (Bruker, Karlsruhe) with a 11.7 T magnet (500.25 MHz ^1H frequency) and a double resonance MAS probe.

Fourier Transform Infrared Spectroscopy

The FTIR spectrum was measured at ambient conditions on a Spectrum BX II spectrometer with a DuraSampler ATR-device (Perkin Elmer).

Bond-Valence-Sum Calculations

Bond-valence sum calculations were performed using the software VaList.[17,18]

Density Functional Theory Calculations

The electronic structure of GeP_2N_4 was modelled using density functional theory (DFT) with WIEN2k, a full-potential all-electron commercially available software package which uses linearized augmented plane waves with local orbitals in a Kohn-Sham scheme.[19,20] Calculations were performed using the Perdew, Burke and Ernzerhof generalized gradient approximation exchange-correlation functional.[21] Calculations were performed using experimental lattice parameters. In this work an $R_{MT}RK_{max}$ = 6.5 was used, with the k-mesh selected so that the total energy per unit cell was stable to within 10^{-5} Ry. This resulted in a 7x9x15 k-mesh for GeP_2N_4.The DFT calculations are used to calculate the electron density and density of states.

Results and Discussion

Scanning Electron Microscopy and Energy-Dispersive X-Ray Spectroscopy

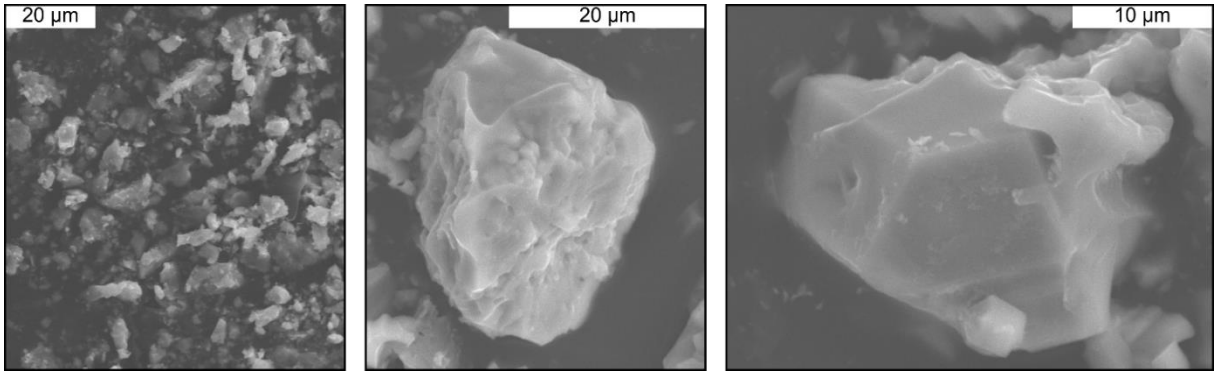

Figure S2.1: SEM images of GeP_2N_4 single crystals. Crystallites of a generic sample were approximately 20 µm in width and length.

EDX measurements were performed on various crystallites in the sample (table S1). No other elements than Ge, P, N and O were detected, where O can be attributed to surface hydrolysis and oxidation due to the harsh washing conditions of the sample (1:1 vol-% H_2O_2 and NaOH). The normalized atomic ratio (Ge : P : N = 1.0 : 2.0 : 4.4) is in very good agreement to the theoretical values (Ge : P : N = 1 : 2 : 4), considering the precision of EDX spectroscopy for light elements.

Table S2.1: Overview of EDX measurements of GeP_2N_4. Results are given in atomic percent. Standard deviations are given in parenthesis.

	1	2	3	4	5	Ø	Norm. (Ge)
Ge	15	14	12	13	11	13(1)	1.0(1)
P	29	27	25	27	24	26(2)	2.0(1)
N	52	55	59	56	60	56(3)	4.4(2)
O	4	4	4	4	5	4(1)	0.3(1)

Structure Determination

Table S2.2: Crystallographic data of GeP_2N_4 from single crystal refinement. Standard deviations are given in parentheses.

Formula	**GeP_2N_4**
Crystal system	orthorhombic
Space group	*Pna*2$_1$ (no. 33)
a / Å	9.5468(12)
b / Å	7.5419(11)
c / Å	4.6941(6)
Cell volume / Å^3	337.98(8)
Formula units / unit cell	4
Calculated X-ray density / g·cm^{-3}	3.745
Molecular weight / g·mol^{-1}	190.57
Linear absorption coefficient / cm^{-1}	9.798
T_{min}/T_{max}	0.879
Temperature / K	293(2)
Absorption correction	multi-scan
Radiation	Mo-Kα (λ = 0.71973 Å)
F(000)	360
θ range / °	3.443 ≤ θ ≤ 33.724
Total no. of reflections	7805
Independent reflections [$I \geq 2\sigma(I)$ / all]	622 / 740
R_{int}	0.0412
Refined parameters	65
Goodness of fit	1.048
R-values [$I \geq 2\sigma(I)$]	*R*1 = 0.024; *wR*2 = 0.0415
R-values (all data)	*R*1 = 0.030; *wR*2 = 0.0428
$\Delta\rho_{max}$, $\Delta\rho_{min}$ / e·Å^3	0.617; –0.728

Table S2.3: Wyckoff position, coordinates, isotropic thermal displacement parameters and occupancy of GeP_2N_4 from single-crystal refinement. Standard deviations are given in parentheses.

Atom	Wyck.	*x*	*y*	*z*	U_{eq}	*occ.*
Ge1	4*a*	0.89051(4)	0.10398(5)	0.2048(3)	0.00705(8)	1
P1	4*a*	0.87476(8)	0.34797(10)	0.7023(7)	0.00408(14)	1
P2	4*a*	0.67062(8)	0.0538(1)	0.7039(6)	0.00338(13)	1
N1	4*a*	0.8318(4)	0.3597(4)	0.3680(9)	0.0067(6)	1
N2	4*a*	0.8095(3)	0.1587(4)	–0.1809(9)	0.0048(6)	1
N3	4*a*	1.0361(3)	0.3287(5)	0.7757(9)	0.0070(7)	1
N4	4*a*	0.6996(4)	0.0169(4)	0.3625(9)	0.0053(6)	1

Table S2.4: Anisotropic displacement parameters (U_{ij} / Å^2) of GeP_2N_4 from single crystal refinement. Standard deviations are given in parentheses.

Atom	U_{11} / Å^2	U_{22} / Å^2	U_{33} / Å^2	U_{12} / Å^2	U_{13} / Å^2	U_{23} / Å^2
Al1	0.0071(1)	0.0074(2)	0.0067(1)	0.0005(1)	–0.0014(4)	–0.0005(4)
P1	0.0041(3)	0.0043(3)	0.0038(3)	–0.0003(3)	0.0001(7)	0.0003(11)
P2	0.0034(3)	0.0032(3)	0.0036(3)	–0.0004(3)	–0.0013(10)	0.0004(8)
N1	0.0109(15)	0.0050(14)	0.004(1)	–0.002(1)	–0.0007(12)	0.0007(11)
N2	0.0062(13)	0.0051(13)	0.003(1)	–0.001(1)	–0.0001(12)	0.0003(11)
N3	0.0029(13)	0.0098(15)	0.008(2)	–0.001(1)	0.0005(11)	0.0006(11)
N4	0.0062(14)	0.0052(15)	0.005(1)	–0.002(1)	–0.0002(12)	–0.0006(11)

Table S2.5: Interatomic distances (Å) of GeP_2N_4 from single-crystal refinement. Standard deviations are given in parentheses.

Atoms	Distance / Å	Atoms	Distance / Å	Atoms	Distance / Å
Ge1–N2	2.012(5)	P1–N3	1.585(3)	P2–N3	1.596(3)
Ge1–N4	2.074(4)	P1–N1	1.625(4)	P2–N2	1.636(4)
Ge1–N1	2.150(4)	P1–N4	1.640(4)	P2–N4	1.650(4)
Ge1–Ge1	3.5127(7)	P1–N2	1.651(4)	P2–N1	1.654(4)
Ge1–P1	2.977(3)	P1–P2	2.920(1)	P2–Ge1	3.168(3)

Table S2.6: Interatomic angles (°) of GeP_2N_4 from single-crystal refinement. Standard deviations are given in parentheses.

Atoms	Angle / °	Atoms	Angle / °	Atoms	Angle / °
N2–Ge1–N4	92.78(15)	N3–P2–N2	108.29(19)	P2–N1–Ge1	129.2(2)
N2–Ge1–N1	92.10(14)	N3–P2–N4	115.69(19)	P2–N2–P1	127.9(2)
N4–Ge1–N1	85.87(15)	N2–P2–N4	105.48(19)	P2–N2–Ge1	120.6(2)
N3–P1–N1	117.4(2)	N3–P2–N1	112.44(19)	P1–N2–Ge1	109.34(19)
N3–P1–N4	113.1(2)	N2–P2–N1	106.58(19)	P1–N3–P2	133.2(2)
N1–P1–N4	106.93(19)	N4–P2–N1	107.77(18)	P1–N4–P2	120.3(2)
N3–P1–N2	102.42(19)	P1–N1–P2	120.1(2)	P1–N4–Ge1	117.5(2)
N1–P1–N2	105.83(19)	P1–N1–Ge1	103.27(19)	P2–N4–Ge1	116.1(2)
N4–P1–N2	110.9(2)				

Comparison of GeP_2N_4 to Paracelsian ($BaAl_2Si_2O_8$) and $LiNdP_8N_{14}$

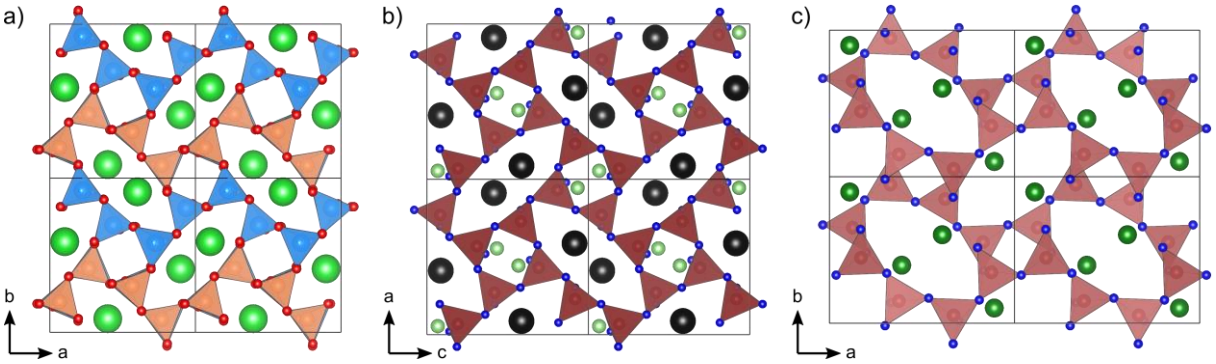

Figure S2.2: Structure comparison of GeP_2N_4 to paracelsian ($BaAl_2Si_2O_8$) and $LiNdP_8N_{14}$. All three compounds share the same network topology, however, the cations of GeP_2N_4 are arranged differently. a) Crystal structure of paracelsian (Ba: green, Si: orange, Al: blue, O: red). b) Crystal structure of $LiNdP_8N_{14}$ (Nd: black, Li: green, P: red, N: blue). c) Crystal structure of GeP_2N_4 (Ge: green, P: red, N: blue).

Rietveld Refinement

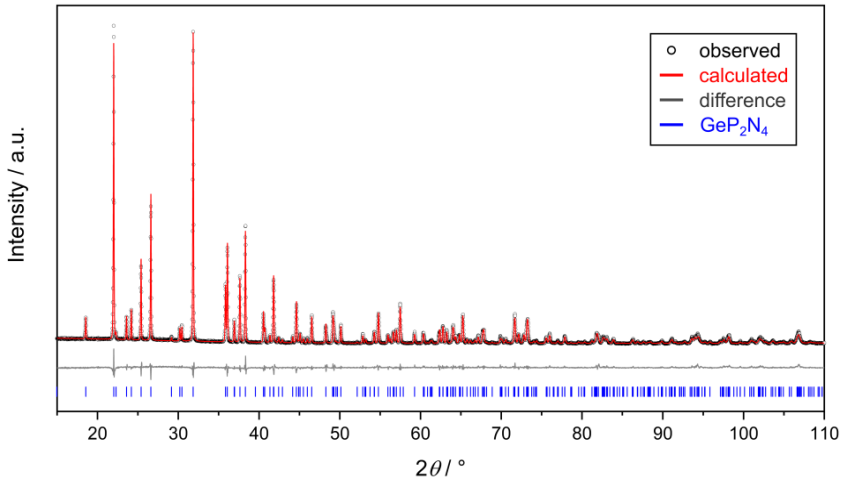

Figure S2.3: Result of the Rietveld refinement of GeP_2N_4. Observed (black circles), calculated (red line) powder X-ray diffraction patterns (Cu-Kα_1 radiation, λ = 1.5406 Å) and difference plot (gray line). Positions of Bragg reflections are given as blue bars.

Temperature-Dependent Powder X-Ray Diffraction

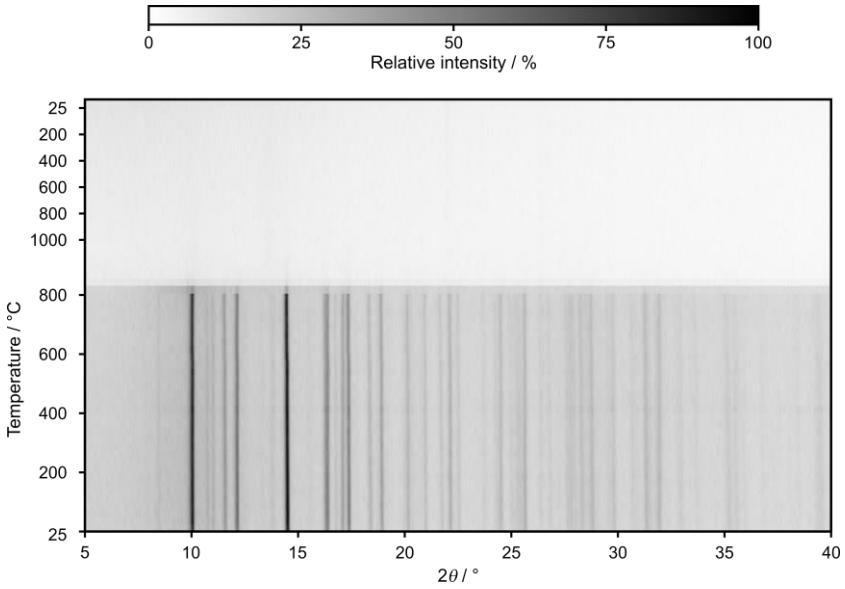

Figure S2.4: Temperature dependent powder X-ray patterns (Mo-$K\alpha_1$ radiation, λ = 0.71073 Å) of GeP_2N_4. No significant change in the unit cell volume is observed until 800°C, which is the threshold of decomposition into an amorphous material. Heating further to 1000°C and subsequent cooling shows neither formation of a new phase nor recrystallisation after decomposition.

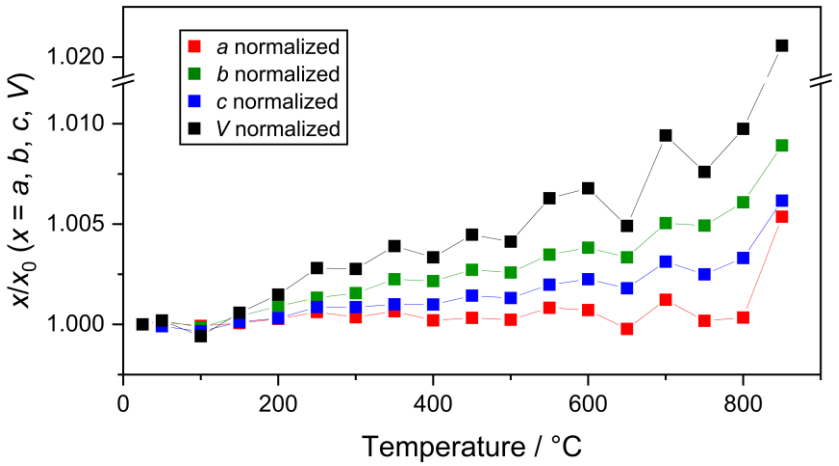

Figure S2.5: Temperature-dependent evolution of the lattice parameters and unit cell volume of GeP_2N_4. The values are taken from Pawley fits of single temperature dependent measurements.

Solid State Magic-Angle Spinning Nuclear Magnetic Resonance Spectroscopy

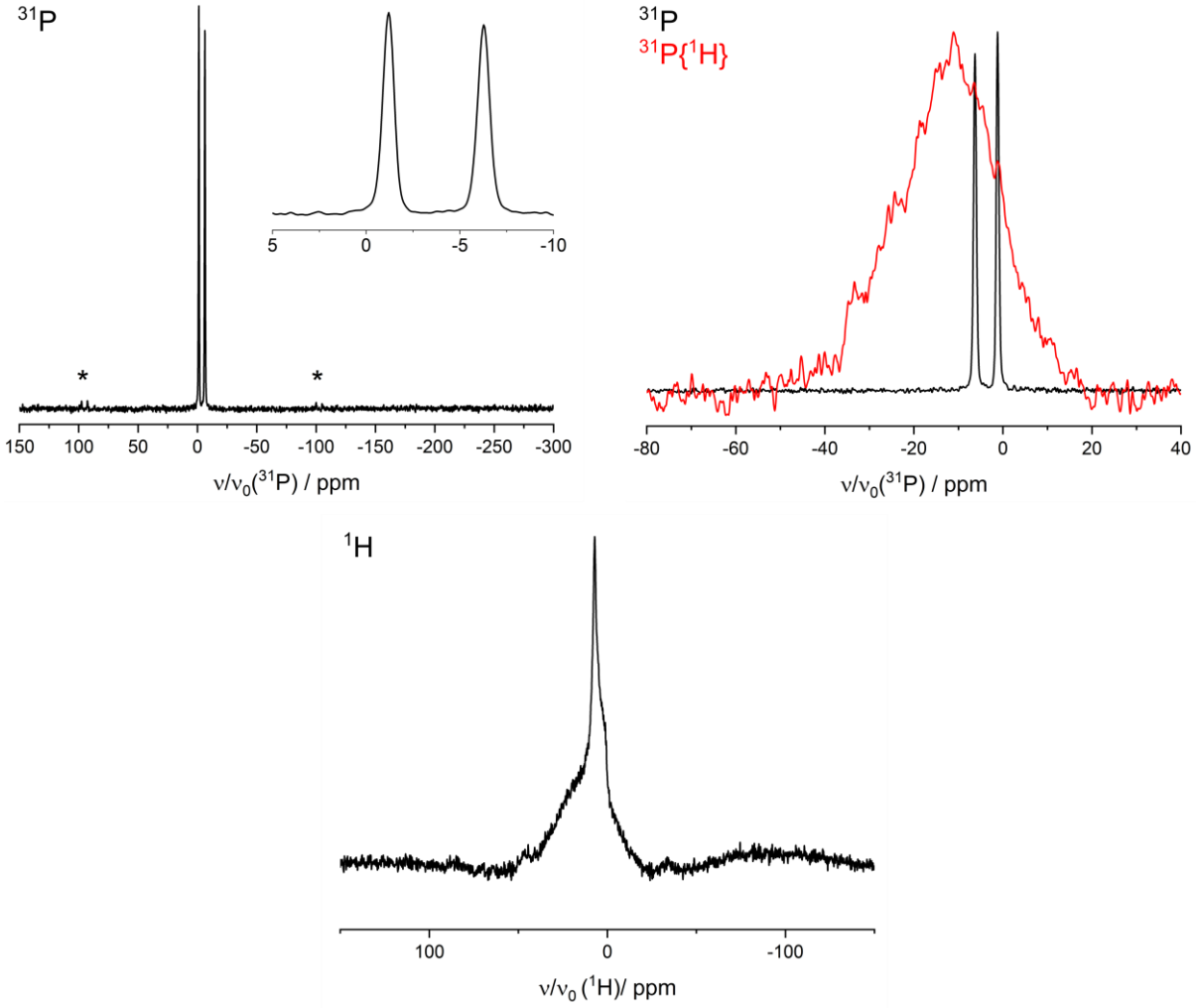

Figure S2.6: ^{31}P, $^{31}P\{^1H\}$ cross polarized and ^1H solid-state MAS NMR spectra of GeP_2N_4. The ^{31}P spectrum shows two signals (δ = –1.20 ppm, δ = –6.27 ppm) with an intensity ratio of 1:1, which can be assigned to the two P sites with the same multiplicity (4*a*). There is no evidence of hydrogen being present in GeP_2N_4, as the broad signal of the $^{31}P\{^1H\}$ cross polarized spectrum does not match with the ^{31}P peaks. This $^{31}P\{^1H\}$ and the ^1H signal may originate from a smallest, partially amorphous side phase, not visible by powder X-ray diffraction.

Fourier Transform Infrared Spectroscopy

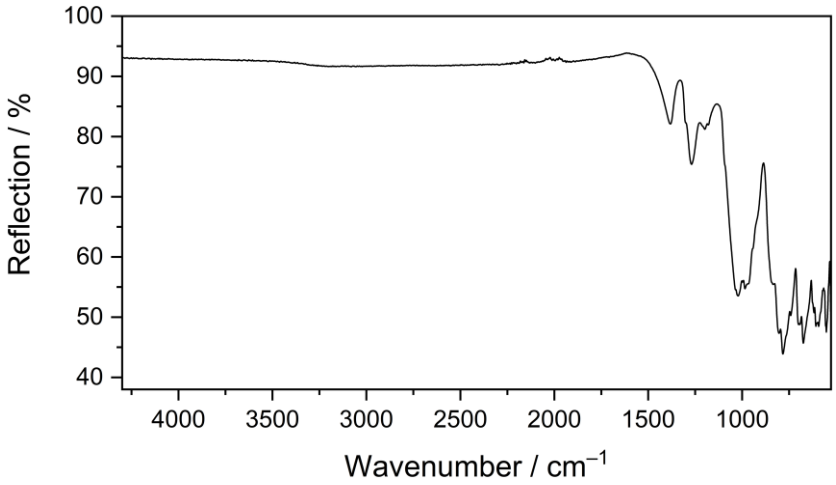

Figure S2.7: FTIR spectrum of GeP_2N_4. Absorption bands in the fingerprint region (<1500 cm^{-1}) originate from the P/N-framework. No other absorption bands, especially no N–H bands, are visible.

Charge Distribution Calculations

Table S2.7: Results of the CHARDI analysis of GeP_2N_4. All effective coordination numbers and mean total charges are in good agreement with the theoretical values.

Polyhedron	**P1 N1–N2–N3–N4**	**P2 N1–N2–N3–N4**	**Ge1 N1–N2–N4**
Average bond length / Å	1.6254	1.6341	2.0783
Polyhedral volume / Å^3	2.1799	2.2276	1.4881
Distortion index (bond length)	0.01272	0.01157	0.02284
Quadratic elongation	1.0075	1.0037	–
Bond angle variance / °^{2}	29.4620	15.2420	–
Effective coordination number (theory)	3.9622 (4.0)	3.9694 (4.0)	2.9127 (3.0)
Total charge (theory):			
P/Ge	5.023 (5.0)	5.015 (5.0)	1.962 (2.0)
N1	–2.938 (–3.0)	–2.938 (–3.0)	–2.938 (–3.0)
N2	–3.170 (–3.0)	–3.170 (–3.0)	–3.170 (–3.0)
N3	–2.865 (–3.0)	–2.865 (–3.0)	–
N4	–3.027 (–3.0)	–3.027 (–3.0)	–3.027 (–3.0)

Bond-Valence-Sum Calculations

Table S2.8: Results of the BVS analysis of GeP_2N_4. All charges are in good agreement with the theoretical values.

	Ge1	P1	P2	N1	N2	N3	N4
Calc.	1.972	5.043	4.933	–2.950	–3.143	–2.857	–2.998
Theo.	2	5	5	–3	–3	–3	–3

Minimal Bonding Ellipsoid Calculations

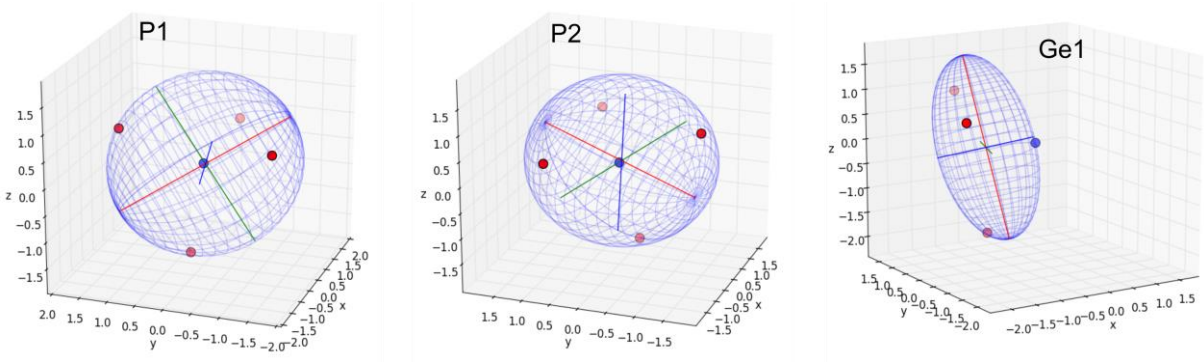

Figure S2.8: Graphical representation of the minimal bonding ellipsoids of both PN_4 tetrahedra and the GeN_3 pyramid fitted by the software PIEFACE (P/Ge in blue, N in red).

Table S2.9: Ellipsoid parameters of both PN_4 tetrahedra and the GeN_3 pyramid in the GeP_2N_4 structure.

	*R*1	*R*2	*R*3	<*R*>	Sigma(*R*)	*S*	Center Displacement	Coord.
P1	1.7185	1.6316	1.5149	1.6217	0.0834	–0.0210	0.0754	4
P2	1.6859	1.6859	1.5751	1.6319	0.0453	–0.0061	0.0764	4
Ge1	1.8487	1.7596	0.8914	1.4999	0.4318	–0.4452	0.8977	3

Density of States

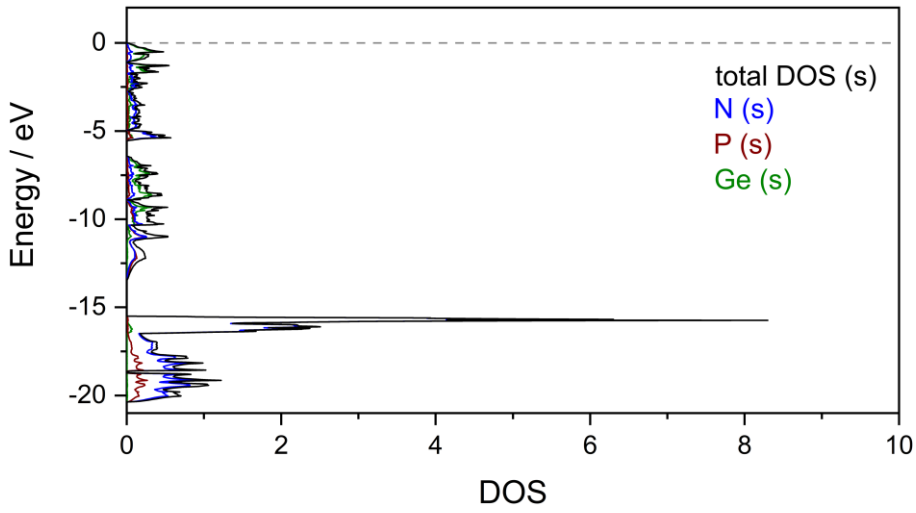

Figure S2.9: Partial and total s-contribution to the density of states.

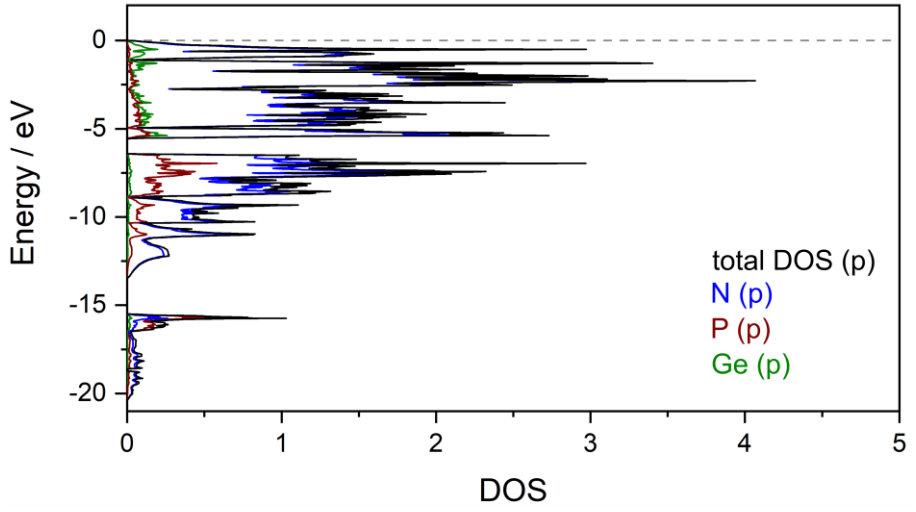

Figure S2.10: Partial and total p-contribution to the density of states.

References

[1] A. Stock, H. Grüneberg, *Ber. Dtsch. Chem. Ges.* **1907**, *40*, 2573.

[2] H. Huppertz, *Z. Kristallogr. Cryst. Mater.* **2004**, *219*, 330.

[3] D. Walker, *Am. Mineral.* **1991**, *76*, 1092.

[4] SAINT, Data Integration Software, Madison, Wisconsin, USA, **1997**.

[5] Bruker-AXS, APEX3, Vers. 2016.5-0, Karlsruhe, **2016**.

[6] Bruker-AXS, XPREP Reciprocal Space Exploration, Vers. 6.12, Karlsruhe, **2001**.

[7] G. M. Sheldrick, SHELXS-97 Program of the Solution of Crystal Structure, University of Göttingen, Göttingen, **1997**.

[8] G. M. Sheldrick, *Acta Crystallogr. C Struct. Chem.* **2015**, *71*, 3.

[9] L. J. Farrugia, *J. Appl. Crystallogr.* **2012**, *45*, 849.

[10] K. Momma, F. Izumi, *J. Appl. Crystallogr.* **2011**, *44*, 1272.

[11] A. A. Coelho, TOPAS-Academic v4.1, Brisbane, **2007**.

[12] H. M. Rietveld, *J. Appl. Crystallogr.* **1969**, *2*, 65.

[13] R. W. Cheary, A. Coelho, *J. Appl. Crystallogr.* **1992**, *25*, 109.

[14] R. W. Cheary, A. A. Coelho, J. P. Cline, *J. Res. Natl. Inst. Stand. Technol.* **2004**, *109*, 1.

[15] OriginLab Corporation, OriginPro 2018G, Northhampton, USA, **1991-2017**.

[16] Oxford Instruments, AZtecEnergy, Abington, **2016**.

[17] N. E. Brese, M. O'Keeffe, *Acta Crystallogr. B Struct. Sci.* **1991**, *47*, 192.

[18] A. S. Wills, VaList - A bond valence calculation and analysis program, London, **2010**.

[19] P. Blaha, K. Schwarz, G. K. H. Madsen, D. Kvasnicka, J. Luitz, R. Laskowski, F. Tran, L. D. Marks WIEN2k, An Augmented Plane Wave Plus Local Orbitals Program for Calculating Crystal Properties, Technische Universität Wien, Wien, **2018**.

[20] P. Blaha, K. Schwarz, F. Tran, R. Laskowski, G. K. H. Madsen, L. D. Marks, *J. Chem. Phys.* **2020**, *152*, 074101.

[21] J. P. Perdew, K. Burke, M. Ernzerhof, *Phys. Rev. Lett.* **1996,** *77*, 3865.

9.3 Supporting Information for Chapter 4

Data of GeP_2N_4

Scanning Electron Microscopy and Energy-Dispersive X-Ray Spectroscopy

The sample of GeP_2N_4 and its EDX and SEM analyses are the same as in a previous work.[1]

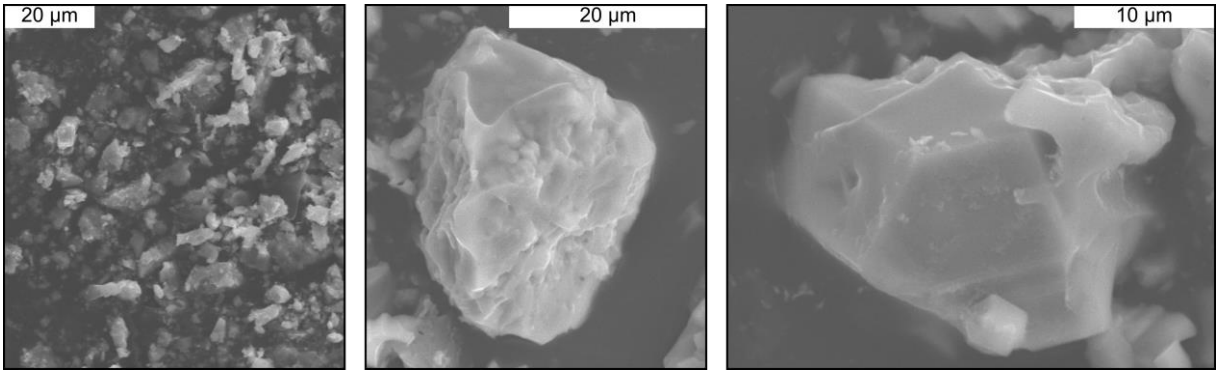

Figure S3.1: SEM images of GeP_2N_4 single crystals. Crystallites of a generic sample were approximately 20 µm in width and length.

Various crystallites (Figure S1) were selected for EDX analyses. The measurements (Table S1) show no other elements than Ge, P, N and O, which might originate from surface hydrolysis owing to the harsh washing conditions (1:1 vol-% conc. NaOH and H_2O_2). The normalized atomic ratio of 1 : 2 : 4.4 (Ge : P : N) is in good agreement to the theoretical values 1 : 2 : 4.

Table S3.1: Overview of EDX measurements of GeP_2N_4. Results are given in atomic percent. Standard deviations are given in parenthesis.

	1	2	3	4	5	Ø	Norm. (Ge)
Ge	15	14	12	13	11	13(1)	1.0(1)
P	29	27	25	27	24	26(2)	2.0(1)
N	52	55	59	56	60	56(3)	4.4(2)
O	4	4	4	4	5	4(1)	0.3(1)

Powder X-Ray Diffraction and Rietveld Refinement

The sample of GeP_2N_4 and its Rietveld refinement are the same as in a previous work.[1]

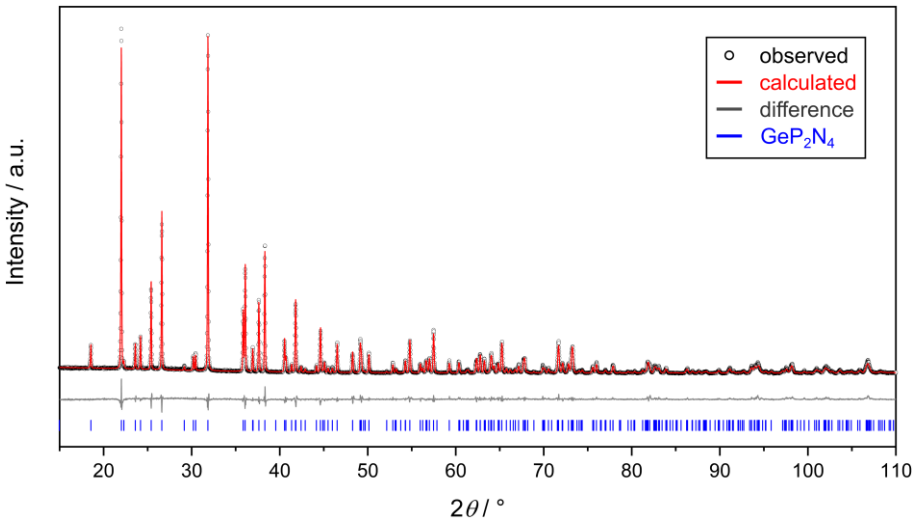

Figure S3.2: Result of the Rietveld refinement of GeP_2N_4. Observed (black circles) and calculated (red line) PXRD patterns and difference plot (gray line). Positions of Bragg reflections are given as blue bars.

Crystallographic Data

Table S3.2: Crystallographic data of GeP_2N_4 from single-crystal XRD refinements in the range from ambient pressure to 44.4(1) GPa. All data sets were measured with synchrotron radiation (λ = 0.2905 Å). For comparison, the lattice parameters monoclinic phase ($P112_1$) are not standardized, to correspond to the lattice parameters of the orthorhombic phase ($Pna2_1$).

Formula	**GeP_2N_4**								
Pressure / GPa	0.00010(1)	7.2(1)	14.2(1)	19.3(1)	21.9(1)	25.3(1)	28.6(1)	36.2(1)	44.4(1)
Crystal system	orthorhombic						monoclinic		
Molecular weight / $g \cdot mol^{-1}$	190.57								
Space group	$Pna2_1$ (no. 33)						$P112_1$ (no. 4)		
a / Å	9.5602(3)	9.3752(4)	9.2994(7)	9.2281(10)	9.202(3)	9.158(4)	9.129(6)	9.070(7)	8.974(6)
b / Å	7.5385(5)	7.3042(5)	7.1437(9)	7.0495(12)	6.945(4)	6.899(5)	6.816(8)	6.698(12)	6.770(8)
c / Å	4.6940(4)	4.59630(16)	4.5288(2)	4.4763(3)	4.4919(3)	4.4653(4)	4.4494(5)	4.4237(10)	4.3182(7)
γ / °	90				91.44(6)	91.66(7)	92.11(10)	93.03(14)	90.39(10)
Cell volume / $Å^3$	338.30(4)	314.75(3)	300.86(5)	291.20(6)	287.0(2)	282.0(2)	276.7(4)	268.4(5)	262.3(4)
Formula units per cell	4								
Calculated X-ray density / $g \cdot cm^{-3}$	3.742	4.022	4.207	4.347	4.411	4.489	4.575	4.716	4.825
Filter (Pt) thickness / µm	150	125	75	100	50	50	50	0	0
F(000)	360								
Observed reflections	1564	1528	1480	1384	1012	962	866	678	702

Independent reflections (>2σ)	893 (882)	1025 (945)	998 (950)	954 (879)	501 (491)	488 (475)	484 (465)	457 (404)	444 (432)
Number of parameters	31	30	31	30	57	57	57	67	87
R_{int}	0.0165	0.0224	0.0186	0.0181	0.0118	0.0167	0.0147	0.0448	0.0160
R_{σ}	0.0096	0.0139	0.0172	0.0135	0.0140	0.0249	0.0183	0.0388	0.0184
*R*1 (all data)	0.0255	0.0332	0.0336	0.0453	0.0438	0.0588	0.0662	0.0737	0.0433
*wR*2 (all data)	0.0656	0.0679	0.0870	0.1236	0.1295	0.1618	0.1891	0.1979	0.1311
Goodness of fit	1.080	1.048	1.104	1.159	1.139	1.086	1.271	1.231	1.156

Table S3.3: Mean interatomic *T*–N (*T* = P, Ge) distances in Å of GeP_2N_4 from single-crystal XRD refinements at different pressure points. The distances and standard deviations were calculated using the average interatomic distances of all corresponding polyhedra.

Pressure / GPa	Mean Ge–N / Å	Mean P–N / Å
0.00010(1)	2.0784(31)	1.6314(34)
7.2(1)	2.0501(40)	1.6169(42)
14.2(1)	2.0356(39)	1.6065(41)
19.3(1)	2.0261(55)	1.5962(59)
21.9(1)	2.026(24)	1.595(24)
25.3(1)	2.033(25)	1.588(27)
28.6(1)	2.043(31)	1.575(32)
36.2(1)	1.997(44)	1.591(45)
44.4(1)	1.970(30)	1.592(31)

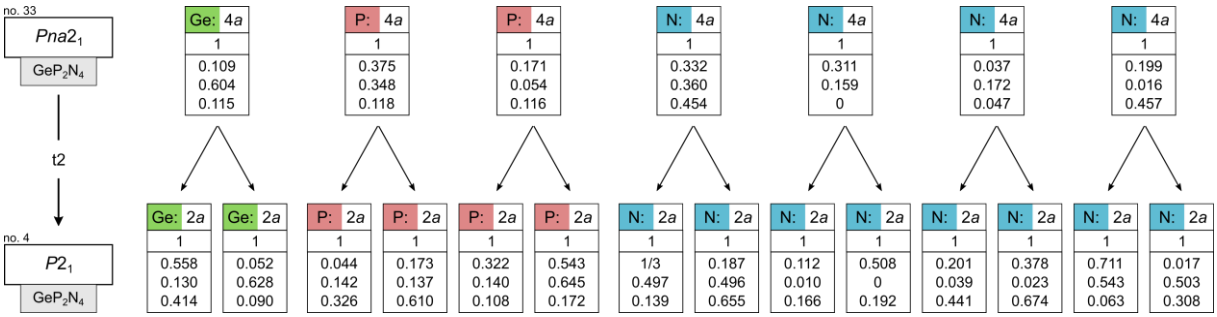

Figure S3.3: Bärnighausen tree for the phase transition of GeP_2N_4 from orthorhombic symmetry (*Pna*2_1) to monoclinic symmetry (*P*12_1). The element symbol is colored, the Wyckoff site symmetry and coordinates are given below. Coordinates for the *Pna*2_1 space group are given at 19.3(1) GPa, coordinates for the *P*12_1 space group are given at 21.9(1) GPa.

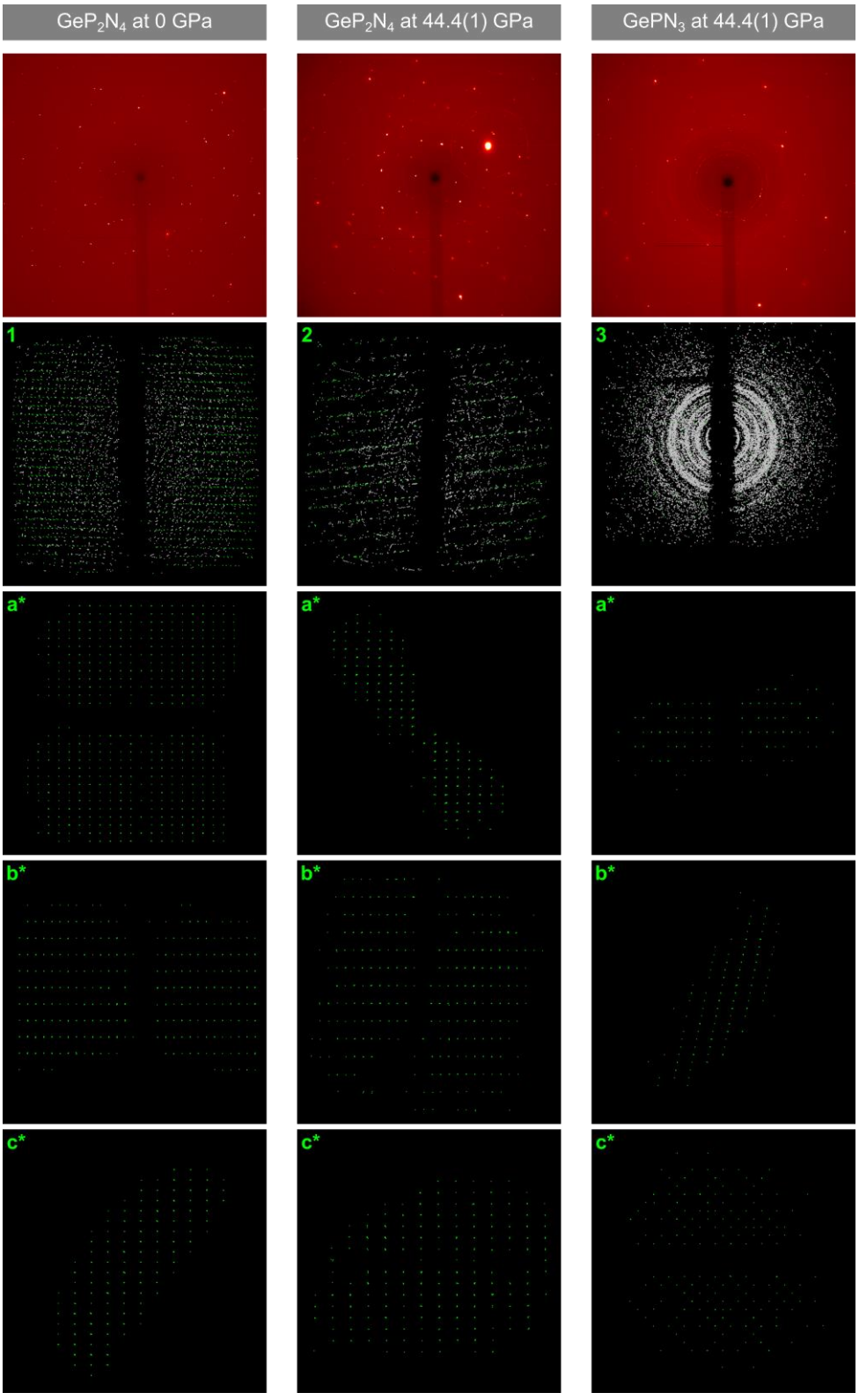

Figure S3.4: Images of the XRD data used for structure elucidation. X-ray diffraction pattern (ω = 0°, $t_{exposure}$ = 1 s) and data sets of GeP_2N_4 before the phase transition (1), GeP_2N_4 after the phase transition (2), and $GePN_3$ after laser heating (3). Images 1–3 show all reflections of the data set (excluding diamond reflections), all other images show only the indexed reflections.

Data of $GePN_3$

Single-Crystal X-Ray Diffraction Refinements

Table S3.4: Crystallographic data of $GePN_3$ at 44.4(1) GPa and ambient pressure from single crystal refinement. Standard deviations are given in parenthesis.

Formula	**$GePN_3$**	
Pressure / GPa	44.4(1)	0.00010(1)
Crystal system	monoclinic	
Space group	*C2/c* (no. 15)	
a / Å	8.666(5)	9.065(5)
b / Å	8.076(4)	8.454(5)
c / Å	4.691(2)	4.8743(11)
β / °	101.00(7)	101.61(3)
Cell volume / $Å^3$	322.3(3)	365.9(3)
Formula units / unit cell	8	
Calculated X-ray density / $g \cdot cm^{-3}$	6.001	5.286
Molecular weight / $g \cdot mol^{-1}$	154.59	
Linear absorption coefficient / cm^{-1}	1.705	1.472
Radiation	Synchrotron (λ = 0.2905 Å)	
Measurement device	PETRA III P2.02	
θ range / °	$1.95 < \theta < 16.03$	$1.95 < \theta < 16.28$
h,*k*,*l* range	$-11 \le h \le 11$ $-8 \le k \le 10$ $-6 \le l \le 6$	$-13 \le h \le 13$ $-6 \le k \le 7$ $-7 \le l \le 7$
F(000)	544	
Observed reflections	390	567
Independent reflections (>2*σ*)	213 (141)	281 (239)
R_{int}; R_σ	0.0621; 0.0897	0.0266; 0.0206
Refined parameters	27	32
Goodness of fit	1.108	1.095
R-values [$I \ge 2\sigma(I)$]	R_1 = 0.0644; *wR*2 = 0.1416	R_1 = 0.0409; *wR*2 = 0.1075
R-values (all data)	R_1 = 0.1048; *wR*2 = 0.1749	R_1 = 0.0513; *wR*2 = 0.1159
$\Delta\rho_{min}$, $\Delta\rho_{max}$ / $e \cdot Å^3$	–1.306; 1.482	–0.873; 0.743

Table S3.5: Wyckoff position, coordinates, isotropic thermal displacement parameters and occupancy of $GePN_3$ from single-crystal XRD refinement at 44.4(1) GPa. Standard deviations are given in parentheses.

Atom	Wyck.	*x*	*y*	*z*	U_{eq}	*occ.*
Ge1	4*e*	0	0.0941(4)	1/4	0.0086(10)	1
Ge2	4*e*	0	0.2789(4)	3/4	0.0103(10)	1
P1	8*f*	–0.1904(7)	0.4087(6)	–0.7980(12)	0.0072(10)	1
N1	8*f*	0.119(2)	–0.092(2)	0.133(4)	0.010(3)	1
N2	8*f*	0.123(2)	0.2525(19)	0.120(3)	0.005(3)	1
N3	8*f*	–0.137(2)	0.4304(19)	–1.111(4)	0.005(3)	1

Table S3.6: Anisotropic displacement parameters (U_{ij} / Å^2) of Ge in $GePN_3$ from single crystal XRD refinement at 44.4(1) GPa. Standard deviations are given in parentheses. Owing to diamond anvil cell data only Ge atoms were refined anisotropically.

Atom	U_{11} / Å^2	U_{22} / Å^2	U_{33} / Å^2	U_{12} / Å^2	U_{13} / Å^2	U_{23} / Å^2
Ge1	0.007(2)	0.009(2)	0.011(2)	0.0	0.004(2)	0.0
Ge2	0.012(2)	0.006(2)	0.015(2)	0.0	0.010(2)	0.0

Table S3.7: Wyckoff position, coordinates, isotropic thermal displacement parameters and occupancy of $GePN_3$ from single-crystal XRD refinement at ambient pressure. Standard deviations are given in parenthesis.

Atom	Wyck.	*x*	*y*	*z*	U_{eq}	*occ.*
Ge1	4*e*	0	0.0991(3)	1/4	0.0093(7)	1
Ge2	4*e*	0	0.2800(3)	3/4	0.0078(7)	1
P1	8*f*	0.3046(2)	0.0901(4)	0.7027(4)	0.0067(11)	1
N1	8*f*	0.1162(7)	0.0911(15)	0.6324(12)	0.0056(11)	1
N2	8*f*	-0.1176(7)	0.2612(16)	0.3794(12)	0.0077(11)	1
N3	8*f*	-0.1425(7)	0.4302(17)	0.8963(13)	0.0098(12)	1

Table S3.8: Anisotropic displacement parameters (U_{ij} / Å^2) of Ge in $GePN_3$ from single crystal XRD refinement at 44.4(1) GPa. Standard deviations are given in parenthesis. Owing to diamond anvil cell data only Ge and P atoms were refined anisotropically.

Atom	U_{11} / Å^2	U_{22} / Å^2	U_{33} / Å^2	U_{12} / Å^2	U_{13} / Å^2	U_{23} / Å^2
Ge1	0.0102(6)	0.009(2)	0.0075(5)	0.0	–0.0001(4)	0.0
Ge2	0.0098(5)	0.006(2)	0.0063(4)	0.0	–0.0009(3)	0.0
P1	0.0057(8)	0.008(4)	0.0060(7)	–0.0002(10)	–0.0008(5)	0.0010(8)

Table S3.9: Interatomic T–N (T = P, N) distances in Å of $GePN_3$ from single-crystal XRD refinements at 44.4(1) GPa and ambient pressure. The mean interatomic distances and standard deviations were calculated using the average of all corresponding polyhedra. Standard deviations are given in parentheses.

Pressure / GPa	44.4(1)	0.00010(1)
P1–N1	1.591(18)	1.673(7)
N2	1.572(16)	1.605(12)
N3	1.593(17)	1.663(13)
N3	1.645(21)	1.667(7)
Ge1–N1	1.893(17)	1.949(6)
N1	1.959(18)	2.066(11)
N2	1.842(17)	1.919(11)
Ge2–N1	1.964(18)	2.057(11)
N2	1.868(14)	1.910(6)
N3	1.905(18)	2.040(11)
Mean P–N	1.590(14)	1.665(8)
Mean Ge–N	1.905(17)	1.990(9)

Table S3.10: Interatomic angles (°) of $GePN_3$ from single-crystal XRD refinement at 44.4(1) GPa. Standard deviations are given in parentheses. High standard deviations are attributed to the lack of high-quality single-crystal data at the pressure points.

Atoms	Angle / °	Atoms	Angle / °	Atoms	Angle / °
N1–Ge1–N1	94.1(8)	N2–Ge1–N1	91.9(7)	N3–Ge2–N3	82.0(7)
N1–Ge1–N3	85.6(8)	N2–Ge1–N3	84.7(7)	N3–Ge2–N3	80.6(7)
N1–Ge1–N3	88.9(7)	N2–Ge1–N3	91.2(7)	N3–Ge2–N2	87.9(7)
N1–Ge1–N2	89.7(7)	N2–Ge1–N3	90.6(7)	N3–Ge2–N2	91.2(8)
N1–Ge1–N3	177.5(9)	N2–Ge1–N3	90.1(6)	N3–Ge2–N2	174.0(8)
N1–Ge1–N1	86.1(6)	N2–Ge1–N2	92.5(6)	N3–Ge2–N3	88.9(7)
N1–Ge1–N2	93.6(6)	N2–Ge1–N3	86.6(6)	N3–Ge2–N3	89.4(6)
N1–Ge1–N3	92.7(6)	N2–Ge1–N2	87.2(6)	N3–Ge2–N1	85.5(6)
N1–Ge1–N2	87.5(6)	N2–Ge1–N1	178.4(8)	N3–Ge2–N2	82.6(6)
N1–Ge1–N2	95.1(7)	N2–Ge2–N3	83.7(7)	N3–P1–N2	113.1(5)
N1–Ge1–N3	84.8(7)	N2–Ge2–N2	93.5(6)	N3–P1–N3	109.0(5)
N1–Ge1–N2	93.1(7)	N2–Ge2–N2	88.9(7)	N3–P1–N3	104.5(5)
N1–Ge1–N1	84.9(7)	N2–Ge2–N1	97.3(7)	N3–P1–N2	110.9(5)
N1–Ge1–N3	86.0(6)	N2–Ge2–N3	93.6(6)	N3–P1–N3	104.5(5)
N1–Ge1–N1	172.3(8)	N2–Ge2–N3	87.8(6)	N3–P1–N2	108.9(6)
N1–Ge1–N1	92.5(7)	N2–Ge2–N1	96.7(6)	N3–P1–N1	104.3(5)
N1–Ge1–N3	95.3(6)	N2–Ge2–N2	174.0(7)		
N1–Ge1–N2	84.7(6)	N2–Ge2–N1	84.0(6)		
N1–Ge2–N2	87.6(7)	N2–P1–N1	105.6(5)		
N1–Ge2–N1	99.1(7)	N2–P1–N2	108.6(5)		
N1–Ge2–N2	88.7(7)	N2–P1–N2	104.7(5)		
N1–Ge2–N1	95.2(7)	N2–P1–N1	109.0(5)		
N1–Ge2–N3	90.2(6)	N2–P1–N3	102.9(5)		
N1–Ge2–N1	87.4(6)	N2–P1–N1	109.4(5)		
N1–Ge2–N1	92.6(7)	N2–P1–N2	107.3(5)		
N1–Ge2–N2	97.3(6)	N2–P1–N1	110.6(5)		
N1–Ge2–N2	175.0(8)	N2–P1–N3	107.2(5)		
		N2–P1–N2	108.5(4)		

Table S3.11: Interatomic angles (°) of $GePN_3$ from single-crystal XRD refinement at ambient pressure. Standard deviations are given in parentheses. High standard deviations are attributed to the lack of high-quality single-crystal data at the pressure points.

Atoms	Angle / °	Atoms	Angle / °	Atoms	Angle / °
N1–Ge1–N1	95.3(3)	N2–Ge1–N1	90.3(3)	N3–Ge2–N3	80.9(3)
N1–Ge1–N3	85.5(3)	N2–Ge1–N3	92.6(4)	N3–Ge2–N3	89.4(2)
N1–Ge1–N3	87.3(3)	N2–Ge1–N3	90.7(4)	N3–Ge2–N2	91.6(3)
N1–Ge1–N2	91.1(3)	N2–Ge1–N3	82.0(3)	N3–Ge2–N2	87.6(3)
N1–Ge1–N3	178.7(3)	N2–Ge1–N3	87.2(4)	N3–Ge2–N2	171.5(4)
N1–Ge1–N1	84.6(3)	N2–Ge1–N2	94.0(2)	N3–Ge2–N3	87.4(2)
N1–Ge1–N2	95.6(3)	N2–Ge1–N3	87.5(3)	N3–Ge2–N1	84.9(2)
N1–Ge1–N3	83.3(3)	N2–Ge1–N2	86.1(2)	N3–Ge2–N2	80.1(3)
N1–Ge1–N2	98.4(4)	N2–Ge2–N2	95.7(3)	N3–P1–N2	115.2(4)
N1–Ge1–N2	94.6(4)	N2–Ge2–N2	88.4(3)	N3–P1–N3	109.6(2)
N1–Ge1–N2	99.4(4)	N2–Ge2–N1	95.6(3)	N3–P1–N3	104.4(2)
N1–Ge1–N1	93.3(2)	N2–Ge2–N3	91.8(3)	N3–P1–N2	112.5(2)
N1–Ge1–N3	85.4(2)	N2–Ge2–N3	90.5(2)	N3–P1–N3	105.2(2)
N1–Ge2–N1	93.3(2)	N2–Ge2–N1	96.8(3)	N3–P1–N2	110.7(2)
N1–Ge2–N2	88.8(3)	N2–Ge2–N2	176.4(3)	N3–P1–N2	108.8(2)
N1–Ge2–N1	95.3(4)	N2–P1–N1	103.5(2)	N3–P1–N1	103.0(2)
N1–Ge2–N3	89.4(2)	N2–P1–N2	106.6(2)		
N1–Ge2–N2	99.4(4)	N2–P1–N2	105.6(2)		
N1–Ge2–N2	86.9(3)	N2–P1–N3	103.6(2)		
		N2–P1–N2	109.4(2)		
		N2–P1–N3	106.7(4)		
		N2–P1–N2	106.4(2)		

Charge Distribution Calculations

Table S3.12: Results of the CHARDI analysis of $GePN_3$ at 44.4(1) GPa. All calculated effective coordination numbers and mean total charges are in good agreement with the theoretical values.

Polyhedron	**Ge1 N1–N1–N1–N1–N2–N2**	**Ge2 N1–N2–N3–N1–N3–N2**	**P1 N3–N2–N3–N1**
Average bond length / Å	1.8982	1.9122	1.6002
Polyhedral volume / $Å^3$	9.0358	9.1760	2.0955
Distortion index (bond length)	0.02151	0.01821	0.01412
Quadratic elongation	1.0068	1.0111	1.0027
Bond angle variance / $°^2$	21.1192	36.8533	9.6274
Effective coordination number (theory)	5.8498 (6)	5.9022 (6)	3.9584 (4)
Total charge (theory):			
P/Ge	3.987 (4)	4.010 (4)	5.001 (5)
N1	–3.062 (–3)	–3.062 (–3)	–3.062 (–3)
N2	–2.933 (–3)	–2.933 (–3)	–2.933 (–3)
N3	-	–3.005 (–3)	–3.005 (–3)

Table S3.13: Results of the CHARDI analysis of $GePN_3$ at ambient pressure. All calculated effective coordination numbers and mean total charges are in good agreement with the theoretical values.

Polyhedron	**Ge1 N1–N1–N1–N1–N2–N2**	**Ge2 N1–N2–N3–N1–N3–N2**	**P1 N3–N2–N3–N1**
Average bond length / Å	1.9779	2.0024	1.6519
Polyhedral volume / $Å^3$	10.1499	10.4977	2.3021
Distortion index (bond length)	0.02957	0.03062	0.01428
Quadratic elongation	1.0119	1.0142	1.0035
Bond angle variance / $°^2$	36.1964	42.8005	13.9154
Effective coordination number (theory)	5.7718 (6)	5.7103 (6)	3.9548 (4)
Total charge (theory):			
P/Ge	+4.010 (+4)	+3.980 (+4)	+5.005 (+5)
N1	–2.917 (–3)	–2.917 (–3)	–2.917 (–3)
N2	–3.117 (–3)	–3.117 (–3)	–3.117 (–3)
N3	-	–2.966 (–3)	–2.966 (–3)

Minimal Bonding Ellipsoid Calculations

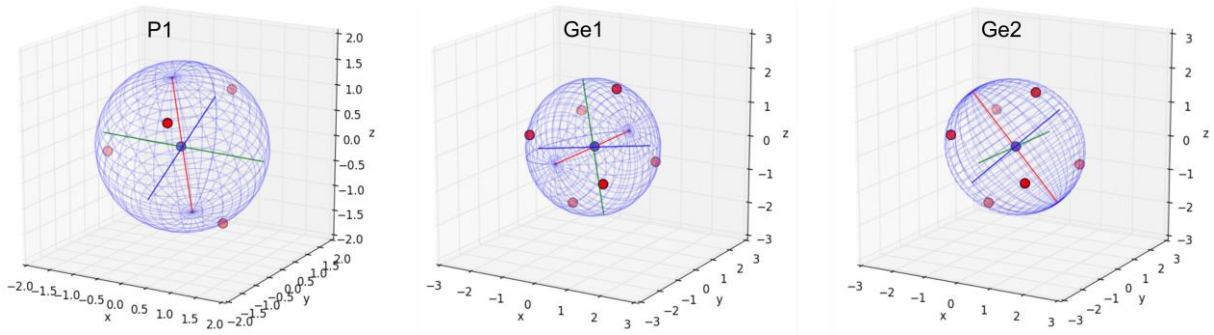

Figure S3.5: Graphical representation of the minimal bonding ellipsoids of the PN_4 tetrahedra and GeN_6 octahedra at 44.4(1) GPa fitted by the software PIEFACE (P/Ge in blue, N in red).

Table S3.14: Ellipsoid parameters of the PN_4 tetrahedra and GeN_6 octahedra in the $GePN_3$ structure at 44.4(1) GPa.

	*R*1	*R*2	*R*3	<*R*>	Sigma(*R*)	*S*	Center Displacement	Coord.
P1	1.6581	1.5829	1.5557	1.5989	0.0433	0.0282	0.0554	4
Ge1	1.9682	1.9440	1.7732	1.8952	0.0868	−0.0755	0.0768	6
Ge2	1.9584	1.9225	1.8450	1.9086	0.0473	−0.0220	0.0447	6

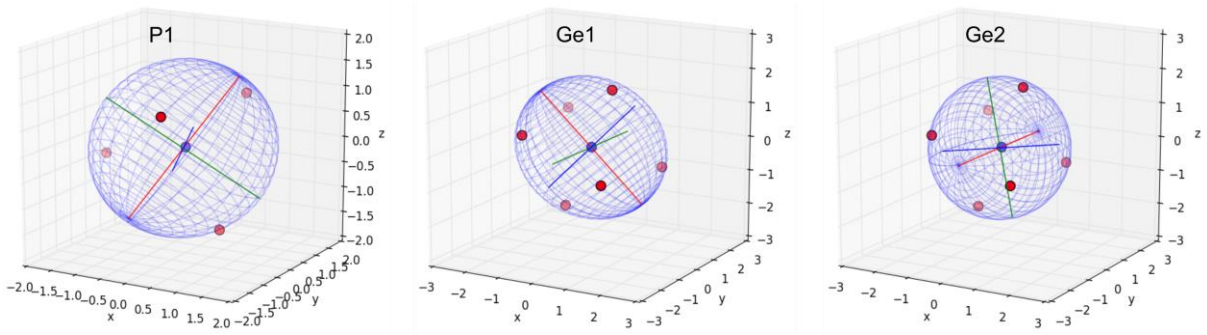

Figure S3.6: Graphical representation of the minimal bonding ellipsoids of the PN_4 tetrahedra and GeN_6 octahedra at ambient pressure fitted by the software PIEFACE (P/Ge in blue, N in red).

Table S3.15: Ellipsoid parameters of the PN_4 tetrahedra and GeN_6 octahedra in the $GePN_3$ structure at ambient pressure GPa.

	*R*1	*R*2	*R*3	<*R*>	Sigma(*R*)	*S*	Center Displacement	Coord.
P1	1.7134	1.6478	1.5888	1.6500	0.0509	0.0025	0.0656	4
Ge1	2.1096	2.0101	1.8805	2.0001	0.0938	−0.0174	0.0232	6
Ge2	2.1062	2.0151	1.7943	1.9719	0.1309	−0.0663	0.0948	6

Density of States

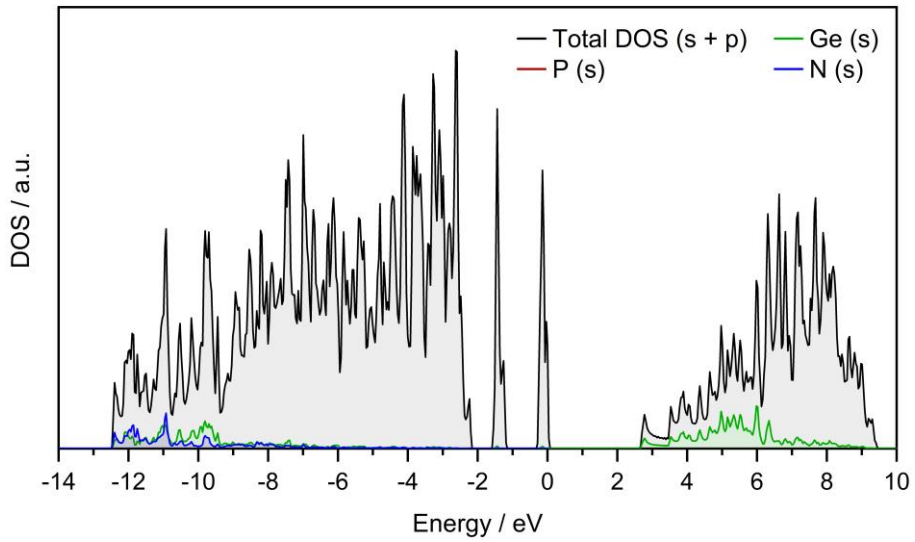

Figure S3.7: Partial and total s-contribution of single elements to the density of states.

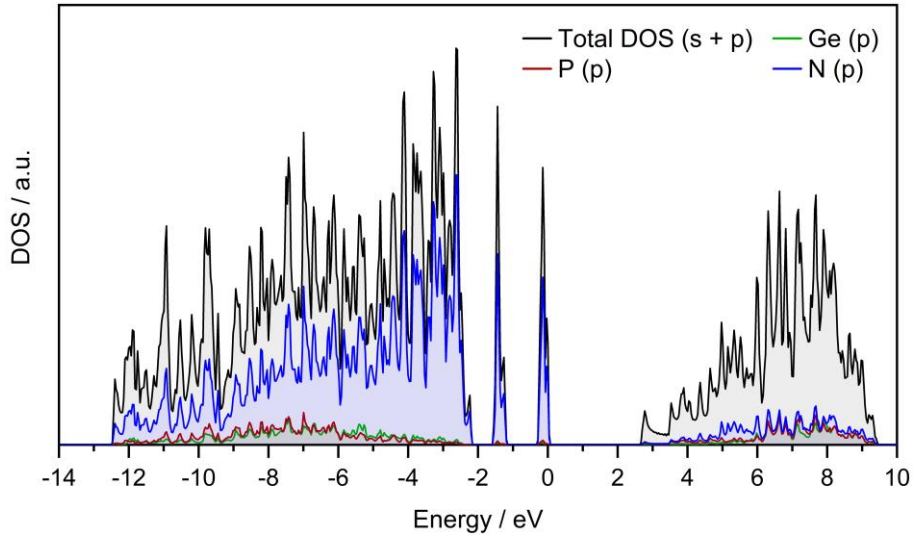

Figure S3.8: Partial and total p-contribution of single elements to the density of states.

References

[1] S. J. Ambach, C. Somers, T. de Boer, L. Eisenburger, A. Moewes, W. Schnick, *Angew. Chem. Int. Ed.* **2023**, *62*, e202215393.

9.4 Supporting Information for Chapter 5

Energy-Dispersive X-Ray Spectroscopy

Table S4.1: Overview of EDX measurements of $Sn_3P_8N_{16}$. Results are given in atomic percent. Standard deviations are given in parentheses.

	1	2	3	4	5	6	Ø	Norm. (Sn)
Sn	10	11	12	13	9	9	10(1)	3.0(4)
P	29	30	33	33	26	27	30(3)	8.3(8)
N	55	55	52	52	60	59	56(3)	15.6(9)
O	6	4	3	3	5	6	4(1)	1.2(4)

Temperature-Dependent Powder X-Ray Diffraction

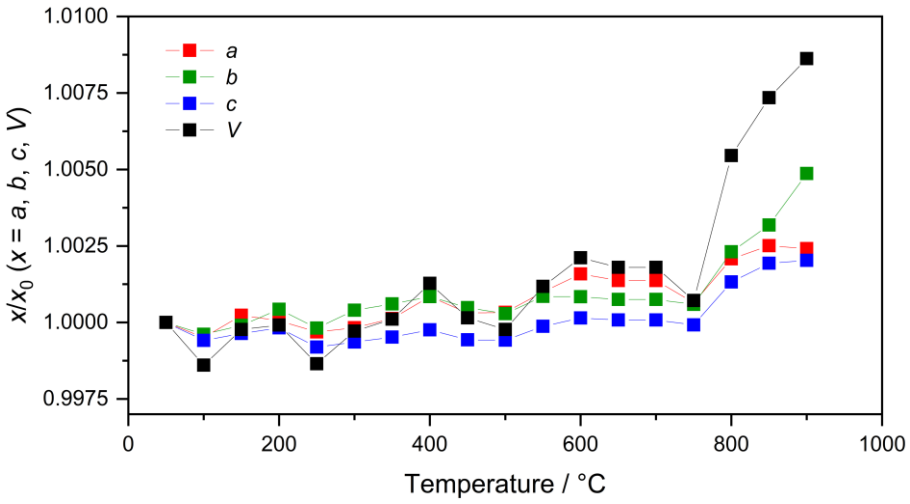

Figure S4.1: Temperature dependent powder X-ray diffraction patterns (Ag-$K\alpha_1$ radiation, λ = 0.55954 Å) of $Sn_3P_8N_{16}$. No significant change in the unit cell volume is observed until 750 °C, which is the threshold of decomposition into molten Sn and an amorphous material.

Crystallographic Data

Table S4.2: Wyckoff positions, coordinates, isotropic thermal displacement parameters, and occupancy of $Sn_3P_8N_{16}$ from single-crystal refinement. Standard deviations are given in parentheses.

Atom	Wyck.	*x*	*y*	*z*	U_{eq}	*occ.*
Sn1	4*i*	0.61037(4)	0	0.27418(9)	0.01285(13)	1
Sn2	4*i*	0.51120(11)	1/2	0.56121(16)	0.0064(3)	0.5
P1	8*j*	0.61211(8)	0.22707(9)	0.6621(2)	0.00317(19)	1
P2	8*j*	0.66366(8)	0.36742(9)	1.2078(2)	0.00277(19)	1
N1	8*j*	0.6082(3)	0.3586(3)	0.4729(7)	0.0045(6)	1
N2	4*h*	1/2	0.1466(4)	1/2	0.0044(8)	1
N3	8*j*	0.6236(3)	0.2548(3)	0.9913(7)	0.0045(6)	1
N4	8*j*	0.7046(2)	0.1343(3)	0.6232(7)	0.0056(6)	1
N5	4*i*	0.6237(4)	1/2	1.0425(10)	0.0048(9)	1

Table S4.3: Anisotropic displacement parameters (U_{ij} / Å^2) of $Sn_3P_8N_{16}$ from single crystal refinement. Standard deviations are given in parentheses.

Atom	U_{11} / Å^2	U_{22} / Å^2	U_{33} / Å^2	U_{12} / Å^2	U_{13} / Å^2	U_{23} / Å^2
Sn1	0.0144(2)	0.0146(2)	0.0067(2)	0	−0.0003(1)	0
Sn2	0.0058(6)	0.0033(3)	0.0120(7)	0	0.0053(6)	0
P1	0.0024(4)	0.0036(4)	0.0032(4)	0.0006(4)	0.0006(3)	0.0002(3)
P2	0.0028(4)	0.0027(4)	0.0029(4)	0.0008(4)	0.0010(3)	0.0000(3)
N1	0.0085(15)	0.003(1)	0.003(1)	0.001(1)	0.004(1)	0.001(1)
N2	0.005(2)	0.004(2)	0.003(2)	0	−0.001(2)	0
N3	0.0059(15)	0.004(1)	0.004(1)	0.000(1)	0.001(1)	−0.001(1)
N4	0.0019(15)	0.007(2)	0.007(2)	0.001(1)	−0.001(1)	−0.004(1)
N5	0.008(2)	0.004(2)	0.004(2)	0	0.003(2)	0

Table S4.4: Interatomic distances (Å) of $Sn_3P_8N_{16}$ from single-crystal refinement. Standard deviations are given in parentheses.

Atoms	Distance / Å	Atoms	Distance / Å	Atoms	Distance / Å
Sn1–N2	2.604(3)	P1–N1	1.679(4)	P2–N1	1.667(5)
Sn1–N4	2.246(3)	P1–N2	1.648(3)	P2–N3	1.572(4)
Sn2–N1	2.110(4)	P1–N3	1.573(4)	P2–N4	1.627(3)
Sn2–N1	2.140(4)	P1–N4	1.621(4)	P2–N5	1.635(3)
Sn2–N5	2.290(5)				

Table S4.5: Interatomic angles (°) of $Sn_3P_8N_{16}$ from single-crystal refinement. Standard deviations are given in parentheses.

Atoms	Angle / °	Atoms	Angle / °	Atoms	Angle / °
N2–Sn1–N2	74.78(16)	N1–P1–N2	109.07(16)	N1–P2–N3	109.5(2)
N2–Sn1–N4	62.08(9)	N1–P1–N3	111.31(18)	N1–P2–N4	105.41(18)
N2–Sn1–N4	108.37(11)	N1–P1–N4	110.3(2)	N1–P2–N5	160.0(3)
N1–Sn2–N1	86.2(3)	N2–P1–N3	110.40(16)	N3–P2–N4	112.40(19)
N1–Sn2–N1	164.77(5)	N2–P1–N4	100.89(16)	N3–P2–N5	111.85(18)
N1–Sn2–N1	90.9(3)	N3–P1–N4	114.30(18)	N4–P2–N5	111.2(3)
N1–Sn2–N5	106.02(14)				
N1–Sn2–N5	89.13(14)				

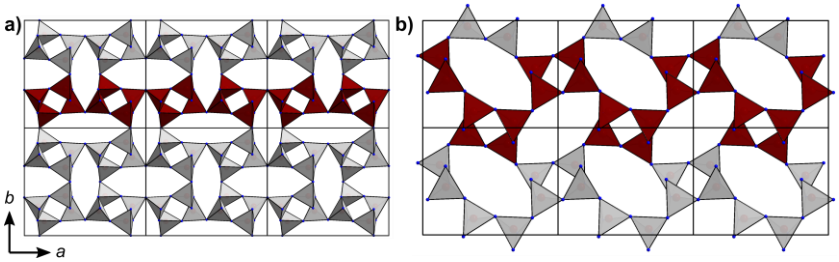

Figure S4.2: Visualization of the differences between the $Sn_3P_8N_{16}$ PN_4 tetrahedra network and the paracelsian network. Both network types form *vierer*-rings of PN_4 tetrahedra along [100]. a) In case of $Sn_3P_8N_{16}$, the interconnection of *vierer*-rings leads to a straight chain. b) In case of the paracelsian type (GeP_2N_4 as example), the interconnection leads to an undulated chain. The differences are reflected in the closely related, but different, point symbols $\{4^2.6^3.8\}\{4^2.6\}$ and $\{4^2.6^3.8\}$ for $Sn_3P_8N_{16}$ and GeP_2N_4, respectively.

Charge Distribution Calculations

Table S4.6: Results of the CHARDI calculation for $Sn_3P_8N_{16}$. All calculated values match the theoretical charges with a maximum deviation of 7%. The theoretical charge of the Sn2 site is +4, however, reduced to +2 due to the 50:50 split position. The low effective coordination number of the Sn1 site can be explained by the unusual long Sn1–N2 bonds (2.604(3) Å).

Polyhedron	**P1 N1–N2–N3–N4**	**P2 N1–N3–N4–N5**	**Sn1 N2–N2–N4–N4**	**Sn2 N1–N1–N1–N1–N5**
Average bond length / Å	1.6300	1.6254	2.4253	2.1578
Polyhedral volume / $Å^3$	2.2055	2.1972	3.5589	7.4357
Distortion index (bond length)	0.02036	0.01630	0.07388	0.02446
Quadratic elongation	1.0057	1.0024	-	-
Bond angle variance / $°^2$	20.4237	9.0956	-	-
Effective coordination number (theory)	3.9065 (4)	3.9278 (4)	3.0787 (4)	4.8361 (5)
Total charge (theory):				
P/Sn	4.977 (5)	5.050 (5.0)	1.895 (2)	2.052 (2)
N1	–2.946 (–3)	–2.946 (–3)	-	−2.946 (−3)
N2	–2.796 (–3)	-	–2.796 (–3)	-
N3	–3.020 (–3)	–3.020 (–3)	-	-
N4	–3.299 (–3)	–3.299 (–3)	–3.299 (–3)	-
N5	-	−2.862 (−3)	-	−2.862 (−3)

Minimal Bonding Ellipsoid Calculations

Table S4.7: Results of the MBE calculation for $Sn_3P_8N_{16}$. In case of P1 and P2, the values describe typical PN_4 tetrahedra.

	*R*1	*R*2	*R*3	<*R*>	Sigma(*R*)	*S*	Center Displacement	Coord.
P1	1.7007	1.6400	1.5409	1.6272	0.0659	−0.0247	0.080174	4
P2	1.6494	1.6263	1.5960	1.6239	0.0219	−0.0046	0.0727	4
Sn1	2.2794	1.9073	1.0380	1.7416	0.5202	−0.2925	1.0772	4
Sn2	2.2883	2.2833	1.8012	2.1242	0.2284	−0.2090	0.3641	5

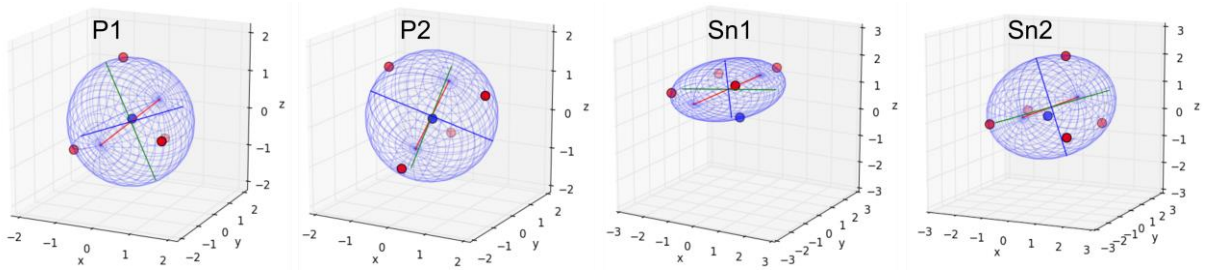

Figure S4.3: Graphical representation of the minimal bonding ellipsoids calculated by the software PIEFACE (P/Sn in blue, N in red).

Solid State Magic-Angle Spinning Nuclear Magnetic Resonance Spectroscopy

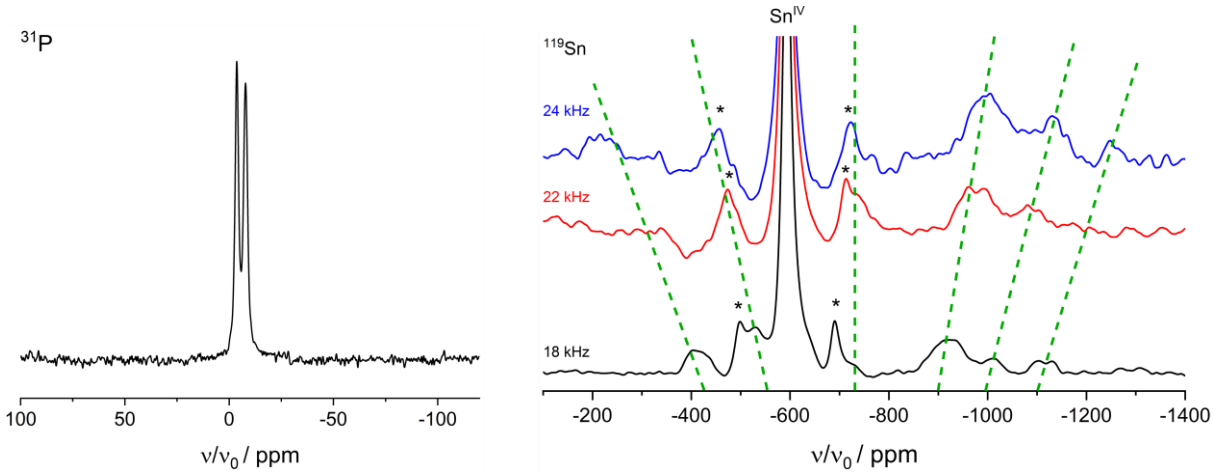

Figure S4.4: ^{31}P and ^{119}Sn solid-state MAS NMR spectra of $Sn_3P_8N_{16}$. For ^{119}Sn, spectra of different spinning frequencies for the identification of the isotropic Sn^{II} signal are shown. The evolution of Sn^{II} signal shifts depending on the spinning frequency are indicated with green dashed lines. The Sn^{IV} signal is cut and its rotational sidebands are indicated with asterisks (*).

To identify the isotropic signal of the Sn^{II} site, ^{119}Sn MAS NMR spectra with different spinning frequencies were recorded. Static solid-state NMR spectra of powdered samples usually show very broad signals for each crystallographic site, often with asymmetric intensity. By magic-angle spinning, the total intensity is collapsed into a single isotropic signal. This, however, only works if the spinning frequency is sufficiently large to average the interaction responsible for the broadening. This is the case for the ^{31}P shown on the left of Figure S4. With insufficient spinning frequency, rotational sidebands remain around the isotropic signal (e.g. in this case for ^{119}Sn). While the isotropic signal always stays at the same position, the positions of the rotational sidebands vary with the spinning frequency, making it possible to identify the isotropic signal of the Sn^{II} site in $Sn_3P_8N_{16}$. Due to hardware limitations, the maximum spinning frequency was by far insufficient to obtain a single isotropic signal, and instead multiple additional sidebands were observed. Comparing the chemical shifts of all signals at spinning frequencies of 18, 22 and 24 kHz, the isotropic signal was found at $\delta \approx -730$ ppm, partially overlapping with a sideband of the Sn^{IV} signal. All spectra are plotted in Figure S4 with additional green dashed lines, indicating the shift of rotational sidebands.

Mössbauer Spectroscopy

Table S4.8: Fitting parameters of the ^{119}Sn Mössbauer spectroscopic measurement for $Sn_3P_8N_{16}$ at 78 K. δ = isomer shift, ΔE_Q = quadrupole splitting, Γ = experimental line width.

Signal	δ / mm · s^{-1}	ΔE_Q / mm · s^{-1}	Γ / mm · s^{-1}	Ratio / %	Ox. Sn
blue	0.49(1)	1.78(1)	0.82(1)	35(1)	+IV
green	3.39(1)	1.69(1)	0.97(1)	65(1)	+II

Density of States

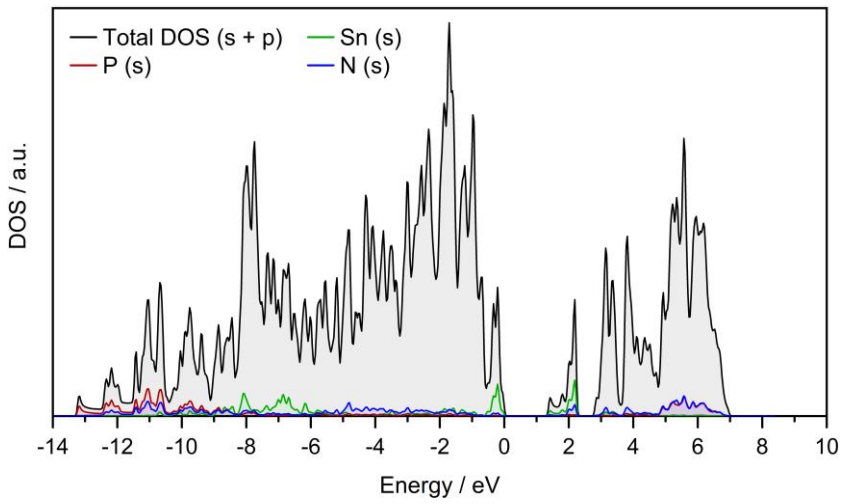

Figure S4.5: Partial and total s-contribution to the density of states.

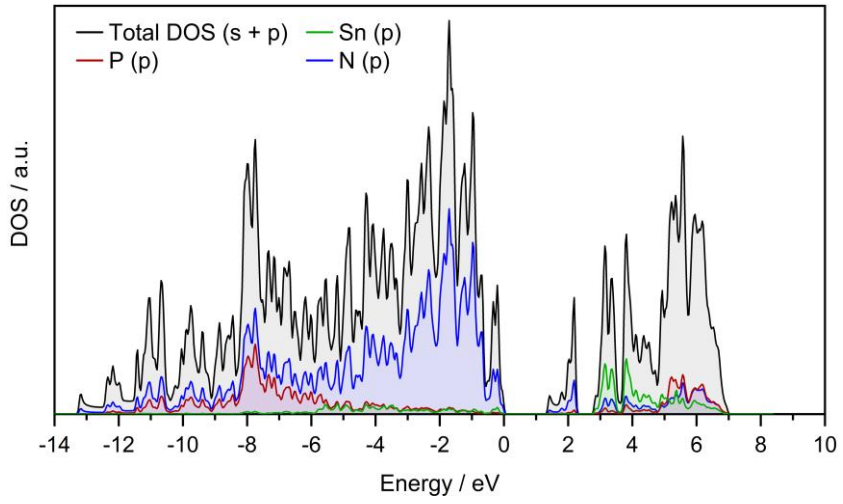

Figure S4.6: Partial and total p-contribution to the density of states.

9.5 Supporting Information for Chapter 6

Schematic Cross-Section of the Assembly

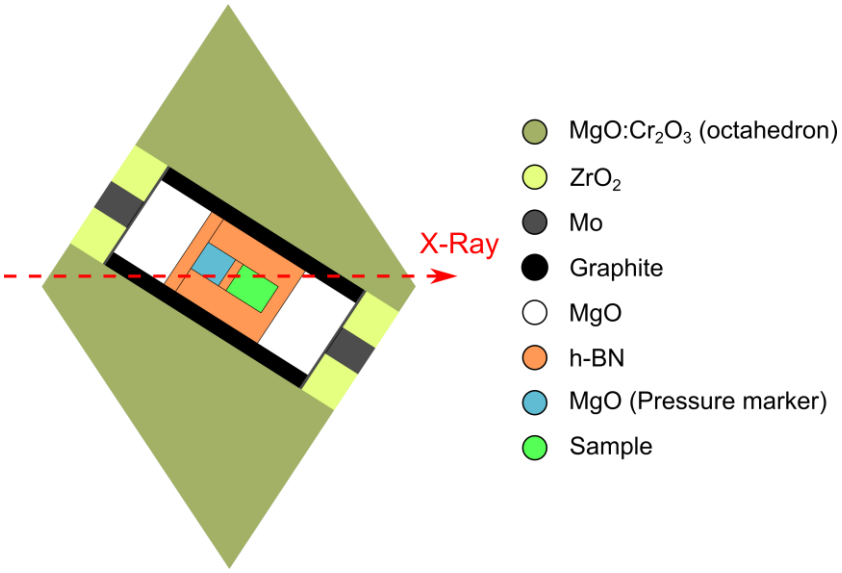

Figure S5.1: Schematic cross-section of the assembly.

Temperature Calibration

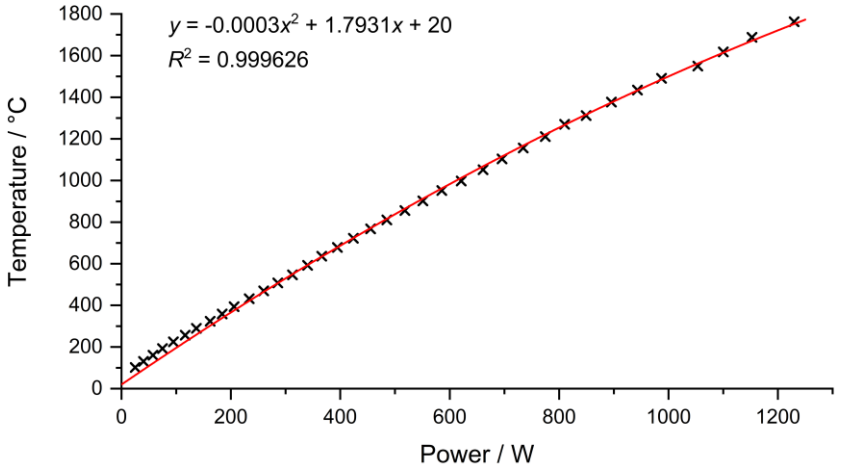

Figure S5.2: Temperature calibration curve for the assembly using DC-heating. The calibration was done at a pressure of 8 GPa using a Pt/PtRh-thermocouple and a bulk BN cylinder instead of the BN crucible. Temperatures were measured in the middle of the BN part and averaged over multiple runs. The data points were fitted with quadratic equation (fixed value of y = 20 °C at x = 0 W).

Pressure Program of the Large-Volume Press

Pressures are specified as hydraulic oil pressure of the large-volume-press (LVP, Aster-15, Max Voggenreiter GmbH, Mainleus, Germany) at beamline P61B, DESY, Hamburg, Germany. Actual sample pressures were determined using MgO as a pressure marker. Tables S1 and S2 show the pressure programs used for experiment 1 and 2, respectively. Heating was done during segment 3 at a constant oil pressure.

Table S5.1: Pressure program of the first experiment for a general overview.

Segment	Target oil pressure / bar	Time / min
1	30	30
2	200	90
3	200	100
4	10	630
5	0	10

Table S5.2: Pressure program for the time-resolved experiment.

Segment	Target oil pressure / bar	Time / min
1	30	30
2	180	90
3	180	110
4	20	180
5	0	20

Locating the Sample

Before starting any measurement, the sample was located using the X-Ray contrast of Zn supported by the added pieces of Ta, shown in figure 1.

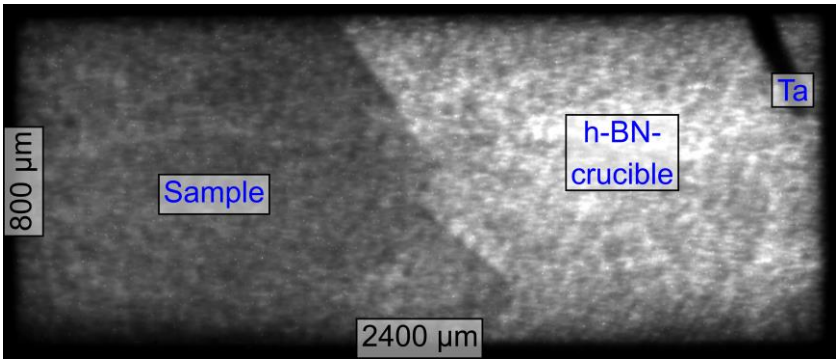

Figure S5.3: X-ray image of the assembly before compression. Sections can be identified by their different X-ray contrast (Ta: black, sample: dark gray, h-BN-crucible: light gray). The image is clipped by surrounding WC-anvils (black) on all sides. The anvil gap (800 µm) is lowered to approx. 200 µm during compression.

Energy-Dispersive X-Ray Spectroscopy

Table S5.3: Overview of EDX measurement points. Results are given in atomic percent. Standard deviations are given in parentheses.

Atom	1	2	3	4	5	6	Ø	Norm. (Zn)
Zn	45	51	45	54	54	44	49(4)	2.0(2)
P	18	19	19	17	22	22	19(2)	0.8(1)
N	31	26	33	26	22	29	28(4)	1.1(1)
O	6	4	3	3	2	5	4(1)	0.2(1)

Chapter 10

Miscellaneous

10.1 List of Publications in this Thesis

The following enumeration contains all publications within this thesis in chronological order, including title, authors, citation, and author contributions.

1. Structural Influence of Lone Pairs in GeP_2N_4, a Germanium(II) Nitridophosphate

Sebastian J. Ambach, Cody Somers, Tristan de Boer, Lucien Eisenburger, Alexander Moewes, Wolfgang Schnick

Angew. Chem. Int. Ed. **2023**, *62*, e202215393

The syntheses and formal analyses were performed by Sebastian Ambach and Tim Reska over the course of his research internship that was supervised by Sebastian Ambach and Wolfgang Schnick. The crystal structure was elucidated by Sebastian Ambach and Lucien Eisenburger. DFT calculations were performed by Cody Somers and Tristan de Boer. Sebastian Ambach wrote the manuscript and Alexander Moewes and Wolfgang Schnick supervised the project. All authors contributed to the discussion of the results and revised the manuscript.

2. Combining MN_6 Octahedra and PN_5 Trigonal Bipyramids in the Mica-like Nitridophosphates MP_6N_{11} (M = Al, In)

Sebastian J. Ambach, Monika Pointner, Sophie Falkai, Carsten Paulmann, Oliver Oeckler, Wolfgang Schnick

Angew. Chem. Int. Ed. **2023**, *62*, e202303580

The syntheses were performed by Sebastian Ambach and Sophie Falkai over the course of her Bachelor thesis that was supervised by Sebastian Ambach and Wolfgang Schnick. X-ray diffraction data collection and structure elucidation was performed by Monika Pointner and Carsten Paulmann. Further data analysis was done by Sebastian Ambach. Sebastian Ambach wrote the manuscript and Oliver Oeckler and Wolfgang Schnick supervised the project. All authors contributed to the discussion of the results and revised the manuscript.

3. Building Nitridic Networks with Phosphorus and Germanium – from $Ge^{II}P_2N_4$ to $Ge^{IV}PN_3$

Sebastian J. Ambach, Georg Krach, Elena Bykova, Kristian Witthaut, Nico Giordano, Maxim Bykov, Wolfgang Schnick

Inorg. Chem. **2024**, *63*, 8502

In situ experiments in the diamond anvil cell and initial data processing was performed by Sebastian Ambach, Maxim Bykov, Elena Bykova and Georg Krach. The structure elucidations were done by Sebastian Ambach. Beam line support during experiments was given by Nico Giordano. DFT calculations were performed by Kristian Witthaut. Sebastian Ambach wrote the manuscript and Wolfgang Schnick supervised the project. All authors contributed to the discussion of the results and revised the manuscript.

4. Mixed Tin Valence in the Tin(II/IV)-Nitridophsophate $Sn_3P_8N_{16}$

Sebastian J. Ambach, Aylin Koldemir, Kristian Witthaut, Sandra Kreiner, Thomas Bräuniger, Rainer Pöttgen, Wolfgang Schnick

Chem. Eur. J. **2024**, *accepted*

The syntheses were performed by Sebastian Ambach and Sandra Kreiner. The structure solution and formal data analysis was done by Sebastian Ambach. Aylin Koldemir conducted the Mössbauer experiments and analyzed the data thereof. DFT calculations were performed by Kristian Witthaut. Thomas Bräuniger supervised the NMR experiments and analyzed the resulting data. Sebastian Ambach wrote the major part of the manuscript. Supervision of the research project was headed by Wolfgang Schnick and Rainer Pöttgen. All authors contributed to the discussion of the results and revised the manuscript.

5. Nitride Synthesis Under High-Pressure High-Temperature Conditions – Unprecedented in-situ Insight into the Reaction

Sebastian J. Ambach, Reinhard M. Pritzl, Shrikant Bhat, Robert Farla, Wolfgang Schnick

Inorg. Chem. **2024**, *63*, 3535

The *in-situ* experiments were performed by Sebastian Ambach and Reinhard Pritzl. Data processing was done by Sebastian Ambach. Shrikant Bhat and Robert Farla provided beam line support during the experiments. Sebastian Ambach wrote the manuscript. Supervision of the research project was headed by Wolfgang Schnick. All authors contributed to the discussion of the results and revised the manuscript.

10.2 List of Publications beyond this Thesis

The following enumeration lists the publications beyond this thesis in chronological order, including title, authors, citation, and author contributions.

1. **Band Gap and Electronic Structure of Defects in the Ternary Nitride BP_3N_6: Experiment and Theory**

   Tristan de Boer, Md F. Al Fattah, Muhammad R. Amin, Sebastian J. Ambach, Sebastian Vogel, Wolfgang Schnick, Alexander Moewes

   J. Mater. Chem. C **2022**, *10*, 6429

2. **The Importance of Lone Pairs to Structure and Bonding of the Novel Germanium Nitridophosphate GeP_2N_4**

   Tristan de Boer, Cody Somers, Teak Boyko, Sebastian J. Ambach, Lucien Eisenburger, Wolfgang Schnick, Alexander Moewes

   J. Mater. Chem. A **2023**, *11*, 6198

3. **High-Pressure Synthesis, Crystal Structure, and Characterization of the New Non-Centrosymmetric Terbium Borate $Tb_3B_{10}O_{17}(OH)_5$**

   Tobias A. Teichtmeister, Christian Paulsen, Sebastian J. Ambach, Klaus Wurst, Lkhamsuren Bayarjargal, Wolfgang Schnick, Huber Huppertz

   J. Solid State Chem. **2023**, *325*, 124170

4. **Simple Molecules under High-Pressure and High-Temperature Conditions: Synthesis and Characterization of α- and β-$C(NH)_2$ with Fully sp^3-Hybridized Carbon**

   Thaddäus J. Koller, Siyu Jin, Viktoria Krol, Sebastian J. Ambach, Umbertoluca Ranieri, Saiana Khandarkhaeva, James Spender, Stewart McWilliams, Florian Trybel, Nico Giordano, Tomasz Poreba, Mohamed Mezouar, Xiaoyu Kuang, Cheng Lu, Leonid Dubrovinsky, Natalia Dubrovinskaia, Andreas Hermann, Wolfgang Schnick, Dominique Laniel

   Angew. Chem. Int. Ed. **2024**, *63*, e202318214

10.3 Conference Contributions and Oral Presentations

1. **Behind the Scenes**
   Sebastian J. Ambach
   Talk, Schnick Group Seminar
   Munich (Germany), 01.07.2020

2. **Neutral Nitridic Networks & *in-situ* HP/HT Experiments**
   Sebastian J. Ambach
   Talk, Lumileds Meeting
   Munich (Germany), 01.12.2020

3. **Phosphorus Nitrides under Pressure – *ex-situ* and *in-situ***
   Sebastian J. Ambach
   Talk, DESY user meeting
   Hamburg (Germany), 01.02.2021

4. **Schicht-Strukturen in Schicht-Arbeit**
   Sebastian J. Ambach
   Talk, Schnick Group Seminar
   Munich (Germany), 23.06.2021

5. **Von alten und neuen Dingen**
   Sebastian J. Ambach
   Talk, Schnick Group Seminar
   Munich (Germany), 13.07.2022

6. **High-Pressure High-Temperature *in-situ* Experiments**
   Sebastian J. Ambach
   Talk, 6. Obergurgl-Seminar Festkörperchemie
   Obergurgl (Austria), 26.01.2023

7. **Structural Influence of Lone Pairs in GeP_2N_4, a Germanium(II) Nitridophoosphate**
   Sebastian J. Ambach, Cody Somers, Tristan de Boer, Lucien Eisenburger, Alexander Moewes, Wolfgang Schnick
   Poster, 11th International Symposium on Nitrides
   Saint-Malo (France), 03.05.2023

8. **Structural Influence of Lone Pairs in GeP_2N_4, a Germanium(II) Nitridophoosphate**
   Sebastian J. Ambach, Cody Somers, Tristan de Boer, Lucien Eisenburger, Alexander Moewes, Wolfgang Schnick
   Poster, 18th European Conference on Solid State Chemistry
   Prague (Czech republic), 10.07.2023

9. **Rauf und runter in der 4. Hauptgruppe**
   Sebastian J. Ambach
   Talk, Schnick Group Seminar
   Munich (Germany), 15.11.2023

10. **Lone Electrons Under Pressure**
    Sebastian J. Ambach
    Talk, 7. Obergurgl-Seminar Festkörperchemie
    Obergurgl (Austria), 01.02.2024

10.4 Deposited Crystal Structures

The Crystallographic Information Files (CIF) of the investigated compounds are provided free of charge by the joint Cambridge Crystallographic Data Centre and Fachinformationszentrum Karlsruhe Access Structures servide (http:www.ccdc.cam.ac.uk/structures) by quoting the corresponding deposition number.

Compound	CSD-
AlP_6N_{11}	2241809
GeP_2N_4	2210954
GeP_2N_4 (0 GPa)	2335702
GeP_2N_4 (44.4 GPa)	2335703
$GePN_3$ (44.4 GPa)	2335704
$GePN_3$ (0 GPa)	2335705
$Sn_3P_8N_{16}$	2341441